



HAL
open science

Two-Polarization dynamics in optically delayed lasers

Chi-Hak Uy

► **To cite this version:**

Chi-Hak Uy. Two-Polarization dynamics in optically delayed lasers. Optics / Photonic. Centrale-Supélec, 2018. English. NNT: 2018CSUP0006 . tel-02860058

HAL Id: tel-02860058

<https://theses.hal.science/tel-02860058>

Submitted on 8 Jun 2020

HAL is a multi-disciplinary open access archive for the deposit and dissemination of scientific research documents, whether they are published or not. The documents may come from teaching and research institutions in France or abroad, or from public or private research centers.

L'archive ouverte pluridisciplinaire **HAL**, est destinée au dépôt et à la diffusion de documents scientifiques de niveau recherche, publiés ou non, émanant des établissements d'enseignement et de recherche français ou étrangers, des laboratoires publics ou privés.



CentraleSupélec

N° d'ordre : 2018-07-TH



CentraleSupélec

Ecole Doctorale C2MP

« *Chimie Mécanique. Matériaux Physique* »

Laboratoire LMOPS

« *Laboratoire Matériaux Optiques, Photonique et Systèmes* »

THÈSE DE DOCTORAT

DOMAINE : SPI

Spécialité : Photonique

Soutenue le
31 octobre 2018

par :

Chi-Hak UY

Two-Polarization dynamics in optically delayed lasers

Composition du jury :

Directeur de thèse :	Marc SCIAMANNA	Professeur, CentraleSupélec
Co-directeur de thèse :	Damien RONTANI	Maître de conférences, CentraleSupélec
Rapporteurs :	Frédéric GRILLOT	Professeur, Télécom ParisTech
	Krassimir PANAJOTOV	Professeur, Vrije Universiteit Brussel
Examineurs :	Stefan BREUER	Dr. Habil., Technische Universität Darmstadt
	Cristina DE DIOS FERNANDEZ	Professeur, Universidad Carlos III de Madrid
	Germano MONTEMEZZANI	Professeur, Université de Lorraine

TABLE OF CONTENTS

	Page
1 Introduction	1
1.1 From maser to laser : the story of Charles H. Townes	2
1.2 Physics of lasers	6
1.2.1 Principle	6
1.2.2 Semiconductor lasers	9
1.2.3 From edge to surface-emitting lasers	11
1.2.4 Relaxation oscillations	12
1.3 Some Applications of lasers	14
1.3.1 Optical communications	14
1.3.2 LIDAR for optical ranging and aerosol detection	15
1.4 Nonlinear dynamics and chaos in laser diodes	16
1.4.1 The strange-attractor of Lorenz	17
1.4.2 Bifurcation diagram of the Lorenz's equations	19
1.4.3 Analogy between lasers and the Lorenz's system	21
1.4.4 Classification of lasers	23
1.4.4.1 Class C lasers	23
1.4.4.2 Class B lasers	24
1.4.4.3 Class A lasers	24
1.4.5 Unlocking nonlinear dynamics in semiconductor lasers	24
1.4.5.1 Different approaches	24
1.4.5.2 Optical feedback and route to chaos	26
1.5 Applications of chaos in laser diodes	29
1.5.1 Chaos for secure communication	29
1.5.2 Chaotic LIDAR for ranging	30

TABLE OF CONTENTS

1.6	Conclusion, objectives and outlines	31
2	Polarization instabilities in VCSELs and non-local correlation property in low-frequency fluctuation regime	33
2.1	Polarization properties in VCSELs	34
2.1.1	Polarization instabilities in VCSELs in comparison with EELs	35
2.1.2	Types of polarization switching	36
2.1.2.1	Polarization selection from gain competition	37
2.1.2.2	Polarization selection from gain competition and losses	39
2.1.3	Prediction of polarization switching from spin relaxation process	41
2.1.4	Application of polarization instabilities	45
2.1.4.1	Random bits generation	45
2.1.4.2	Logical gates	46
2.1.4.3	High-frequency oscillation generation	47
2.1.4.4	Reservoir computing based on two polarization modes	47
2.2	VCSEL under optical feedback and low-frequency fluctuation regime	49
2.2.1	Steady-States and External Cavity Modes	50
2.2.2	Low-Frequency Fluctuation mechanism	52
2.2.3	LFF in polarization modes of VCSELs	54
2.2.4	Observation of double-peak structures in the literature	58
2.3	Experimental investigation	59
2.3.1	Experimental setup	59
2.3.2	LFF : Double peak and correlation features in the RF spectrum	61
2.4	Physical origin of the double-peak structure	64
2.4.1	Phase-space dynamic and mode/antimode interaction	65
2.4.2	Double-peak structure with a single-mode model	69
2.5	Conclusion	70
3	Vectorial Rogue Wave in VCSEL light polarizations	73
3.1	Observations of Rogue Wave	74
3.1.1	Freak wave in oceanography	74
3.1.2	Identification of rogue waves	75
3.1.3	Rogue Waves in optics and motivation	77
3.2	Observations of Extreme Events in VCSELs	79

3.2.1	Two types of extreme events in VCSELs	81
3.3	Extreme events statistics	84
3.3.1	Deviation from a Gaussian distribution	84
3.3.2	Waiting times between successive events	85
3.4	Generation rate of extreme events	87
3.4.1	Vectorial Extreme events	89
3.4.2	Noise effect on the generation rate of EEs	90
3.4.3	Differences between Type-I and Type-II LFF	91
3.5	Modal competition effect on the EEs generation rate	93
3.6	Conclusion and perspective	95
4	Sustained oscillations accompanying polarization switching in a laser diode	97
4.1	Square-wave modulation in optics	98
4.2	Bifurcation to high-frequency oscillation in square-wave regime	102
4.2.1	Description of the experimental setup	103
4.2.2	An overview on the observed dynamics	104
4.2.3	Effects of the feedback ratio and the injection current	105
4.2.4	Influence of the delay	106
4.3	Numerical Investigation	108
4.3.1	Rate equations for EEL subjected to a PROF	108
4.3.2	Bifurcation scenario leading to sustained oscillations	109
4.3.3	Influence to the delay	111
4.3.4	Effect of the laser parameters	113
4.3.4.1	Pump parameter P	113
4.3.4.2	Carrier to photon lifetime ratio T	115
4.3.4.3	Linewidth enhancement factor α	117
4.3.4.4	Gain coefficient ratio k and TM additional losses β	118
4.3.5	Effect of noise	119
4.4	Analytical investigation on the sustained oscillations frequency	122
4.4.1	Steady states	123
4.4.2	Hopf bifurcations	124
4.4.3	Approximations	125
4.5	Conclusion and perspectives	127

TABLE OF CONTENTS

5	Optical chimera in light polarization	129
5.1	Chimera state : a coexistence of coherence and incoherence	130
5.1.1	Demonstration of spatially extended chimera states	131
5.1.1.1	Chemical oscillators	131
5.1.1.2	Optoelectronic oscillators	132
5.1.1.3	Mechanical oscillators	133
5.1.2	Chimera states in optical spectrum and virtual-space	134
5.1.2.1	In the optical spectrum of a mode-locked laser	135
5.1.2.2	In a virtual space from a time-delay system	135
5.1.3	Discussion on optical chimera state	138
5.2	Chimera state in laser polarization	140
5.2.1	Experimental setup	140
5.2.2	Theoretical model	142
5.2.3	Observation of virtual chimera states	142
5.2.4	Stabilization of multi-headed chimeras with a 2^{nd} delay	144
5.2.5	Multi-stability and chimera-heads mechanisms	147
5.2.6	Influence of the initialization and of the feedback strength	149
5.2.6.1	Influence of the initialization	149
5.2.6.2	Influence of the PROF strength	150
5.3	Conclusion	154
6	Conclusion	157
6.1	Summary, contributions and perspectives	157
7	Résumé de la thèse	167
	Bibliography	177

INTRODUCTION

More than fifty years after their invention, lasers keep improving their performances; and their application domains are constantly broadening [1]. It has become a fundamental tool in various fields of metrology as in telemetry to measure distances, for gyroscopes to measure angular speeds, for lidar to detect objects, their motions and even sometime their shapes. In the latter case, it also allows the detection of pollution in air and the measurement of the Earth's surface topology. Lasers have also paved the way for safer, more precise and/or new treatments in medicine as for the cure of glaucomas which can cause vision losses, to burn cancerous tumors, and even in plastic surgery for long-term hair removal and cellulite erasing. It is also a powerful tool in industry for welding and cutting materials, in telecommunication with the development of fiber optics, in chemistry for spectroscopy and astronomy for the exploration of cosmological physics.

The goal of this introduction is to present the context of this thesis and to provide the required basics to follow the thesis work. It is also an opportunity to acknowledge the work of great scientists that laid the foundation for laser modern applications such as Charles H. Townes, inventor of the maser, pioneer of the laser who persevered through thick and thin in his research.

This Chapter is organized as follows : first we introduce the story of laser as it was related by Townes in his autobiography published in 1999 [2]. Then, we explain what

a laser is and its principle of operation. We also provide details on the well-spread semiconductor lasers. Secondly, we highlight the discovery of chaos and nonlinear dynamics and how lasers are able to display such dynamics. We emphasize on the importance of chaotic lasers in many innovative applications. Finally, we introduce the main objectives of our work and summarize the outlines of the thesis.

1.1 From maser to laser : the story of Charles H. Townes

The goal of this section is to recall the work of Charles H. Townes (1915-2015), inventor of the maser¹ and Nobel Laureate in 1964. In his book *How the Laser Happened* published in 1999 [2], Townes relates about his adventure that led him to design the first maser despite the criticisms of famous physicists.

In 1935, Townes was one of the only two students in physics from Furman University. He was offered an assistantship at Duke University, where he worked on Van de Graff generators, an accelerator of protons using static electricity. At that time, he failed to get a full-time fellowship in several other universities better known for their physics programs. Nevertheless, with hindsight, he will later be always grateful for those failures as he decided afterward to go to Caltech without any financial support in 1937. His PhD thesis was on the separation of stable isotopes of oxygen, nitrogen and carbon upon which he improved his spectroscopy skills. This later served him as a starting point for the realization of the first maser. In 1939, he got a position at AT&T's Bell Labs and quickly worked on military radar bombing systems as the United States were about to get involved in the World War II. The purpose of his work was probably aimed to be used for the atomic bomb just after the discovery of nuclear fission. One of the challenge he faced was to reach a sub-centimeter aiming-accuracy that would be achieved by generating an electromagnetic wave at the same order of wavelength. He did extensive study of ammonia (NH₃), a highly present molecule in the Pacific showing strong resonances at sub-centimeter wavelength. The war ended and Townes never reached such accuracy. However, his research on ammonia absorption led him to pursue in sub-centimeter wavelength

¹microwave amplification by stimulated emission of radiation

generation from molecular spectroscopy. In 1950, he was invited to join Columbia University by Isidor Isaac Rabi, who received the Nobel prize in physics in 1944.

In 1951, a small committee of physicists including Townes gathered to find a proper way to generate sub-centimeter wavelength. It was already known at that time that molecular transitions involve absorption and emissions at millimeter-wavelength. However, in order to get an output energy sufficiently high, the sample had to be shined by a tremendous amount of power. The meeting ended without any convincing solution. However, it was during this meeting that Townes thought about making a cavity in which excited molecules would be placed. From the stimulated emission theory of Einstein, the electromagnetic wave would be amplified after crossing the sample of molecules [see Fig. 1.1]. He kept the idea for himself as he wasn't that sure yet how far it would go.

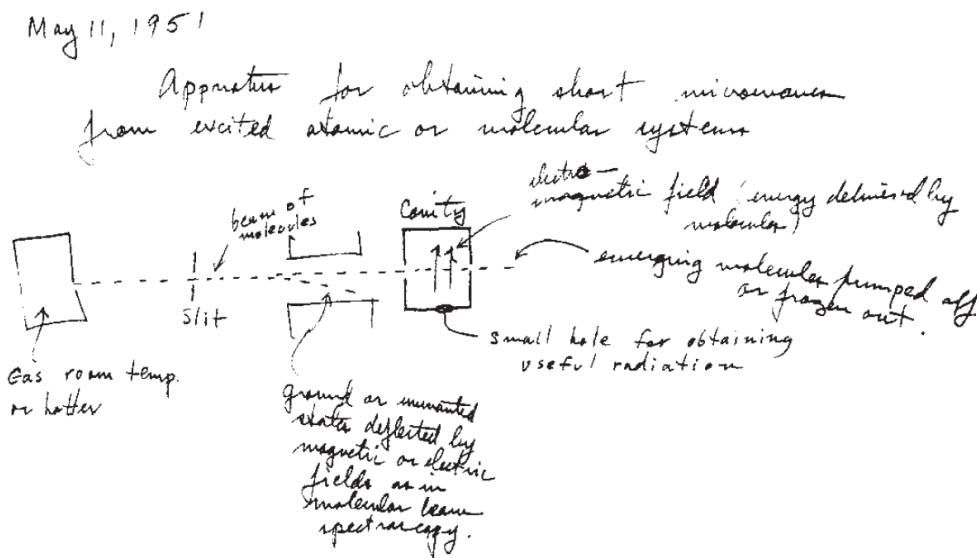


Figure 1.1: First draft of a maser drawn by Townes during the sub-centimeter committee meeting in 1951. It consists on a constant beam of excited molecules sent into a cavity. The figure is taken from Ref. [2].

Back to Columbia University, he double-checked his first calculations based on ammonia as the excited medium. He predicted not only an amplification of the wave, but also a coherent beam at nearly a constant wavelength. With Jim Gordon, a freshly graduated student from MIT and Herb Zeiger, a former PhD student of Isaac Rabi in the field of molecular beam, Townes launched his first experimental

project on maser. For this first attempt, they settled on using the strongest ammonia transition at 1.25 cm. Two years after the beginning of the project, the maser was still not running and Townes and his coworkers faced a lot of criticism from Rabi and Kusch². As reported by Townes in his book, he was told : "*you should stop the work you are doing. It isn't going to work. You know it's not going to work. We know it's not going to work. You're wasting money. Just stop!*".

Three months later, after carefully trying different angles for the gas beam and looking for the good material for the cavity to lower the losses, Jim Gordon has achieved the first working maser. It was in April of 1954. The same day, they decided to name this device *maser* which stands for "*microwave amplification by stimulated emission of radiation*" [3, 4]. The picture in Fig. 1.2 shows J. Gordon and C.H. Townes with another maser build after the prototype. This second maser was build to measure the maser spectral purity by making both masers beating together.

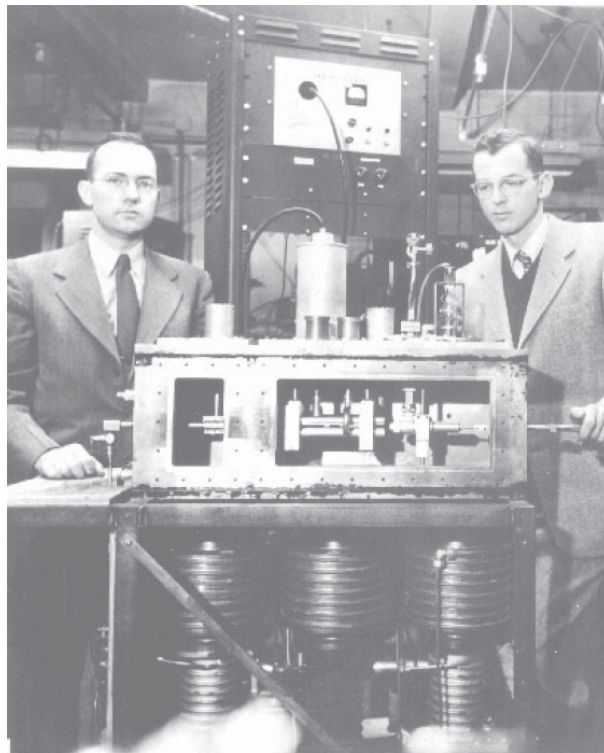


Figure 1.2: J. Gordon (right) and C.H. Townes (left) with the second maser at Columbia University.

²future Nobel Laureate in 1955 and chairman of the department at the time

With this demonstration, masers have aroused interest of many groups in spectroscopy and atomic clocks. Some have even stated maliciously that maser stood for "*means of acquiring support for expensive research*" and indeed it did give Townes research support. However, still this maser wasn't of great use as it wasn't tunable in wavelength and wasn't neither at sub-centimeter wavelength.

In 1958, with Schawlow, one of this his former post-doc and actual brother-in-law, he published one of the most important paper for the future design of optical maser *i.e.* laser which stands for "*Light amplification by stimulated emission of radiation*" [5]. They theoretically considered a Fabry-Perot cavity and explained how the cavity selects resonant wavelengths while suppressing the others. It was in 1960, that Theodore Maiman demonstrated for the first time a working laser [6] using a ruby crystal and two layers of aluminum forming the aforementioned Fabry-Perot cavity. The next year, Ali Javan, a former PhD student of Townes, demonstrated the helium-neon laser [7]. In 1962, Robert N. Hall [8] demonstrated the first semiconductor laser.



Figure 1.3: (left to right) Theodore Maiman, Ali Javan and Robert N. Hall

Charles H. Townes received in 1964 the Nobel Prize in physics³ for the invention of maser that paved the way for lasers. Since then, lasers have been used in numerous fields of research, leading to important Nobel Prize discoveries : D. Gabor in 1971 for holography, N. Bloembergen, A. Schawlow, K.M. Siegbahn in 1981 for laser spectroscopy, S. Chu, C. Cohen Tannoudji, W.D. Phillips in 1997 for atom cooling

³that he shared with Bassov and Prokhorov, two Russians that independently worked also on maser

using laser, and B.C. Barish, Rainer Weiss, K. Thorne in 2017 for laser interferometry technique used in the LIGO detector and for the observation of gravitational waves.

1.2 Physics of lasers

The underlying theory of maser, described in the previous section, has later inspired the invention of laser. In this section, we will explain the main aspects of this theory and introduce semiconductor laser.

1.2.1 Principle

Laser is an acronym which stands for *light amplification by stimulated emission of radiation*. The mechanism of stimulated emission was predicted in 1916 by Albert Einstein [9] from quantum theory [10]. Stimulated emission provides a second coherent photon with the similar energy than the incoming photon, hence it creates a coherent amplification of the light. The energy of a photon E_{phot} is given by $E_{phot} = h\nu$ with h the Plank constant and ν the electromagnetic frequency of the photon. However, stimulated emission also competes with other light-matter processes : the spontaneous emission and the absorption. In Fig. 1.4, we describe these mechanisms and consider a single atom with two atomic levels : E_1 and E_2 which are respectively the ground-state and the excited-state (*i.e.* $E_2 > E_1$). The three mechanisms are described as follow :

- **Absorption** [Fig. 1.4 (a)] : an incoming photon is absorbed by an atom in the energy level E_1 . The atom goes to the excited energy level E_2
- **Spontaneous emission** [Fig. 1.4 (b)] : the atom is already in its excited energy level E_2 . Without any external perturbation, the atom spontaneously goes down to the ground state E_1 by emitting a photon of energy $E_{phot} = E_2 - E_1$. Here the photon has a random phase.
- **Stimulated emission** [Fig. 1.4 (c)] : the atom is already in its excited energy level E_2 . An incoming photon of energy $E_{phot} = E_2 - E_1$ stimulates the transition of the atom toward the ground state E_1 . The process is accompanied by the emission of an additional photon with identical phase and frequency to the incoming photon : it brings light amplification.

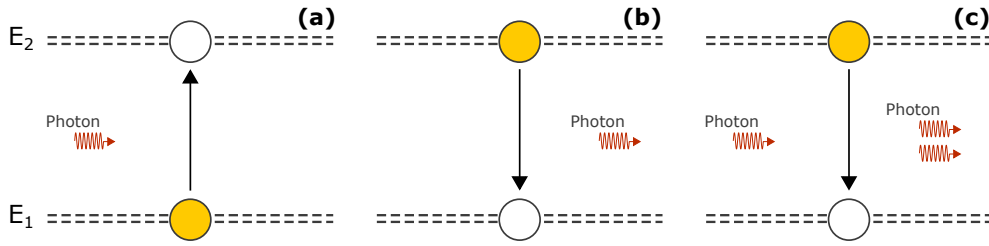


Figure 1.4: Light-matter mechanisms in a two-energy level system with E_1 the energy of the ground state and E_2 the energy of the excited state (a) Absorption of a photon by an atom in its ground state E_1 causing its transition to the excited state E_2 . (b) Spontaneous emission of a photon by an atom in its excited state E_2 causing its transition to the ground state E_1 . (c) Stimulated emission by an atom in its excited state E_2 due to the stimulation of an incoming photon. The transition of the atom toward the ground-state E_1 creates a second identical photon.

Hence, when stimulated emission becomes the dominant process, light amplification is obtained. However, it requires to have more atoms in the excited state than in the ground state. This situation is called *population inversion*. It can be obtained with different methods called *pumping*. For the gas maser of Townes [3], population inversion was achieved by continuously injecting excited molecule of ammonia. For the ruby laser of Maiman [6], the pumping is achieved from a light source that cause absorption. For the Helium-Neon [7] and the semiconductor laser [8], the pumping is achieved by applying an electrical current to the active medium.

Finally, wavelength selection is performed by placing the gain medium inside a resonant optical cavity. Traditionally, the resonator is a simple Fabry-Perot cavity made of parallel and partially reflecting mirrors. Only electromagnetic waves which satisfy the boundary conditions imposed by the mirrors can constructively propagate back and forth in the cavity. They are called modes of the laser and their optical frequency difference Δf is given by the *Free-Spectral Range* (FSR) :

$$(1.1) \quad \Delta f = FSR = \frac{c}{2L},$$

with $c = 299792458$ m/s the speed of light and L the length of the Fabry-Perot cavity. Furthermore, only modes that have an energy, hence an wavelength, that matches the difference of energy between the ground-state and the excited-state of the active medium can be amplified. The cavity also reduces the amount a pumping necessary

to achieve population inversion as it ensures a large number of photons in the gain medium which participate in the stimulated-emission process.

The laser starts to emit a coherent beam of photons when the gain in the cavity exceeds the losses (caused by absorption and by photons exiting the cavity). This particular state, where the gain equalizes the losses, is called the *laser threshold*. Figure 1.5 shows a typical instance of light-pump curve of a laser. When the pump energy is too low to compensate the losses in the cavity, the laser emission is mostly driven by the spontaneous emission. On the contrary after the threshold, population inversion is reached, the stimulated emission becomes the dominant process and coherent emission of light is obtained.

In summary, lasing effect requires three main ingredients:

- A gain medium with stimulated emission (*i.e.* amplification),
- A pump to ensure population inversion,
- A resonator to select the emission wavelength and to reduce the amount of pumping necessary for lasing.

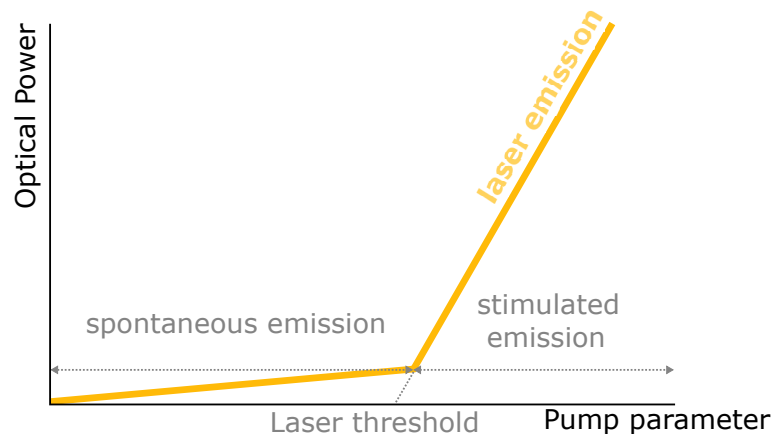


Figure 1.5: Illustration of a typical light-pump curve of a laser. Before the threshold, the laser emission is mostly driven by spontaneous emission of incoherent light. At the threshold, the gain equalizes the losses in the laser cavity. A coherent light is obtained beyond the threshold point where stimulated emission becomes the dominant radiative process.

1.2.2 Semiconductor lasers

Semiconductor laser (or *laser diode*) is today one of the most common type of lasers. Due to their small size, they are mass-produced at a very low-cost. Here, we introduce their basic structure and mechanism.

In semiconductor lasers, radiative transitions typically occur between upper energy states in the conduction band and lower energy states in the valence band. Conduction and valence bands are separated by an energy band-gap where electrons are forbidden. At zero temperature, electrons occupy energy states in the valence band. On the contrary, when increasing the temperature, some of the electrons might occupy energy states in the conduction band leaving an empty space in the valence band called *holes* that can be considered as a virtual positively charged particle.

In addition, as seen previously, population inversion is a vital condition to obtain optical amplification. The simplest semiconductor structure to achieve population inversion in the so called *p-n junction* in which a p-type semiconductor is in contact with a n-type semiconductor. p- and n-type semiconductors are defined by their *doping i.e.* the addition of impurities in the material. In p-type semiconductor, the doping creates an excess of holes while in n-type, it creates an excess of electrons.

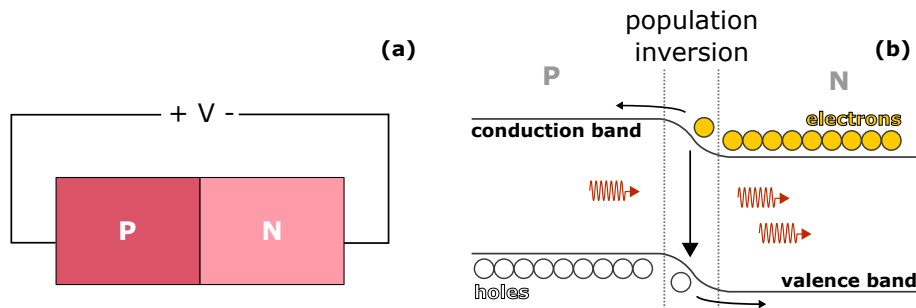


Figure 1.6: (a) Illustration of a p-n junction with a forward bias V . (b) Corresponding energy band diagram. Population inversion is achieved at the junction.

When these two semiconductors are in contact, diffusion of carriers occurs : the electrons diffuse toward the p-region and the holes toward the n-region. The diffusion stops when an equilibrium is reached. This effect creates a difference of potential at the junction which acts as barrier of potential preventing any further electrons to flow toward the p-region and holes toward the n-region. The barrier can be lowered by applying a *forward bias* between the p-region and the n-region allowing the

electrons in the n-region to drift toward the p-region and the hole in the p-region to drift toward the n-region. This constant stream of carriers creates a tiny region at the junction where population inversion is observed as depicted in Fig. 1.6. A p-n junction is also referred to as a *homojunction* because the band gap is similar in both the p and n-regions.

Although laser action can be obtained from an homojunction, it has soon been found to be unsatisfactory as it requires low temperature, high pumping current and it was difficult to maintain a continuous-wave operation [11]. In 1963, Herbert Kroemer, Nobel Laureate in 2000, proposed another structure where a small band gap material is placed in between two higher band gap materials. This structure is called *double heterostructure* [12]. In Fig. 1.7, we show a typical double heterostructure. The double barrier surrounding the active region (p-region here) prevents the electrons to flow toward the p^+ -region and the holes toward the n^+ -region. This greatly reduces the threshold current as it leads to a better carrier confinement. In addition, it provides a waveguide-like structure as the cladding layers have usually a smaller refractive index than the active layer. Hence, this structure also improves the gain uniformity along the direction of propagation in the active medium and enhances the stimulated emission process.

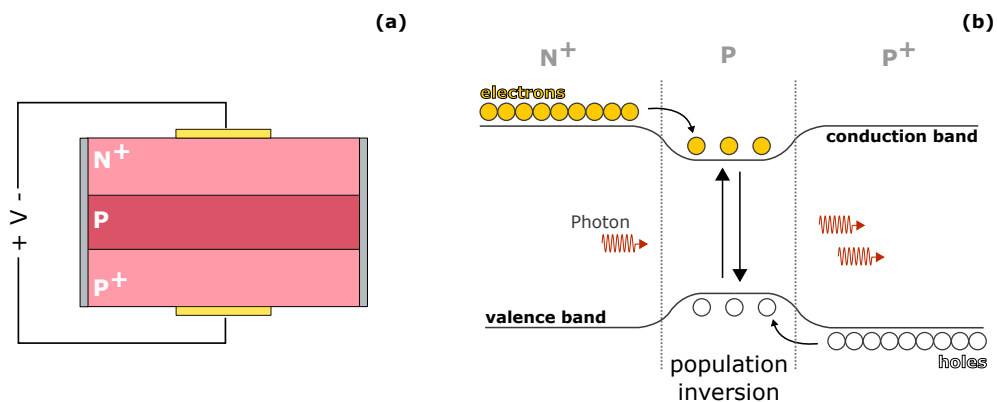


Figure 1.7: (a) Illustration of a double heterostructure made of two p-n junctions. (b) Corresponding energy band diagram. Population inversion is achieved in between the two p-n junctions.

1.2.3 From edge to surface-emitting lasers

Historically, the Edge-emitting laser (EEL) in Fig. 1.8 (a) is the original structure proposed for semiconductor lasers [12]. Its energy-band diagram rely on the double heterostructure shown in Fig. 1.7. The resonator length is typically about few hundreds of micrometer to one millimeter which is sufficient to achieve high-gain without the need of high-quality Fabry-Perot mirrors. In fact, the resonator is simply based on Fresnel reflections at the air/semiconductor interfaces (with usually a power reflectivity of $\approx 30\%$). The light is emitted from the edge of the device *i.e.* orthogonal to the semiconductor growth direction. In addition, due to the geometry of the active region, EEL shows a larger region of amplification in the x-direction than in the y-direction. As a result, the polarization of the output light is usually polarized linearly in the x-direction called the *TE-mode* while the *TM-mode* polarized in the y-direction is depressed.

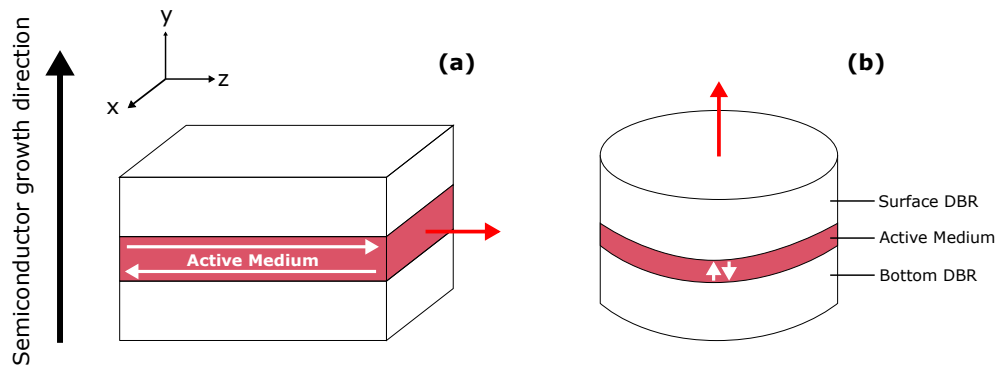


Figure 1.8: Illustration of (a) an EEL emitting a laser beam orthogonally to the semiconductor growth direction and (b) a VCSEL having the active medium in between two DBR. The light is pointed in the same direction as the semiconductor growth direction.

However, one main drawback of EEL is that, due to their direction of emission, one cannot test the laser directly on the wafer or neither making a 2D-array of it without cleaving it first. In 1979, Soda *et al.* proposed a double-heterostructure which allows the emission of a $1.2\ \mu\text{m}$ light in the semiconductor-growth direction : the vertical-cavity surface-emitting laser (VCSEL) [13]. In addition, contrary to EELs which typically have a cavity length of the order of micrometers, the VCSEL cavity length is usually of the order of nanometers. As a result, to keep a reasonable threshold

current value, one has to decrease the losses, hence increasing the mirror reflectivity dramatically. In the first VCSEL proposed, the mirrors were made from gold [14]. However, although gold has almost a reflectivity of 95% at 1.2 μm wavelength, the device still requires a tremendous amount of pumping current with a threshold at 900 mA (11kA/cm²). The need of high-reflectivity mirrors has led to the use of distributed Bragg reflectors in which different layers of semiconductor with alternatively low and high refractive indices are stacked vertically. The first proposal was made by Ogura *et al.* in 1987 [15] following by a great improvement in term of reflectivity (in the order of 99%). This has allowed a threshold current of about 1 mA in 1989 by Jewell *et al.* [16].

In addition of its capability to emit light from the surface, VCSEL demonstrates nowadays very low threshold current (≈ 0.5 mA) and emits a quasi-perfect circular beam due its cylindric structure compared to EELs which usually emits elliptical beam. Furthermore, as we will discussed in Chapter 2 VCSELs show intriguing polarization properties which are detrimental for telecommunication applications but might also bring interesting dynamical behaviors. Indeed, contrary to EEL, the geometry of the active region in VCSEL does not favor any polarization direction resulting in polarization instabilities [17, 18].

1.2.4 Relaxation oscillations

As we have seen, laser operation relies on the interplay between photons and carriers, which is at the origin of what is called *relaxation oscillations*. For example, an increase of the pumping current leads to an enhancement of the population inversion in the active medium. Thus, as more electrons are excited, the stimulated emission rate increases creating more photons in the cavity and enhancing the optical power. However, while stimulated emission processes occur, more and more carriers are consumed. The decrease in carrier weakens the stimulated emission rate leading to lower optical power until the carriers build up again. The loop occurs periodically several times and manifests itself by damped oscillations of the laser output power until the laser settles on his new operating point. This dynamic is referred to as *relaxation oscillations*. The corresponding frequency is usually of the order of 1 to 15 GHz in semiconductor lasers.

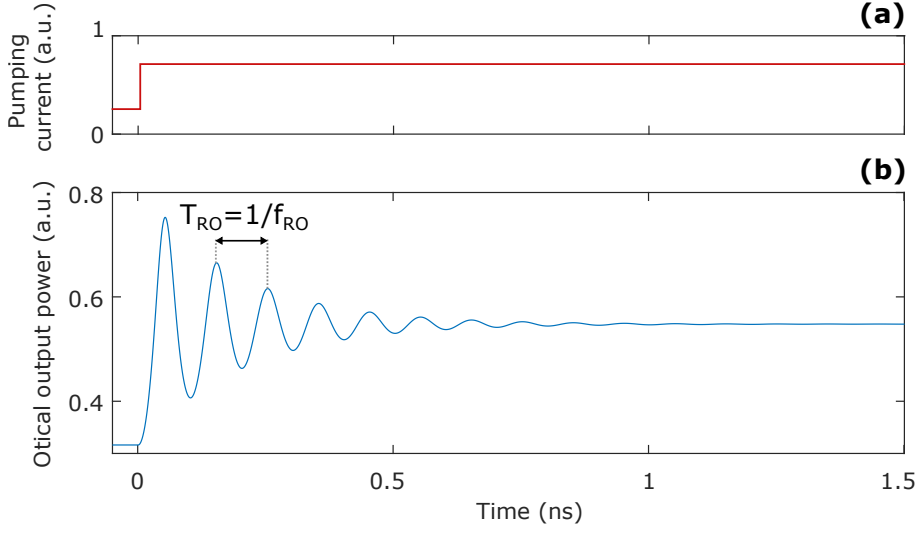


Figure 1.9: (a) Step in pumping current occurring at $t=0$. (b) Before the step, the laser is operating in a continuous wave emission. At $t=0$, the pumping current is increased resulting in relaxation oscillations of the output power at a frequency $f_{RO} \approx 11$ GHz. The oscillations' amplitude decreases until reaching another steady-state with higher optical power.

The law that drives the relaxation oscillation frequency f_{RO} to the pumping current J is given by :

$$(1.2) \quad f_{RO} = \frac{1}{2} \sqrt{\frac{1}{\tau_c \tau_p} \left(\frac{J}{J_{th}} - 1 \right)},$$

where τ_c is the carrier lifetime, τ_p is the photon lifetime and J_{th} is the pumping current at the laser threshold. The relaxation oscillation frequency is in the same range that the direct modulation frequency limit *i.e.* the maximum frequency achieved by a modulation of the pumping current.

Experimentally, f_{RO} can be deduced by applying a step of current as described in Fig. 1.9 or by measuring the *relative intensity noise* (RIN) of the laser. The RIN describes the temporal fluctuation of the laser output power when operating at constant parameters (fixed current and temperature). It is usually visualized in the Radio-Frequency (RF) domain and is characterized by a peak at the relaxation oscillation frequency f_{RO} . When measuring the RIN of a laser on a RF spectrum analyzer, one has to subtract the noise of the equipments N_{eq} from the RF obtained

signal N_{meas} [19]. N_{eq} is mainly driven by the thermal noise N_{th} which can be measured before switching on the laser. For a more accurate measure of RIN, the shot-noise N_{sn} of the photodiode has to be also measured. Shot-noise originates from random excitations of carriers in the photodiode which depends on the mean optical intensity that reaches the detector.

1.3 Some Applications of lasers

In the previous sections, we have related the story that led to the invention of lasers and their fundamental physics. In the following, we have selected two applications of lasers which have revolutionized modern society such as optical telecommunication, and optical ranging. Of course, there would be many additional laser applications to cite, and more details can be found in many books [1, 14, 20].

1.3.1 Optical communications

The rise of modern optical communications is related to the invention of four main components : semiconductor lasers, low-loss optical fibers [21], optical amplifiers [22] and photodetectors as shown in Fig. 1.10.

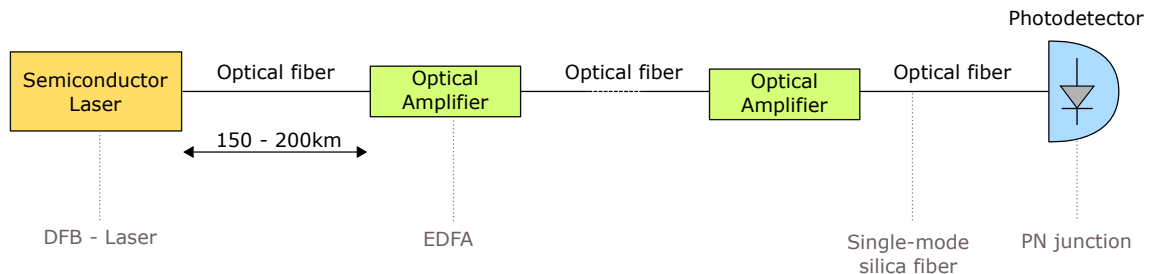


Figure 1.10: Illustration of modern optical communication architecture. A semiconductor laser emits a modulated light into an optical fiber. Each 150 – 200km an optical amplifier amplifies the optical signal until reaching a photodetector.

Back to basics, modern communications are digital implying that the signal is modulated as function of bits "0" or "1". For example, in optical links, the absence of light defines a "0" and the detection of light a "1"⁴. Nowadays, optical signals can

⁴in fact, there are many techniques of modulation as the PSK, ASK, QAM...

achieved data rate about 2.5 Gb/s to 40 Gb/s; this means light is modulated in this range of frequency. As a comparison, the first Internet system based on electrical links could only transmit data at 56kb/s ! The advantages of semiconductor lasers are threefold : 1/ they have low energy consumption and high optical power, 2/ the optical linewidth is narrow which allows multiplexing at hundred of wavelengths in a single fiber, 3/ they support high modulation speeds. In the latter case, lasers are limited to ≈ 10 GHz and external modulators are used to increase the modulation speed. Indeed, as we will see later, a modulation frequency of the pumping current close to the relaxation oscillation frequency may induce unwanted erratic fluctuations.

The second main discovery that led to optical communication was the optical fiber technology. Charles K. Kao received the physics Nobel Prize in 2009 for this discovery. The most widespread silica fiber has only an attenuation of 0.2dB/km at wavelength close to 1.5 μ m (also called the *conventional band* or *C-band*). Although the signal power is divided by a factor two after 15 km, propagation over 150 to 200 km is easily achieved. As a comparison, at this range of modulation frequency, electrical signal would be completely lost after hundreds of meters. The transverse profile of the fiber is also crucial : a single mode fiber (with a core diameter $< 8 \mu$ m) is mandatory to minimize temporal deformation of the optical signal. Nonetheless, very lately, multi spatial modes multiplexing in multimode fibers [23] are under investigation in order to increase the data rate in optical telecommunication. A new world record of 10 Pb/s in a single fiber has been achieved with this technique [24] in 2017.

After 150 km of propagation in fibers, an optical amplifier is placed. The underlying physics behind amplifiers also rely on stimulated emission of light. The most common technology is the Erbium-Doped Fiber Amplifier (EDFA) [22] that can directly amplify the light inside a doped fiber. Usually, the amplifier is pumped by a 980 nm laser. Finally, the light is detected by a semiconductor photodetector whose physics are very similar to semiconductor lasers. Instead of stimulated emissions at its PN junction, photodetectors create pairs of electrons and holes from absorption of light hence modifying the voltage at the junction.

1.3.2 LIDAR for optical ranging and aerosol detection

LIDAR stands for light detection and ranging. Similarly to RADARs, LIDAR are used for ranging applications but using light instead of microwaves. For LIDARs, a

laser emits pulses at nanosecond scales. When the light encounters an obstacle, a part of it is reflected back to the LIDAR. The position of the obstacle is deduced by measuring the delay between the emission and the detection time.

It is also possible to measure the speed of the obstacle using the Doppler effect. To do so, there are two main techniques : either measuring the deformation of the pulse shape by a moving object or by measuring the optical frequency shift of the light. The latter technique is called *heterodyne detection*.

LIDAR technology is used in a variety of fields such as for measuring the wind direction map and amplitude for wind farms, for the detection of threats in military context, for the detection of obstacles for future autonomous cars, drones and robots, for elevation measurement, for speed measurement of cars by police officers etc. Lately, an impressive technique has been reported for the detection of hidden objects [25] relying on the measurement of photons scattered by several objects in the environment. They used a femtosecond pulsed laser in order to achieve a better signal-to-noise ratio on their detector.

1.4 Nonlinear dynamics and chaos in laser diodes

Dynamical systems can be found in a large variety of subjects going from physics to biology, chemistry and engineering [26]. It has first started in the 17th century when Newton found the differential equations for the laws of motions and objects gravitational interactions such as gravitational motion of planets. Following Kepler's empirical laws, he solved the two-body problem taking the example of the earth trajectory around the Sun. However, physics have struggled for decades on the three-body problem when adding for example the moon dynamics into the equations. In the 19th, Poincaré demonstrated that this problem doesn't have an explicit solution *i.e.* one cannot find an explicit set of formulas that gives the positions of the moon, sun and earth simultaneously. This discovery by Poincaré is often considered as the first step towards what is called today *nonlinear dynamics*, *i.e.* a dynamical motion that does not directly and linearly relate to the changes in their operating conditions. However, due to the complexity of such systems, Poincaré's works have encountered only a little impact in the scientific community until the 50's with the invention of computers. It was in 1963 that Edouard Lorenz demonstrated from numerical

simulations that a set of deterministic equations⁵ describing a simple model of the atmosphere may result in a complex trajectory [27] : more specifically, an aperiodic dynamic that never repeats itself and that shows an utmost sensitivity to initial conditions. Such a dynamics has later been referred to as *chaos* [28].

In 1975, Haken showed theoretically the close analogy between laser equations and those used by Lorenz [29]. In this section, we will first introduced the work of Lorenz and the basics of chaotic dynamics and develop its analogy with lasers.

1.4.1 The strange-attractor of Lorenz

In 1963, while investigating convective fluids for weather prediction, Lorenz showed that a nonlinear system described by three state-variables shows large regions of parameters where the solutions never settle down on a periodic state or an equilibrium state. It was the first demonstration of *chaos*. The model he used is given by a set of three simple equations [27] :

$$(1.3) \quad \frac{dX}{dt} = -\sigma X + \sigma Y,$$

$$(1.4) \quad \frac{dY}{dt} = -XZ + rX - Y,$$

$$(1.5) \quad \frac{dZ}{dt} = XY - \beta Z,$$

where σ , r and β are the parameters of the system and X , Y and Z the state variables. As an example, we show in Fig. 1.11 (a-c) the time evolution of the state variables when taking the parameters $\sigma = 10$, $r = 30$ and $\beta = 8/3$. All three variables shows an erratic behavior despite no randomness (such as noise) is introduced in the equations. In Fig. 1.11, we show the trajectory of the system in the phase space where each axis stands for one state variable. The trajectory consists on two wings centered around two fixed points. In this dynamic, the system remains confined around what has been called a *strange attractor* as it bounds all trajectories in its neighborhood.

⁵without any random variables

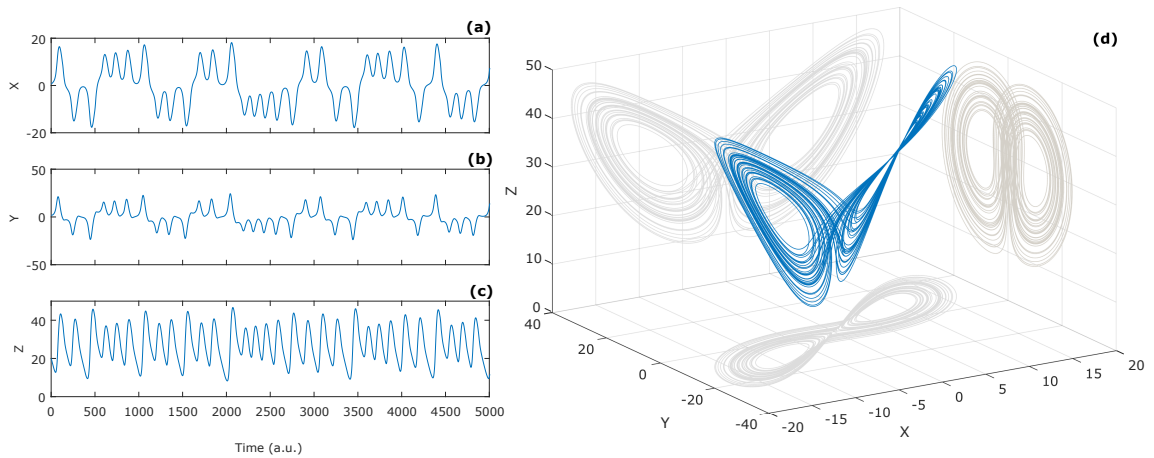


Figure 1.11: Time-evolution of the state variables (a) X, (b) Y and (c) Z and (d) the corresponding trajectory in the phase space. The simulated parameters are $\sigma = 10$, $r = 30$ and $\beta = 8/3$.

This attractor was also referred to as the *Butterfly* of Lorenz for its comparison to a butterfly and that has given the expression : the *butterfly effect*. The butterfly effect is a metaphor in chaos theory illustrating the sensitivity on initial conditions. Indeed, two nearby trajectories of a chaotic system diverge from each other exponentially fast. We illustrate this sensitivity in Fig. 1.12 (a) where we show the time evolutions of the variable X for two different sets of initial conditions $[X_0, Y_0, Z_0]$ while keeping the parameters fixed. In blue, we have initialized with $[0, 1, 1.05]$ while in orange we have chosen a different but yet very close set $[0.000001, 1.000001, 1.05000001]$. At the beginning, both time series remain quasi-identical until $t > 5000$ where differences appear. This is confirm in Fig. 1.12 (b), where the Euclidean distance⁶ between the two attractors is shown. At first, both trajectories are following the same journey until their distance increases quickly around $t = 5000$. However, they remain confined relatively close to each other as they are both attracted towards the same attractors.

⁶taking into account X, Y and Z

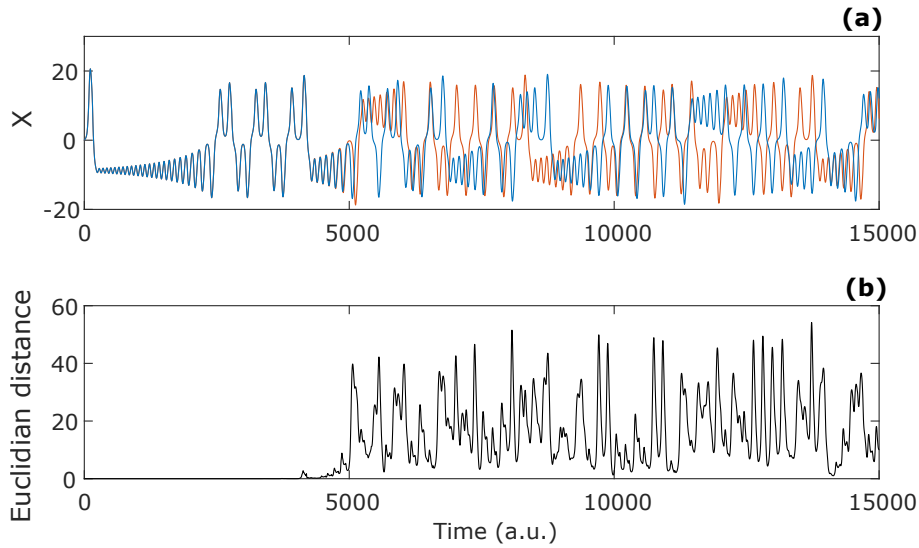


Figure 1.12: (a) Time evolution of the variable X for two different initializations. In blue, $[X_0, Y_0, Z_0] = [0, 1, 1.05]$ and in orange, $[X_0, Y_0, Z_0] = [0.000001, 1.000001, 1.05000001]$. (b) Corresponding Euclidean distance between the blue and the orange attractor.

In summary, a chaotic system can be described by the following three criteria :

- Aperiodicity : the trajectory does not settle on a steady state nor into periodic or quasi-periodic orbit as time goes to infinite.
- Determinism : the equations that model the system do not include any random term. Complex dynamics arise from the intrinsic nonlinearity.
- Sensitivity to initial conditions : for two very close initial states, their trajectories diverge exponentially fast.

1.4.2 Bifurcation diagram of the Lorenz's equations

Although chaotic dynamics is easily found from direct simulations of Eqs. (1.3)-(1.5), many different dynamics and complex waveforms can also be obtained when varying the simulation parameters. We show in Fig. 1.13 different solutions obtained when varying the parameter r . For $r = 0$ in Fig. 1.13 (a), the system is in its quiescent state with no fluctuation of its variables. Increasing r in Fig. 1.13 (b), chaotic fluctuation is observed. For $r = 160$ in Fig. 1.13 (c), X oscillates quasi-periodically at two different

frequencies and finally for high values of r in Fig. 1.13 (d), a periodic train of pulses is observed.

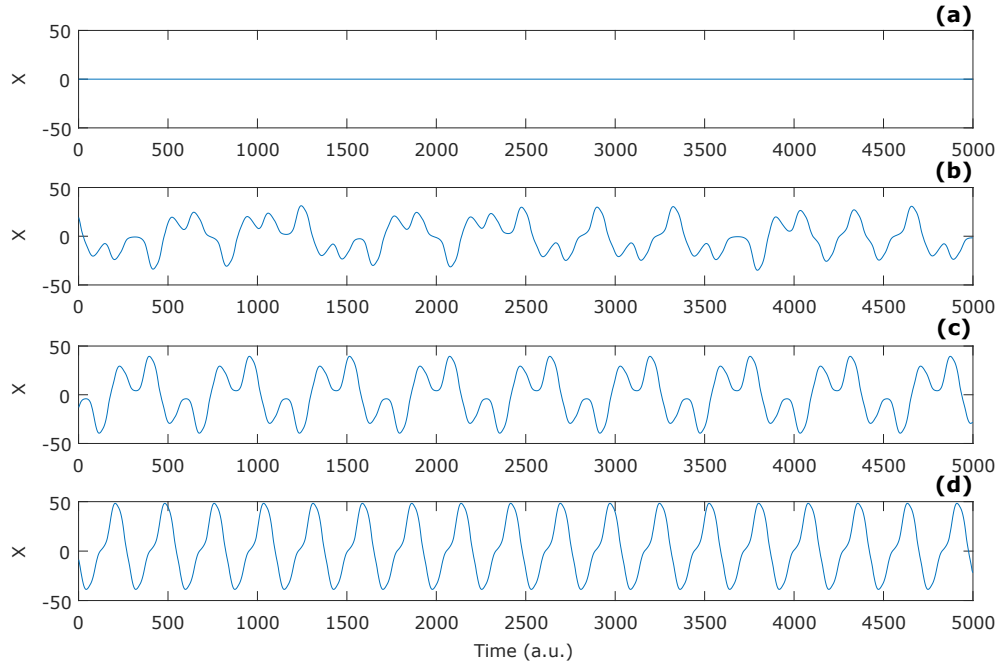


Figure 1.13: Time evolution of the variable X in the Lorenz equations for (a) $r = 0$, (b) $r = 100$, (c) $r = 160$ and (d) $r = 250$. Other parameters are identical to those used in Fig. 1.11

In order to have a more comprehensive snapshot of the different dynamics exhibited by the system, one convenient tool is the *bifurcation diagram*. It displays for each value of the parameter r , all the minimum and maximum values (hence extrema values) taken by one state variable. In addition, as we have seen in Fig. 1.13, the qualitative dynamic of the Lorenz's equations can change as the parameter r evolves. These modifications are called *bifurcations* and the range of stability of the outcome dynamic is suggested by the analysis of the bifurcation diagram in Fig. 1.14. Although it does not give any information on the waveform of the resulting dynamic, the different dynamical regimes are easily deduced : for $r < 25$, only one point is displayed per value of r : this is a steady-state; for $25 < r < 150$ and $168 < r < 219$ there is a large number of points, sign of chaotic behavior, for $150 < r < 168$ and $29 < r < 230$, X oscillates quasi-periodically with 6 values of extrema and finally for $r > 230$, X oscillates periodically with only 2 extrema.

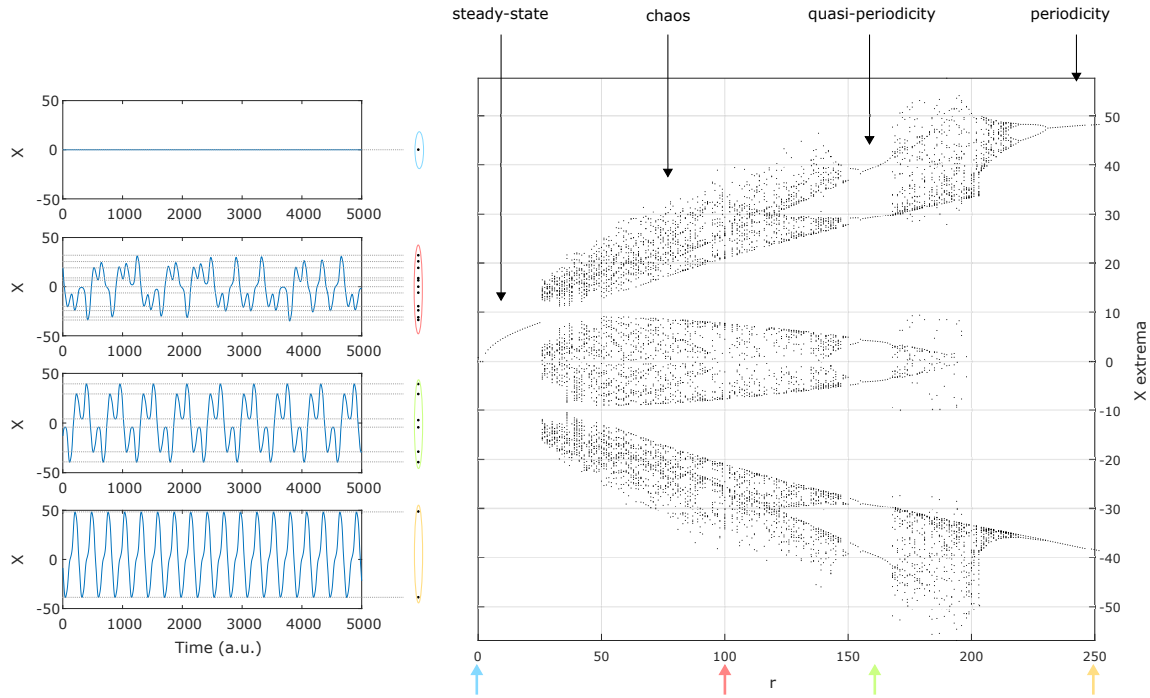


Figure 1.14: Construction of a bifurcation diagram based on the Lorenz's equations. r is the bifurcation parameter and X the variable of interest. Other parameters are identical to those used in Fig. 1.11

1.4.3 Analogy between lasers and the Lorenz's system

In 1975, Haken [29] demonstrated mathematically the close analogy between the model of Lorenz in Eqs. (1.3)-(1.5) and the commonly used Maxwell-Block equations that model laser dynamics. By neglecting the diffusion of carrier and the diffraction of the electrical field in the laser cavity, one can show that lasers can be modeled by the following system of equations :

$$(1.6) \quad \frac{dE}{dt} = -\kappa(1 + i\theta)E + P,$$

$$(1.7) \quad \frac{dP}{dt} = -\gamma_{\perp}(1 - i\theta)P + \gamma_{\perp}a(1 + i\theta^2)NE,$$

$$(1.8) \quad \frac{dN}{dt} = -\gamma_e(N - \mu) - (EP^* - E^*P),$$

with E the slowly varying electrical field, P the macroscopic dipolar polarization,

N the normalized carrier inversion with respect to transparency⁷, θ the normalized detuning, μ the normalized injection current, γ_{\perp} the dipolar polarization relaxation rate, γ_e the carrier decay rate from spontaneous emission and non-radiative recombination, a the differential gain at the laser frequency, κ the field decay rate.

This system of equations can be redefined by introducing the real and imaginary parts of E and P and considering the following variables

$$(1.9) \quad E \equiv \sqrt{\frac{\gamma_{\perp}\mu}{2\kappa r}} (E_r + iE_i),$$

$$(1.10) \quad P \equiv \sqrt{\frac{\gamma_{\perp}\mu}{2\kappa r}} (P_r + iP_i),$$

$$(1.11) \quad N \equiv \mu - \frac{\mu}{r}N,$$

$$(1.12) \quad r \equiv \frac{\mu a}{\kappa}(1 + \theta^2),$$

$$(1.13) \quad t \equiv t\gamma_{\perp},$$

$$(1.14) \quad \sigma \equiv \kappa/\gamma_{\perp},$$

$$(1.15) \quad b \equiv \gamma_e/\gamma_{\perp},$$

With these changes, the model reads :

$$(1.16) \quad \frac{dE_r}{dt} = -\sigma(E_r - \theta E_i - P_r),$$

$$(1.17) \quad \frac{dE_i}{dt} = -\sigma(E_i - \theta E_r - P_i),$$

$$(1.18) \quad \frac{dP_r}{dt} = -P_r - \theta P_i + rE_r - NE_r,$$

$$(1.19) \quad \frac{dP_i}{dt} = -P_i + \theta P_r + rE_i - NE_i,$$

$$(1.20) \quad \frac{dN}{dt} = -bN + E_r P_r + E_i P_i,$$

Finally, if we consider a single longitudinal mode operation for which $\theta = 0$ and if $E_i = P_i = 0$ [30, 31], we obtain :

⁷when the photons lost in the cavity from absorption equalize the photons created by emission

$$(1.21) \quad \frac{dE_r}{dt} = -\sigma(E_r - P_r),$$

$$(1.22) \quad \frac{dP_r}{dt} = -P_r + rE_r - NE_r,$$

$$(1.23) \quad \frac{dN}{dt} = -bN + E_r P_r,$$

which are the Lorenz equation described previously in Eqs. (1.3)-(1.5). As a result, lasers might be thought as good candidates for chaotic behavior. Nonetheless, although the above equations are analogous to the Lorenz's system, chaos is not always achieved by every single lasers. Indeed, the model of Lorenz implicitly suggests comparable relaxation time-scale for each variables which implies that each variable contributes to the dynamic of the system. In lasers though, this is not always true and the dipolar polarization variable P_r might, in some cases, be adiabatically eliminated from the equations. The laser dynamics in that case is a motion in the plane, hence preventing the observation of chaos [28].

1.4.4 Classification of lasers

In Eqs. (1.6)-(1.8), we have taken into consideration different time constants : κ the field decay rate, γ_{\perp} the dipolar polarization relaxation rate and γ_e the carrier decay rate which have been included in the parameters σ and β in Eqs. (1.21)-(1.23). The stability of lasers have been classified in three groups depending of these time scales : classe A, B and C [32, 33].

1.4.4.1 Class C lasers

When all the time constants κ , γ_{\perp} and γ_e are in the same order, we must considered all three equations (1.6)-(1.8). As illustrated with the Lorenz's model, several dynamics including chaos can be obtained. This class encompasses NH_3 laser [34, 35], Ne-Xe lasers emitting a $3.51\mu\text{m}$ [36], and He-Ne lasers emitting at $3.39\mu\text{m}$ [37, 38]. We show an example of route to chaos made of successive period double of the optical power in Fig. 1.15. It shows the optical spectrum of the measured signal. The different solutions are obtained by tilting one mirror of the Fabry-Perot cavity forming the cavity. While tilting the mirror from it's ideal position, the output optical power

shows first oscillation at a frequency of 7 MHz followed by successive period doubling (or frequency halving) : a period-2 at 3.5 MHz, a period-4 at 1.75 MHz and a period-8 at 0.875 MHz until it reaches fully developed chaos in Fig. 1.15 (e).

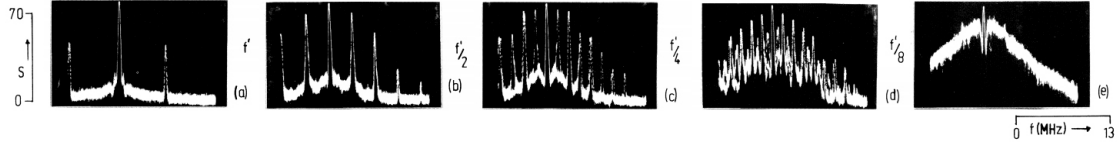


Figure 1.15: Experimentally observation of the optical spectrum of an He-Ne laser emitting a $3.39\mu\text{m}$ when tilting one Fabry-Perot mirror. (a) Period-1 oscillations, (b) Period-2 oscillations, (c) Period-4 oscillations, (d) Period-8 oscillations, (e) chaos. The figure is taken of Ref. [38]

1.4.4.2 Class B lasers

In class B lasers, the dipolar polarization rate γ_{\perp} is high enough compared to κ and γ_e that the equation (1.7) can be adiabatically removed from the system of equations. As a result, class B laser are only modeled by 2 equations making them intrinsically stable [28]. However, as we will see in the next section, instabilities can be unlocked with class B laser by the addition of external perturbations. Class B lasers encompass semiconductor, CO_2 and fiber lasers.

1.4.4.3 Class A lasers

Class A lasers are characterized by their long photons lifetime *i.e.* κ is very small compared to γ_{\perp} and γ_e . Therefore, the equation for the population inversion N and the dipolar polarization P can be adiabatically eliminated. As a result only the equation for the field E remains. Class A laser are the most stable lasers. It comprises visible He-Ne, Ar-ion and dye lasers.

1.4.5 Unlocking nonlinear dynamics in semiconductor lasers

1.4.5.1 Different approaches

As we have seen, class B lasers are intrinsically stable. During the last 40 years, many techniques have been employed to unlock nonlinear dynamics as it can be useful for various applications (see Section 1.5). In Fig. 1.16, we summarize the main

configurations that allow rich nonlinear dynamics in semiconductor lasers [39]. For all of them, the idea is to increase the number of degrees of freedom of the system from 2 to 3 or even infinite for some cases.

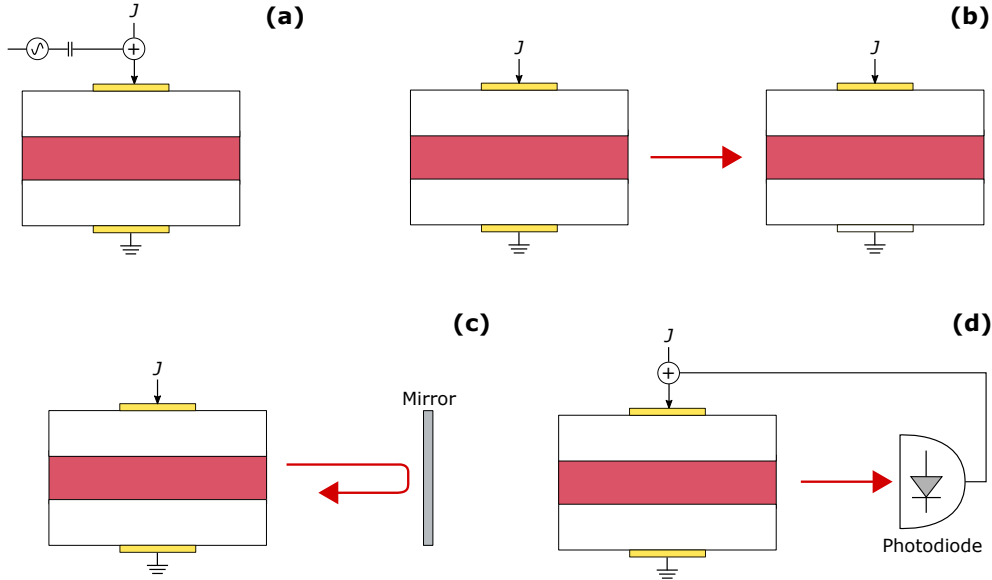


Figure 1.16: Different ways to unlock nonlinear dynamics in semiconductor lasers. (a) Direct current modulation, (b) Optical injection, (c) Optical feedback and (d) Opto-electronic feedback.

- **Direct modulation** in Fig. 1.16 (a): Under certain conditions, direct modulation of the laser injection current can induce chaotic pulsing. It requires a modulation frequency of the order of the relaxation oscillation frequency with a relatively high modulation depth [40, 41]. In Ref. [42], the polarization properties of VCSEL have been numerically explored under the influence of direct modulation, and chaos was achieved on a broader range of parameters than found in EELs.
- **Optical injection** in Fig. 1.16 (b): A laser called *master* injects its light into the cavity of another laser, the *slave*. A large variety of dynamic can be unlocked when varying the optical frequency detuning between the master and the slave or by increasing the injected power [43, 44]. Some studies have focused on different polarization states of the injected light : either orthogonal to the naturally emitted light of the slave laser [45] or parallel [46]. In other study,

the master laser is settled on an already chaotic dynamic [47]. Optical injection might also induce the so-called *injection locking* where the laser emission wavelength locks on the master laser wavelength. Injection locking has been shown to enhance the modulation frequency limit of the slave laser [48].

- **Feedback** in Fig. 1.16 (c-d) : There are two main configurations of feedback : the optical feedback and the opto-electronic feedback. In optical feedback experiment, a fraction of the laser light is re-injected in the cavity. In opto-electronic feedback experiment, the emitted light is detected by a photodiode and re-injected in the laser through its injection current. In both cases, the feedback induces a time-delay τ which competes with the internal time-scale of the lasers. However they differs in the sense that opto-electronic feedback is *incoherent* *i.e.* it does only influence the carrier population while optical feedback is said to be *coherent* as it interferes with the electrical field. We will later develop the case of optical feedback.
- It is also worth mentioning that chaos has been also achieved in solitary VCSELs. In some cases, a nonlinear coupling can occur between two-polarization modes, hence unlocking series of bifurcations when changing the injection current or the temperature or the strain inside the cavity. This has been reported in a quantum-dots VCSEL [49] where the active region is made of tiny dots of active material or in quantum-well VCSELs subjected to a mechanical strain [50]

1.4.5.2 Optical feedback and route to chaos

Among the above mentioned techniques to unlock nonlinear dynamics in semiconductor lasers, optical feedback is probably the easiest way as it only requires a simple mirror as shown in fig. 1.17. In this configuration, the external mirror (placed at a distance L of the laser) and the output facet of the laser form an *external cavity*. As discussed above, the round-trip time of the light inside the external cavity induces a delay $\tau = \frac{2L}{c}$ that interplays with the internal time scale of the laser *i.e.* the relaxation oscillation period $T_{RO} = 1/f_{RO}$.

Another parameter of importance in external cavity laser is the feedback ratio. It is defined as the ratio between the power of the feedback light and the total output

power of the laser. It can be easily tuned by introducing a variable attenuator in the light path.

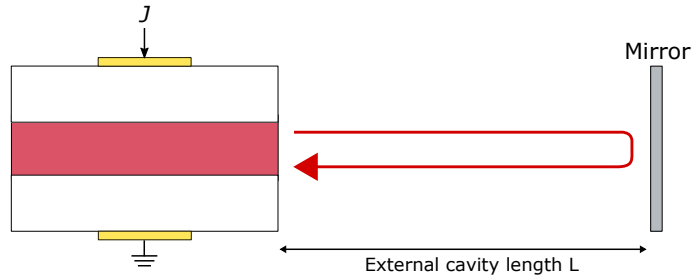


Figure 1.17: Laser diode subjected to an optical feedback. A mirror is placed at a distance L in front of a laser and reflect a small amount of the light back into the laser.

In 1986, Tkach and Chraplyvy identified five dynamical regimes in external cavity lasers based on qualitative modification of the optical spectrum properties [51]. The transition from one regime to another depends of both the external cavity length (or delay) and the feedback ratio as shown in Fig. 1.18.

- **Regime I** : At very small feedback levels (less than 0.001%), the laser optical spectrum narrows or broadens depending on the phase of the feedback
- **Regime II** : Regime II is unlocked when the frequency shift induced by the feedback has multiple solutions also called *external cavity modes* (ECM). ECMs are stationary solutions whose optical frequency is shifted by $n \frac{c}{2L}$ with n an integer. This regime occurs for a small feedback level (less than 0.01%). Experimentally, the laser hops on these different solutions hence leading to different peaks in the optical spectrum. When looking at the corresponding time traces, the hopping is seen as a fluctuation of the optical power. Each ECM is associated with a certain gain *i.e.* a certain level of output power.
- **Regime III** : For a very narrow region of feedback ratio (close to 1%), the optical spectrum narrows for all phases of the feedback (all external cavity lengths). In this regime, the feedback favors one mode over the others.
- **Regime IV** : For moderate value of feedback (about 1%), sidebands appear on the optical spectrum separated from the emission peak by a frequency equal to

the relaxation oscillation frequency f_{RO} . When looking at the corresponding time trace, the sideband is seen as undamped oscillations at f_{RO} . As the feedback is increased, the sidebands broaden leading to *coherence collapse* i.e. chaotic oscillations that reduce the temporal coherence of the laser.

- **Regime V** : For high value of feedback (higher than 10%), the external cavity acts as an extension of the laser. The laser operates on a single narrow longitudinal mode.

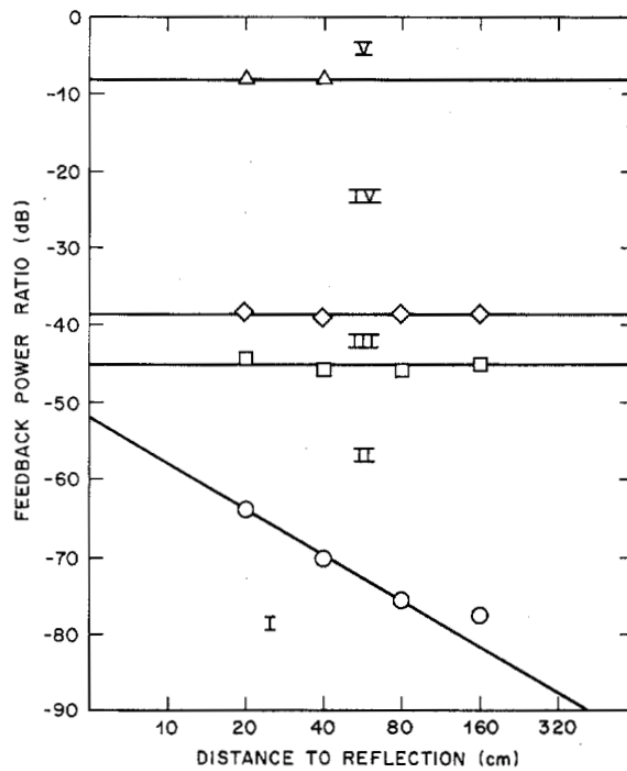


Figure 1.18: Five dynamical regimes of an external cavity laser as function of the distance to reflector L and the feedback ratio. Figure taken from Ref. [51].

Although this classification does not provide an in-depth view on the different dynamics that are unlocked with optical feedback, it summarizes the expected behaviors of such system demonstrating for example the need of high suppression ratio isolator (> 40 dB) to prevent any feedback effect. In particular, it does not

relate to some specific features of external-cavity diode dynamics such as the *Low-Frequency Fluctuations* [52–54] - that we will investigate in Chapter 2 - or neither the *Regular Pulse Packages* regime obtained for short external cavity ($\tau < T_{RO}$) [55–57]. Different dynamical behaviors also can be obtained when designing the external cavity by including for example : a) a phase-conjugated mirror known to unlock self-pulsing oscillation of the output power at multiples of the external cavity frequency $f_{EC} = 1/\tau$ [58, 59], b) a polarization rotating element such as Faraday-rotator leading to square-wave modulation of the output power [60, 61], c) a wavelength filter such as Fabry-Perrot resonators [62] or grating mirrors [63] which only reflects a narrow window of wavelength favoring one ECM over the others, hence stabilizing the laser. The field of laser diode nonlinear dynamics therefore remains very active considering the numerous configurations that unlock complex dynamics and also considering the development of new laser diodes with new physics.

1.5 Applications of chaos in laser diodes

In Section 1.3, we have introduced two examples of laser applications that have greatly impacted modern society : optical telecommunication and optical ranging. We hereby provide extensions of such technologies when using chaotic oscillations of laser diodes. More examples can be found in Ref. [39].

1.5.1 Chaos for secure communication

As described in Section 1.3.1, lasers are ubiquitous in today telecommunication system. *Cisco* has predicted to reach by 2021 an annual IP traffic of 3.3 ZB (3.3 trillions of GB) compared to the 1.2 ZB in 2016 with more than 58% of the world population connected to internet [64]. This expansion of telecommunication combined to the democratization of digital money transaction requires safer data transmission. Although the most promising technology is the *quantum-key distribution* (QKD) with an impressive demonstration in 2017 by the Chinese satellite Micius [65] , chaos-based telecommunication can also improve the data security and can be easily incorporated in actual infrastructure [66].

The chaos-based telecommunication relies on the synchronization of two similar laser diodes through optical injection [67–69], one at the emitter side and the other

one at the receiver side. While the emitter's laser (master) is forced into chaotic oscillation through *e.g.* optical feedback, the receiver's laser (slave) is injected with the light provided by the first one. When both lasers are almost identical and operate in similar conditions (current and temperature), the receiver's laser can exhibit identical chaotic oscillations compared to the emitter's. The chaotic signal is used here as a carrier and the message is carefully encoded in the chaotic carrier. Since synchronization occurs between the two chaotic signals (at the emitter and at the receiver), a simple subtraction of the chaotic output of the receiver with the input of the receiver (chaos+message) yields the message decoding. In addition, as the synchronization can only be achieved by the use of an identical laser, decryption of the message can be hardly performed by a spy. This experiment has already been conducted in the city of Athens, Greece [66].

1.5.2 Chaotic LIDAR for ranging

LIDAR usage is expected to grow quickly in the next few years in crowded environment such as cities and highways. As a result, the probability for on LIDAR device to detect pulses from other LIDAR (causing failures of detection also called *ghost images*) also increases. In addition, classic LIDAR are vulnerable to jamming *i.e.* when someone intentionally shines a LIDAR detector, also causing *ghost images*.

In order to prevent such issue, randomly-modulated LIDARs have been proposed [70]. It consist on the emission of randomly modulated optical power through an external modulator. Then, the position of a target is deduced from the cross-correlation between the emitted and the back-scattered signal. As a result, other sources of light contributed solely to noise. However, this technique still has two drawbacks : first, the electronic of modulation needs to be fast which is then very costly, second, it often relies on a pre-designed sequence of random bits that can be detected and reproduced by a jammer.

By contrast, chaotic lidar (CLIDAR) can overcome such problematic as it doesn't require fast electronic and chaos is by nature unpredictable [71]. It can be achieved by an optical feedback [71] or from an optical injection [72]. However, improvements of CLIDAR is still required for better energy-efficiency. Indeed, usually, the detection electronic is relatively slow (< 1 GHz) while chaotic laser tends to distribute its energy around the relaxation oscillation frequency (≈ 10 GHz) which results in

energy losses by the equivalent detection low-pass filter. In 2018, Cheng *et al.* [73] proposed a solution based of an homodyne interference arm that redistributes the energy toward low-frequency regions improving the signal-to-noise ratio by 20dB.

1.6 Conclusion, objectives and outlines

In summary, we have briefly introduced the physics of semiconductor lasers and emphasized two types of structure : the Edge-emitting lasers (EEL) and the Vertical-cavity surface-emitting lasers (VCSEL). These devices have revolutionized our modern society with innovative applications. In addition, we bring to light how laser diodes can exhibit nonlinear dynamics including chaos under external perturbation and how it can be of use for data security and lidar technology.

The work presented here is devoted to the generation of nonlinear dynamics in EEL and VCSEL by mean of optical feedback. More specifically, we bring a focus on the polarizations physics of the emitted light. VCSELs can exhibit nonlinear dynamics simultaneously in two polarization modes when subjected to an isotropic optical feedback [57, 74–76]. On the contrary, EELs show a strongly dominant polarization due to its active medium geometry. As a result, under an isotropic optical feedback, only the dominant polarization is excited. For the depressed polarization to participate in the overall dynamic, some studies have modified the external cavity by adding polarization sensitive components [60, 77–79]. In the following, we will investigate both configurations with VCSEL and EEL and analyze the interplay between the polarization modes. These topics have been selected during my PhD for their fundamental and/or applied interests.

In **Chapter 2**, we report on the main findings on polarization instabilities in VCSELs. First, we introduce the so-called San Miguel, Feng Monoley (SFM) rate equations which are commonly used to model VCSEL polarizations dynamics. Then, we briefly present the VCSEL physics under isotropic optical feedback and focus and the Low-Frequency Fluctuation (LFF) regime. We analyze both experimentally and numerically polarization correlation properties and highlight an intriguing double-peak structure in the RF spectrum of both polarizations. This latter observation is explained in the manuscript in the framework of the dynamical trajectory in the phase-space around stable ECMs and their unstable counterparts.

In **Chapter 3**, we study the generation of high intensity pulses in the total intensity output of VCSEL when operating in LFF regime. Statistics of these pulses show close similarities with the oceanic rogue-waves (RW) which are giant waves emerging on calm seas. We also investigate on the effect of polarization competition on the generation rate of RWs which results in a saturation of the number of RWs when varying the feedback ratio in contrast with the case of single-polarization emission.

In **Chapter 4**, we investigate the dynamic of EEL subjected to polarization rotated optical feedback (PROF) leading to square-wave (SW) modulation with a periodicity close to twice the external cavity delay. We report on a novel bifurcation resulting in the appearance of fast oscillations on the plateaus of the SW. The experiment and the numerics show that the frequency of these oscillations is neither equal to the external cavity frequency nor to the relaxation oscillation frequency. Analytical study proves that the frequency of those oscillation is proportional to f_{RO} with a coefficient that depends on the laser parameters, hence can be significantly larger than f_{RO} .

In **Chapter 5**, we show that our PROF experiment is suitable for the study of asymmetry emerging from spatially extended system such as ring of oscillators. This asymmetry is defined as the coexistence of coherence and incoherence and has been referred to as *chimera-state*. This is a new paradigm in network systems discovered in 2002 by Kuramoto and Battogtokh [80]. Only few experiments have been able to prove its existence until now but chimera-state is expected to be a generic feature in general physics. From a space-time analogy, we demonstrate that lasers under PROF configuration are able to produce chimera-state with different pattern solutions made of one or several regions of coherence and incoherence called *multi-headed chimera*.

In **Chapter 6**, we summarize and conclude on our main findings and discuss about further investigations.

POLARIZATION INSTABILITIES IN VCSELS AND NON-LOCAL CORRELATION PROPERTY IN LOW-FREQUENCY FLUCTUATION REGIME

In this chapter, we focus on vertical-cavity surface emitting lasers (VCSEL). We first introduce the polarization instabilities in VCSEL and explain its physical origin. We also introduce the *San Miguel, Feng and Moloney* (SFM) rate equations, which consist of a four-level approach to model the polarization behavior of VCSEL. Although polarization instabilities are detrimental for modern telecommunication systems, we provide here a discussion about their possible interest for future application in communication and information processing.

Secondly, we present the basic physics behind VCSEL under isotropic optical feedback and more specifically in the so-called *Low-Frequency Fluctuations* (LFF) regime. We unveil, both numerically and experimentally, new correlation properties of the polarization modes that couple non-locally two different time-scales of the polarization dynamics. We furthermore investigate the appearance of an intriguing double-peak structure in the vicinity of the external-cavity frequency observed in the RF spectrum of the modes. An exploration of the literature shows that such feature is more generic than expected as it has been observed in different dynamical regimes and laser systems. However, the physical origin remained elusive over almost three

decades.

Finally, we provide a physical interpretation of these particular features and connect them with the trajectory of the system in the vicinity of ruins of stable and unstable external-cavity modes. We perform a detailed study of the parametric influence (pumping current and time delay) and show that our interpretation for the double-peak holds also for EELs with a simple model that only takes into account one polarization mode, a single round-trip in the external-cavity and one longitudinal mode.

This work has been partially reported in the following journal publication :

Uy, C. H., Rontani, D., Breuer, S., and Sciamanna, M. (2017). Non-local correlations via chaotic itinerancy in VCSEL with optical feedback. *Optics express*, 25(6), 6914-6923.

2.1 Polarization properties in VCSELS

As discussed in Chapter 1, the VCSEL is considered as one of the most spectacular recent improvement of semiconductor laser technology allowing cheaper growth process and enabling more efficient optical interconnection [81] and parallel information transmission [82]. For example, in December 2017, *Apple*, the multinational firm, announced an investment of 390 millions of U.S. dollar in *Finisar*, one of the largest VCSEL manufacturer worldwide, as VCSEL is rumored to feature the facial recognition technology in the next generations of mobile devices developed by Apple.

"VCSELS power some of the most sophisticated technology we've ever developed and we're thrilled to partner with Finisar over the next several years to push the boundaries of VCSEL technology and the applications they enable."

Jeff Williams, *Chief Operating Officer at Apple*

However, since its first demonstration in 1979 by Soda *et al.* [13], their polarization direction of emission has shown to be very difficult to predict even among VCSELS that are grown in the same wafer [83]. In addition, although the light emission is usually linearly polarized, its direction may also switch with a slight change of the operating parameters [84]. This polarization instability has prevented the use of VCSEL in data transmission technologies, where stable polarization direction is

required. In addition, polarization switchings enhance the noise in such system [85] which then deteriorates the signal to noise ratio in data communication.

2.1.1 Polarization instabilities in VCSELS in comparison with EELs

In 1984, Chen *et al.* [86] demonstrated that a free-running edge-emitting laser (EEL) is able to switch in polarization between two main linear and orthogonal modes : the transverse electric (TE) and the transverse magnetic (TM) modes. The switching may occur while changing the operating temperature of the laser or its injection current. Physically, a change of the operating temperature modifies the gain of each polarization; the mode that has the highest gain is the lasing one. However, for EELs, stabilizing one polarization can be easily achieved by tuning the laser cavity dimensions [87]. Usually, in stable polarization operation, the mode that emits is the one that is parallel to the active region often called as the *TE mode*. It experiences the highest reflectivity at the facet of the laser [87] and has a better confinement inside the amplifying cavity [88].

In VCSELS, the circular symmetry of the active region does not favor any preferential direction of polarization. Hence, it is not possible to infer the direction of polarization only by purely geometric considerations. In fact, the main effects that set the direction of polarization are the elasto-optic effect (through residual semiconductor-growth defects) and the electro-optic effect (through the applied voltage of the laser) [18]. Both of these effects create a birefringence inside the active region resulting in two favored polarization modes oriented along the main orthogonal axes of this birefringence. As a result these two modes experience different refractive indices. As a consequence of the result birefringence, the two polarization mode exhibit different wavelengths. In most cases, VCSELS are linearly polarized along the $[110]$ and $[1-10]$ crystal axis [83] due to the electro-optic effect [89] and unintentional strain induced during the manufacturing [90]. We respectively name them X and Y polarization modes.

Therefore, unlike EELs, a precise design of the cavity dimension in VCSEL does not guarantee a single linearly polarized emission. In standard VCSELS not using any polarization control design, polarization switchings are usually observed when varying the injection current [17, 84, 91], the operating temperature [92, 93], or

both [18]. As a matter of fact, the laser temperature usually increases with the driving current. Dynamical random switching is also observed when operating close to a switching point [91]. The VCSEL then randomly hops in time between the two polarization modes. The result polarization mode hopping has been explained as the consequence of spontaneous emission noise inducing hops in a bistable system [94].

2.1.2 Types of polarization switching

Contrary to EELs, assessing the direction of the lasing polarization in VCSEL requires a deep analysis of its gain property and of the crystal birefringence. However, as we will see in this section, the knowledge of such properties is not always sufficient to explain all the polarization switchings observed when varying the current. Indeed, when considering the optical frequency of the X and Y polarization modes, two different types of switching can occur :

1. Type 1 : the laser switches from the high frequency mode towards the low frequency mode
2. Type 2 : the laser switches from the low frequency mode towards the high frequency mode

We show in fig. 2.1 a polarization-resolved light-intensity curve measured from a 850 nm VCSEL at constant temperature. Two polarization switchings is observed. When increasing the current, the high frequency polarization switches into low frequency one at ≈ 7.6 mA. This is called a Type 1 switching. On the contrary, a further increase of current leads to a so-called Type 2 switching from the high-frequency to the low-frequency mode at ≈ 8.8 mA.

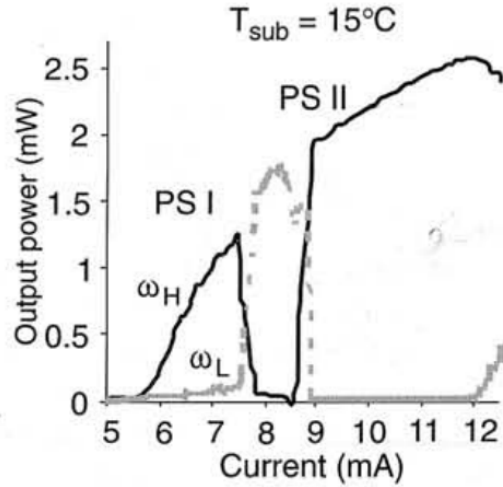


Figure 2.1: Polarization-resolved light-intensity curve of a 850 nm AlGaAs/GaAs VCSEL at 15°C. At low current, the high frequency (ω_H) polarization lases. A Type 1 switching occurs at 7.6 mA and the low frequency (ω_L) is lasing. Another switching of Type 2 occurs at 8.7 mA and the high frequency polarization turns on again. The figure is taken from Ref. [18]

2.1.2.1 Polarization selection from gain competition

In 1994, Choquette *et al.* [95] have interpreted the polarization switching phenomenon as an interplay between the laser gain spectrum and the optical frequency detuning between the two polarization modes. At constant current and temperature, the lasing polarization is the one that benefits from the highest gain in the laser cavity. In Fig. 2.2 (a), Y polarized mode with highest frequency has a higher gain than the X polarized mode with the lowest frequency. The Y mode is therefore the lasing polarization. When increasing the current (and therefore the temperature), the laser gain curve and both polarization wavelengths red shift.

However, the red shifts between the gain and the polarization wavelength do not present similar slope when varying the current. While the gain curve shifts at 0.32–0.34nm/°C, the polarization wavelengths shifts at 0.046–0.09nm/°C [14]. There is a difference of almost one order of magnitude. The gain curve shifts is explained in Ref. [96] by a shrinkage of the band-gap with an increase of temperature, while the wavelengths shift is due to a modification of the refractive index with the temperature [97].

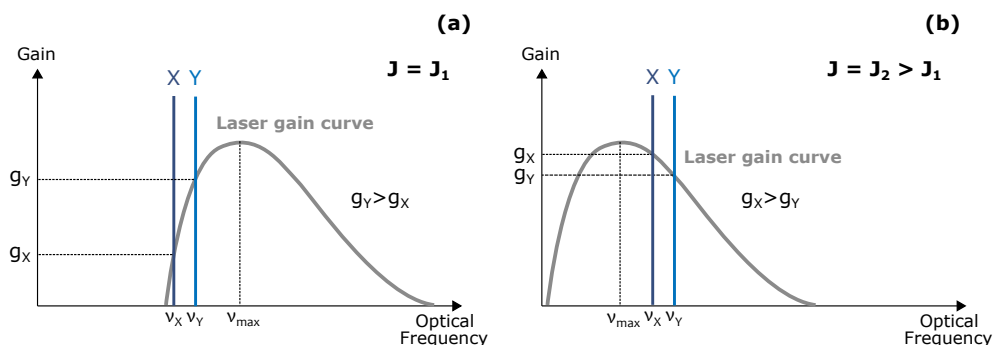


Figure 2.2: Type 1 polarization switching principle. Red shifts of the optical-emission frequencies and laser gain curve when increasing the injection current J from (a) to (b). In (a), the Y polarization (high frequency) lases and in (b), the X polarization (low frequency) lases.

The combination of these two effects explains the Type 1 polarization switching but not the Type 2 switching observed in Fig. 2.1. Indeed, in Fig. 2.1, the Type 2 switching occurs for even higher current than the Type 1 and a switch between the low frequency polarization toward the high frequency is still observed. Choquette's interpretation [95] is not sufficient to explain the entire mechanism of polarization switching in VCSEL. Hence, another explanation was proposed and involved the transverse profile of the light propagating in the laser cavity [98, 99] and the VCSEL's birefringence. The wavelength difference between both polarizations induces a difference in the refractive indices experienced by each mode. As a result, one polarization mode is more confined in the cavity than the other mode and exhibits a slightly larger optical intensity in the center of the device. An increase of current induces an increase of the confined mode intensity and hence a decrease of the exited carriers density at the center of the cavity¹. In contrast, a larger density of carrier is found at the edge of the cavity. This effect has been called the *Spatial Hole Burning* (SHB) [100]. Due to the SHB effect, a further increase of current leads to a better overlap of the less-confined mode with the carrier distribution inducing a polarization switching. SHB also explains switching between higher-order transversal modes [99].

¹Stimulated emission is faster than the diffusion rate of carriers.

2.1.2.2 Polarization selection from gain competition and losses

In the previous explanations of polarization switching in VCSEL, only the difference of gain between the two polarizations was considered : (i) the birefringence of the laser and its gain spectrum select the lasing polarization, (ii) the birefringence defines the confinement of both modes and a competition for the carriers determines the lasing mode. However, although the birefringence induces difference of gains, it also induces difference of losses in the cavity.

In addition, the proposal of Choquette *et al.* [95] does not explain polarization switching when the laser is initially operating on the blue part of the gain. Indeed, considering the situation of Fig. 2.2 (b) as the initial state, the gain maximum located at ν_{max} is never reached by the polarization modes with a further increase of current.

In 1999, the proposal of Choquette *et al.* has been extended considering the losses spectrum of the laser [101] that are also wavelength dependent. The explanation adds the effect of absorption of photons in the Bragg reflectors [102] that modifies the net gain² experienced by the polarization modes. The polarization with the highest net gain is the lasing one. In Fig. 2.3, we illustrate three different scenarios considering gain, loss, and birefringence. The Y polarization is the high-frequency mode and the X is the low-frequency mode. g_i and l_i are the gain and losses experienced by the i^{th} polarization mode ($i = X, Y$), respectively.

1. In Fig. 2.3 (a), at $J = J_1$, $g_Y - l_Y > g_X - l_X$. Y is lasing. At $J = J_2 > J_1$, although $g_Y < g_X$, $g_Y - l_Y > g_X - l_X$. Y is still lasing. No switching occurs.
2. In Fig. 2.3 (b), at $J = J_1$, $g_Y - l_Y > g_X - l_X$. Y is lasing. At $J = J_2 > J_1$, $g_X - l_X > g_Y - l_Y$. X is lasing. A Type 1 polarization switching occurs.
3. In Fig. 2.3 (c), at $J = J_1$, $g_Y - l_Y < g_X - l_X$. X is lasing. At $J = J_2 > J_1$, although $g_Y < g_X$, $g_Y - l_Y > g_X - l_X$. Y is lasing. A Type 2 polarization switching occurs.

²Considering both the gain spectrum of the laser and the absorption

CHAPTER 2. POLARIZATION INSTABILITIES IN VCSELS AND NON-LOCAL CORRELATION PROPERTY IN LOW-FREQUENCY FLUCTUATION REGIME

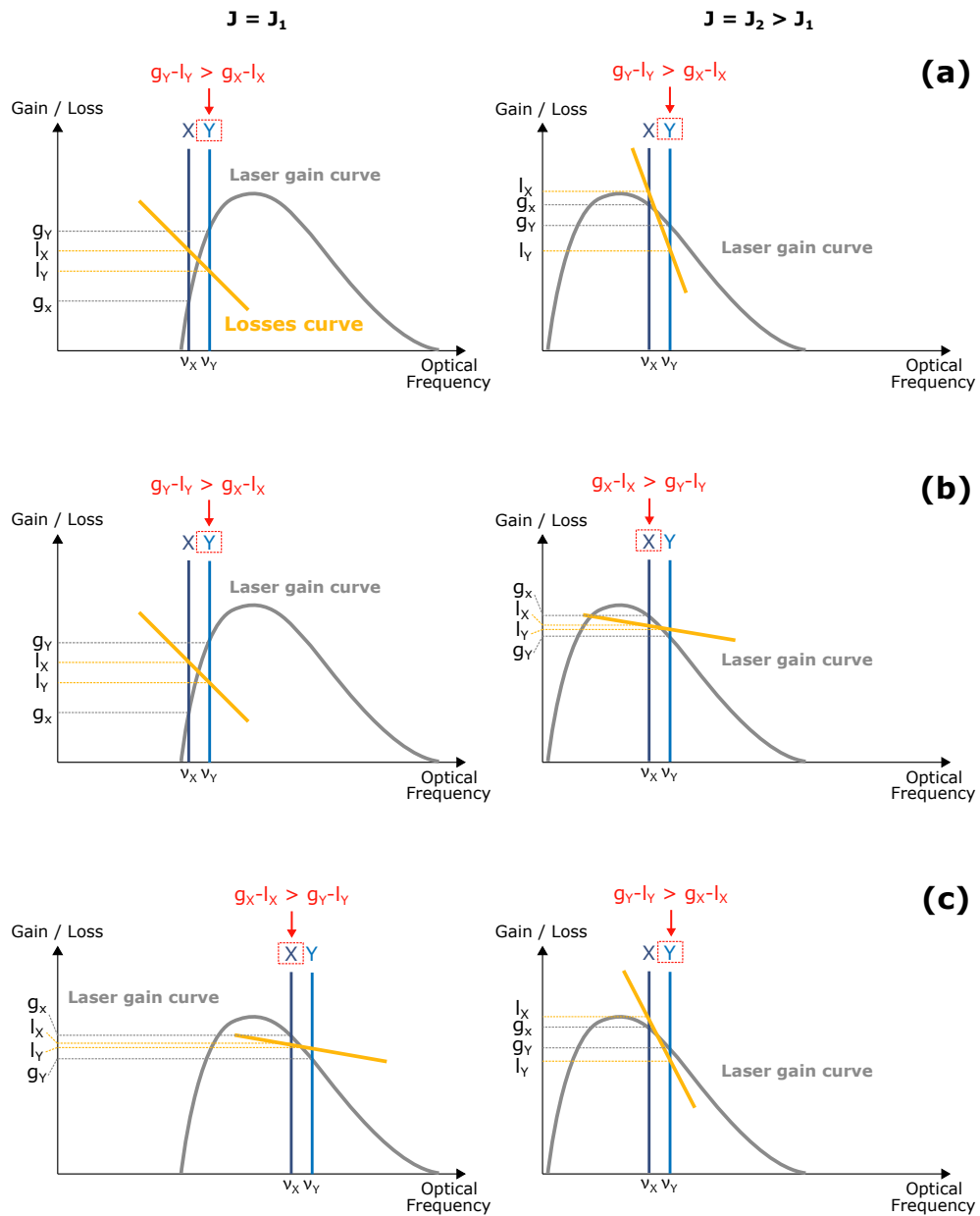


Figure 2.3: Gain and loss spectrum as function of the optical frequency. (left) low value of current and (right) higher value of current. Different scenarios are depicted : (a) no switching, (b) Type 1 switching and (c) Type 2 switching

Hence, considering the balance between gain and loss in a VCSEL, both types of polarization switching can be explained. Notice that another condition is to have always one polarization with a gain higher than loss. Otherwise, the VCSEL operates only in the spontaneous-emission regime.

2.1.3 Prediction of polarization switching from spin relaxation process

As discussed above, extensive studies have been conducted to explain polarization instabilities observed in VCSEL. The essential polarization features are explained by a study of the birefringence and the polarization gain and loss inside the VCSEL cavity.

A distinctively different approach that also describes polarization switching mechanism in VCSEL was brought by San Miguel *et al.* in 1995 [103] with the so-called *spin-flip model* (SFM). This model describes the active quantum-well medium as a four-energy level system instead of the usual two-level system accounting for the conduction band and valence band. In the SFM framework, the radiative energy transition between the conduction band and the valence band is replaced by radiative transitions between discrete energy levels being spin degenerate. The model considers separately the photons generated by the recombination of spin-up (\uparrow) and spin-down (\downarrow) electrons and holes as illustrated in Fig. 2.4. The spin-up channel generates left (-) circularly polarized light while the spin-down channel generates right (+) circularly polarized light. Both population of spin-up (\uparrow) and spin-down (\downarrow) carrier populations are only connected through the spin-flip relaxation process that tends to equilibrate both populations with opposite spins. In the valence band, the two populations of holes are coupled using a very fast spin relaxation rate i.e. the spin relaxation of holes in the valence band is assumed to be instantaneous. Furthermore, in VCSELS, the total angular momentum (m_j) for electrons in conduction bands (CB) and hh in valence bands (VB) is respectively $\pm 1/2$ and $\pm 3/2$

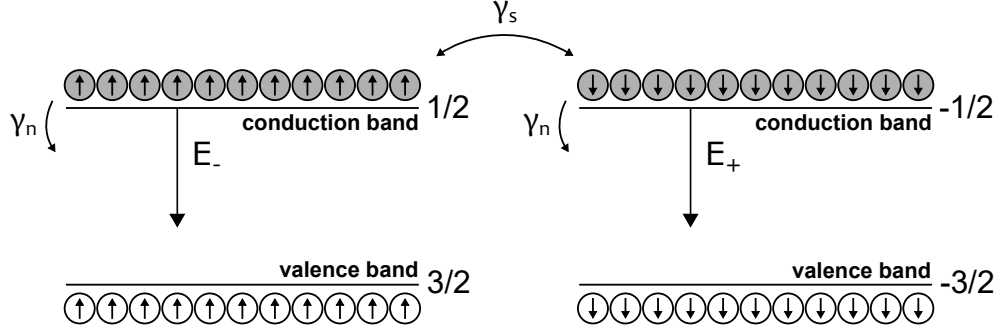


Figure 2.4: Illustration of the four-level system considered in the SFM model with two radiative transition : emission of photons from recombination of spin-up (\uparrow) electrons and holes and emission of photons from recombination of spin-down (\downarrow) electrons and holes. The two channels are coupled by the spin-flip relaxation rate γ_s

In its general form, the SFM model considers the fundamental transverse mode of the VCSEL while neglecting the diffusion of carriers and the diffraction of the electrical field. The model reads :

$$(2.1) \quad \frac{dE_{\pm}}{dt} = \kappa E_{\pm} - i\omega_0 E_{\pm} + \kappa(1 + i\alpha)(N \pm n)E_{\pm},$$

$$(2.2) \quad \frac{dN}{dt} = -\gamma_n(N - \mu) - \gamma_n(N + n)|E_+|^2 - \gamma_n(N - n)|E_-|^2,$$

$$(2.3) \quad \frac{dn}{dt} = -\gamma_s n - \gamma_n(N + n)|E_+|^2 + \gamma_n(N - n)|E_-|^2,$$

E_{\pm} are the right (+) and left (-) circularly polarized slowly varying electric field amplitudes. N is the difference between the upper and lower state populations and n is the difference between populations inversions of the spin up (\uparrow) and spin down (\downarrow) radiations channels. The fixed parameters are α the linewidth enhancement factor, $\omega_0 = \kappa\alpha$ is the shift in optical frequency compared to the one at threshold ($\omega_0 = 0$ at threshold) when no anisotropy is considered, μ is the normalized injection current ($\mu = 1$ at threshold). κ is the cavity decay rate of the electrical field, γ_n is the decay rate of the total carrier number and γ_s is the spin-flip rate..

Analyzing the equation (2.1), one may notice that each polarization states are coupled to a different population inversion variables $N + n$ and $N - n$ that arise from the four-energy levels assumption. Therefore, two cases can be mathematically discriminate:

(i) **The case of a very large** γ_s induces a very fast relaxation of n to zero : Equation 2.3 can be therefore adiabatically eliminated and the fields E_{\pm} are then coupled to a unique population N . The model reduces to a standard two-energy level model with two polarization modes.

(ii) **The case of a small** $\gamma_s \rightarrow \gamma_n$ where the two field amplitudes E_{\pm} are coupled to two different population N_+ and N_- . In this case, the equation (2.2) becomes [74]:

$$(2.4) \quad \frac{dN_{\pm}}{dt} = -\gamma_N[N_{\pm} - \mu + 2N_{\pm}|E_{\pm}|^2].$$

In addition, as previously discussed, VCSELS often admit two preferred orthogonal linear polarization modes that are aligned with respect to the crystal axes. Each of those polarization modes experience a different refraction index due to the birefringence of the crystal and therefore have a slightly different wavelength. This optical frequency splitting can be modeled through the linear phase birefringence parameter γ_p . In addition, as the gain and loss vary with the wavelength, the two polarization modes do not experience the same amplification. This different gain-to-loss ratio is modeled with the linear dichroism parameter γ_a . These two effects were incorporated in the model by Martin-Regalado *et al.* in 1997 [84]. Introducing γ_p and γ_a in Eq. (2.1) leads to:

$$(2.5) \quad \frac{dE_{\pm}}{dt} = \kappa(1 + i\alpha)(N_{\pm}n - 1)E_{\pm} - i\gamma_p E_{\mp} - \gamma_a E_{\mp}.$$

Experimentally, as the easiest measured quantities are the linear horizontal and vertical polarization field intensities $|E_x|^2$ and $|E_y|^2$, respectively; it is worth mentioning that the circular polarizations E_+ and E_- are related to the linear ones with the following relationship :

$$(2.6) \quad E_x = \frac{E_+ + E_-}{\sqrt{2}},$$

$$(2.7) \quad E_y = -i \frac{E_+ - E_-}{\sqrt{2}}.$$

Equations (2.1)-(2.3) can then be written in the basis of the two linearly polarized components $E_{x,y}$ as follows :

$$(2.8) \quad \frac{dE_{x,y}}{dt} = \kappa(1+i\alpha)[(N-1)E_{x,y} + inE_{y,x}] - (\gamma_a + i\gamma_p)E_{x,y},$$

$$(2.9) \quad \frac{dN}{dt} = -\gamma_n[N - \mu + N(|E_x|^2 + |E_y|^2) + in(E_yE_x^* - E_xE_y^*)],$$

$$(2.10) \quad \frac{dn}{dt} = \gamma_s n - \gamma_n[n(|E_x|^2 + |E_y|^2) + iN(E_yE_x^* - E_xE_y^*)].$$

We summarize the meaning of each parameters and variable in table (2.1)

Symbol	Meaning of the parameter	Domain
$E_{x,y}$	Slowly varying field amplitude of X and Y polarizations	\mathbb{C}
N	Population difference between conduction and valence bands	\mathbb{R}
n	Population difference between spin up and down	\mathbb{R}
k	Field decay rate	\mathbb{R}^+
α	Linewidth enhancement factor	\mathbb{R}^+
γ_a	Linear dichroism	\mathbb{R}
γ_p	Linear birefringence	\mathbb{R}
γ_n	Decay rate of N	\mathbb{R}^+
μ	Normalized injection current	\mathbb{R}

Table 2.1: **Parameters and variables of the San Miguel-Feng-Moloney model**

The SFM model when including linear birefringence and linear anisotropy has been shown to reproduce qualitatively well both type 1 and 2 of polarization switching [18, 84, 104, 105]. It also introduces a novel framework to study polarization dynamics through spin interaction. Although it remains unclear if the spin physics is necessary to model all experiments using VCSELS, it often reproduces well experimental findings [49, 106–108] and is today widely used in spin-injected VCSEL experiments [109]. In addition, the SFM model also predicts a dynamical polarization-switching scenario where the VCSEL emits initially in one linear polarization state; an increase of the injection current leads to an elliptical polarization state³ that bifurcates to a limit-cycle dynamic of both polarization modes, then to chaotic oscillation and finally to the emission of the orthogonal polarization mode only. This scenario has been recently observed experimentally in Ref. [49, 50]. An extension of the model accounting for the transverse profile of the light is given in Ref. [110].

³where both orthogonal polarization mode are excited

2.1.4 Application of polarization instabilities

As discussed so far, VCSELS demonstrate complex polarization behaviors. Although the mechanisms leading to the selection of one direction of polarization seems to be well understood, controlling it remains a long-run challenge [111]. On the other hand, some groups have tried to take advantage of such polarization instabilities for future application.

2.1.4.1 Random bits generation

In 2014, Virte *et al.* [112] demonstrated that polarization-chaos exhibited from a simple free-running VCSEL can be efficiently used for chaos-based random number generation at very high-speed [see Fig. 2.5]. They reached a bitrate of 100 Gbits/s without the need of unusual or complex post-processing techniques thanks to chaotic fluctuations of the output polarizations and random polarization switchings of the device. Nevertheless, they also showed that a bitrate of 560 Gbits/s is also achievable when considering more complex post-processing.

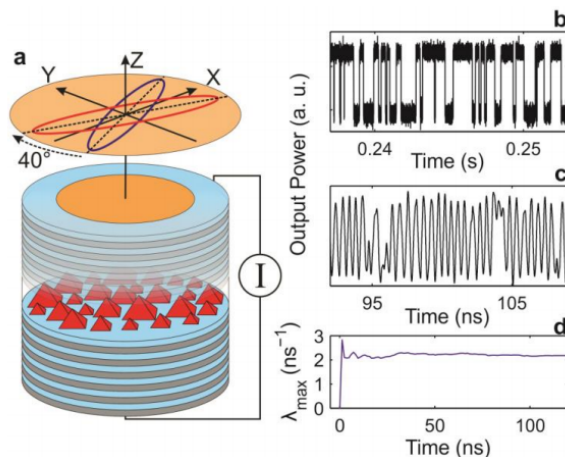


Figure 2.5: Experimental observations showing chaotic polarization mode hopping in a quantum-dot VCSEL. (a) Artist view of a Quantum Dot VCSEL with multiple quantum dots confined between two mirrors. At threshold the laser emits X linearly polarized light; Driven by constant injection current, the device can exhibit chaotic mode hopping between two non-orthogonal elliptically polarized modes (red and blue ellipses) separated by about 40 degrees. (b-c) Polarization resolved output power time trace showing the chaotic polarization mode hopping at a constant injection current of 2.0 and 2.6 mA respectively. (d) Estimation of Largest Lyapunov exponent for the time-series in (c). The figure and caption are taken from Ref. [49]

2.1.4.2 Logical gates

Another application of polarization instabilities has been provided in 1985 by Liu *et al.* [113]. They showed a simple electro-optical logical-gate system based on polarization switchings in an edge-emitting laser. They were able to reproduce usual *AND*, *OR*, *NAND* and *NOR* gates. Their study were further carried out in 2006 by Mori *et al.* [114] using an all-optical VCSEL based system [see Fig. 2.6]. Taking advantage of the low electrical consumption of VCSELs, their weak polarization stability and low response time, they demonstrated that VCSEL are capable of low-energy logical computation at high frequency rate. They also achieved an all-optical buffer memory system based on the same system [115].

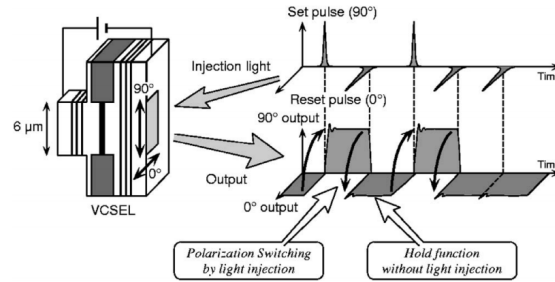


Figure 2.6: All optical flip-flop system using a polarization bistable VCSEL. Optical pulses are injected in the VCSEL with a chosen polarization state. At each pulse, the emitted polarization of the VCSEL switches toward the polarization of the pulse. The figure is taken from Ref. [114]

2.1.4.3 High-frequency oscillation generation

Based on the electron spin orientation effect on the generation of left or right polarization in VCSEL, generation of high-frequency oscillations was achieved by *spin-injection technique* [109, 116, 117]. In such experiments, the injection of electrons with determined spin leads to simultaneous emission of both polarization modes of the VCSEL. Due to the birefringence of the device, a beating can be measured at a frequency equal to the optical frequency splitting of the polarization modes. Modulation speed above 80 GHz have been demonstrated in Ref. [118].

2.1.4.4 Reservoir computing based on two polarization modes

In addition, the recently introduced reservoir computing approach has proved to be a very efficient way to process time dependent data [119]. It often relies on nonlinear interactions between several oscillators called *nodes*. The essential idea of reservoir computing is to consider a fixed architecture of inter-connected nodes (the so called *reservoir*) on which data are injected and to measure the output of it. For a perfect reservoir, each different input data leads to a different output allowing for example classification. Besides the optimization of the inter-connexion between nodes, there are two ways to obtain the best reservoir performances : 1/ having as many nodes as possible (to the detriment of higher experimental complexity) and/or 2/ having nonlinear oscillators with the highest dynamical dimension as possible. For the second part, semi-conductor lasers have proved to be one of the

most promising technology [120] as they combine complex non-linear interactions between the electrical field and the gain material, low energy consumption and fast dynamics. In addition, the configuration proposed in Ref. [120, 121] associates both a complex oscillator (being the laser) and a high number of nodes while keeping the system configuration simple. To do so, they rely on a unique laser subjected to a feedback loop that mathematically transforms the system into an infinite dimension one where the nodes are virtually placed on the loop as illustrated in Fig. 2.7. In order to improve such system, one can also rely on the polarization properties of VCSELS, that, as discussed previously, increases the complexity of the device compared to its edge-emitting laser counterpart. Promising results have already been observed in our group by *Ir. J. Vatin - PhD student* [122].

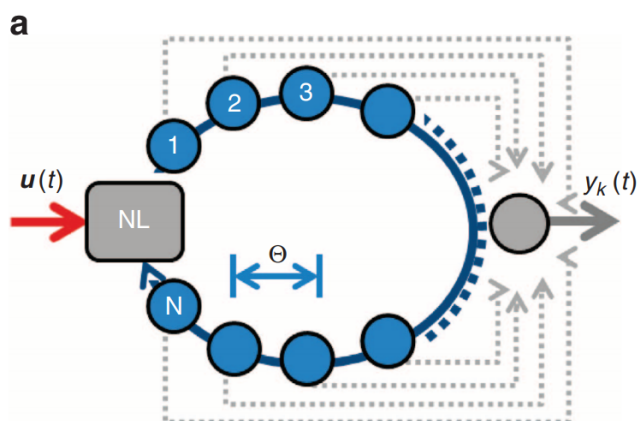


Figure 2.7: Illustration of time-delayed laser configuration for reservoir computing. Virtual nodes are placed periodically on the delay line. NL is a non-linear element (*e.g.* a laser diode). $u(t)$ is the input can be either a modulation of current or a modulated optical injection. $y_k(t)$ is a combination of the signals measured on each virtual nodes. The figure is taken from Ref. [120].

However, in such configuration, a good understanding of the dynamical properties of the delayed laser is mandatory to efficiently solve tasks. The response of the system has to be sufficiently complex in order to discriminate different inputs but not too complex as quasi-similar inputs have to be classified in the same group [121]. Furthermore, if one wants to use the polarization dynamics of VCSEL for reservoir computing, an in-depth comprehension of their physics and correlation is also required.

2.2 VCSEL under optical feedback and low-frequency fluctuation regime

As discussed in the Introduction, external-cavity laser-diodes have received a lot of attention for their capability to exhibit a wide variety of dynamics hence enabling new applications [39], such as the previously mentioned reservoir computing [121], secure communication [123], random number generation [124–126], small-displacement measurement [127] and blood flow [128]. Since its recent advent, VCSELs have gathered a lot of studies especially for their polarization properties. More specifically, optical feedback was used to control polarization switchings in VCSELs [75, 129, 130], or to explore the effect of polarization [76] in common chaotic behavior observed in single-polarization EELs such as, regular pulse packages [57], coherence collapse [131, 132], and low-frequency fluctuation (LFF) [74, 133–137]. The last mentioned LFF dynamics is a widely studied regime in external-cavity laser diode as it involves many fundamental mechanisms, such as mode/anti-mode interaction, noise triggered dynamics, and polarization competition described in the following sections.

We base our study on the SFM model and add the effect of the isotropic optical feedback. The equations read

$$(2.11) \quad \frac{dE_{x,y}}{dt} = \kappa(1 + i\alpha)[(N - 1)E_{x,y} + inE_{y,x}] - (\gamma_a + i\gamma_p)E_{x,y} + \eta E_{x,y}(t - \tau)e^{-i\phi_0},$$

$$(2.12) \quad \frac{dN}{dt} = -\gamma_n[N - \mu + N(|E_x|^2 + |E_y|^2) + in(E_y E_x^* - E_x E_y^*)],$$

$$(2.13) \quad \frac{dn}{dt} = \gamma_s n - \gamma_n[n(|E_x|^2 + |E_y|^2) + iN(E_y E_x^* - E_x E_y^*)],$$

with the delay $\tau = 2L/c$, which is the round-trip time of the light inside the external cavity of length L at the speed of light c . Spontaneous emission noise can be included by adding the term $F_{x,y}$ in Eq. 2.11 with $F_x = [\beta_{sp}(N + n)/2]^{1/2}\xi_1 + [\beta_{sp}(N - n)/2]^{1/2}\xi_2$ and $F_y = iF_x$. β_{sp} is the spontaneous emission rate and $\xi_{1,2}$ are two complex uncorrelated white Gaussian noises with zero mean and unitary variance. The other parameters are described in Table 2.1.

2.2.1 Steady-States and External Cavity Modes

While the free-running VCSEL has its own steady-states as described previously, adding an external perturbation such as the optical feedback, creates new equilibrium states called external-cavity modes (ECM). For simplicity, we do not consider here the spontaneous emission effect and only focus on a deterministic analysis. The ECM solutions verify the as following [74]:

$$(2.14) \quad E_{x,y} = A_s^{x,y} \exp[i(\omega_s^{x,y} - \omega_0)t], \quad N = N_s^{x,y}, \quad n = 0,$$

with ω_0 the optical pulsation of the free-running laser and ω_s the optical pulsation at the new equilibrium state. Inserting Eq. (2.14) in Eq. (2.11) leads to :

$$(2.15) \quad 0 = \kappa(N - 1)A_s^{x,y} \mp \gamma_a A_s^{x,y} + \eta A_s^{x,y}(t - \tau) \cos(\mp \omega_s^{x,y} \tau + \omega_0 \tau),$$

$$(2.16) \quad \omega_s^{x,y} - \omega_0 = \kappa \alpha (N - 1) - \gamma_p + \eta \frac{A_s^{x,y}(t - \tau)}{A_s^{x,y}} \sin(\mp \omega_s^{x,y} \tau + \omega_0 \tau).$$

Looking at steady-states *i.e.* $A_s^{x,y} = A_s^{x,y}(t - \tau)$, we simplify the equations (2.15) and (2.16) and give the following transcendental equations for ω_s :

$$(2.17) \quad \omega_s^{x,y} - \omega_0 = \pm \alpha \gamma_a \mp \gamma_p - \eta (\alpha \cos(\omega_s^{x,y} \tau) + \sin(\omega_s^{x,y} \tau)),$$

2.2. VCSEL UNDER OPTICAL FEEDBACK AND LOW-FREQUENCY FLUCTUATION REGIME

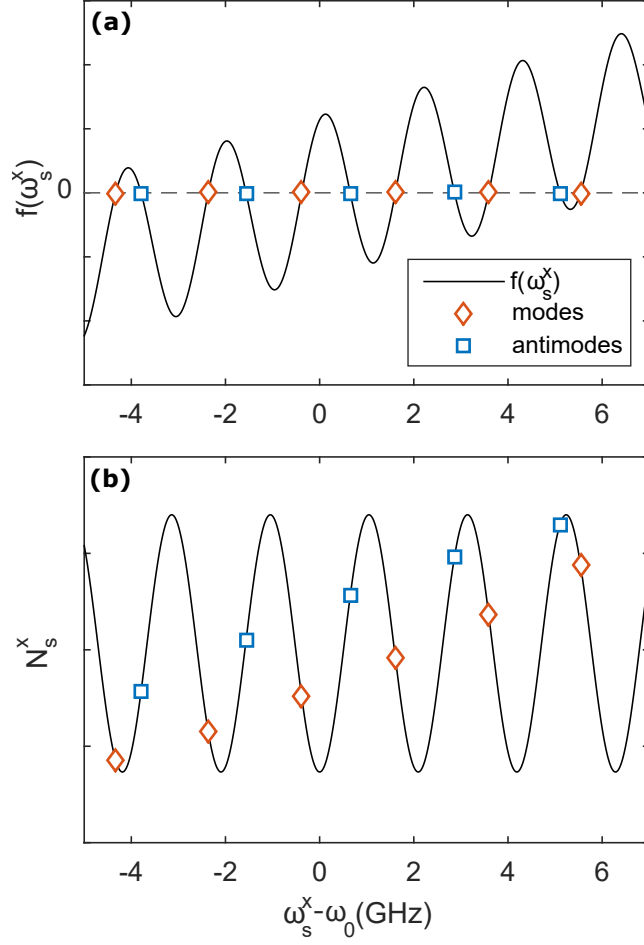


Figure 2.8: (a) Graphical solutions of Eq. (2.17) for parameters of [74] with $\eta = 2$ and $\mu = 1.1$. (b) Modes (\diamond) and antimodes (\square) in the phase plane $(N_s^x, \omega_s^x - \omega_0)$, N_s^x for continuous variation of ω_s^x is displayed in black curve

The solutions of Eq. (2.17) are found graphically in Fig.2.8(a) and correspond to the values of $\omega_s^x - \omega_0$ for which $f(\omega_s^x - \omega_0) = 0$. The function f is defined as follows :

$$(2.18) \quad f(\omega_s^{x,y} - \omega_0) = \omega_s^{x,y} - \omega_0 \mp \alpha \gamma_a \pm \gamma_p + \eta(\alpha \cos(\omega_s^{x,y} \tau) + \sin(\omega_s^{x,y} \tau))$$

The shape of the function f suggests that the number of solutions increases with the feedback rate η because the amplitude of the sinusoidal term increases. On the contrary, in the limit case where $\eta = 0$ (*i.e.* for the free-running laser), f becomes a linear function with only one solution. A small-signal analysis [138]

shows stable and unstable solutions called external cavity **modes** and external-cavity **antimodes**, respectively. They both appears in pairs through the so-called *saddle-node bifurcation* when increasing the feedback rate. The *saddle* and the *node* correspond to the antimode the mode respectively.

Each mode (*resp.* antimodes) has a specific position in the phase-space ($N_s^x, \omega_s^x - \omega_0$) as shown in Fig.2.8(b) which corresponds to a certain gain and optical pulsation. They are organized on an ellipse with the modes on the upper part and the antimodes on the bottom part as demonstrated by Mork *et. al.* in Ref.[139].

2.2.2 Low-Frequency Fluctuation mechanism

Low Frequency Fluctuations (LFF) dynamic is a typical dynamical regime encountered in laser diodes with optical feedback [140]. First reported in 1977 by Rish and Vourmard [141], LFF refers to a slow-fast modulation of the output power where sudden drops occur at a frequency much lower than the relaxation-oscillation frequency f_{RO} of the laser or the external-cavity frequency f_{EC} . This results from the interaction between the attractive trajectory around external-cavity modes and the repelling motion of the induced by antimodes as described in Ref. [53]. Indeed, as illustrated in Fig. 2.9, the trajectory of the system consists of a chaotic motion around the maximum gain mode. This can lead to a collision with an antimode (also called *saddle-node*) occurring randomly due to deterministic chaotic motion or induced by noise. The antimode repels the system far from the maximum gain mode inducing a sudden drop in the total output power. The system recovers from the collision by a slower itinerancy among the so-called *attractor ruins* [53] which are the destabilized external-cavity modes created by the feedback.

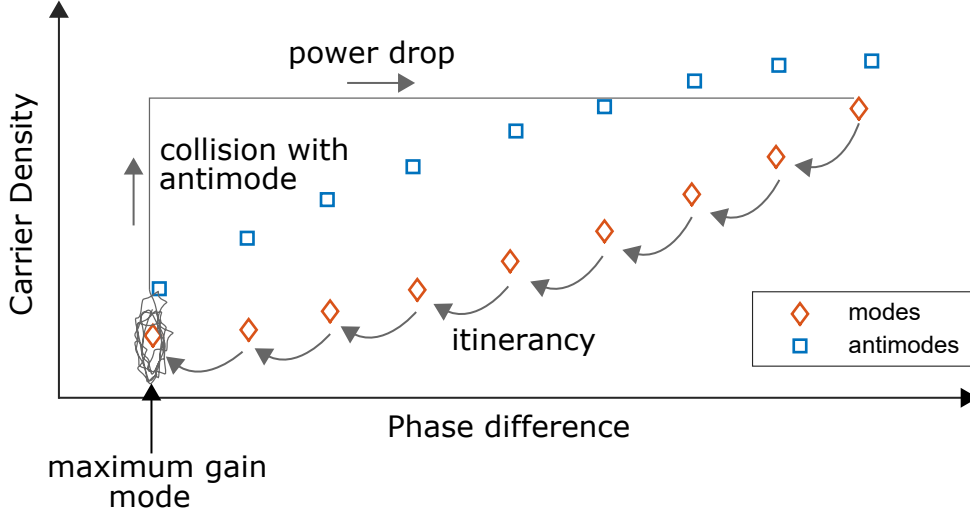


Figure 2.9: Illustration of the LFF for a laser diode subjected to optical feedback. The trajectory is shown in the phase-space formed by the carrier density and the phase difference $\phi_Y(t) - \phi_Y(t - \tau)$ with ϕ_Y being the pulsation ω_s^y multiplied by the delay τ .

The mean frequency of the LFF drops is usually of the order of MHz to hundreds of MHz, but LFF also consists of faster dynamics (observed experimentally using high-bandwidth detection such as a streak-camera [142]). Although LFF measured in an EEL usually occurs in the total output power, it occurs in both orthogonal polarization modes in VCSEL [74, 133].

A typical time trace of LFF obtained from the SFM model (Eqs. (2.11)-(2.13)) is shown in Fig. 2.10 (a). We show only the dynamic in the Y linear polarization-mode (Y-LP mode) but analogous behavior is also observed in the X-LP mode. Considering a large bandwidth for the detection in the simulations (resolution of 1 ps), power drops (indicated by red arrows) are almost indistinguishable : at this fine resolution, LFF consists on high intensity pulses after the drop followed by a gradual recovery where the amplitude decreases until the next power drop.

In Fig. 2.10 (b), we show the corresponding time evolution of the phase difference $\phi_Y(t) - \phi_Y(t - \tau)$ as it depicts the trajectory of the system around the ECM. Before the drop, the trajectory remains around the maximum gain mode region at $\phi_Y(t) - \phi_Y(t - \tau) = -230$ rad. Just after the drop, the phase difference increases far from the maximum gain mode value. The system then slowly recovers by visiting several ECMs until reaching again the maximum gain mode.

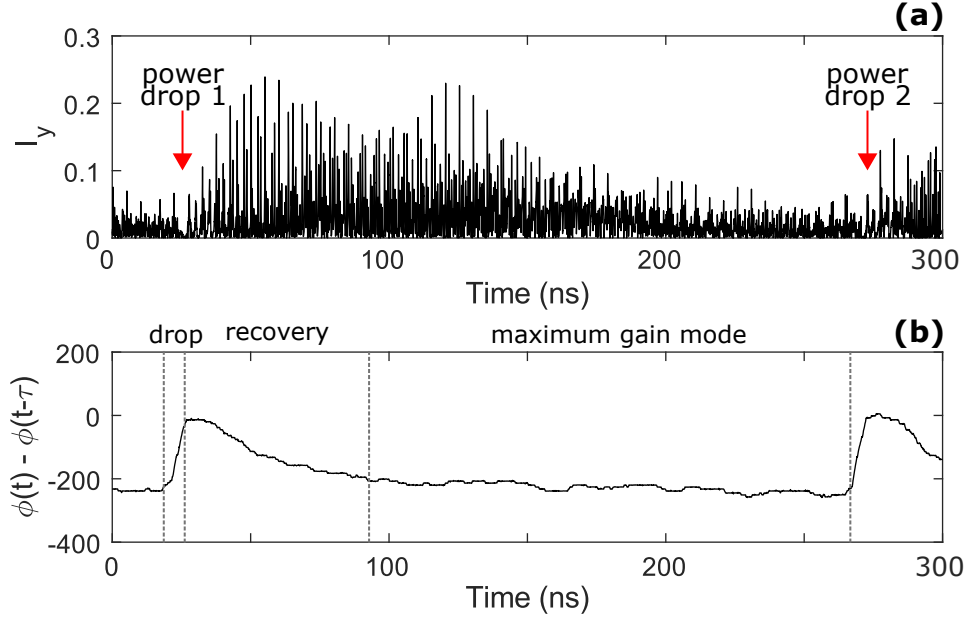


Figure 2.10: LFF dynamics obtained from the SFM model with feedback. Time evolution of (a) Y-LP mode intensity $I_y = |E_y|^2$ and (b) the phase difference $\phi_Y(t) - \phi_Y(t - \tau)$. The parameters are $\mu = 1.02$, $\eta = 10$ GHz, $\tau = 5$ ns, $\kappa = 300$ GHz, $\alpha = 3$, $\phi_0 = 6$ rad, $\gamma_n = 1$ ns $^{-1}$, $\gamma_s = 5$ ns $^{-1}$, $\beta_{sp} = 10^{-4}$ ns $^{-1}$, $\gamma_a = 0.5$ rad.ns $^{-1}$, $\gamma_p = 2$ rad.ns $^{-1}$.

The polarization properties of VCSELS also lead to interesting behavior in LFF : the two polarization modes interact with each other. Hence, not only the Y-LP mode exhibits LFF modulation but so does the X-LP mode.

2.2.3 LFF in polarization modes of VCSELS

Using the SFM model, LFF has been predicted in VCSELS by Masoller *et al.* in 1999 [74]. They show that both polarization coexist in LFF regime and exhibit simultaneous power drops *i.e.* they are correlated at low frequency component of the LFF. They also demonstrated that polarization modes are strongly anti-correlated at frequency higher than the slow LFF modulation leading to quasi-quiescent modulation in between drops. Still in 1999, Guidici *et al.* [133] reported both theoretically and experimentally on the observation of LFF in VCSEL. Contrary to the results of Masoller *et al.*, they observed an anti-correlated behavior of the polarization modes at the LFF frequency, *i.e.* when one polarization drops in power, the other one bursts. However, although they used the SFM model for their simulations, they also ac-

counted for multiple round-trip effects in the external cavity, a feature that was not considered by Masoller *et al.* [74].

In 2003, Sciamanna *et al.* [134] has linked both results using the SFM model (Eqs. (2.11)-(2.13)) accounting for one round-trip inside the external-cavity. They demonstrated that VCSELs can, in fact, exhibit two types of LFF :

- Type-I LFF : both LP-modes are correlated at the low-frequency scale *i.e.* they both show drops of power simultaneously
- Type-II LFF : one LP-mode is dominant (the other one being depressed) and the two polarization modes are anti-correlated at the low-frequency scale *i.e.* the dominant mode shows drops of power while the depressed one bursts.

Therefore, the type of LFF does not depend on whether single or multi-round-trip in the external cavity but rather depends on the VCSEL parameters such as the birefringence γ_p and the anisotropy γ_a . In 2003, Sondermann *et al.* [135] have experimentally explored the effect of the dichroism (birefringence and anisotropy effects) on the LFF regime in VCSEL. Although they only reported on Type-I LFF, they showed that the dichroism highly impacts the average power exhibited by the depressed polarization mode.

In Fig. 2.11, we give an example of the two different types of LFFs considering the time evolutions of both polarization intensities ($I_X = |E_x|^2$ and $I_Y = |E_y|^2$) obtained numerically in the framework of the SFM model (Eqs. (2.11)-(2.13)). Here, we only considered one round-trip inside the external-cavity. The delay is chosen at $\tau = 5$ ns to match our experimental results (see Sec. 2.3). We operate at $\mu = 1.02$, just above the current threshold ($\mu_{thr} = 1$). Other parameters are chosen equal or in the same range of those considered in the study of LFF of Masoller *et al.* [74] : $\kappa = 300$ GHz, $\alpha = 3$, $\phi_0 = 6$ rad, $\eta = 10$ GHz, $\gamma_n = 1$ ns⁻¹, $\gamma_s = 5$ ns⁻¹, $\beta_{sp} = 10^{-4}$ ns⁻¹ and $\gamma_p = 2$ rad.ns⁻¹. The anisotropy parameter γ_a is varied from 0.01 rad.ns⁻¹ in Fig. 2.11 (a.1) - (a.2) to 0.5 rad.ns⁻¹ in Fig. 2.11 (b.1) - (b.2) that show polarization-resolved Type-I LFF and Type-II LFF, respectively. The dynamics are averaged on a 2 ns sliding window and displayed in orange over the 1 ps time-resolved signal.

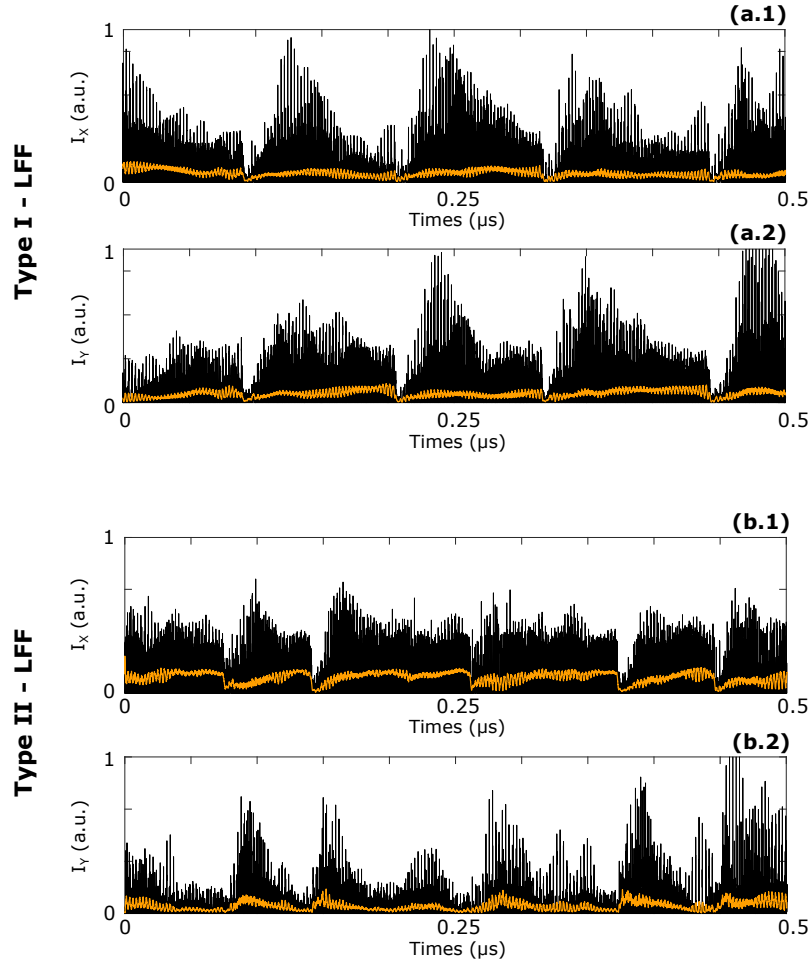


Figure 2.11: Time evolution in Type-I LFF regime ($\gamma_a = 0.01 \text{ rad.ns}^{-1}$) of (a.1) the X-LP mode intensity I_x and (a.2) the Y-LP mode intensity I_y . Time evolution in Type-II LFF regime ($\gamma_a = 0.5 \text{ rad.ns}^{-1}$) of (b.1) the X-LP mode intensity I_x and (b.2) the Y-LP mode intensity I_y .

For both types of LFF and both polarizations, the dynamic (black curve) consists on high-intensity pulses and the drop can only be distinguished from the average signal (orange curve). We observe for the Type-I LFF [Fig. 2.11 (a.1) - (a.2)] a correlated behavior at the slow time-scale *i.e.* they both exhibit simultaneous drops of power. We observe a Type-II LFF instance in Fig. 2.11 (b.1) - (b.2)] where both polarization modes are anti-correlated at the slow time-scale.

Another feature of interest has been reported in 2003 by Naumenko *et al.* [136, 143] in Type-I LFF regime. They reported experimentally on the appearance of

a double-peak structure at the external-cavity frequency, when analyzing the RF spectrum. This double-peak is observed in the RF spectrum of both polarization modes and the splitting between the peaks depends on the current. This result has been investigated in more details in Ref. [144]. While looking for the correlation property between the LP-modes displayed by this double-peak, they observed that the low-frequency peak of the structure shows anti-correlation while the high-frequency counterpart shows correlation. To perform such analysis, they computed the *cross-spectral density* (CSD), which is mathematically defined by

$$(2.19) \quad CSD(f) = \tilde{I}_x(f)\tilde{I}_y^*(f) + \tilde{I}_y(f)\tilde{I}_x^*(f),$$

with $\tilde{I}_x(f)$ (resp. $\tilde{I}_y(f)$) the Fourier Transform of the X-LP (resp. Y-LP) intensity and * denotes the complex conjugate. Positive (resp. negative) value of the CSD at a frequency f means that the LP-modes are correlated (resp. anticorrelated) at this frequency.

However, one can also wonder if this correlation property remains true for both types of LFF. We show in Fig. 2.12, the RF spectrum of each polarizations in Type-I and Type-II LFF, corresponding to the time evolution reported in Fig. 2.11. We observe the double-peak structure around the external-cavity frequency f_{EC} in each LP-modes and for both types of LFF [for Type-I in Fig. 2.12(a.1)-(a.2) and for for Type-II in Fig. 2.12(b.1)-(b.2)]. The structure consists on two peaks located at $f^- = 170$ MHz and $f^+ = f_{EC} = 200$ MHz. As in Ref. [144], the CSD of the Type-I LFF in Fig. 2.12 (a.3) shows anticorrelation at f^- and correlation at f^+ . However, this situation changes for the Type-II LFF in Fig. 2.12 (b.3). Indeed, while f^- still exhibits anti-correlation, f^+ changes from the Type-I and also shows anti-correlation. This preliminary result suggests that there is a non-local correlation property between the low LFF frequency (that defines Type-I and Type-II LFF) and the f^+ frequency.

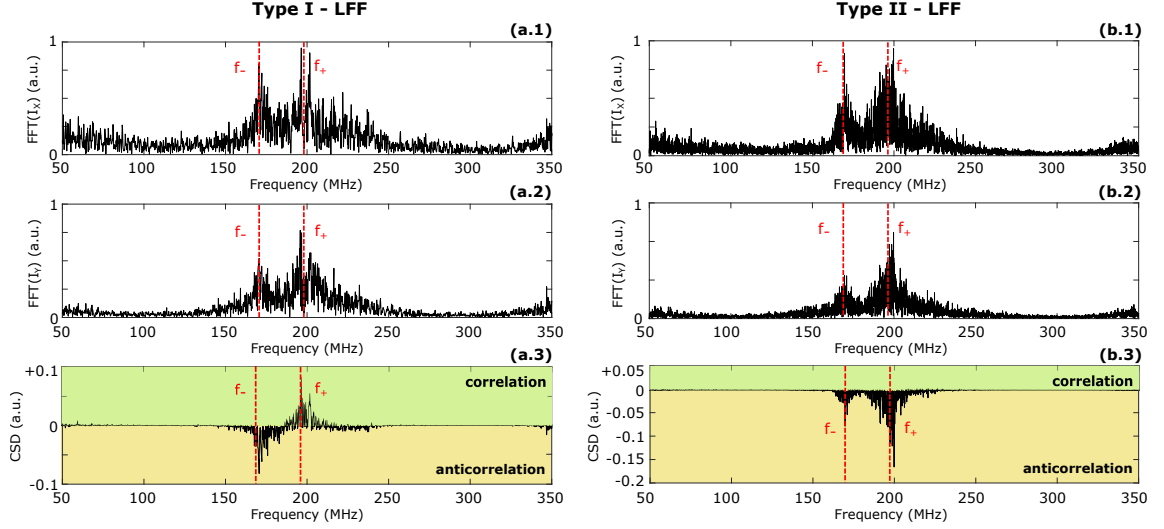


Figure 2.12: RF spectrum in Type-I LFF regime ($\gamma_a = 0.01 \text{ rad.ns}^{-1}$) of (a.1) the X-LP mode intensity I_x and (a.2) the Y-LP mode intensity I_y and (a.3) the corresponding CSD. RF spectrum in Type-II LFF regime ($\gamma_a = 0.5 \text{ rad.ns}^{-1}$) of (a.1) the X-LP mode intensity I_x and (a.2) the Y-LP mode intensity I_y and (a.3) the corresponding CSD.

2.2.4 Observation of double-peak structures in the literature

The first observation of such double-peak structure appearing in the vicinity of the external-cavity frequency has been reported in 1989 by Sacher *et al.* [145] in the RF spectrum of an EEL output power that operates in the LFF regime. Similarly, Langley *et al.* [146], Besnard *et al.* [147] in 1994 and Giudici *et al.* [148] in 1997 also observed a similar structure in LFF regime. However, that observation did not receive in depth experimental consideration and its physical origin was unexplored.

Later, in VCSEL, as mentioned above, double-peak structure has been reported in 2003 [135, 136] and in 2005 [144] in LFF regime. They observed an intriguing correlation behavior for the two peaks of the structure. In 2006, Tabaka *et al.* [57] also reported on such double-peak structure with also different correlation property between the two peaks. They observed such phenomenon for an external-cavity VCSEL in the short cavity regime *i.e.* when f_{EC} is higher than the relaxation oscillation frequency f_{RO} , that operates in regular pulse package (RPP) regime.

Multiple assumptions were made as for the origin of the double-peak. In Ref. [147], the double-peak power spectrum is explained by the influence of multiple round-trips in a slightly misaligned external cavity. However, as demonstrated numerically in

Ref. [144] and from our simulations in Fig. 2.12, a model that only accounts for one round-trip is sufficient to induce the double-peak structure. In 1994, Van Exter *et al.* [149] explained the double-peak by a competition between longitudinal emission modes of the laser diode but we will show in Sec. 2.4.2 that a simple single-mode model is also sufficient to reproduce the double-peak structure.

Therefore, to the best of our knowledge, a detailed physical explanation of this generic phenomenon has remained elusive for almost 30 years, thus motivating further theoretical and experimental exploration. In particular, the link between the double peak power spectrum and the properties of the deterministic chaotic dynamic remains to be elucidated.

2.3 Experimental investigation

In the previous section, we have explained the physical mechanism behind the LFF dynamics in laser diodes. In VCSEL, the LFF regime cannot be explained by inspecting only the total output power but needs to consider the VCSEL polarization dynamics. Furthermore, many groups have reported the existence of a double-peak structure in the vicinity of the external-cavity frequency in LFF regime that has also been observed in polarization mode of VCSEL. Still, this double-peak structure may exhibit quite intriguing correlation properties between the VCSEL polarization.

In this section, we experimentally investigate LFF regime induced in a VCSEL by an isotropic optical feedback. We study the LP-mode dynamics and their correlation properties at the slow LFF time-scale and also at the external-cavity frequency scale. We will confirm our numerical findings and explore the behavior of such double-peak structure when varying the injection current and the delay.

2.3.1 Experimental setup

We design an experiment to measure the polarization dynamics within a large frequency range that encompasses the bandwidths of the chaotic dynamics and the relaxation oscillation frequency. The experimental setup, shown in Fig. 2.13, comprises an AlGaAs/GaAs VCSEL emitting at 850 nm with a solitary threshold current of $J_{th}^s = 0.45$ mA at 15°C, which was measured under controlled thermal fluctuations within $\pm 0.01^\circ\text{C}$. The output beam shows a single transverse mode with

Gaussian profile in the range of currents where we operate the VCSEL *i.e.* up to 0.9 mA. The laser beam is collimated by a microscope objective before reaching a first 50/50 beam splitter. The first arm corresponds to the external cavity and uses a 99.9% reflectivity mirror and a variable attenuator to control the feedback strength. The measurement arm comprises a 50/50 beam-splitter, two polarizers and optical isolators to separate the two LP modes before coupling into two single-mode optical fibers. The measurement arm is designed so that we can guarantee a balanced coupling efficiency and identical traveling distances from the laser source. Finally, the two LP modes are measured by two identical photodiodes LeCroy OE425 with 4.5 GHz bandwidth and two Newport 1554-B with 12 GHz bandwidth, which are connected to either a 4 GHz Lecroy Waverunner 640Zi oscilloscope with 40 GSamples/s or a 26.5 GHz Rohde & Schwarz FSW26 spectrum analyzer. The VCSEL emits in its Y-LP mode at threshold and switches to X-LP at pumping current 0.75 mA. X-(Y-) LP mode is the low (high) frequency mode hence the switching is of type I [17]. In the following, we shall operate in the range 0.48 – 0.56 mA, well below the switching point.

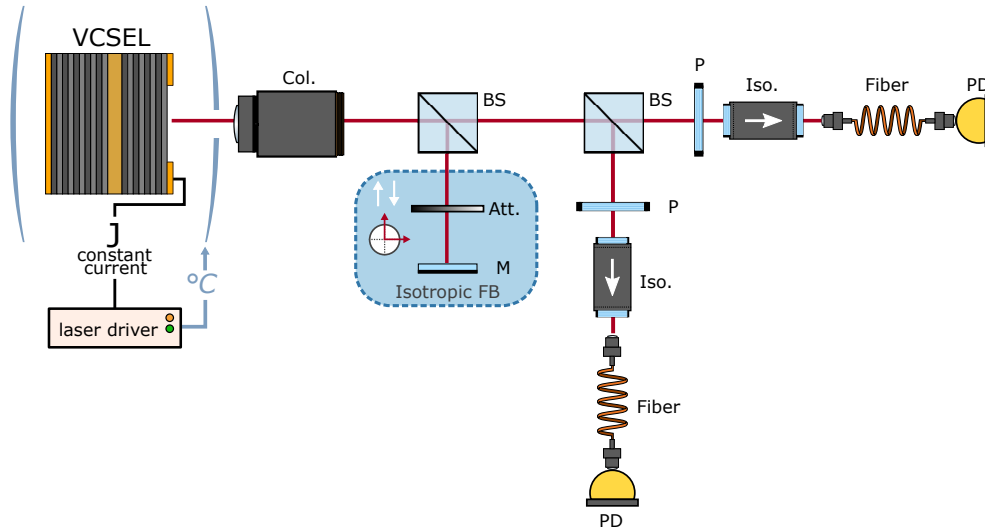


Figure 2.13: Experimental setup. Col: collimating microscope objective, BS: beam-splitter, P: polarizer, Iso: isolator, Att : attenuator, M: mirror, PD: photodiode.

We select an external cavity length of $L_{ext} \approx 75$ cm corresponding to a time-delay of $\tau = 2L_{ext}/c \approx 5$ ns. This ensures the so-called long cavity regime, where the external cavity frequency $f_{EC} = 1/\tau$ is much smaller than the relaxation oscillation f_{RO} of the

free-running VCSEL, which has been estimated to be about 1.37 GHz at 0.48 mA by relative intensity noise (RIN) measurements.

2.3.2 LFF : Double peak and correlation features in the RF spectrum

In the experimental conditions described in section 2.3.1 with a pumping current range [0.43 mA, 0.6 mA], the VCSEL exhibits LFF dynamics, as shown in Fig. 2.14(a) and 2.14(b). Y is the dominant LP-mode and shows drops of power, while X is the depressed one and shows bursts. this is a typical instance of Type-II LFF which we can most likely attribute to a large dichroism of our device [134]. Anti-correlation between the LP mode dynamics manifests itself on a slow time-scale as also confirmed by CSD calculation in Fig. 2.15(a) at ~ 20 MHz, the mean drops/bursts frequency f_{LFF} .

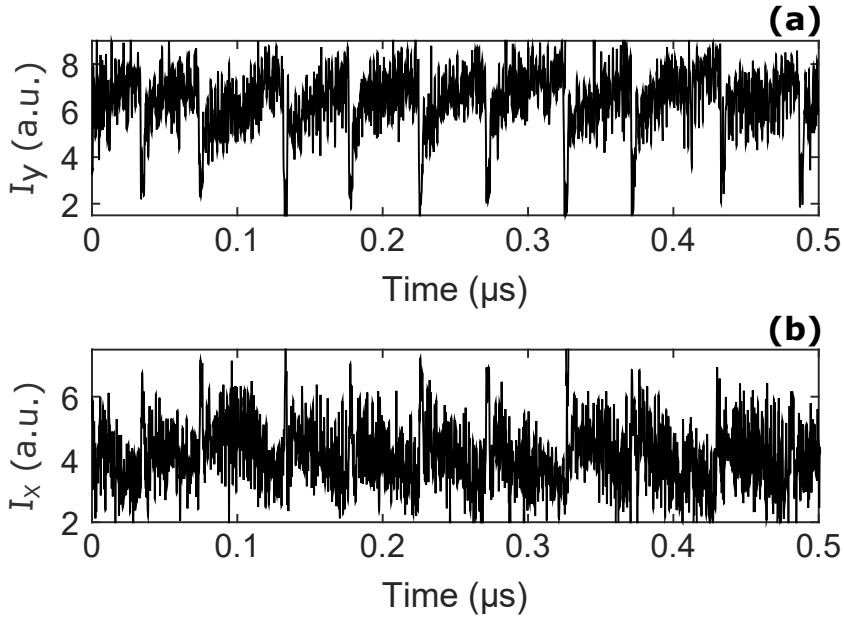


Figure 2.14: Intensity time series of (a) the Y-LP mode and (b) the X-LP mode of VCSEL in the LFF Type-II regime. The pumping current is $1.2J_{th}^s = 0.54mA$, time delay $\tau \approx 5$ ns, temperature $15^\circ C$, and 14% threshold reduction.

At a frequency $f \approx f_{EC}$, the CSD shows an anti-correlated behavior. Most importantly, the CSD shows a double-peak structure with two peaks f_- and f_+ in the

spectral vicinity of f_{EC} . The frequency separation of $\Delta f = f_+ - f_-$ is about 20 MHz. The CSD confirms that the dynamics of the two LP modes at these two frequencies are anti-correlated between the two LP modes. Anticorrelation at both f_- and f_+ frequencies confirm our numerical findings in Fig. 2.12 (b.3) for Type-II LFF. This result, however, differs from previous studies [136, 144] on Type-I LFF, where it was found that the X-LP and Y-LP modes are correlated at the second frequency f_+ .

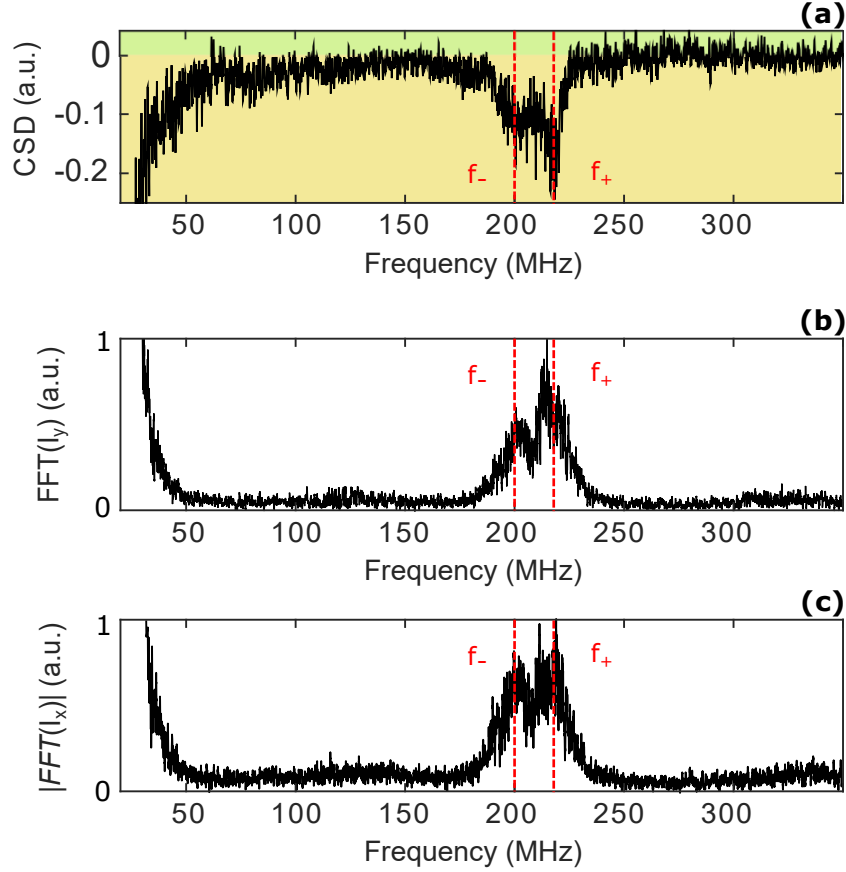


Figure 2.15: (a) CSD between X-LP and Y-LP modes. RF spectrum of (b) Y-LP mode intensity and (c) the X-LP mode intensity. f_- and f_+ are the two main components of the discussed double-peak structure. The fixed parameters are identical to those used in Fig. 2.14

Furthermore, in order to confirm that the double-peak structure is also observed in the RF spectrum of both polarization modes, we compute respectively in Fig. 2.15 (b) and (c) the modulus of the Fourier Transform (FFT) of the time evolution shown in Fig. 2.14 (a) and (b) of the Y and X-LP modes. We considered here a time window

of 20 μs that correspond to approximately 400 occurrences of LFF drops/bursts. We observe that the double-peak structure is also present in the vicinity of f_{EC} .

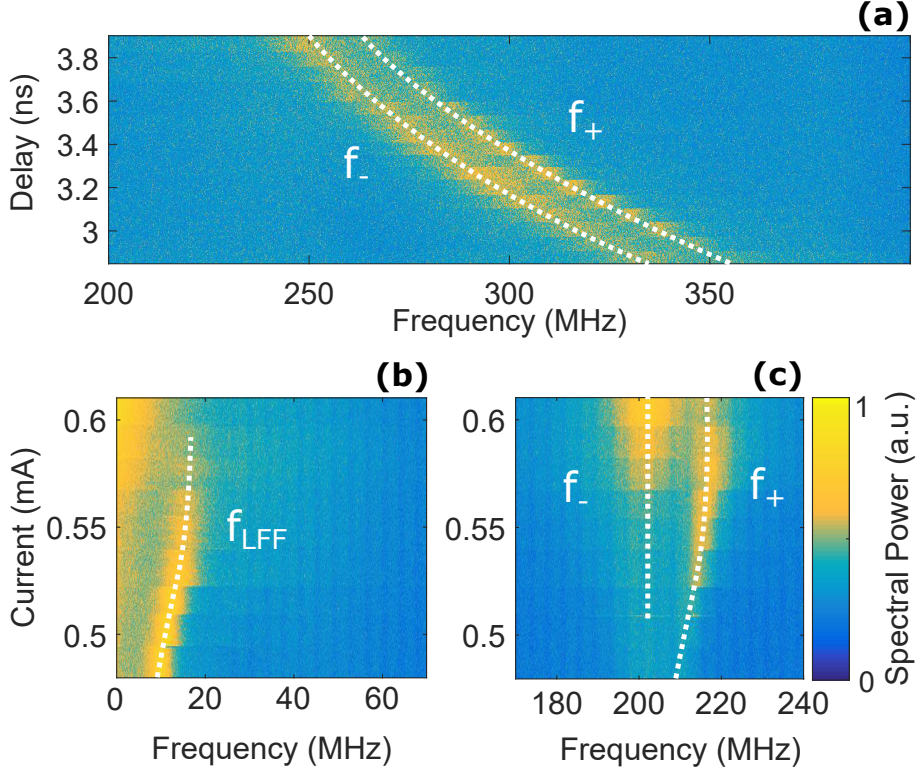


Figure 2.16: Spectrogram of the Y-LP mode in the frequency range (a) $f \in [200 \text{ MHz}, 400 \text{ MHz}]$ as function of the external-cavity delay (b) $f \in [0 \text{ MHz}, 70 \text{ MHz}]$ and (c) $f \in [170 \text{ MHz}, 240 \text{ MHz}]$ as a function of the pumping current. f_- and f_+ are the two main components of the discussed double-peak structure and f_{LLF} is the slow LFF frequency at the drop/burst scale. The fixed parameters are identical to those used in Fig. 2.14.

The shape of the structure is more noisy in 2.15 (c) as the X-LP is more depressed and bursts from the noise floor. Hence, we will focus on the RF spectrum of the Y-LP mode in order to investigate its behavior when varying the external-cavity delay in Fig. 2.16(a) and the injection current in Fig. 2.16 (b) and (c).

The experimental spectrogram⁴ in Fig. 2.16 (a) as function of the delay shows

⁴The spectrograms are recorded from the FSW26 Rohde&Schwarz RF spectrum analyzer with a sweep time of 0.1 s over the frequency range [1Hz,1GHz]. We use a 12.5 GHz bandwidth photodiode. Each line of the spectrograms are averaged from 15 measurements with 50 kHz of resolution bandwidth.

that the peak separation Δf is not affected by the variation of the delay. However, the double-peak structure always remains in the vicinity of f_{EC} . Finally, when varying the current in Fig. 2.16 (b) and 2.16(c), the spectrogram shows that the lowest frequency peak f_- is not affected by an increase of pumping current, while the highest one at f_+ shifts towards higher frequencies when increasing the current. Interestingly, the frequency deviation of f_+ evolves similarly to that of the average modulation LFF frequency (close to ~ 20 MHz) with varying pumping current.

In summary, although our VCSEL only exhibits Type-II LFF, we have confirmed here that LFF modulation leads to the appearance of a double-peak structure in the RF spectrum of both polarization modes. In addition, we also confirm our numerical findings in that both peaks reveal anti-correlation at those frequencies between the LP modes. When comparing our results to our numerical observations and to previous experimental results [135], we do show here that the low frequency correlation (at LFF time scale) also influences the correlation property at higher frequency *i.e.* at f_+ . Anticorrelation at f_{LFF} (hence Type-II LFF) also brings anticorrelation at f_+ and *vice versa*. Finally, we have shown that the two frequencies making the double-peak structure evolve with the delay as does the external-cavity frequency, and we investigated its behavior when varying the current.

However, these results are still not sufficient to state on the physical nature of the double peak structure. Hence, an in-depth numerical study is provided in the next section.

2.4 Physical origin of the double-peak structure

So far, we have seen that VCSEL polarization instabilities may lead to two different types of LFF dynamics in the polarization modes when subjected to isotropic optical feedback. We also notice, both numerically and experimentally, the presence of a double-peak structure in the vicinity of the external-cavity frequency that shows different correlation signatures depending of the type of LFF. In the following, we will demonstrate that this double-peak structure arises from the interaction between external-cavity modes and antimodes et more precisely from their attraction and repelling motion.

2.4.1 Phase-space dynamic and mode/antimode interaction

As shown in Sec. 2.2.1, the delay creates multiple fixed points : the external-cavity mode and antimodes, that, as explained by Sano *et al.* [53] are intrinsically linked to the LFF regime. As the number of those fixed points increases with the feedback strength, we chose to restrict our following investigation to low value of feedback. In addition, the idea here is to understand the physical origin of the double-peak structure. Hence, we intentionally omit the polarization-mode competition by choosing a set of parameters where only one mode is dominant while the other mode is highly depressed.

Therefore, we simulate the SFM equations (Eqs. (2.11)-(2.13)) and considered the following parameters : $\mu = 1.02$, $\eta = 3$ GHz, $\tau = 5$ ns, $\kappa = 300$ GHz, $\alpha = 3$, $\phi_0 = 6$ rad, $\gamma_n = 1$ ns⁻¹, $\gamma_s = 50$ ns⁻¹, $\beta_{sp} = 10^{-4}$ ns⁻¹, $\gamma_a = 0.5$ rad.ns⁻¹ and $\gamma_p = 2$ rad.ns⁻¹. This set of parameters is still in the same range of parameters used in previous study on LFF [74]. Figure 2.17(a) shows the RF spectrum of the lasing Y-LP mode. We still observe the double-peak structure close to $f_{EC} = 200$ MHz.

Additional insight into the physical origin of the double peak is provided by analyzing the VCSEL dynamics in a projection of the infinite dimension phase-space. Figure 2.17(b) shows the projection of the trajectory in the plane $(|E_y(t)|, \phi_y(t) - \phi_y(t - \tau) + \phi_0)$, where $\phi_y(t)$ is the phase of the dominant Y-LP mode and $\phi_y(t) - \phi_y(t - \tau) + \phi_0$ is the phase difference between the Y-LP mode and its time-delayed version. When comparing Fig. 2.17 (b) with Fig. 2.17 (c), we observe that the chaotic trajectory is attracted towards the ECM with maximum gain corresponding to the largest phase difference, but visits also a set of other ECMs. While pulsating around the position of the maximum gain mode [represented by a diamond in Fig. 2.17(c)], the trajectory is repelled by the close proximity of an antimode [represented by a square in Fig. 2.17(c)].

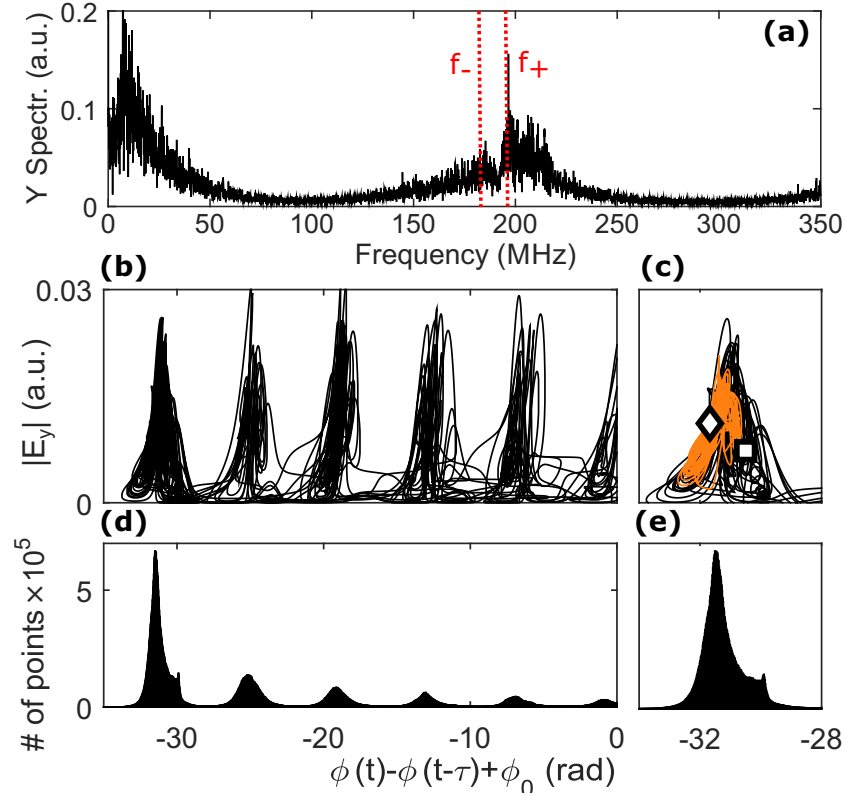


Figure 2.17: (a) Numerical RF spectrum of the intensity of the Y-LP mode in external cavity frequency window, (b) trajectory in the phase space and (c) a zoom into the attractor of highest phase shift, (d) the histogram showing the number of points as function of the phase shift and (e) its corresponding zoom into the attractor of highest phase shift region. The parameters are identical to those used in Fig. 2.11 except for $\eta = 3$ GHz and $\gamma_s = 50$ ns⁻¹.

To give a dynamical interpretation to the observed double-peak structure, we analyze the frequency content of phase space trajectories remaining in the vicinity of either the maximum gain mode or the antimode. Figure 2.18(a) shows a typical drop-out event of LFF dynamics associated with the trajectory in the projected phase-space of Fig. 2.17(b). Similar time-series are found at different time-locations in the numerical simulations as the system encounters many times similar trajectories in phase-space after a drop-out. These typical time series have two distinct dynamical behaviors marked by the orange and green time-windows in Fig. 2.18(a) : the orange window displays a dynamic corresponding to the trajectory around the maximum gain mode [orange trajectories in 2.17(c)], whereas the green window shows the

typical time evolution around the corresponding antimode. In Fig. 2.18(b), we show the RF spectrum obtained by computing the concatenation of a large number of such orange time-windows. We notice the complete suppression of the peak at f_- in the double peak structure. By contrast, considering the additional green time-windows, the f_- component of the double-peak structure arises in Fig. 2.18(c). In Fig. 2.18(d) and 2.18(e), we further increase the window size in the phase-space and, thus, consider more points in the time-domain. As a result, we recover the original double-peak structure shown in Fig. 2.17(a). As a result, we have demonstrated here that the high-frequency part f_+ of the double peak structure arises from the trajectory of the system around the maximum gain mode while the low-frequency component f_- is associated to the trajectory around the corresponding antimode.

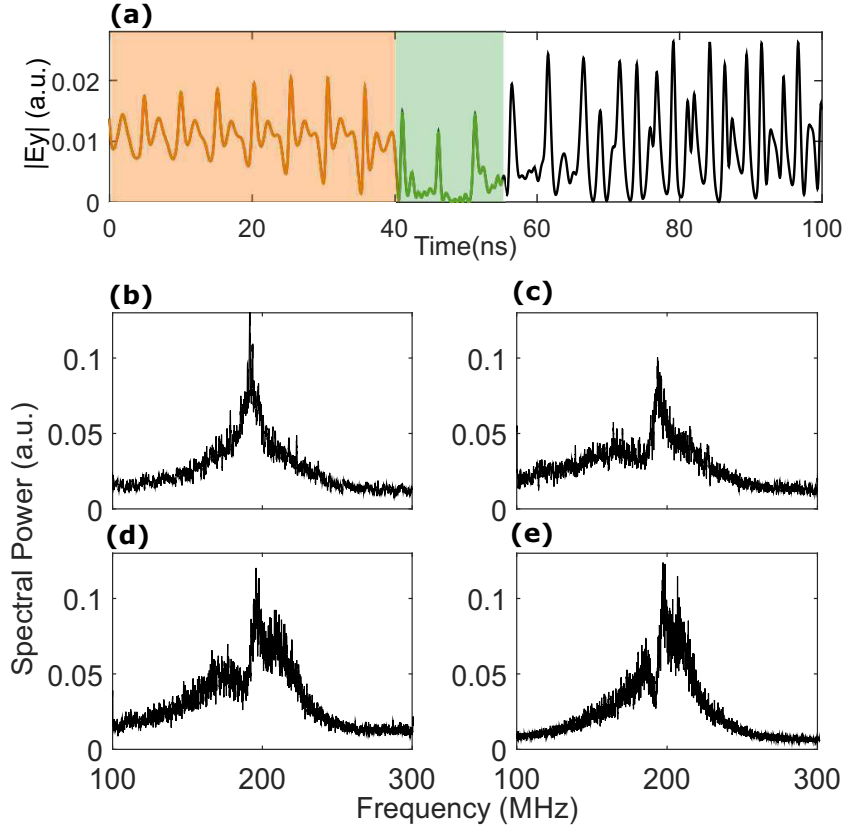


Figure 2.18: (a) Typical time trace of a LFF drop-out event of the Y-LP mode. RF spectra computed by considering different window sizes in the phase space in Fig. 2.17(b). For $\phi_Y(t) - \phi_Y(t - \tau) + \phi_0$ range : (b) from -35 to -31 rad, (c) from -35 to -27 rad, (d) from -35 to -16 rad, (e) from -35 to -0 rad.

Finally, we show in Fig. 2.19 that the double-peak structure studied numerically behaves similarly as in the experiment when varying the parameters τ (delay) and μ (pumping current). In Fig. 2.19(a), the double-peak structure follows the external-cavity frequency when varying the delay. Furthermore, Fig. 2.19(b) shows that increasing the pumping current does not impact the first frequency component f_- of the double peak structure while the second frequency component f_+ shifts to higher values. This is also the case for the low frequency modulation. For higher values of pumping current $\mu > 1.025$, the dynamics of the system moves from LFF regime towards the so-called coherence-collapse (CC) regime with no clear low-frequency signature which is translated in the spectrogram by a slow fading of the low frequency component. Numerical simulations and experiments confirm there is a strong link between the low-frequency component (corresponding to power dropouts) and the highest frequency f_+ of the double peak structure. Indeed, (anti-)correlation at the low frequency leads to (anti-)correlation at f_+ and when the low frequency component shifts with varying the parameters, f_+ shifts also.

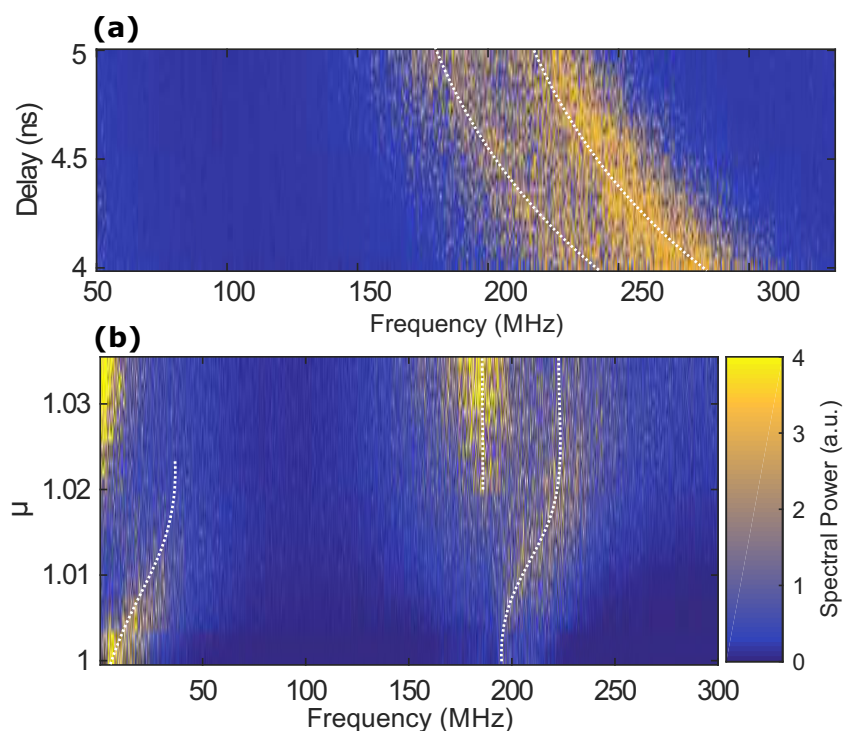


Figure 2.19: Spectrograms of the Y-LP mode as a function of (a) the delay τ and (b) the pumping current μ . Other parameters are the same as in Fig. 2.17. The spectral resolution is of 0.2 MHz

2.4.2 Double-peak structure with a single-mode model

Appart from the correlation analysis, similar double-peak spectral signatures have been reported in previous studies on external-cavity laser diode in different dynamical regimes. This naturally raises the question of the generality of such spectral properties and their physical interpretation. For example, in Ref. [147], the explanation of the double-peak signature relied on multiple round-trips in the external cavity of a chaotic VCSEL. In Ref. [149], the authors based their explanation on the competition between longitudinal modes of an EEL subjected to a weak feedback. Finally, in Ref. [144], it was proposed that a still unexplained nonlinear mixing between the external-cavity frequency and the relaxation-oscillation frequency of a VCSEL was responsible for the appearance of the double-peak structure.

Here, we provide an alternative explanation relying on the chaotic itinerancy in the phase-space due to the interplay between stable and unstable ECMs in LFF regime. Interestingly, and by contrast to these earlier explanations, our approach does not require the inclusion of longitudinal mode competition or multiple round trips in cavity. This is evidenced in Fig. 2.20(b) where we simulate the single-mode LK equations with a single round-trip feedback [150, 151] :

$$(2.20) \quad \dot{E}(t) = 1/2(1 + i\alpha)(G_{N,|E|^2} - 1/\tau_p)E(t) + \gamma e^{-i\omega_0\tau} E(t - \tau),$$

$$(2.21) \quad \dot{N}(t) = pJ_{th} - N/\tau_s - G_{N,|E|^2}|E(t)|^2,$$

$$(2.22) \quad G_{N,|E|^2} = G_N(N - N_0)/(1 + \epsilon |E|^2),$$

where $E(t) = |E(t)| e^{i\phi(t)}$ is the slowly varying envelop of the complex electric field, N is the carrier density in the active region, $G_{N,|E|^2}$ is the optical gain, α is the linewidth-enhancement factor, ϵ is the saturation coefficient, N_0 is the carrier density at transparency, G_N is the differential gain, ω_0 is the angular frequency of the solitary laser, γ is the feedback rate, τ_p is the photon lifetime, τ_s is the carrier lifetime, J_{th} is the threshold current, p is the pumping factor and τ the external cavity delay. Used parameters are listed in the caption of Fig. 2.20 and lead to a chaotic LFF dynamics. Except for the specific correlation properties driven by the VCSEL polarization competition in Fig. 2.12, the double peak structure is well reproduced numerically.

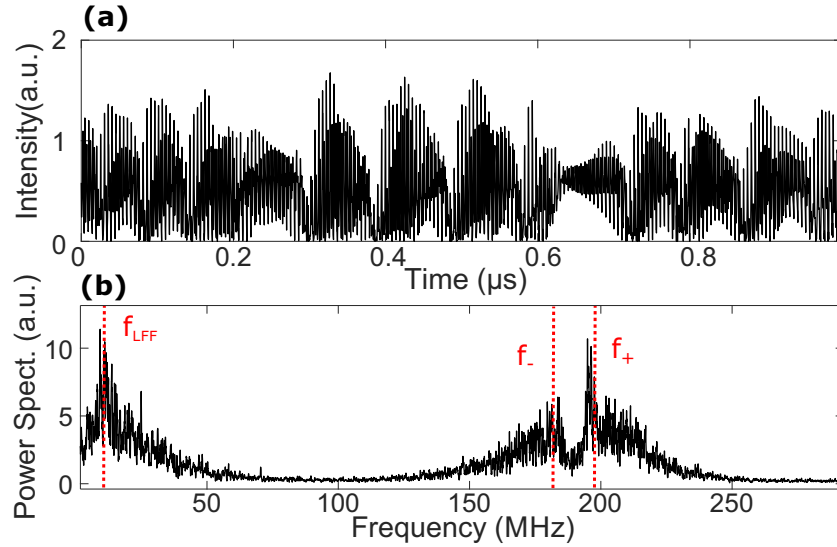


Figure 2.20: Numerical (a) time trace of the output intensity and (b) power spectrum for $\tau_p = 1.66$ ps, $\tau_s = 1$ ns, $\alpha = 3$, $\epsilon = 5 \times 10^{-7}$ m³, $G_N = 1.5 \times 10^4$ m³ · s⁻¹, $N_0 = 1.5 \times 10^8$ m⁻³, $J_{th} = 1.9 \times 10^{17}$ m⁻³ · s⁻¹, $p = 1$, $\gamma = 3$ GHz, $\tau = 5$ ns, $\omega_0\tau = 0$ rad.

2.5 Conclusion

In summary, in this chapter, we have introduced the polarization instabilities that occur in VCSEL and show that their mechanisms highly differ from those in EEL. Several explanations have been proposed in order to model the polarization behavior in VCSEL based on the gain and loss spectrum sensitivity to the temperature and current. Although such instabilities are detrimental to modern telecommunication technologies, many groups have demonstrated that it could also be of use for future applications such as high-speed random-bit generation, high-speed modulation and neuro-inspired computing.

In a second part, we have explained the basic physics of VCSEL under isotropic optical feedback based on the investigation of the SFM model and introduced a commonly encountered dynamics in laser diode : the low-frequency fluctuations (LFF) that arises from the interaction of fixed points that are either stable, the external-cavity modes (ECM), or unstable, the antimodes. More specifically, we discussed about observations of LFF in the polarization dynamics of VCSELS, which can be classified in two different types depending on the polarization-correlation property

at the slow LFF frequency : Type-I, where both polarizations show power drops, and Type-II, where one polarization drops while the other one bursts. We also observe that LFF may lead to the appearance of an intriguing double-peak structure in the vicinity of the external-cavity frequency in the RF spectrum of both polarization modes. While the polarization modes are always anti-correlated at the low-frequency part of the structure, the high-frequency component relates to either correlation or anti-correlation between polarization modes. The choice between correlation or anticorrelation is linked to the correlation property at low LFF frequency. Therefore, we qualify the reported correlation properties as *non-local* since they relate to each other but at different time-scales or frequencies. In addition, we show that such a double-peak structure is not only specific to LFF in VCSEL, but has been observed many times in other systems or dynamical regimes which makes this more general than expected.

In a third part, we compared the numerical simulations with our experimental results. We show that LFF in VCSEL indeed leads to the observation of the above mentioned double-peak structure and more specifically that, in Type-II LFF, both peaks of the structure leads to anti-correlated behavior between the two polarization modes. We note that the high-frequency peak of the structure behaves similarly to the slow LFF frequency both in its correlation property and its shift in frequency-location while varying the current.

Finally, we provide a physical interpretation of these particular features and connect them with the trajectory of the system in the vicinity of ruins of stable and unstable external cavity modes. We perform a detailed study of the parametric influence (pumping current and time delay). We also confirm that our explanation holds for EEL and doesn't necessarily arise from multi-round trips effect in the external-cavity nor from longitudinal modes interactions effect as first thought in previous works.

VECTORIAL ROGUE WAVE IN VCSEL LIGHT POLARIZATIONS

In this chapter, we report on the occurrence of extreme events in the polarization dynamics of vertical-cavity surface-emitting lasers (VCSEL) with optical feedback. We have identified two types of extreme events based on numerical simulations : vectorial and scalar events corresponding to the emission of high-power pulses in both linear polarizations simultaneously and in single linear polarization, respectively. We show that these two types of events follow the typical statistics of rogue waves. Finally, we observe that light emission in both polarizations leads to a larger generation rate of extreme events with a saturation over a wide range of feedback strength by comparison to a single polarization mode emission.

This Chapter is organized as follows. First, we introduce the concept of Rogue Wave in oceanography and its analogy in optics. Then, we report on the numerical observation of extreme events (EE) in the output power of an external-cavity VCSEL. We propose a classification for 2 types of EEs : scalar or vectorial. Next, we analyze their intensity distribution and temporal statistics and demonstrate that they bare the usual characteristics of Rogue Waves. We study the generation rate of EEs in a two-polarization emission VCSEL and compare it to the case of single-polarization emission. We found that multimode emission when increasing the feedback ratio leads to a saturation in term of generation rate of EEs which is different from what

was traditionally known about RW in laser diode with optical feedback when the feedback is increased. After that, we provide a statistical and physical interpretation of this saturation. Finally, in a last section, we summarize our findings.

This chapter is based on the following publication :

C. H. Uy, D. Rontani, and M. Sciamanna, (2017). Vectorial extreme events in VCSEL polarization dynamics. *Optics letters*, 42(11), 2177-2180.

3.1 Observations of Rogue Wave

3.1.1 Freak wave in oceanography

Created by earthquakes, eruptions, landslides [152] or driven by storm [153], ocean waves can reach monstrous heights as for tsunamis [154] that cause mass destructions when they strike on lands. Those kind of waves are now well-documented even if their prediction still remain a challenge [155]. For centuries, sailors have reported incredible stories [156] about terrifying waves that suddenly arise and strike without warning from an apparently calm sea and disappear as quickly. For example, in 1498, Columbus and his fleet of six ships encountered a huge wave, as high as the masts "*raising the ships to the top of waves as high as hills*" [157]. Columbus named this area the "*Mouth of the Serpent*". In 1861, the Bishop Lighthouse in the Celtic Sea was struck by a wave that was high enough to hit the fog-bell placed 30 m above the sea level [158]. However, all those tales were openly mocked until the 20th century, when the reports on such waves were more easily spread around the globe. This kind of wave was named *freak wave* [159], *extreme wave* [160] or *rogue wave* (RW) [161]. Rogue waves are characterized by their abnormally high magnitude but also by their unexpected random occurrence and rarity that makes it difficult to observe and to study.

The first reliable testimony was brought in 1933 by the crew of the USS Ramapo, an US tanker. They faced a RW in the Pacific and measured its size : 34 m high, 300 to 450 m large and a time duration of 14.8 s [158]. Rare are also the number of available pictures of RW : In 1980, Philippe Lijour crew-member of the French oil tanker *Esso Languedoc* was able to picture the 25 m high RW that slammed his ship [see Fig. 3.1].



Figure 3.1: Rare picture of a rogue wave taken by the French Philippe Lijour aboard the supertanker Esso Languedoc in South Africa. The wave completely struck the 25m high mast on starboard (right of the boat). The mean wave-height at that moment was in between 5 – 10m

3.1.2 Identification of rogue waves

To quantify rogue waves events, one must define a criteria to discriminate among a whole population of events (waves), which are considered as extreme. Although a universal definition of rogue waves hasn't been stated yet, they are often identified from a certain height threshold related to the variation of the sea elevation during a certain time duration [162]: To be identified as a rogue wave, the height H_i of a wave has to exceed twice the value of the significant wave height H_s . H_s is usually defined as four times the standard deviations 4σ of the whole population height of waves. From a first approximation [162], H_s is equal to the mean value of the largest one third wave height population $H_{1/3}$. Hence, in order to obtain the value of $H_{1/3}$ from a wave height time evolution, the usual procedure is as follows :

1. Identification of all local maximum
2. Sorting the identified maximum as function of their height

3. Averaging over the one third largest height that gives $H_{1/3}$

$H_{1/3}$ is shown to be usually $\approx 5\%$ lower than 4σ [163, 164].

In the following, we rely on the definition of $H_{1/3}$ and defined the abnormality index AI as in Ref. [162] :

$$(3.1) \quad AI = \frac{H_i}{H_{1/3}},$$

Therefore, a wave of height H_i is a rogue wave if its associated abnormality index $AI > 2$. We show in Fig. 3.2 an illustration of the process to discriminate a rogue wave among a population of waves. The data corresponds to the elevation η of the sea recorded the 1st of January 1995 at the Draupner platform in North Sea [165]. Waves are identified at each local maximum of the trace and marked in Fig. 3.2 by red dots. The local maximum elevations are isolated and sorted. $H_{1/3} = 5.65$ m is then deduced from the average of the third highest values and provides the RW threshold $AI = 2$ which corresponds to $2H_{1/3} = 11.3$ m. Therefore, all waves higher than this threshold is considered as a RW. In this 1150 s length record, the 18.6 m wave located at $t = 0$ s is here identified as a RW.

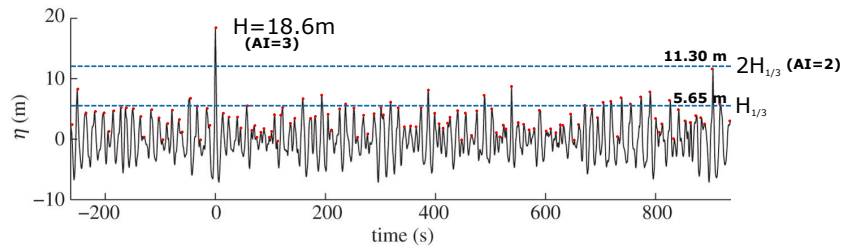


Figure 3.2: Time evolution of the elevation of the sea recorded at the Draupner platform the 1st of January 1995. The figure is taken from Ref. [165]. We added red dots and threshold lines to clarify the notion of $H_{1/3}$, $2H_{1/3}$ and $AI > 2$.

Therefore, the abnormality-index is simple tool to discriminate RWs from a population of waves. Nonetheless, the analysis of oceanographic RW and its underlying physics remain a long-run challenge as their existence might be caused by many factors that scientist still struggle to catch all-together. Indeed, the onset of RW probably come from the interaction of wind, small displacements of the seabed, waves coming far from the observation of the RW and collision of counter-propagating waves

[162]. Hence, a proper study of RW where all parameters are known and drivable requires the use of large scale experiments with huge basins of water [166]. Thus, the growth of interest in the topic and the need of smaller scale experiment has led to many other studies dealing with waves of different physical nature [167] such as in acoustic [168], in electromagnetic microwave [169], in plasmonic [170], in quantum physics [171] and in optic [172–174].

3.1.3 Rogue Waves in optics and motivation

In the previous section, we have seen that RW can acquire incredible power causing huge destructions on ships and oil platform. They are characterized by their rarity, their suddenness and their dreadful height. Understanding their mechanisms is therefore essential and probably vital to prevent more disasters. However, as discussed by Kharif *et al.* [162], too few data on RW are available so far making difficult to confirm the validity of theoretical models. To overcome such a limitation, one can develop new measurement devices [175] or find more convenient analogous systems. Indeed, the idea of rogue waves can be also applied to any kind of data since the definition of the abnormality index does not impose any conditions on their physical nature. In particular, there have been multiple observations of rogue waves, also called extreme events (EEs), in optics.

The onset of high-intensity pulses has been reported in the nonlinear propagation of light in optical fiber by Solli *et al.* [172] in 2007. In Fig. 3.3 (a), we show the experimental setup they use; it consist on sending optical pulses into a micro-structured nonlinear fiber. They observed in Fig. 3.3 (b) the appearance of extremely intense pulses, *i.e.* EEs at the output of the fiber that are in average 20 to 40 times more powerful than the average power of other peaks (almost indistinguishable at low intensity values of the signal). Increasing the input optical power, they were able to increase the number of EEs.

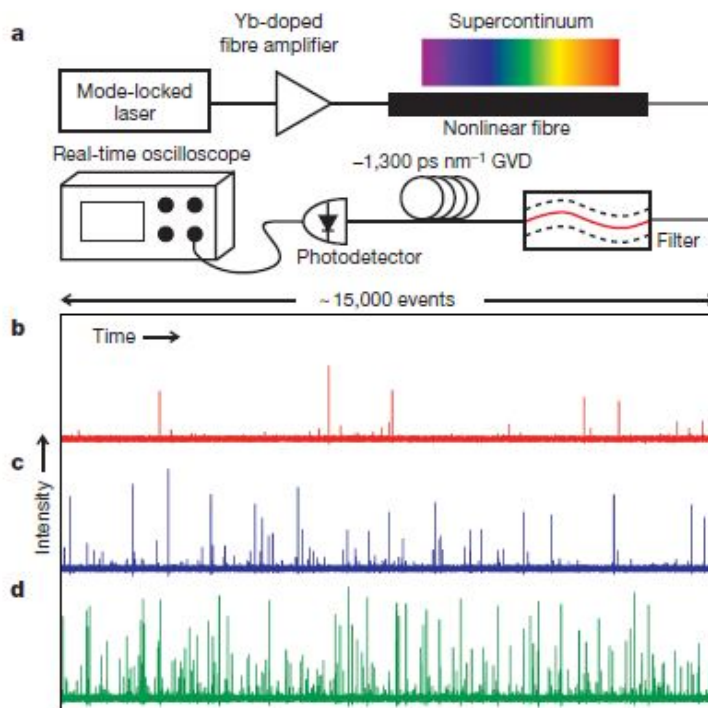


Figure 3.3: Experimental observation of optical rogue waves. (a) Schematic of experimental apparatus. (b–d) Single-shot time traces containing roughly 15,000 pulses each and associated histograms for increasing power level. The rogue events reach intensities of at least 30–40 times the average value. Figure and legend from Ref. [172].

Since then, many studies on optical EEs have been conducted in various experiments dealing with 1D or 2D data streams. In 2D spatially-extended systems, EEs are detected from the output beam profile of the light after being disturbed by a linear medium (SLM modulation [176, 177] or multimode fiber [178]) or non-linear one (non-linear cavity [173], photorefractive crystal [179, 180] and Kerr cells [181]).

In the 1D counterpart, optical EEs have been observed *e.g.* in telecommunication data streams [182]. The appearance of such high intensity peaks inside a fiber creates locally nonlinearities and therefore degrades the transmitted signal. Such phenomenon represents a limitation for high-speed optical communication. The need of higher bandwidth imposes shorter and shorter pulses (*i.e.* broader optical spectrum) and are therefore more sensitive to fiber dispersion effect. A RW might randomly appears when, due to the dispersion, several pulses overlap creating a

more intense pulse.

It has also been demonstrated in recent studies that those EEs can also emerge in the chaotic dynamics of a laser diode subjected to optical injection [183] or feedback [59, 174, 184, 185]. Among EEs created by an external-cavity laser diode, different cases have been considered : short [184] and long cavities [185] formed by a conventional mirror and phase-conjugated feedback (PCF) [59, 174]. In all these works, EEs are found to emerge from the chaotic oscillation of the optical output power. In 2013, Reinoso *et al.* [184] has identified critical bifurcation points from which EEs arise when varying the feedback strength . They demonstrated that the mechanism creating the EEs are related to the trajectory of the system among its external-cavity modes (see Chapter 2). In 2016, Choi *et al.* [185] studied similar system but in long cavity regime. They confirmed the observation of Ref. [184] and showed that in low-frequency fluctuation regime, the number of EEs increases with the feedback ratio which has also been demonstrated in PCF experiments [59, 174]. They found that the time-interval between successive EEs follows a log-Poisson distribution depicting their randomness. Furthermore, PCF experiments [59, 174] also report on two types of EEs : lone EEs and trains of EEs that occur randomly in time or in groups separated by the delay value, respectively. This two types of EEs influence the time-interval statistics which is shown to follow two log-Poisson distributions meaning that the occurrence of EEs are not fully random.

Although not completely elucidated, the mechanism forming EEs in external-cavity lasers is intrinsically related to the induced chaotic dynamics. Their generation rate depends on the feedback strength and the delay might drive their temporal partition. However, in all the previous studies, only the total output power fluctuation has been considered as a source of EEs. In the following, we will focus on the capability of a VCSEL to produce EEs in its polarization and demonstrate its impact on the generation rate of EEs in the total output power of a laser diode.

3.2 Observations of Extreme Events in VCSELS

As discussed in the previous section, experiments in optics are convenient to study RWs as they are more flexible than in hydrodynamic or oceanography. In addition, depending on the system, they might also provide solid analogy with their oceano-

graphic counterparts as discussed in Ref. [172] where the light propagation follows the nonlinear Schrödinger equations (NLSE) model which is also a commonly used model for wave propagation in oceans [186]. The growth of investigation in optical domain has also raised new problematics specific to the field such as signal deterioration caused by EEs in telecommunication systems [182] and motivates further studies on optical experiment than might also not obey to the NLSE model.

The vast majority of studies on EEs has focused on scalar EEs occurring in a single state variable (*e.g.* optical intensity). Nonetheless, certain photonic devices, such as VCSEL, are known to present modal competition between two orthogonal linear polarization (LP) modes. Such a device is also likely to present *vectorial* EEs arising from polarization interactions. An in-depth understanding of *vectorial* EEs might also be of interest for telecommunication as polarization multiplexing is now a widely adopted technique for doubling the data bandwidth in telecommunication [187]. Hence, following the findings of Vergeles *et al.* [182], *vectorial* EEs might also be detrimental for optical communication which motivates our study on such interaction.

For this purpose, we focus in the following on the emergence of vectorial EEs in VCSEL which can stem chaotic dynamics with the addition of optical feedback [39, 74, 188]. This multi-mode emission could potentially lead to the emergence of *vectorial* EEs, where both polarization modes would be activated simultaneously and show abnormal intensity levels leading to very high intensity pulse in the total output power. The vectorial terminology is used in reference to vectorial rogue waves in optical fibers [189]. To characterize an EE, we use the previously described *abnormality index* (AI).

In this Section, we unveil that VCSELs subjected to isotropic optical feedback can generate both scalar and vectorial EEs observed in the power of one or two polarization modes. We characterize the intensity distribution and return times of these two kinds of extreme events and demonstrate they satisfy well-established criteria derived from hydrodynamics. We also observe the effect of the emission in both polarization modes on the generation of EEs. We unveil that this particular modal competition leads to a saturation in term of relative number of EEs (relative to the total number of intensity peaks) when varying the feedback strength. This saturation contrasts with observations made for a laser diode without modal competition [185]. We will later relate this saturation to the VCSEL polarization dynamical

behavior.

We model the temporal evolution of a VCSEL using the well-known Spin-Flip Model (SFM) [103], including spontaneous emission noise and isotropic optical feedback [74, 188] as already used in Chapter 2 :

$$(3.2) \quad \begin{aligned} \dot{E}_{x,y} = & \kappa(1+i\alpha)[(N-1)E_{x,y} + inE_{y,x}] - (\gamma_a + i\gamma_p)E_{x,y} \\ & + F_{x,y} + \eta E_{x,y}(t-\tau)\exp(-i\phi_0), \end{aligned}$$

$$(3.3) \quad \dot{N} = -\gamma_n[N - \mu + N(|E_x|^2 + |E_y|^2) + in(E_y E_x^* - E_x E_y^*)],$$

$$(3.4) \quad \dot{n} = -\gamma_s n - \gamma_n[n(|E_x|^2 + |E_y|^2) + iN(E_y E_x^* - E_x E_y^*)],$$

where $E_{x,y}$ are the complex slow-varying amplitudes of the (X,Y)-LP modes, N is the carrier difference between the conduction and valence bands, and n is the difference between the population inversions of the spin up and down radiation channels. κ is the field decay rate, γ_n is the decay rate of N , γ_s is the spin-flip relaxation rate, α is the linewidth enhancement factor, μ is the normalized injection current, γ_a is the linear dichroism and γ_p is the linear birefringence. τ is the external cavity delay, η is the feedback rate, and $\phi_0 = \omega_0\tau$ is the feedback phase, where ω_0 is the optical frequency of the polarization mode in the absence of birefringence and feedback. Spontaneous emission noise is taken into account through $F_x = [\beta_{sp}(N+n)/2]^{1/2}\xi_1 + [\beta_{sp}(N-n)/2]^{1/2}\xi_2$ and $F_y = iF_x$. β_{sp} is the spontaneous emission rate and $\xi_{1,2}$ are two complex uncorrelated white Gaussian noises with zero mean and unitary variance. In the following, we use fixed parameters values for : $\kappa = 300$ GHz, $\gamma_n = 1$ ns⁻¹, $\gamma_s = 10$ ns⁻¹, $\alpha = 3$, $\mu = 1.07$, $\phi_0 = 6$ rad and $\beta_{sp} = 10^{-4}$ ns⁻¹.

3.2.1 Two types of extreme events in VCSELS

In order to perform our analysis on EEs, we simulate numerically the SFM model on time traces of tens of microseconds, which are long enough to provide sufficient statistics on the intensity peaks. We choose the parameters such that the VCSEL operates in the so-called low-frequency fluctuations (LFF) regime [53, 74, 134]. Indeed, as previously discussed in Chapter 2, this peculiar regime of chaotic dynamic gathers many different mechanisms of external-cavity laser [53]. LFF arises from the interplay between the external-cavity modes and antimodes. It is also strongly driven by the noise that randomly repels the system from the strong attraction of a mode. LFF is characterized by fast and abrupt power dropouts at irregularly spaced

time-intervals. They are followed by a first phase of recovery, where the VCSEL emits intense pulses and a second phase where it oscillates with low amplitude around its quiescent state. Hence, a good candidate window for the temporal location of EEs is the recovery phase of LFF. In addition, LFF in VCSEL is not only characterized by the dynamic of the total output power $I_{tot}(t) = |E_x(t)|^2 + |E_y(t)|^2$ but also by the interplay between the two polarization modes. As demonstrated in the previous Chapter, LFF in the polarization can be symmetric (correlated at the low frequency scale) or asymmetric (uncorrelated at the low frequency scale) hence modifying the statistical property of the produced EEs.

Figure 3.4(a) shows the AC part ($\langle I_{tot} \rangle = 0$) of the total optical intensity $I_{tot}(t) = |E_x(t)|^2 + |E_y(t)|^2$ in the LFF regime. For the parameters of Fig. 3.4, LFF involves dynamics in both X- and Y-LP modes.

In Fig. 3.4(a), the gray dashed line shows the intensity threshold corresponding to $AI = 2$. As expected from the dynamical features of LFF, EEs are predominantly located just after a drop of power in the first recovery phase marked by an arrow. In Fig. 3.4(b.1), we show a zoom on the first stage of recovery of the total intensity $I(t)$. Figs. 3.4(b.2)-(b.3) show the temporal evolution in the same time window of the modal intensities $I_{x,y}(t) = |E_{x,y}(t)|^2$ of the (X,Y) LP modes. For each time series, we define a corresponding threshold as the distribution of peaks varies between the total and modal intensities.

Using Figs. 3.4(b.2)-(b.3), we analyze how the emergence of EEs in each LP mode may result in the appearance of EEs in the total intensity. We unveil two separate scenarios. In the first scenario, we observe EEs in the total intensity that results from EEs present only in a single polarization mode. We mark this class of events by a blue square in Figs. 3.4(b.2)-(b.3) and we call them *scalar events*. In the second scenario, we have EEs present in both polarization modes and occurring at nearly identical times (we have considered that two events are quasi-simultaneous when their time-separation is below 30 ps). We call them *vectorial events* and they are marked by red squares.

To observe the overall polarization behavior of VCSEL when showing either a scalar or a vectorial EE, we show in Figs. 3.4 (c-d) the trajectory of the system in the so-called Poincare sphere [49]. The sphere is embedded in a 3D-space (S_0, S_1, S_2) with S_i the Stokes parameters defined as [49] :

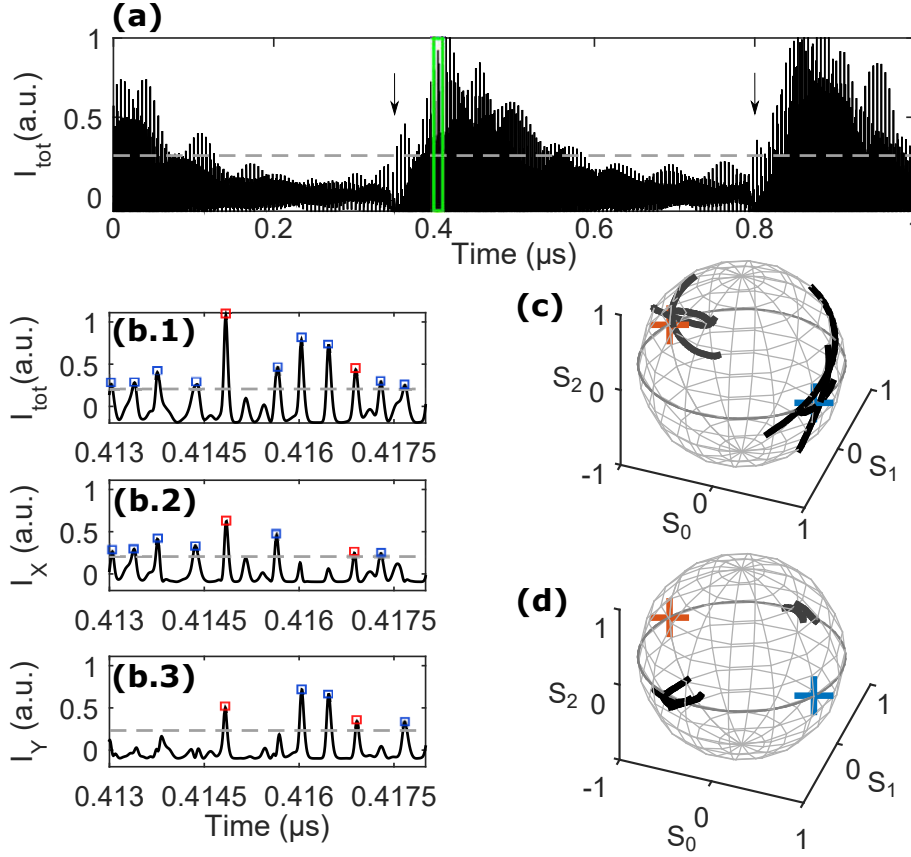


Figure 3.4: (a) Dynamics of the total intensity $I_{tot}(t)$ in LFF regime. (b.1-b.3) Zoom on the polarization resolved intensity $I_{x,y}(t)$ for the window indicated in panel (a). The gray dashed line indicates the detection threshold of an EE $AI = 2$. The blue and red squares mark scalar and vectorial EEs, respectively. Poincare spheres for (c) scalar EEs and (d) vectorial EEs. Parameters are $\gamma_a = 0.01 \text{ rad.ns}^{-1}$, $\gamma_p = 0.1 \text{ rad.ns}^{-1}$ and $\eta = 25 \text{ GHz}$.

$$(3.5) \quad S_0 = \frac{|E_x(t)|^2 - |E_y(t)|^2}{I_{tot}} \quad S_1 = \frac{2\text{Re}[E_x(t)E_y(t)]}{I_{tot}} \quad S_2 = \frac{2\text{Im}[E_x(t)E_y(t)]}{I_{tot}}.$$

When the VCSEL is linearly polarized along the X (resp. Y) direction, the trajectory is located around the blue (resp. orange) cross (+) marked on each sphere. On the equator, the light is diagonally polarized. On the north (resp. south) pole, the light is right (resp. left) circularly polarized. Finally, on any other point of the sphere, the light is elliptically polarized. In Fig.3.4 (c), we show typical trajectories during several scalar EEs arising from X or Y-LP mode for a 80 ps time window centered

on an EE. When the EE arises from X- (resp. Y-) LP mode, the trajectory is mainly located around the blue (resp. orange) (cross) indicating that the light is strongly linearly polarized along the X (resp. Y) direction. However, scalar EE can also show important excursion on the sphere towards elliptically polarized state since when one LP component shows an EE, the other LP component may show a pulse although the pulse intensity is not considered as an EE. Finally, in Fig.3.4 (d), we show the system' trajectory in windows centered on several vectorial EEs. The light is then only diagonally polarized.

3.3 Extreme events statistics

3.3.1 Deviation from a Gaussian distribution

To confirm that the EEs detected in the total intensity $I(t)$ have similar properties to those found in previous studies, we compute the distribution of events as a function of their magnitude. Figure 3.5 shows in log-scale such a distribution for identical parameter values to those of Fig. 3.4 while increasing the feedback rate η . For $\eta = 5$ GHz (blue dots), we observe a Gaussian distribution of the peak intensities. Increasing η leads to a clear deviation from the Gaussian distribution especially at large intensity $I(t)$ with the presence of a fat tail, one of the hallmarks of rogue waves [173, 174, 179, 183, 185, 190–192].

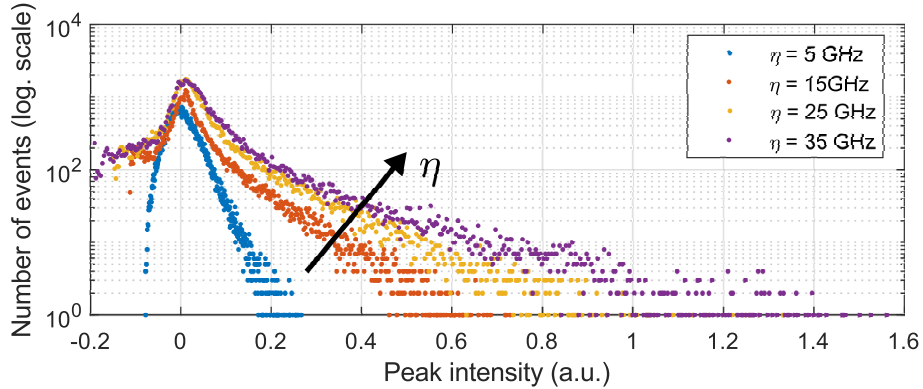


Figure 3.5: Evolution of the distribution of the peak intensity when increasing the feedback rate. Same parameters as in Fig. 3.4.

A statistical indicator that describes the deviation of a distribution tail from its

Gaussian shape is the kurtosis $Kurt(X)$ defined as follows [193]:

$$(3.6) \quad Kurt(X) = \mathbb{E} \left[\left(\frac{X - \mu}{\sigma} \right)^4 \right]$$

where \mathbb{E} is the mathematical expectation, X is a variable, μ its mean value and σ its standard deviation. $Kurt(X) = 3$ for a Gaussian distribution increases if the distribution has fatter tails compared to a Gaussian distribution. The kurtosis of a signal increases with the number of EEs and/or their intensity. Its a commonly used physical quantity in oceanographic study of RW [162, 194, 195].

We show in Fig. 3.6, the evolution of the kurtosis of the peak intensity distribution in I_{tot} as function of η . Without feedback $\eta = 0$ GHz, no dynamic is observed in the total output power of the VCSEL *i.e.* the signal variation is only driven by the noise β_{sp} that has a Gaussian distribution, hence giving $Kurt(I_{peaks}) = 3$. Increasing η , leads to an increase of the kurtosis value meaning that the tail of the peak intensity distribution deviates from its Gaussian shape and shows a higher number of high intensity peaks and/or more intense peaks. We also observe a saturation of the kurtosis for $\eta > 20$ GHz meaning that the tail of the distribution does not go up anymore for high value of feedback. This feature is confirmed in the following.

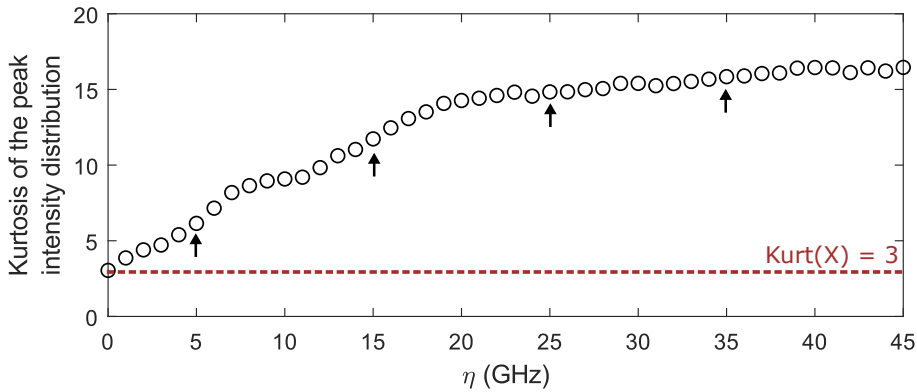


Figure 3.6: Kurtosis of the peak intensity distribution as function of the feedback rate η . The arrows indicates the the kurtosis value corresponding to the distribution reported in Fig. 3.5. The parameters are identical to those used in Fig. 3.4.

3.3.2 Waiting times between successive events

We just saw that increasing the feedback ratio leads to an increase of the number of extreme events. We hereby study their temporal statistics. Indeed, studies of external

cavity feedback [174] and of nonlinear optical cavity using a temporally driven liquid crystal light-valve [190] showed that the distribution of the time separation between two consecutive EEs follows a Log-Poisson law meaning that their occurrence times are statistically independent [196, 197]. It also means that the time separation can be either very small or very large [196].

Figure 3.7(a) displays the statistics of the waiting time $w_n = \log(t_{n+1}/t_n)$ in log-scale between two successive EEs in the total intensity $I(t)$ occurring at time t_n and t_{n+1} . To properly fit the empirical distribution in log-scale, one cannot use a single straight line. Two lines with different slopes are necessary, thus implying that events with low and large time-separations $t_{n+1} - t_n$ follow different Poisson laws with their respective rate parameters. This behavior was already reported in edge-emitting laser (EEL) diode with phase-conjugate feedback (PCF) [59, 174]. This suggests that the existence of two Poisson laws originates from the optical feedback effect.

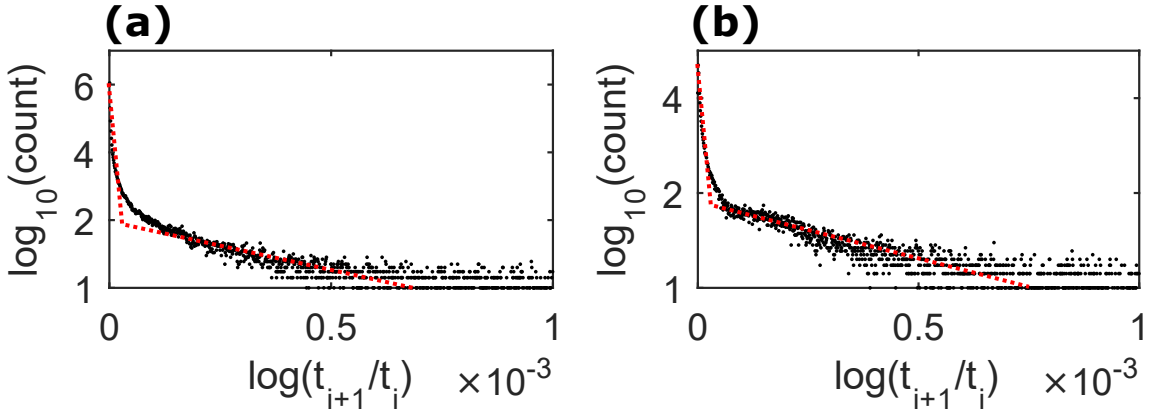


Figure 3.7: Waiting times between consecutive EEs in $I_{tot}(t)$, for either scalar (a) or vectorial (b) EEs. Same parameters as in Fig. 3.4.

Figure 3.7(b) displays a similar distribution of w_n for vectorial EEs only. These two distributions suggest that either vectorial or scalar EEs detected in the VCSEL dynamics have similar temporal properties to those detected in chaotic EELs optical feedback.

The observation of two log-Poisson distributions also suggests that the occurrence times of EEs are not completely random. As explained in Ref. [174], the delay induced by the optical feedback creates two types of EEs : (i) *lone pulses*, which seem to be randomly distributed *i.e.* are not correlated to their precedent or following

counterparts, and (ii) *multiple pulses* which are train of EEs temporally separated by one value of the delay. Those two kinds of EEs are at the origin of the two log-Poisson statistics.

In Fig. 3.8, we show an example of 6 successive EEs recorded from our system that are separated by the delay. This kind of EEs are only marginal among the whole population of EEs. With the parameters of Fig. 3.4, we have estimated, from a population of 100700 EEs, that only 7.15% of them are of this type. This observation is also of interest in oceanographic RW where some questions remain such as to know if RW can appear in groups [198].

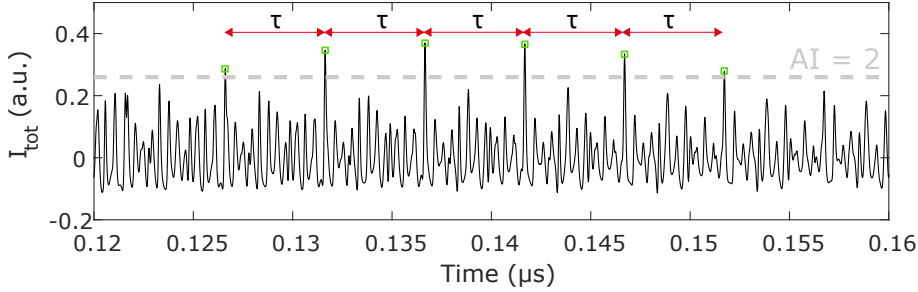


Figure 3.8: Successive EEs temporally separated by the delay in I_{tot} . Green squares indicate the EEs and the gray dashed line is the EEs threshold $AI = 2$. Same parameters as in Fig. 3.4.

3.4 Generation rate of extreme events

As demonstrated in the previous section, EEs generated from an external-cavity VCSEL follows usual statistics of RWs. In this section, we focus on the generation rate of EEs, *i.e.* the ratio between the number of EEs and the overall population of events (peaks). We study its evolution when varying the feedback rate η . Indeed, in time-delayed photonic devices, η is a key parameter controlling the generation rate of EEs [174, 184, 185]. In Fig. 3.9, we plot as a function of η the relative number of EEs. We analyze the influence of η for single- and multi-polarization light emission of the VCSEL. We obtain each case by choosing two different sets of values for (γ_a, γ_p) as these parameters mainly control the relative gain of each LP mode. In a single-polarization emission, the relative number of EEs increases steadily with the increase of η after an initial plateau for $\eta \in [5, 15 \text{ GHz}]$. This evolution is reminiscent

of experimental and theoretical studies conducted on single-mode edge-emitting laser with optical feedback [185]. However, when the VCSEL has a multi-mode emission, we observe a qualitatively different behavior : The relative number of EEs grows rapidly in the range $\eta \in [5, 15 \text{ GHz}]$ and then saturates for $\eta \in [15, 45 \text{ GHz}]$. Beyond these values of feedback strength, LFF regime either disappears and we have a steady-state behavior or the time duration between successive drops become too long [199], hence requiring much longer simulation traces in order to have a significant amount of events to analyze.

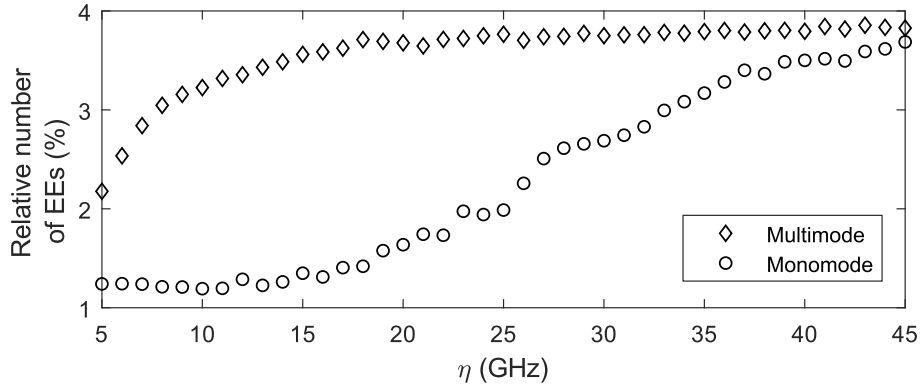


Figure 3.9: Relative number of EEs versus η for a two-polarization mode emission in I_{tot} (black \diamond) with $\gamma_a=0.01 \text{ rad.ns}^{-1}$, $\gamma_p=0.1 \text{ rad.ns}^{-1}$ and for a single-mode emission (\circ) with $\gamma_a=5 \text{ rad.ns}^{-1}$ and $\gamma_p=5 \text{ rad.ns}^{-1}$. Other parameters are as in Fig.3.4.

In Fig. 3.10, we show the generation rates of EEs for each LP-mode in the two-polarization emission case. Their time evolutions are studied separately. Similarly to Fig. 3.9, we observe a saturation of the relative number of EEs in $\eta \in [15, 45 \text{ GHz}]$ for both LP-modes and a similar behavior between them in the whole range of η considered here. This similarity is due to a Type-I LFF regime that was introduced in Chapter 2. Indeed, in Type-I LFF, both LP-modes behave similarly. The case of Type-II LFF is discussed in Sec. 3.4.3.

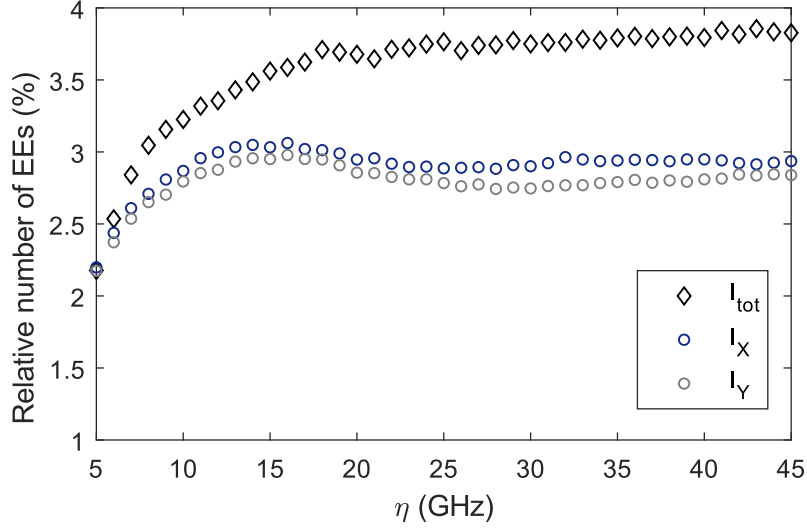


Figure 3.10: Relative number of EEs versus η for a two-polarization mode emission in the X-LP (blue), in the Y-LP (gray) and in the total (black) intensity

3.4.1 Vectorial Extreme events

As shown in the previous section, VCSELs can randomly exhibit vectorial extreme events. We focus here on the effect of η on the generation of vectorial EEs. We monitor this property in Fig. 3.11(a) by plotting the ratio of vectorial EEs with respect to the entire number of EEs detected in $I(t)$ as a function of η . We notice that they represent between 2 and 13% of the total number of EEs for the range $\eta \in [5, 45 \text{ GHz}]$: occurrences of vectorial EEs are rare among rare events but their evolution is similar to that of the entire population of EEs shown in Fig. 3.9 with a saturation for $\eta \in [15, 45 \text{ GHz}]$. In addition to the generation rate, in Fig. 3.11(b), we also analyze the average magnitude of vectorial EEs by comparison to their scalar counterparts. We observe that they are consistently more intense for the entire range of feedback strength.

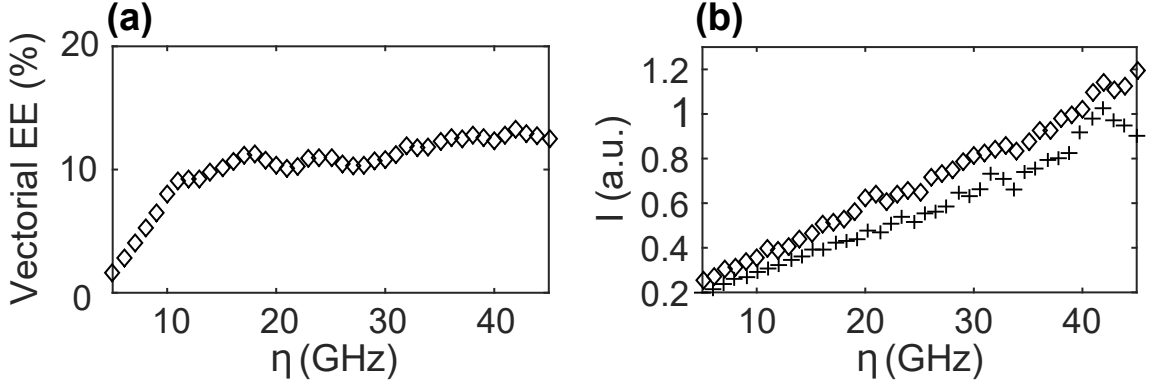


Figure 3.11: (a) Proportion of vectorial EEs among all EEs in the two-polarization case and (b) average intensity of vectorial EE (\diamond) and scalar EE (+) as function of η .

3.4.2 Noise effect on the generation rate of EEs

The above simulations report on the low-frequency fluctuations dynamics that has been shown to be driven by the amount of noise as discussed in the previous Chapter. Therefore, we expect to observe an influence of the noise parameter β_{sp} on the statistics of EEs.

In Fig 3.12, we show the generation rate of EEs in the total intensity as function of η for different value of β_{sp} . We observed a similar saturation effect on the generation rate with a similar level of saturation ($\sim 4\%$). However, the value of η that marks the beginning of saturation becomes higher when β_{sp} decreases. In fact, the stronger the noise is, the more frequent the occurrence of dropouts becomes and therefore the higher the number of high-intensity peaks is. As a result, increasing the noise parameter β_{sp} leads to a faster growth of the relative number of EEs in Fig.3.12. Finally, for high values of η , the statistics asymptotically merge as the dynamic is there less driven by the noise and more by the feedback effect.

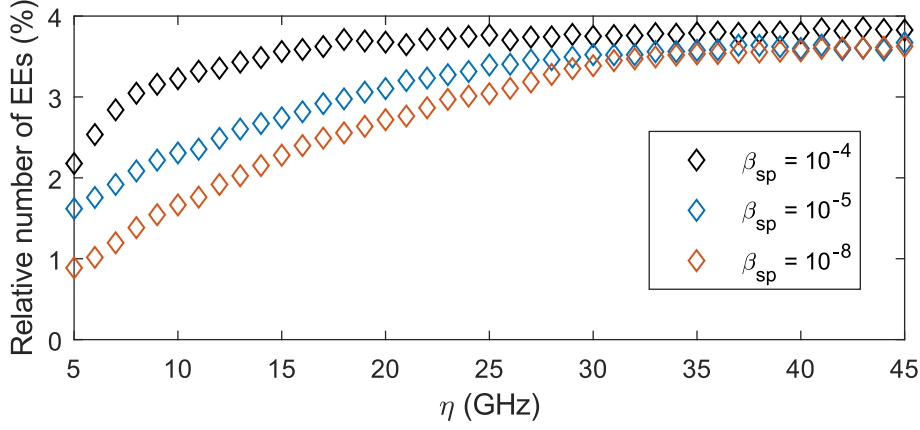


Figure 3.12: Relative number of EEs versus η for a two-polarization mode emission in I_{tot} for $\beta_{sp} = 10^{-8}$ (orange), $\beta_{sp} = 10^{-5}$ (blue) and $\beta_{sp} = 10^{-4}$ (black)

3.4.3 Differences between Type-I and Type-II LFF

As shown in Chapter 2, two types of LFF can be obtained in VCSELs :

- Type-I LFF : both LP-modes are correlated at the low-frequency scale *i.e.* they both show drops of power at the same time
- Type-II LFF : one LP-mode is dominant while the other one is more depressed and they are anti-correlated at the low-frequency scale *i.e.* the dominant mode shows drops of power while the other one bursts.

We are here interested in the difference in term of EEs generation rates between these two types of LFF. In Fig. 3.13n we show the EEs generation rates of Type-I and Type-II LFF as function of the feedback rate η . The Type-II is obtained by choosing $\gamma_a = -0.1 \text{ ns}^{-1}$ and $\gamma_p = 5 \text{ ns}^{-1}$. As observed previously, the relative number of EEs in Type-I LFF has a constant growth in $\eta \in [5, 15 \text{ GHz}]$ followed by a saturation. Similarly, the Type-II LFF demonstrates the same behavior but has a lower saturation value at 3.2%.

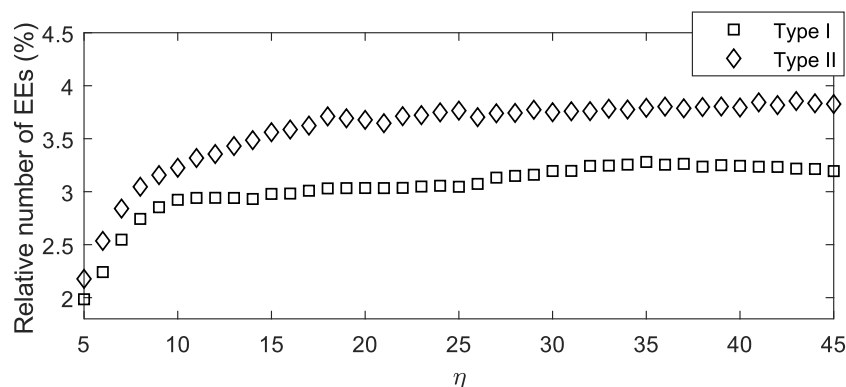


Figure 3.13: Relative number of EEs versus η for a two-polarization mode emission in Type-I LFF (\diamond) and Type-II LFF (\square)

We observe differences in the modal origin of the EEs between the Type-I and Type-II LFF. In Fig. 3.14, we show the proportion of EEs in the total intensity that are provided by the X-LP mode or the Y-LP mode when varying the feedback rate η . As a consequence of the modal behavior symmetry of Type-I LFF, in Fig. 3.14 (a), half of the EEs in the total intensity are provided by one mode and the other half by the other mode. For Type-II LFF however, EEs are mainly provided by the dominant mode (the X-LP mode here). This is all the most important when the value of η is low with a partition of 87% from X and 13% from Y when $\eta = 5$ GHz. This difference is due to fact that the Y-LP mode is depressed and therefore does not provides sufficiently strong pulses to be considered as extreme. Nevertheless, the partition equilibrates around 55% from X and 45% from Y when increasing η . It suggests that for high value of feedback, the normally depressed mode has a higher gain and demonstrates pulses almost as high as the dominant mode.

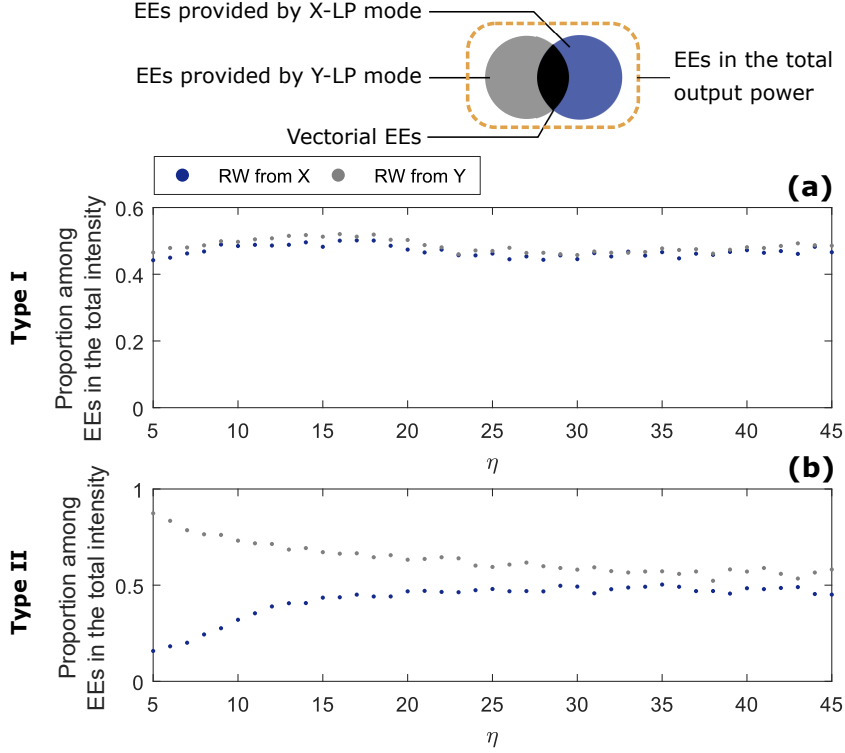


Figure 3.14: Proportion of EEs in the total intensity I_{tot} provided by peaks in the X-LP mode (blue) and in the Y-LP mode (gray) and vectorial extreme events (black) in (a) Type-I LFF and (b) Type-II LFF

3.5 Modal competition effect on the EEs generation rate

So far the key observations in the properties of EEs generated by VCSEL in their two-polarization mode emission are (i) the presence of vectorial EEs and (ii) the observation of a rapid saturation in relative number of EEs (both scalar and vectorial) as the feedback strength increases. In our case, the modal competition leads therefore to an additional control parameter in the generation of EEs in VCSELs. We will provide below an explanation to this saturation mechanism from the statistical properties of the total intensity time series.

For a two-polarization mode emission of the VCSEL, the saturation in relative number of EEs as a function of η implies that for different operating points, the proportion of intense versus small peaks remains unchanged. However, as we bring

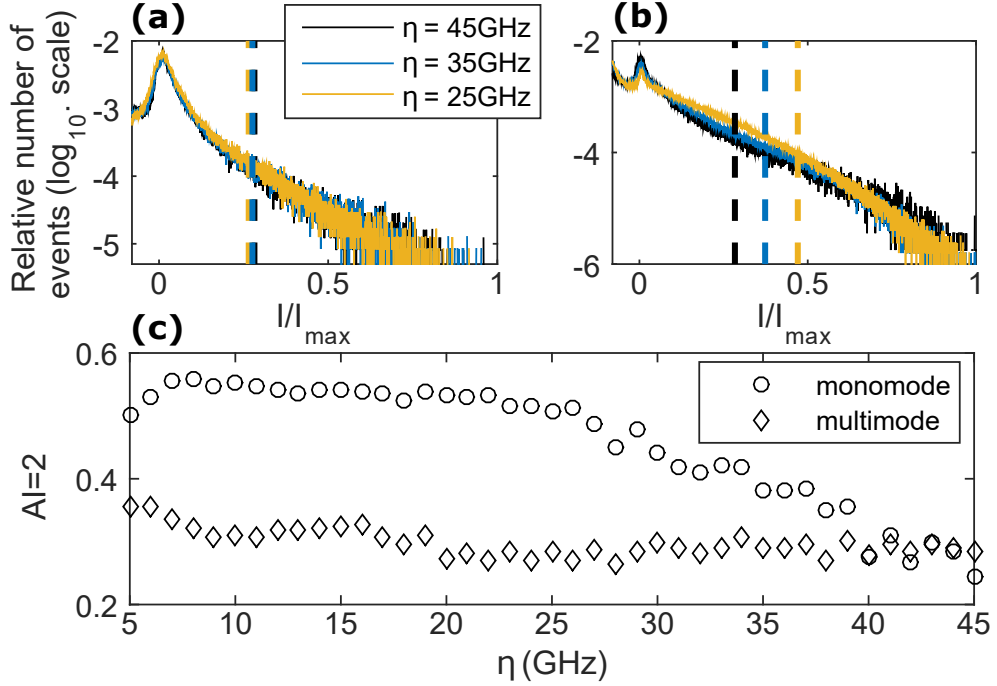


Figure 3.15: Normalized peak intensity distributions for different values of η for (a) two-polarization mode emission and (b) single polarization mode emission. The vertical dashed lines indicate the normalized intensity ($AI = 2$) threshold for the detection of EEs for a given η (yellow $\eta = 25$ GHz, blue $\eta = 35$ GHz and black $\eta = 45$ GHz). (c) Evolution of the normalized intensity threshold for the detection of EEs versus η for two-polarization mode (\diamond) and single-polarization mode (\circ) emission.

more energy with an increase in feedback strength, the average intensity of LFF dynamics increases. In Fig. 3.15(a), we propose to analyze the distribution of the normalized intensity peaks $I(t)/I_{max}$ for different values of feedback strength. We plot the distributions in normalized intensity for three increasing values of $\eta = 25$, 35 and 45 GHz. We observe that they overlap strongly and tends toward a stationary distribution as η increases. As a result, the normalized intensity threshold for the detection of an EE (indicated by a vertical dashed line in Fig. 3.15(a)) does not vary significantly and leads to similar relative number of EEs when $\eta > 15$ GHz.

By comparison, for a single-polarization mode emission of the VCSEL, we observe in Fig. 3.15(b) a significant modification of the shape of the distributions. The main difference between single- and two-polarization mode emission is located below the mean value i.e. under $I/I_{max} = 0$ (as we used the AC part of the signal). Specifically,

in single-polarization mode emission, the number of peaks below the mean value is way more significant than in the multi-mode case. Indeed, modal competition leads to total intensity fluctuations mainly around its mean-value due to anti-phase dynamics between the LP-modes [188], while single-polarization emission leads to more intensity values around the spontaneous emission level [188, 200]. Thus, in single-polarization mode case, having a high number of peaks below the mean-value leads to a shift of the normalized intensity threshold of EEs to lower value of intensity and, hence, to an increase in relative number of EEs as the proportion of events with high normalized intensity is relatively unchanged.

Finally, we display in Fig. 3.15(c) the evolution of the normalized intensity threshold for the detection of EEs (*i.e.* $AI=2$) as a function of feedback strength η in the case of multi- and single-polarization mode emission. The trend for the two-polarization emission case is confirmed with stable value of the threshold around 0.28 for $\eta > 15$ GHz. For the single polarization mode case, we observe a monotonic decrease for $\eta > 15$ GHz, which explains the increase in relative number of EEs considering also the change in the distributions shown in Fig. 3.15(b).

Thus, we have shown that modal competition in VCSEL influences the generation rate of EEs. It maintains the total intensity around its mean value and compensates the expansion of the total intensity distribution, which explains the saturation in term of relative number of EEs and kurtosis shown in Fig. 3.6. To the best of our knowledge, a similar saturation was observed only once for an EEL with PCF [59]. The saturation mechanism is EEL from PCF originates from the specific high-frequency self-pulsations of PCF laser systems and such explanation does not hold for our study.

3.6 Conclusion and perspective

In conclusion, we have demonstrated that extremes events occurring in a VCSEL subjected to optical feedback show similar feature than those encounter in other field such as oceanography : a stretching of the Gaussian intensity distribution when increasing the control parameter and the observation of randomly located EEs which translates into a log-Poisson distribution of the waiting time between consecutive EEs. However, the presence of a delay induced by the external cavity has also an

effect of the temporal distribution of EEs. Indeed, we observed the appearance of train of EEs that are regularly spaced by the delay. Therefore, as also pointed out by the L-Shaped log-Poisson distribution, the delay creates some correlation between each events.

By contrast with previous reports on EEs from laser diodes, we have studied the occurrence of EEs from another viewpoint that is the impact of the polarization competition effect on the generation of EEs. The interplay between the polarization modes in VCSEL induced by optical feedback has two important consequences on the generation of optical extreme events : first, this can create a new type of *vectorial extreme events*, where both X- and Y-LP modes emit quasi-simultaneously abnormal high intensity pulses. Theses extreme events are on average the most intense events in the VCSEL dynamics. Second, the relative number of rogue waves (vectorial or not) undergoes a clear saturation effect as the optical feedback strength increases. As a result, modal competition is another control parameter that can drive the generation rate of EEs.

Finally, we have seen that taking independently, the polarization modes also show a saturation in their generation rate of EEs. In that case, the saturation can't be explained from a result of mode competition and might requires an in-depth comparison with the monomode case and to take into account all state variables being the electrical fields, the carrier density and the spin population difference. Indeed, in a multimode case, both polarization modes share partly the available carriers which might also explains the saturation. However, this is only speculative and needs a deeper study.

Now, an experimental confirmation has also to be done. The main challenge for an experimental investigation of such EEs is to measure short duration pulses (typically ≤ 100 ps) over a long time window (typically ≥ 100 μ s) using VCSELs which generally have low mean power (less than 2 mW). Therefore it would require high-sensitivity, high-speed and low-noise photodiode.

SUSTAINED OSCILLATIONS ACCOMPANYING POLARIZATION SWITCHING IN A LASER DIODE

In this chapter, we report experimentally and theoretically on a bifurcation scenario leading to the emergence of oscillations at a frequency higher than the relaxation-oscillation frequency in a laser diode showing polarization switching. More specifically, we use a time-delayed rotating optical feedback to induce slow periodic polarization switching accompanied by fast oscillation on their plateaus. This phenomenon originates from a clear bifurcation point that marks the transition between sustained and damped oscillations on the plateaus. Analytical study reveals also that the frequency of this new oscillatory dynamics is independent of the time delay.

This chapter is based on the following publication :

Uy, C. H., Weicker, L., Rontani, D., and Sciamanna, M. (2018). Sustained oscillations accompanying polarization switching in laser dynamics. *Optics Express*, 26(13), 16917-16924.

The plan of our Chapter is as follows. In Sec. 4.1, we briefly summarize the motivation and the state-of-the-art in optical square-wave generation. We describe the experimental setup in Sec. 4.2 and report the observation of fast oscillations in the output power of the depressed polarization of our laser diode. We also analyze the behavior of those oscillations when varying the experimentally accessible parameters.

In Sec. 4.3, we detail the numerical model and confirm our experimental findings. The bifurcation diagram provides the overall scenario giving birth to the fast oscillations dynamic. A bifurcation point is identified and an in-depth Hopf bifurcation analysis is developed in Sec. 4.4. Finally, an approximate formula to the frequency of these oscillations is given. Section 4.5 summarizes the reported results and provides some perspectives.

4.1 Square-wave modulation in optics

Envisioning the future optical computer in order to overtake the limitation of electronic devices, optical square-wave generation is of interest. Indeed, high amplitude square-wave (SW) modulation is a commonly encountered waveform in electronic and digital processing taking advantage of the fast transition between two level intensities of the SW signal. It is widely used to synchronize each elemental part of a machine by giving it a time reference called "*clock*". For a common double data rate (DDR) CPU, a data transfer is initialized at each transition, rise and fall.

In 1980, K.Ikeda *et. al.* [201] proposed a simple delay system in a passive ring cavity containing a non-linear dielectric medium that is irradiated by a constant power laser light [see Fig. 4.1]. They demonstrated that this system is capable of showing chaotic behavior at the output of the ring cavity but also periodic square-wave modulation at a periodicity of twice the round-trip time. In Ref. [202], harmonics of the SW modulation frequency has also been predicted.

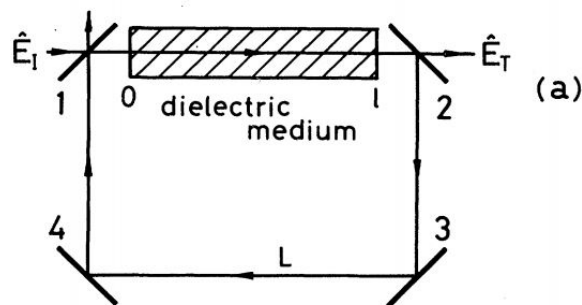


Figure 4.1: Experimental configuration of a ring cavity containing a dielectric medium used in Ref. [201]. E_I is the optical input field and E_T is the measured output field.

Generating SW with semiconductor laser was also a obvious continuation as they are now widely used in telecommunication network for their speed performances, small sizes and low production price among other factors as discussed in the introduction.

In 1982, Mitsuhashi *et al.* showed that an external cavity laser diode configuration allows the control of the polarization of the output light. A polarizer is inserted in the external cavity and, depending on its orientation, the laser can emit either in its main axis direction of polarization (TE), in the orthogonal direction (TM), which is normally depressed, or in both direction with an oscillatory dynamics [77].

In 1990, Loh *et al.* have demonstrated an all-optical setup generating SW from a laser diode based on an external cavity [78]. They replaced the polarizer of Ref. [77] by a quarter-wave plate [see Fig. 4.2] and showed SW modulation frequency up to 620 MHz (half of their external-cavity frequency).

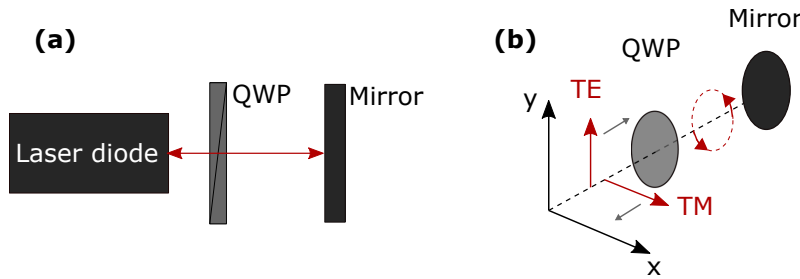


Figure 4.2: (a) Schematic experimental configuration used in Ref. [78] for the observation of SW modulation. (b) Polarization state along the optical path.

Using a VCSEL, Jiang *et al.* [203] reached a SW modulation frequency of 5 GHz [203] in 1993 followed by the group of Choquette [204] who was able to reach 9 GHz in 1998. These reported experiments are milestones in the field of optical SW generation as they do not require expensive fast electronics to reach such high frequency. In 2011, it has also been proposed to use this setup for generation of random bits at high speed up to 4Gb/s [205] where a very long delay of 90.9ns induces chaotic oscillation of the laser output power.

Another application was proposed in 2001 by Rogister *et al.* [206]. They envisioned to use a polarization-rotated feedback laser diode for secure communication keying based on random switching of polarization modes. In their study, a polarizer is added after the quarter-wave plate to filter the naturally depressed polarization of the laser.

Doing so, the experiment ensures a complete suppression of multi-round-trip effect inside the external cavity. In 2003, Heil *et al.* [207] showed that, unlike isotropic feedback, this configuration does not decrease the threshold current of the laser and neither its slope in the stimulated emission operation. He also concludes that instability arises for relatively strong feedback compared to the case of isotropic feedback but did not report any SW modulations. In 2006, Gavrielides *et al.* [60] demonstrated in this configuration that square-wave oscillations can arise from a Hopf bifurcation phenomenon with a periodicity of twice the delay and proposed a normalized coupled rate equations to model the system. He identified the critical parameter that allows or not the appearance of SW modulation : the losses of the depressed mode (named β in Ref. [60]) has to be small enough; or in other words, the gain of the depressed polarization should be close to the gain of the naturally lasing one. He also noted that the SW is also accompanied by highly damped oscillation at the relaxation oscillation frequency when the signal transitions between low and high intensity state of the SW. In his work, the quarter-wave plate is replaced by a Faraday rotator that also turns the polarization of the incoming light by 90° after one round-trip [see Fig. 4.3]. In 2010, with the same experimental setup, Gavrielides *et al.* [208] show that the SW solution also coexists with more complex waveform made of pulses at an unknown frequency and small plateaus but still with a periodicity of twice the delay.

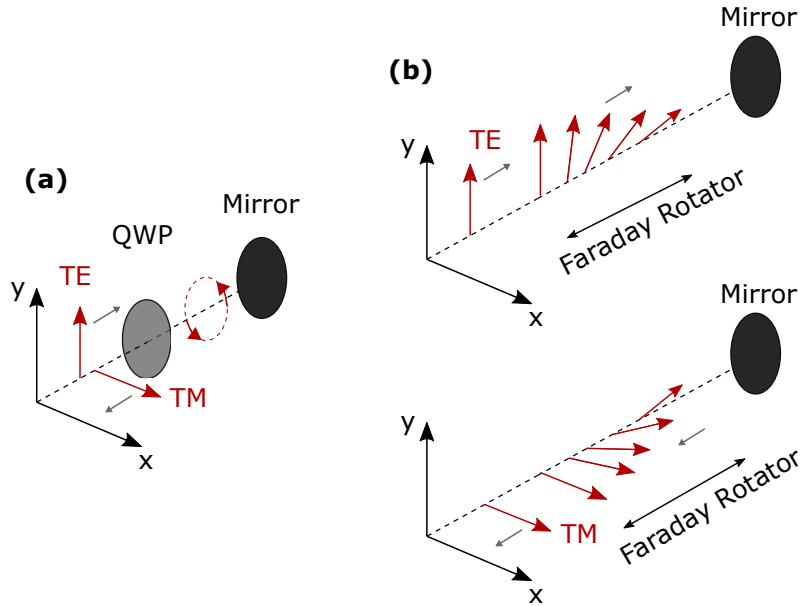


Figure 4.3: Comparison between quarter-wave plate (QWP) and Faraday rotator effect on an incoming linearly polarized light (a) A linearly polarized light (TE) is converted into a circular polarized light after the QWP. The mirror reflect the light into the QWP that transforms again the light into a linear polarized light along an orthogonal direction (TM) (b) A linearly polarized light (TE) is slowly turned by 45° during its propagation into the Faraday rotator. The mirror reflect the light back into the rotator that turns again slowly the polarization by 45° . At the output, the light has been turned by 90° (TM) compared to the input polarization (TE).

In 2012, Sukow *et al.* [209] investigated similar experiment with a VCSEL. As for EEL, they observed the emergence of SW modulation with a periodicity of twice the delay and analyzed the regularity of the modulation when varying experimentally the current and numerically the birefringence. In addition, they observe numerically high amplitude oscillations on the upper state of the SW generated in the depressed polarization mode of the laser. The frequency of those oscillation was not studied in-depth but the authors noticed that for their parameters, this frequency was close to twice the value of the relaxation-oscillation frequency of their VCSEL. They were unable to observed such phenomenon experimentally due to their small bandwidth of detection.

In the following, we focus on the same setup as the one of Sukow *et al.* [209] and Gavrielides *et al.* [60, 208] *i.e.* with the filtering of one polarization that has been called in [60] *Polarization rotated optical feedback* (PROF) and also referred as

cross-polarization reinjection in [210, 211]. We experimentally generate square-wave (SW) polarization switching with a PROF configuration and show experimentally for the first time not damped but sustained oscillation on the upper and lower level of the SWs hence, confirming earlier numerical simulations of Sukow *et al.* [209]. In addition, we provide an in-depth study of such oscillations and prove that its frequency is not only twice the relaxation-oscillation frequency as mentioned by Sukow *et al.* but can also go well beyond. We also show that although the delay is required to induce such dynamic, its frequency doesn't scale with the delay.

4.2 Bifurcation to high-frequency oscillation in square-wave regime

As discussed in the previous section, laser diodes subjected to a PROF may exhibit SW modulation as a periodicity close to twice the external-cavity delay. Interestingly, it has been predicted with a VCSEL that fast oscillations can appear on the upper state of the SW at a frequency higher than the SW modulation and the relaxation-oscillation frequency [209]. In this section, we experimentally revisit the generation of SW in an EEL. We first describe our experimental setup and show the whole panel of dynamics that can be obtained with a PROF setup. We report on the observation of a bifurcation leading to the predicted fast-oscillations on plateaus which may also exist on both the upper and lower states of the SW. Finally, we study the behavior of this oscillation frequency when varying the feedback ratio, the current and the delay. Strikingly, that oscillation frequency can be very high, much larger than both f_{RO} and the external-cavity frequency, and remains constant when varying the time-delay.

4.2.1 Description of the experimental setup

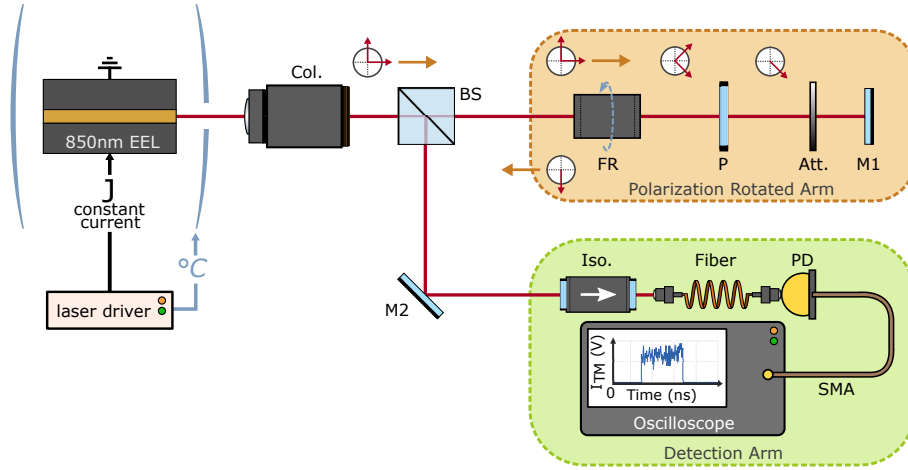


Figure 4.4: Experimental Setup. EEL : Edge-Emitting Laser, C : Collimator, BS : non-polarizing beamsplitter, P : polarizer, M : mirror, PD : photodiode. The polarization state of the laser signal is schematically represented on the light path.

The experimental PROF configuration is identical to the one used in Ref. [60, 61, 208, 211]. We sketch it in Fig. 4.4. It includes an edge-emitting laser (EEL) JDS SDL-5400 lasing at 852 nm. We operate at 60 mA (four times the threshold current) and at 25°C. The beam is collimated and sent into two arms with a 30/70 non-polarizing beam-splitter allowing for a maximum feedback ratio of 49%. The feedback ratio is deduced from the calibration of the attenuation wheel and from the knowledge of the transmittance of the beam-splitter. A Faraday rotator is inserted in the external cavity and turns both TE and TM polarizations by 45°. The TM mode is then filtered with a polarizer while the mirror reflects the TE mode to the rotator, which turns again the polarization by 45°. As a result, the TE mode is injected in the laser with the same direction as the TM mode. Such a configuration also ensures the total suppression of multi-round-trip effects. In the detection arm, we measure the dynamics of the TM mode with a 12 GHz bandwidth Newfocus 1554-B photodiode and a 36 GHz bandwidth Lecroy oscilloscope. The delay is set to $\tau = 8$ ns (*i.e.* an external-cavity length of $L = 1.2$ m).

4.2.2 An overview on the observed dynamics

In this section, we provide a first insight on the overall behavior of the laser when changing the feedback ratio by adjusting the attenuation wheel. Figure 4.5 shows experimental time series of the normally depressed TM mode and the corresponding RF spectra for different values of the feedback ratio. For low level of feedback, the laser emits a constant intensity in the TE mode. Increasing the feedback strength leads to undamped relaxation oscillations of the output power at a frequency of about 3.8 GHz [Fig. 4.5(a)]. For higher feedback, the system exhibits first quasi-periodicity [Fig. 4.5(b)] and chaos [Fig. 4.5(c)] and then switches to SW solutions with 2τ -periodicity accompanied by sustained fast oscillations on the plateaus [Fig. 4.5(d)]. The corresponding RF spectrum, shown in panel (d.1), highlights a frequency comb with a spacing of $f_{EC}/2 = 62.5$ MHz, i.e. harmonics of the SW oscillation frequency, and a frequency peak at 6.4 GHz related to the frequency of oscillations on the plateaus. An intense peak at $f_{EC}/2$ MHz is also observed but not shown here (for clarity purpose). We note that the frequency on plateau is neither close to f_{RO} nor to f_{EC} or any of their harmonics. Finally, for high values of feedback, oscillations on the plateaus become damped leaving only a 2τ -periodic SW [Fig. 4.5(e)]. The corresponding RF spectrum does not show any significant peak anymore but only the aforementioned frequency comb [Fig. 4.5(e.1)]. This last case in Fig. 4.5(e) matches earlier observations where the polarization switchings are accompanied by damped oscillations at f_{RO} [60, 61]. The SW dynamics also coexists with more complex waveforms made of several pulses and small plateaus [Fig. 4.5(f)] that have been already reported in Ref. [208] with a similar setup.

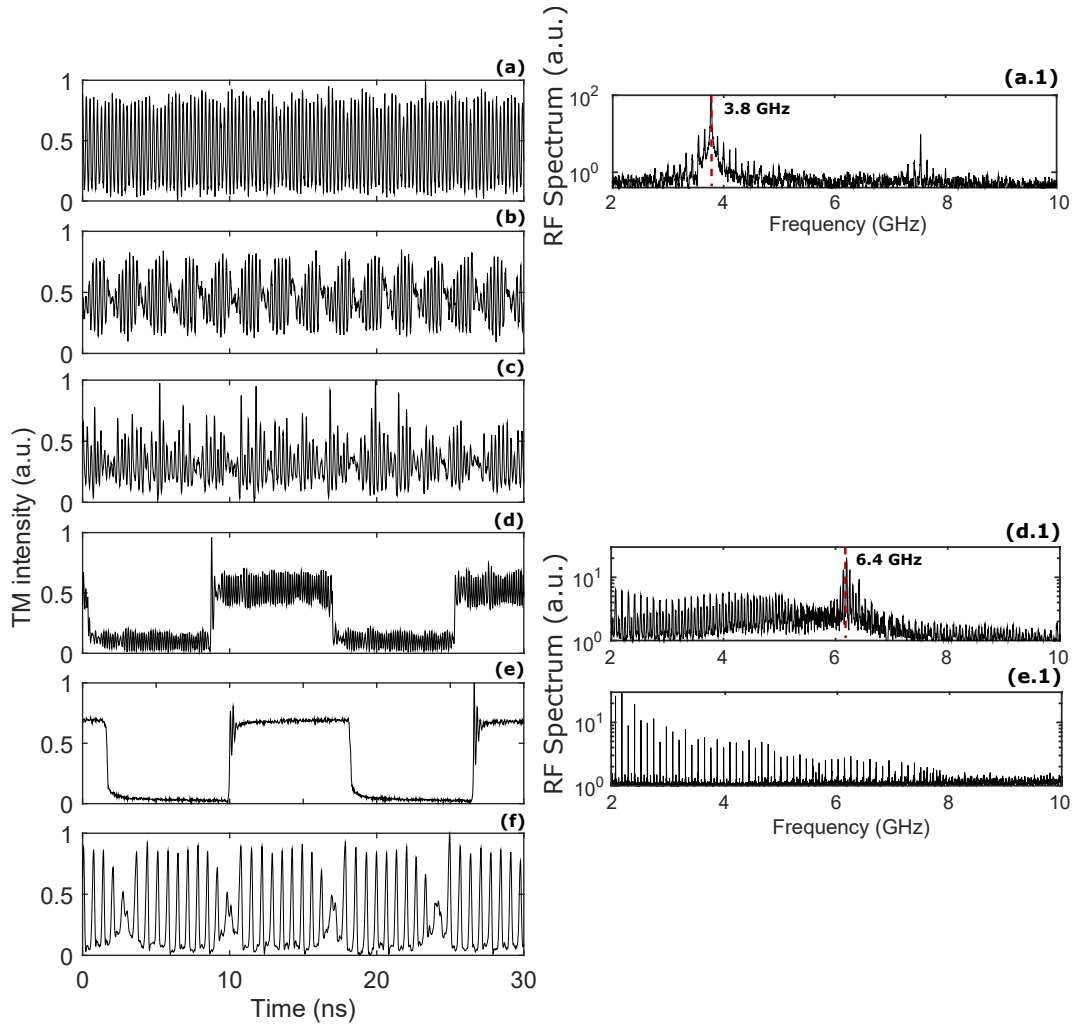


FIGURE 4.5. Experimental time traces of the TM modes for (a) 20%, (b)23%, (c)26%, (d)30%, (e-f)37% feedback ratio. The delay is fixed at $8ns$. (a.1) (d.1) and (e.1) are the RF spectrum corresponding to the time traces in (a) (d) and (e) respectively.

4.2.3 Effects of the feedback ratio and the injection current

We have seen in the previous section that a bifurcation leads to the appearance or disappearance of the fast-oscillations on plateau when varying the feedback ratio. Here, we focus on the influence of tunable experimental parameters on this peculiar frequency. In Fig. 4.6(a), we analyze first the effect of the feedback ratio. Compared to Fig. 4.5, we have increased the current to 95 mA so that the fast-oscillations

remain undamped in a larger span of feedback ratio. Although the uncertainty on the feedback ratio is fairly large ($> 0.4\%$), we observe a clear increase of the fast oscillations frequency when increasing the feedback ratio. In Fig. 4.6(b), we then analyze the variations of the frequency on plateaus when varying the injection current. We compare it to the first observed limit-cycle frequency at low value of feedback ratio which we found in Fig. 4.5(a) as being close to the free-running f_{RO} . As we increase the current, the frequency of the first limit-cycle also increases similarly to the increase of f_{RO} with current. Besides, an increase of the oscillation frequency on plateaus is also observed when the current increases. This frequency remains always at a higher value than the first limit-cycle frequency and hence than f_{RO} .

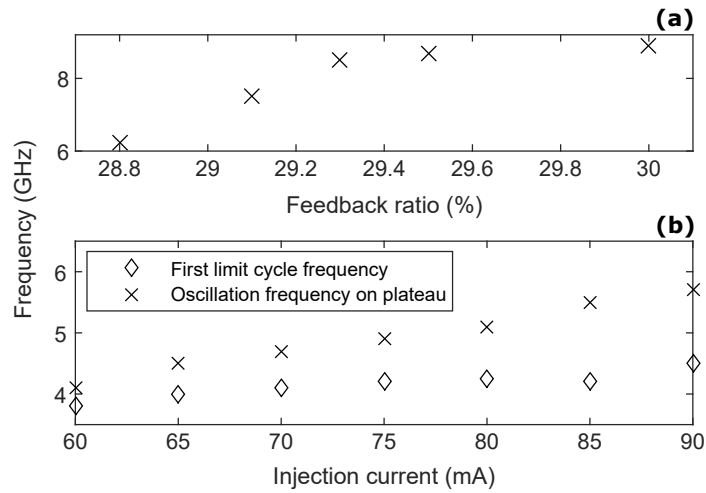


Figure 4.6: Oscillation frequency on plateaus for (a) a current of 95 mA and increasing feedback ratio, (b) a feedback ratio of 28% and increasing current. In (b), comparison is shown with the frequency of the first limit-cycle dynamics for a feedback ratio of 20%.

4.2.4 Influence of the delay

Although changing the feedback ratio leads to a variation of the frequency observed on the plateaus of the SW, changing the time delay does not. In Fig. 4.7, we compare the RF spectra when increasing the feedback ratio for two different values of delay (8.9ns and 12.8 ns). We focus here on the RF spectra observed in SW regime with oscillations on plateaus. A vertical offset is added between each measurement for clarity purpose.

4.2. BIFURCATION TO HIGH-FREQUENCY OSCILLATION IN SQUARE-WAVE REGIME

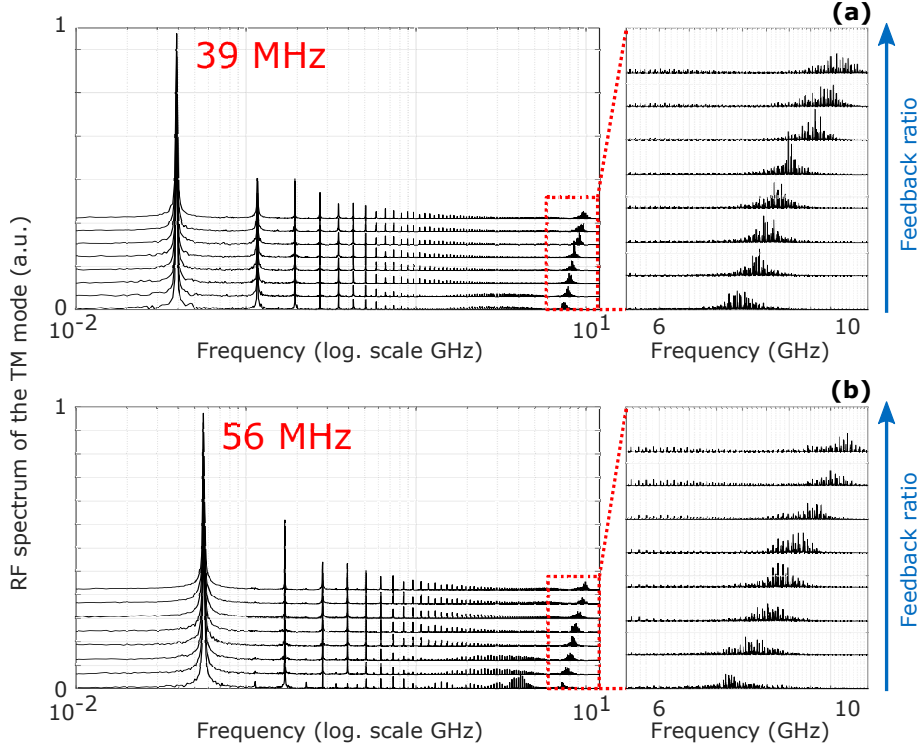


Figure 4.7: (Left) RF spectra and (right) zoom of the red window for increasing value of feedback ratio. (a) $\tau = 12.8$ ns and (b) $\tau = 8.9$ ns. Other parameters are identical to those used in Fig. 4.8

In Fig. 4.7 (a), for a delay of 12.8 ns, a dominant peak is observed at a frequency $f = 39$ MHz which is at half of the external cavity frequency $f_{EC} = 78$ MHz. This peak is associated to the 2τ -periodic SW modulation. Several harmonics of this frequency is also observed and form a frequency comb with an inter-spacing of $f_{EC}/2$. Such comb is caused by the square waveform, in contrast with a pure sin modulation that would lead to an unique sharp peak. In the GHz domain [see the zoom in Fig. 4.7 (a) right panel], a resonance is observed and is located in the region of frequency corresponding the frequency of modulation observed on the plateaus of the SW. As reported previously, this frequency increases when increasing the feedback ratio and evolves here in between 7 GHz and 10GHz.

Similar behavior is observed when changing the delay down to 8.9 ns in Fig. 4.7 (b). The dominant peak corresponding to the SW modulation frequency is shifted to $f = f_{EC}/2 = 56$ MHz compared to the previous case. The resulting frequency comb has here an inter-spacing of 56 MHz. Finally, in the GHz domain [see the zoom in

Fig. 4.7 (b) right panel], the oscillation frequency on plateaus also increases with the feedback ratio but, more importantly, it evolves in the same range of frequency as for the previous value of delay suggesting no dependence on f_{EC} .

Hence, modifying the delay does not influence the mean location of the frequency peak associated to the fast-oscillation on plateau but changes the structure of the frequency comb by modifying its inter-spacing of $f_{EC}/2$. We will show in the following that this result is also confirmed numerically and analytically.

4.3 Numerical Investigation

Our experimental findings have demonstrated the existence of a bifurcation between Fig. 4.5(d) and Fig. 4.5(e) where the high-frequency oscillations appear from the steady-state dynamic on the plateaus. In order to understand the origin of such oscillations, we provide here a numerical study of our system. First, we present the commonly used rate equations that describe the PROF setup. Next, we confirm our experiment observations from a bifurcation analysis and provide a detailed investigation on the effects of the laser parameters, the feedback parameters and the noise on the observed main frequencies (the first-limit cycle frequency, the SW modulation frequency and the frequency of the fast-oscillations on plateau).

4.3.1 Rate equations for EEL subjected to a PROF

The PROF setup can be modeled mathematically with a modified Lang-Kobayashi model [60, 150, 207] that takes into account both the TE and TM modes of the laser. As the TM mode is always filtered after the Faraday rotator and the delayed TE mode aligned with the original TM mode direction, the output TE field does not experience any feedback term. The model hence reads as follows

$$(4.1) \quad \dot{E}_1 = (1 + i\alpha)NE_1 + n_1,$$

$$(4.2) \quad \dot{E}_2 = (1 + i\alpha)k(N - \beta)E_2 + \eta\sqrt{k}E_1(s - \theta) + n_2,$$

$$(4.3) \quad T\dot{N} = P - N - (1 + 2N)(|E_1|^2 + |E_2|^2),$$

where $E_{1,2}$ are the slowly-varying amplitude of TE and TM fields, respectively. s is the time normalized with respect of the photon lifetime τ_p . N is the carrier density, $\theta = \tau/\tau_p$ the normalized delay, α the linewidth enhancement factor, η the feedback

rate, T the ratio of carriers to cavity lifetime, k the gain coefficient ratio between the TM and TE modes, $\beta = \frac{1}{2k}(1 - k)$ the TM mode additional losses, and P the pump parameter above threshold. The terms $n_j = \sqrt{R}\xi_j$ ($j = 1, 2$) in Eq. 5.7 and Eq. 5.9 model spontaneous emission noise for each mode of the laser; it corresponds to two uncorrelated white Gaussian noises with variance R and zero mean.

For the sake of comparison with existing literature on PROF [60, 61, 79, 212], we considered very similar parameters :

Parameter	Value
P	0.6
k	0.96
β	0.02
T	250
α	2
R	10^{-12}

Table 4.1: List of the fixed parameters used in the simulations

We have fixed $\theta = 7000$, so that it matches the experimental delay value $\tau = 8$ ns when considering a realistic value for laser diodes $\tau_p = 1.14$ ps. For our parameters, the dimensionless free-running f_{RO} is given by $f_{RO} = 1/(2\pi) \times \sqrt{2P/T} = 0.011$ (or 9.64 GHz for $\tau_p = 1.14$ ps). The need of comparison with previous bifurcation analyses gives here a different value of f_{RO} compared to the experiment. However, one can still adjust the parameters to obtain the experimental value of f_{RO} and the observed bifurcation scenario remains qualitatively very similar to the one reported here. In addition, although we have experimentally estimated the feedback ratio, the coupling efficiency of the feedback light into the laser cavity is unknown and therefore the feedback rate η remains a free bifurcation parameter.

4.3.2 Bifurcation scenario leading to sustained oscillations

Using the aforementioned parameters, we show in Fig. 4.8(a) the bifurcation diagram with η as the bifurcation parameter. For low values of $\eta < 0.013$, we observe a stable steady-state. At $\eta = \eta_{H_1} = 0.013$ we observe a first bifurcation H_1 leading to an oscillatory dynamics at a frequency $f_{RO} = 0.011$ [see Fig. 4.8(b) and its zoom in panel (f)]. For $0.0336 < \eta < 0.0345$, the laser switches into quasi-periodicity and further

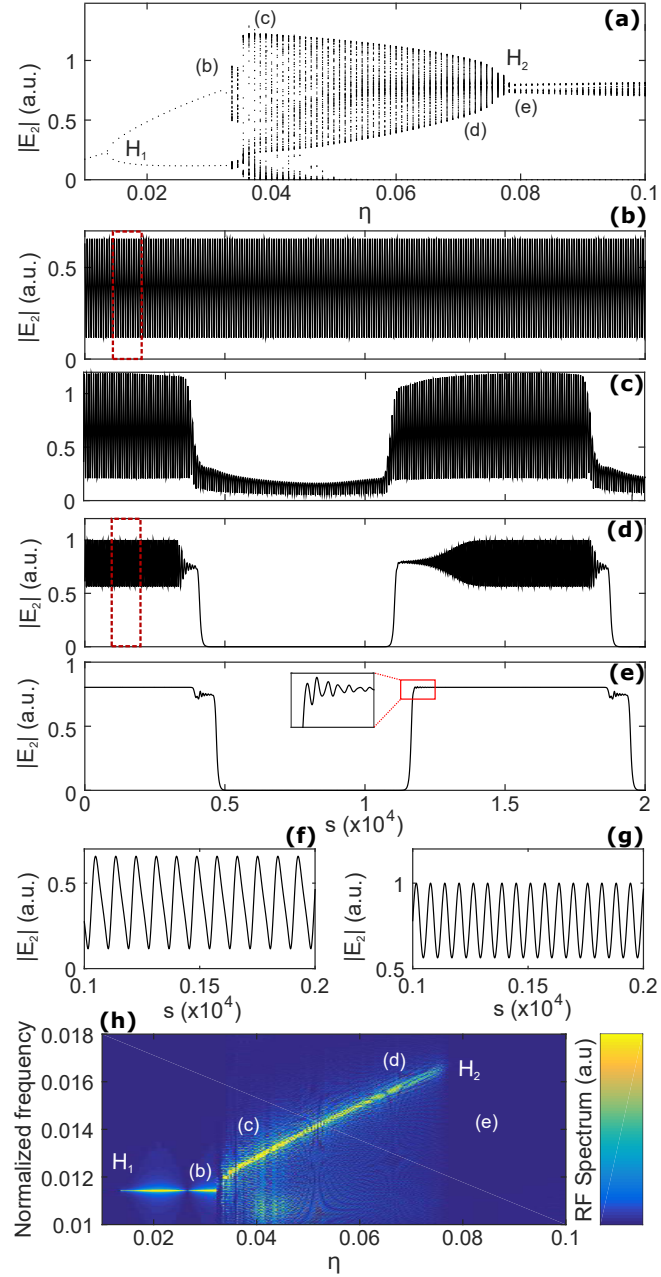


Figure 4.8: (a) Numerical bifurcation diagram as function of η . Time traces of $|E_2|$ at (b) $\eta = 0.03$, (c) $\eta = 0.04$, (d) $\eta = 0.072$, (e) $\eta = 0.08$. (f) and (g) are zooms of (b) and (d) in the dashed box respectively. (h) is the RF spectrogram corresponding to (a).

into a narrow region of chaos. Increasing the value of η leads to 2θ -periodic SW with fast oscillations on both plateaus [see Fig. 4.8(c)]. The oscillations on the lower state completely disappear from $\eta > 0.05$, but the upper state oscillations are still present [see Fig. 4.8(d) and its zoom in 4.8(g)]. We observe that the oscillations of the plateau have a higher frequency than f_{RO} . In this range of feedback, those fast oscillations create a large number of amplitude extrema corresponding to the scattered area of points in the bifurcation diagram. Finally, for $\eta > \eta_{H_2} = 0.078$, only SW without oscillations on the plateaus are observed [Fig. 4.8(d)]. Furthermore, we notice a bifurcation point H_2 at $\eta = 0.078$ that marks the transition between SW with and without fast oscillations on the plateaus. The frequency observed at H_2 is $f_{H_2} = 0.0165$, *i.e.* higher than f_{RO} . This particular point is investigated further.

The spectrogram in Fig. 4.8(h) summarizes the evolution of the RF spectra when varying η . At the first limit-cycle, for low value of η , the frequency of oscillations remains close to f_{RO} and there is no influence of η in this regime. By contrast, in the SW regime with oscillations on the plateaus, as η increases, the frequency of the oscillations on plateaus also increases; this is in agreement with the experimental observation of Fig. 4.6(a). As the dynamic does not only consist of a pure oscillatory regime but is also composed of a slower SW modulation, the spectrogram shows a dominant peak for the fast oscillations superimposed on a broad comb of frequency components at multiples of $f_{EC}/2 = 7.1 \times 10^{-5}$ (or 62.2 MHz for $\tau_p = 1.14$ ps). Finally, for $\eta > 0.078$, the dynamic consists of pure SW modulation without oscillation. Therefore, the spectrogram does not show any relevant frequency signature in the high frequency range considered here.

As shown in Fig. 4.8(a), the fast oscillations on the plateaus have a modulation amplitude that greatly varies as one approaches the bifurcation point H_2 . At $\eta = 0.04$, the modulation amplitude of the TM field intensity $|E_2|^2$ reaches a maximum of 95% of the background SW modulation.

4.3.3 Influence to the delay

In order to confirm that the frequency of oscillation on plateaus does not scale with the delay we compare here the numerical observations when varying its value. In Fig. 4.9, when varying the time delay from 2500 to 25000, we do not observe qualitative change in the sequence of bifurcation leading to the oscillations on plateaus [see Fig.

4.9 (left)] and neither in the corresponding spectrograms [see Fig. 4.9 (right)]. Only small discrepancies are observed at the H_2 bifurcation point when comparing the case where $\theta = 2500$ in Fig. 4.9 (a) with the cases where $\theta = 7000$ and $\theta = 25000$ in Fig. 4.9 (b-c) :

- Quasi-identical value of η_{H_2} : it is slightly shifted down to $\eta = 0.074$ for $\theta = 2500$, but asymptotically tends to $\eta = 0.078$ for higher values of delay θ .
- Quasi-identical value of f_{H_2} : f_{H_2} is at a lower value 0.0162, but tends to 0.0166 when increasing the delay θ .

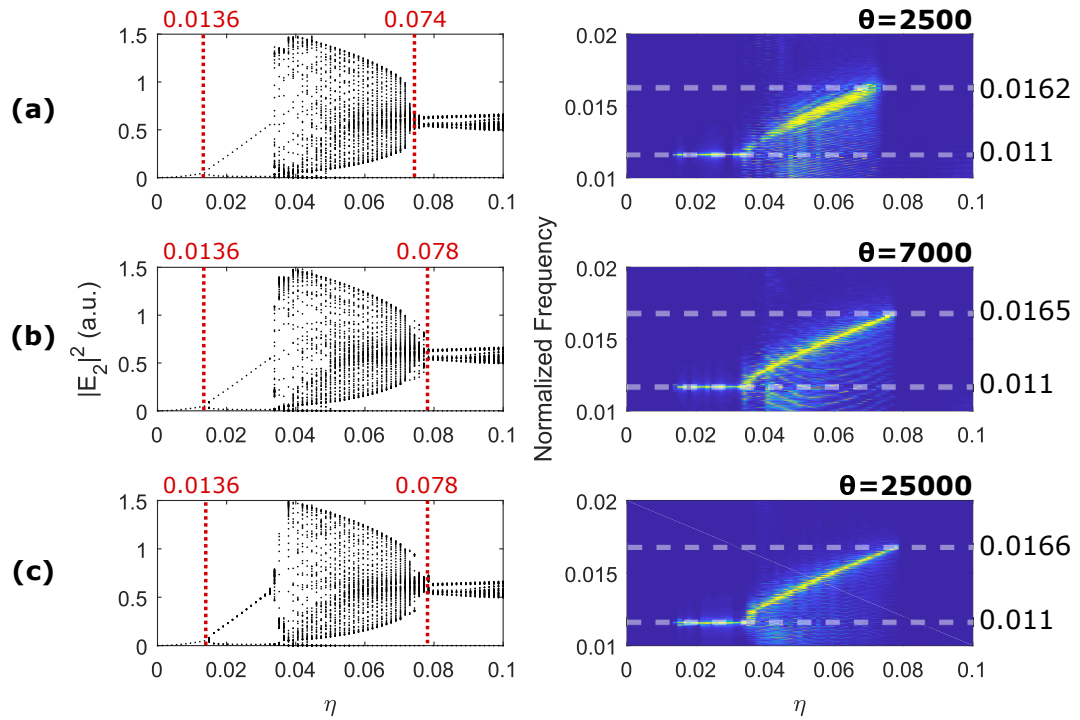


Figure 4.9: (Left) Bifurcation Diagrams and (Right) spectrograms for (a) $\theta = 2500$, (b) $\theta = 7000$ and (c) $\theta = 25000$. Other parameters are identical to those used in Fig. 4.8

The main effect of the delay is observed at lower frequency when looking at the SW modulation frequency scale. In Fig. 4.10, we compare for different values of delay, the spectrograms at low values of frequency that encompass the SW modulation frequency at $f_{EC}/2$ and several harmonics. Varying the delay changes the SW modulation frequency $f_{SW} = f_{EC}/2$ hence modifying the inter-spacing of the resulting

frequency comb. In addition, one can also note the amplitude of the frequency comb peaks (color coded) that alternatively switches between high value and low value. High intensity peaks are located at odd harmonics of f_{SW} while weak intensity peaks are located at even harmonics of f_{SW} . This feature is reminiscent of specific SW solutions of the system as discussed in Ref. [79]. Indeed, an Hopf bifurcation analysis of the model shows that only odd harmonics of f_{SW} are solutions of the system. In other words, only $2\theta/(2n + 1)$ -periodic SW can be obtained. This is further discussed in Chapter 5.

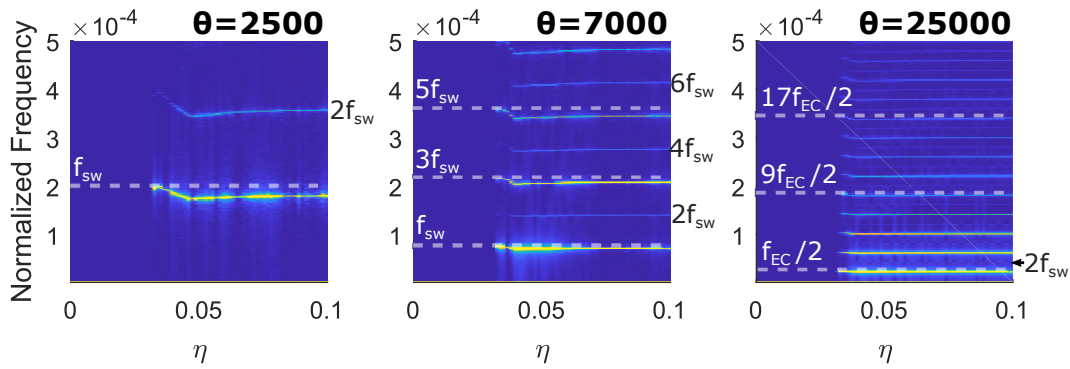


Figure 4.10: Spectrograms for (left) $\theta = 2500$, (middle) $\theta = 7000$ and (right) $\theta = 25000$. The frequency range encompasses the SW modulation frequency at $f_{EC}/2$ and several harmonics. Other parameters are identical to those used in Fig. 4.8

In summary, apart from the SW modulation frequency and the resulting frequency comb, the influence of the delay on the fast oscillations on plateau remains negligible. This is again in agreement with the experiment where the delay had no influence on the frequency of the fast oscillations on plateaus.

4.3.4 Effect of the laser parameters

In the following, we compare the bifurcation scenario and the associated RF frequency when varying the parameters of the laser being P , T , α and k .

4.3.4.1 Pump parameter P

In Fig. 4.11, we compare the bifurcation scenario and the corresponding spectrogram for different value of the pump parameter P . Increasing the value of P does not

modify the overall scenario reported previously. However, both the values of η_{H_1} and η_{H_2} are shifted to higher values. η_{H_1} goes from 0.014 for $P = 0.4$ to 0.018 for $P = 1.5$ and η_{H_2} goes from 0.064 for $P = 0.4$ to 0.123 for $P = 1.5$. In addition, the region where SW with oscillations on plateau exist become larger as P increases. Hence, in order to study such dynamic experimentally, it would be recommended to have the injection current as high as possible. On the other hand, varying P also impact the modulation frequencies of interest :

- Increasing P also increases f_{RO} as :

$$(4.4) \quad f_{RO} = \frac{1}{2\pi} \sqrt{\frac{2P}{T}},$$

- The frequency f_{H_2} at H_2 also increases with P

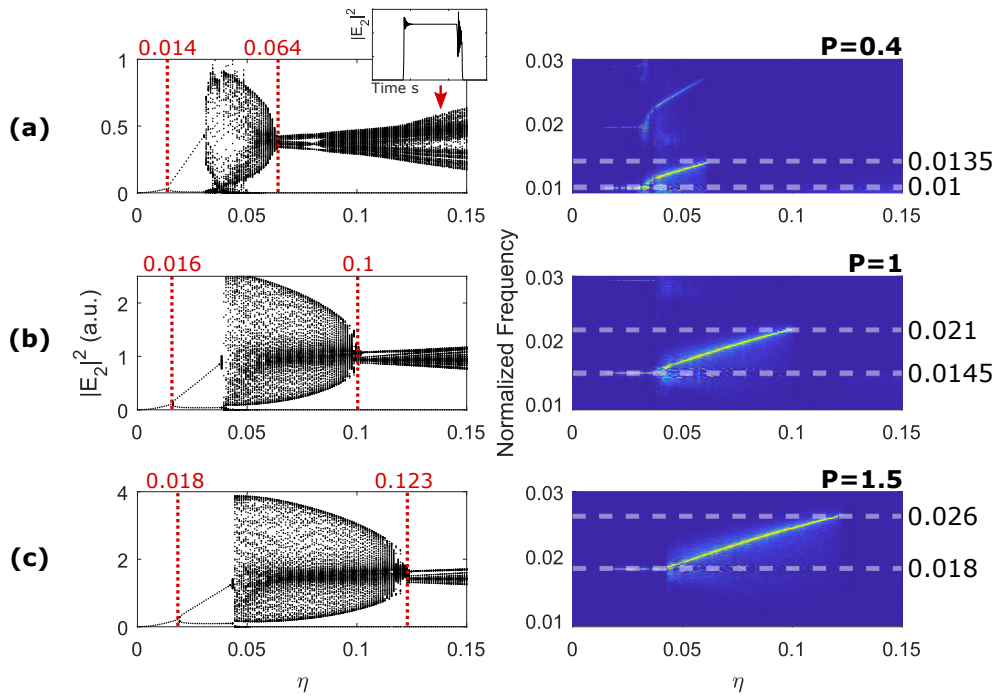


Figure 4.11: (Left) Bifurcation diagrams and (Right) spectrograms for (a) $P = 0.4$, (b) $P = 1$ and (c) $P = 1.5$. Other parameters are identical to those used in Fig. 4.8

Looking closely to the bifurcation diagram in Fig. 4.11 (a), the trail associated to the SW regime without oscillations on plateau goes wider as η increases. This is due

to damped oscillations at each transition (rise and fall) of the SW. The associated time-trace for $\eta = 0.135$ is displayed in the inset above the bifurcation diagram. The damped oscillations have a higher amplitude at the "fall" transition and is reminiscent of an intermediate plateau that exists without noise. This is further discussed in Sec. 4.3.5

In summary, observation of the fast oscillations accompanying SW modulation is favored when the injection current is high as it enlarges the range of feedback rate where those fast oscillations on plateau exist. In addition, increasing the current also leads to an increase of its oscillation frequency.

4.3.4.2 Carrier to photon lifetime ratio T

In Fig. 4.12, we compare the bifurcation scenario and the corresponding spectrogram for different values of the carrier to photon lifetime ratio T . Increasing the value of T shrinks to region where SW with oscillation on plateau is observed. For $T > 1000$ (and our set of parameters), such dynamic is no longer observed without adjusting the pump parameter P or the gain ratio k . Varying T also impacts the modulation frequencies of interest :

- Increasing T diminishes f_{RO} as predicted by Eq. 4.4
- Increasing T also diminishes the frequency f_{H_2} at H_2

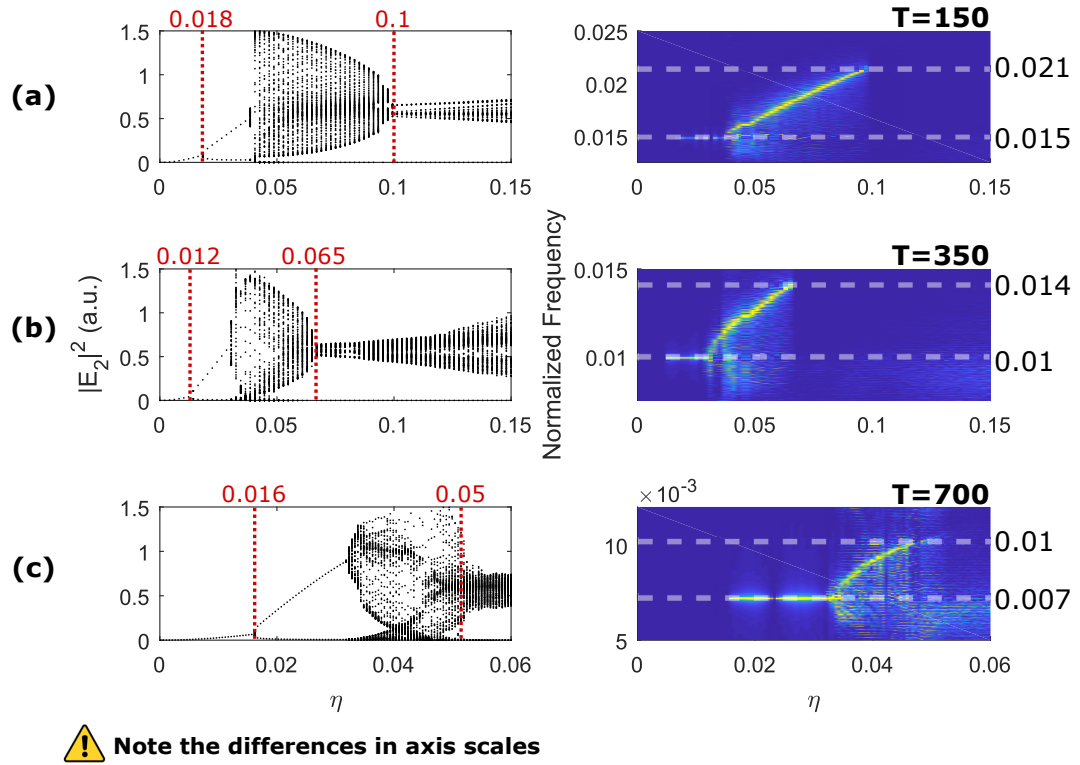


Figure 4.12: (Left) Bifurcation Diagrams and (Right) spectrograms for (a) $T = 150$, (b) $T = 350$ and (c) $T = 700$. Other parameters are identical to those used in Fig. 4.8

In addition, η_{H_2} diminishes when T increases. It goes from $\eta_{H_2} = 0.1$ for $T = 150$ down to $\eta_{H_2} = 0.05$ for $T = 700$. On the other hand, η_{H_1} first diminishes for $150 < T < 350$ and then increases for higher value of T . Its evolution as function of T is shown in Fig. 4.13. For $T \rightarrow 0$, η_{H_1} tends to infinite, reaches a minimum value $\eta_{H_1} = 0.01235$ for $T = 400$ and then slowly increases with T .

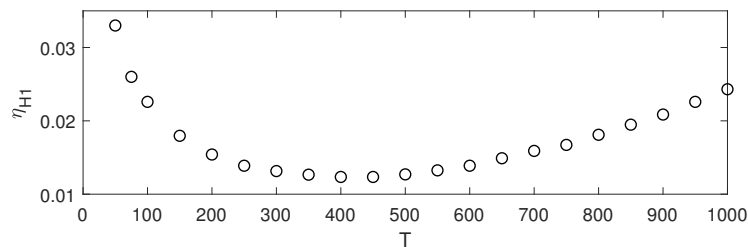


Figure 4.13: Variation of η_{H_1} as function of T

4.3.4.3 Linewidth enhancement factor α

In Fig. 4.14, we compare the bifurcation scenario and the corresponding spectrogram for different values of the linewidth enhancement factor α . Increasing the parameter α moves the H_2 bifurcation to higher value of η . It also enlarges the region where SW with oscillation on plateau is observed. In addition, looking at the bifurcation diagram for $\alpha = 5$, a secondary bifurcation appears at $\eta = 0.1$ suggesting even more complex behavior.

- Increasing α does not influence f_{RO}
- Increasing α also increases the frequency f_{H_2} at H_2

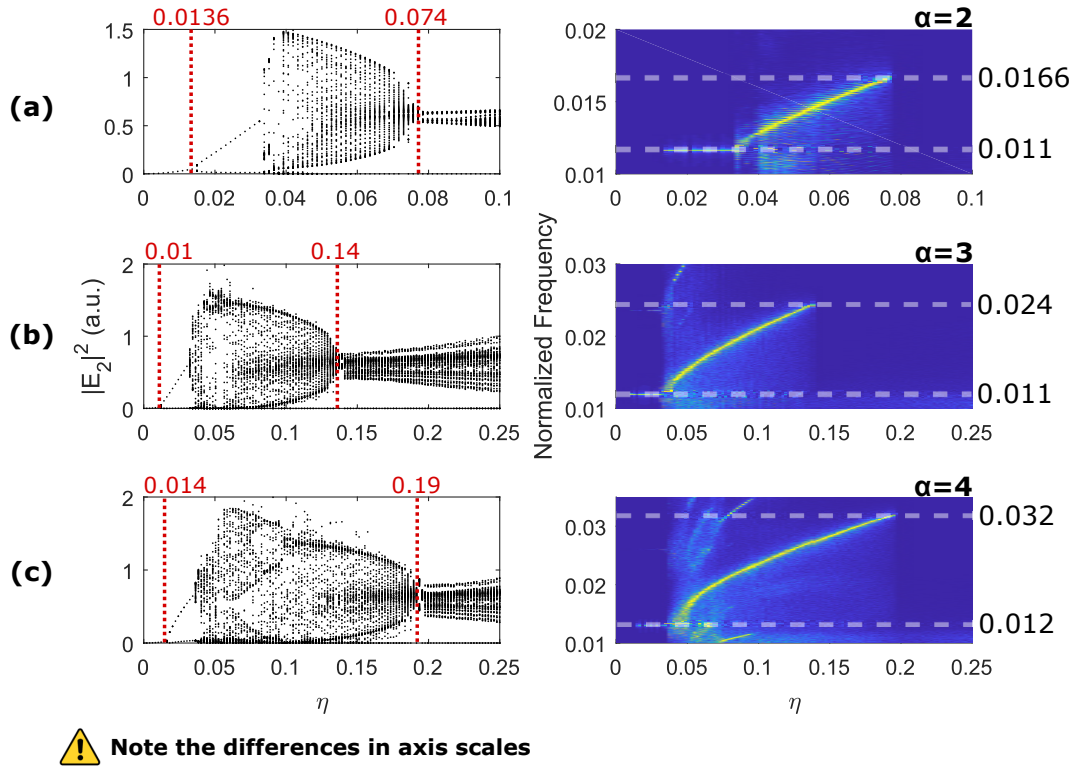


Figure 4.14: (Left) Bifurcation Diagrams and (Right) spectrograms for (a) $\alpha = 2$, (b) $\alpha = 3$ and (c) $\alpha = 4$. Other parameters are identical to those used in Fig. 4.8

Hence, although having the smallest α -factor has been of interest in many works in order to reach high modulation speed with low phase-noise [213], the frequency of

oscillations on plateaus is favored by high-value of α . It has also been demonstrated that the highest is α , the easiest is the SW modulation [60].

4.3.4.4 Gain coefficient ratio k and TM additional losses β

The TE-TM gain ratio k (or $\beta = \frac{1}{2k}(1-k)$) is a crucial parameter to observe oscillations on plateaus : decreasing its value drastically shrinks the feedback range where those oscillations are observable. Same limitation has been reported for the observation of simple SW modulation with an identical setup [60]. Nevertheless, similar dynamics are observable for low values of k but adjustment of the other parameters is then needed. In Fig. 4.15, we have chosen $P = 6$ and $\alpha = 3$ in order to observe the oscillations on plateaus when varying k within $[0.8 - 0.9]$.

- η_{H_1} shifts to lower value when increasing k
- η_{H_2} slightly shifts to higher value when increasing k
- The region where oscillations on plateaus are observed becomes larger when increasing k
- The frequency at H_1 shows a dependency on k : increasing k diminish its value toward 0.036 which is the theoretical value of f_{RO} for this set of parameters
- The frequency at H_2 increases with k

Hence, for a laser diode that has a strongly depressed TM mode (i.e. low value of gain ratio k), observations of the sustained oscillations accompanying SW modulation could be achieved only by increasing the injection current value or by modifying the linewidth enhancement factor (e.g. for high temperature). Another option would be to modify the TE-TM gain ratio itself using a mechanical stress on the laser [214] that is known to both change the polarization gain and optical detuning (that we have considered here equal to 0).

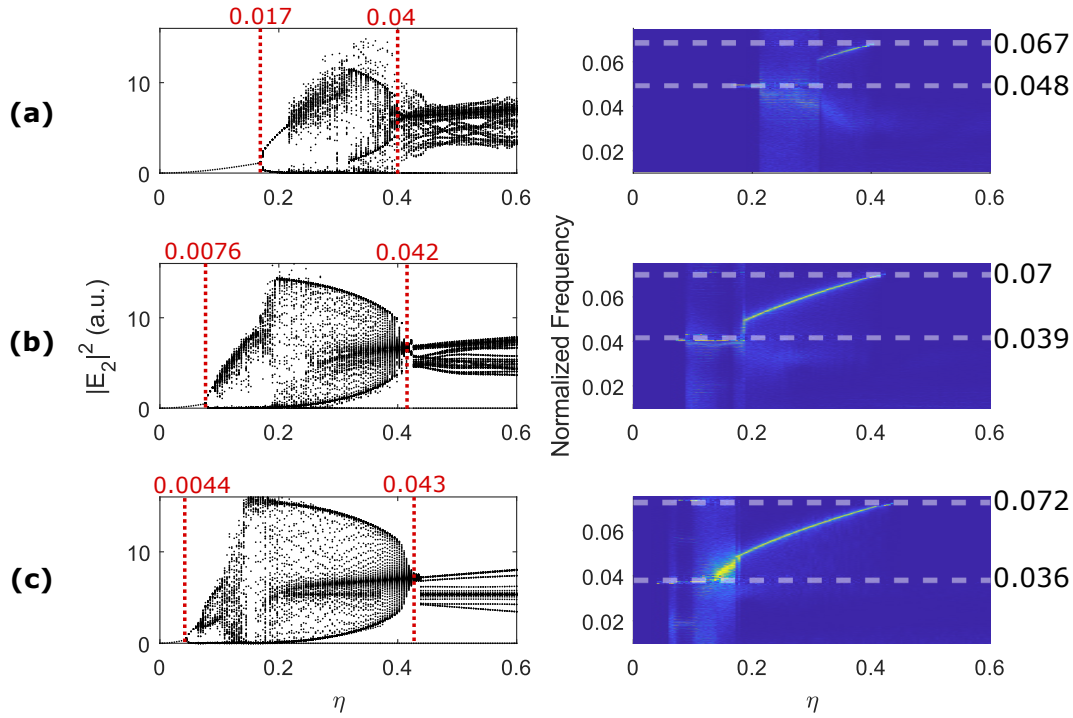


Figure 4.15: (*Left*) Bifurcation Diagrams and (*Right*) spectrograms for (a) $k = 0.8$, (b) $k = 0.85$ and (c) $k = 0.9$ for $P = 6$ and $\alpha = 3$. Other parameters are identical to those used in Fig. 4.8

4.3.5 Effect of noise

We report here the effect of noise on the bifurcation scenario leading to the appearance and disappearance of SW modulation on plateau, the modulation waveform and the frequency of the fast oscillations on plateau. In Figure 4.16, the parameters used are identical to those used in Fig. 4.8 with respectively the noise parameter $R = 10^{-12}$ and $R = 0$ in the left and right column.

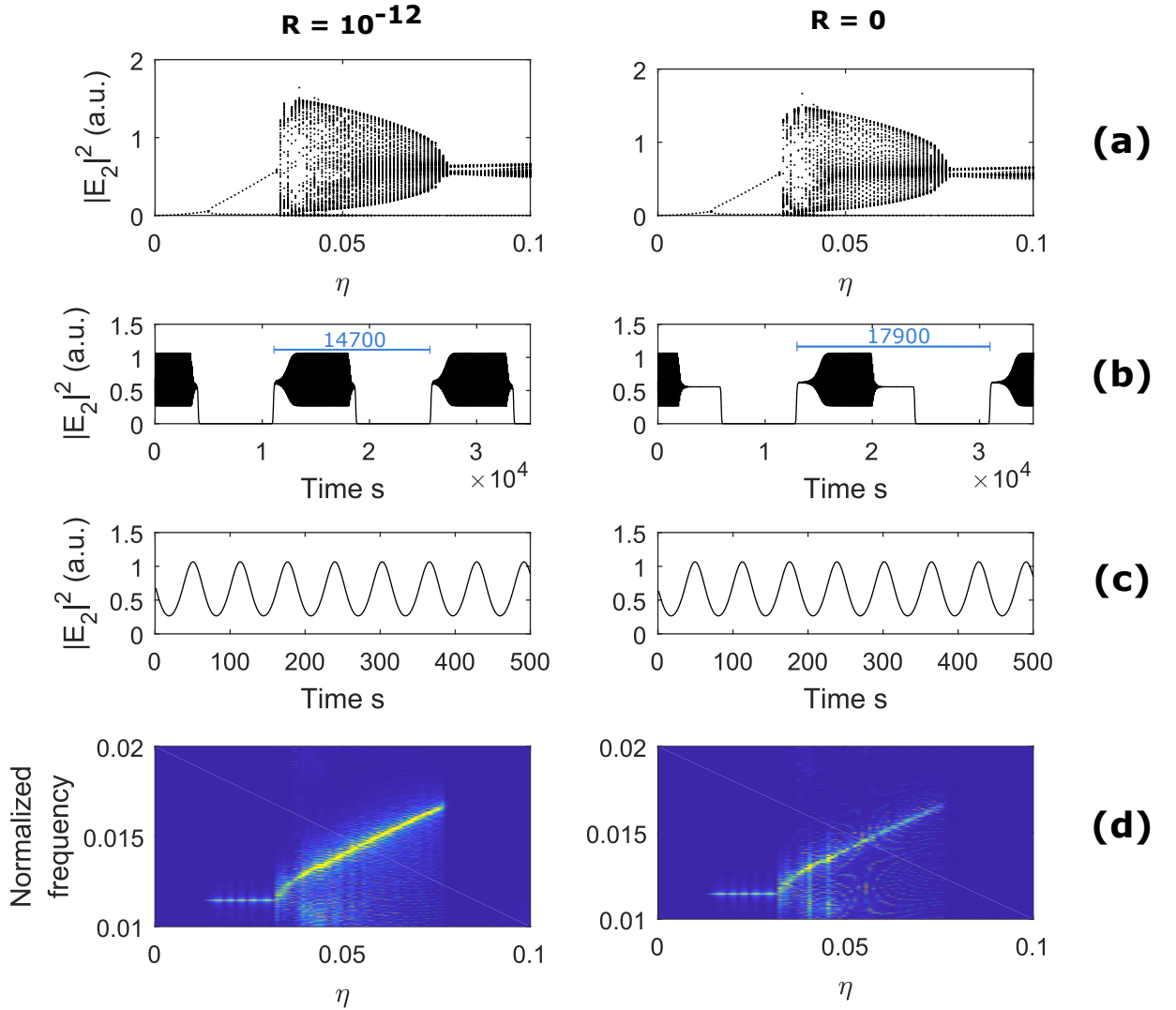


Figure 4.16: (left column) $R = 10^{-12}$ and (right column) $R = 0$. (a) Bifurcation diagrams of $|E_2|^2$ versus η , (b) time evolutions of $|E_2|^2$ for $\eta = 0.07$, (c) zooms on the first 500 time units of panels (b) and (d) corresponding spectrograms. Other parameters identical to those used in Fig.4.8.

From the analysis of the bifurcation diagrams in Fig. 4.16 (a), no qualitative difference is observed between both cases : the H_1 bifurcation is located at the same value of feedback $\eta = 0.013$ and the H_2 bifurcation at $\eta = 0.078$ and the intensity levels of the $|E_2|^2$ extrema are identical for a fixed value of η . Nevertheless, difference is observed when taking a closer look at the temporal evolution of the TM mode intensity $|E_2|^2$ in Fig. 4.16 (b). We show here the case where $\eta = 0.07$ but the following

observation remains valid in the range of feedback $[0.035, 0.078]$, where oscillations on plateaus are observed. With and without noise, a SW modulation with oscillations is obtained. However, the periodicity of the SW is different : it is of $14700 \approx 2\theta$, when including noise, whereas it is of 17900 without noise. In addition, the duty-cycles *i.e.* the percentage of time that the signal spends on the upper level of the SW compared to the SW periodicity are also different: Having noise leads to a duty-cycle of 52%, while no noise leads to a duty-cycle of 61%. This discrepancy is due to the appearance of a secondary plateau just after the fast oscillations that affects both the duty-cycle and the SW periodicity. Yet, the fast oscillations dynamics on plateaus is not impacted by noise as depicted in Fig. 4.16 (c) : both its waveform and frequency remain unchanged, as confirmed by identical spectrograms in Fig. 4.16 (d).

In Fig. 4.17, we compare the spectrogram in a range of frequency that encompasses the slow SW modulation frequency when including noise (*left*) or not (*right*). As reported in the previous paragraph, with noise, only SW modulation of periodicity very close to $f_{EC}/2$ is obtained; hence, giving a constant frequency in the spectrogram when varying η . In contrast, without noise, an additional plateau increases the SW periodicity. In Fig. 4.17 (*right*), the frequency peak shifts to lower frequency as η increases suggesting that the additional plateau duration increases with the feedback rate.

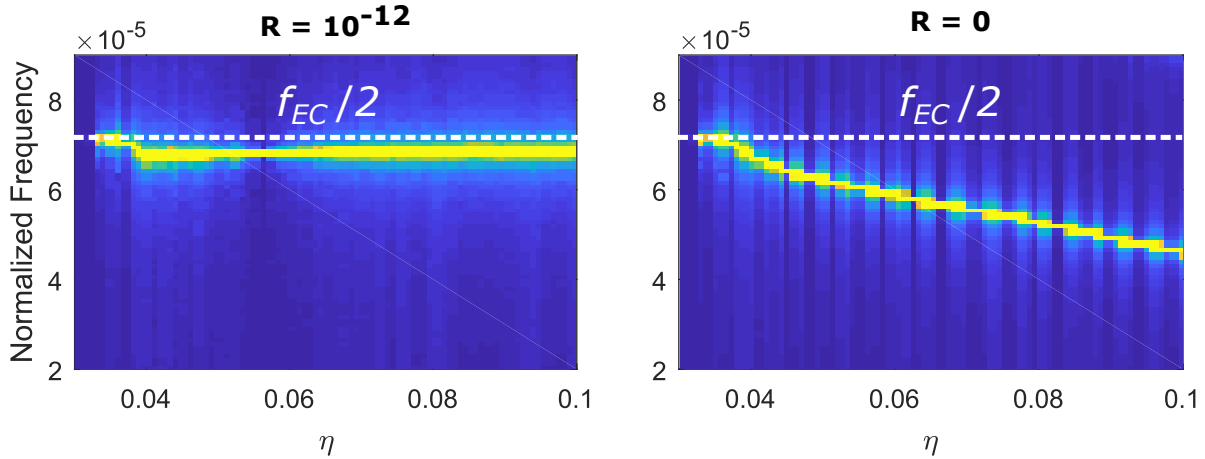


Figure 4.17: (a) Numerical time evolution of (a) A_1 , (b) A_2 and (c) N for $\eta = 0.07$ and other parameters identical to those used in Fig.4.8. No noise is included here $R = 0$.

In summary, although the absence of noise changes the slow SW periodicity by

allowing an additional plateau in the SW dynamic, no significant modification is observed on the frequency of the fast oscillation on plateaus and on the bifurcation scenario leading to them. Hence, ignoring the noise is still valid for further analytical study without loss of generality. In addition, the inclusion of noise (even a very small quantity) is mandatory numerically in order to match experimental observation of 2τ -periodic SW.

4.4 Analytical investigation on the sustained oscillations frequency

To unveil the key parameters driving the evolution of these fast oscillations, we study the stability of the different plateaus of the SW solutions as proposed by Gavrielides *et al.* in Ref. [60]. Because only high-intensity plateau of E_2 destabilizes, we can restrict the study to these plateaus.

As a starting point, we consider Eqs. (5.7)-(5.10) and introduce the following decomposition:

$$E_j = A_j \exp(i\phi_j) \quad \text{with } (j = 1, 2),$$

and define a new variable $\Phi \equiv \phi_1(s - \theta) - \phi_2$. We obtain a new system of delayed differential equations

$$(4.5) \quad \frac{dA_1}{dt} = NA_1,$$

$$(4.6) \quad \frac{dA_2}{dt} = k(N - \beta)A_2 + \eta\sqrt{k}A_1(t - \theta)\cos(\Phi),$$

$$(4.7) \quad \frac{d\Phi}{dt} = \Omega + \alpha[N(t - \theta) - k(N - \beta)] - \eta\sqrt{k}\frac{A_1(t - \theta)}{A_2}\sin(\Phi),$$

$$(4.8) \quad T\frac{dN}{dt} = P - N - (1 + 2N)(A_1^2 + A_2^2).$$

We are interested by the destabilization of the upper plateau for A_2 of square-wave solutions which corresponds to the particular case $A_1 = 0$, $N(s - \theta) = 0$, $A_1(s - \theta) = \sqrt{P}$ as illustrated in Fig. 4.18. We substitute these values into Eqs. (4.5)-(4.8); this leads to a system of three ordinary differential equations:

4.4. ANALYTICAL INVESTIGATION ON THE SUSTAINED OSCILLATIONS FREQUENCY

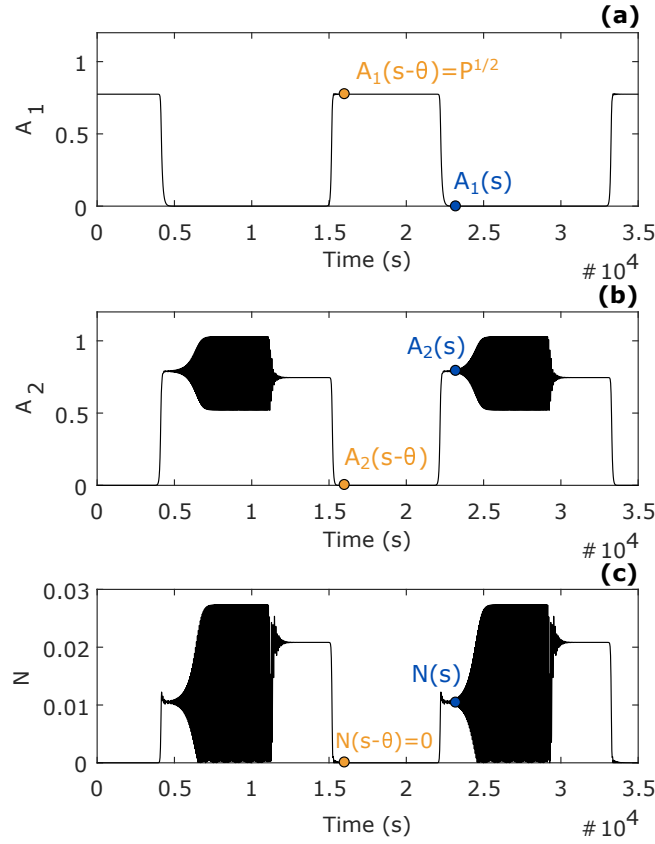


Figure 4.18: (a) Numerical time evolution of (a) A_1 , (b) A_2 and (c) N for $\eta = 0.07$ and other parameters identical to those used in Fig.4.8. No noise is included here $R = 0$.

$$(4.9) \quad \frac{dA_2}{dt} = k(N - \beta)A_2 + \eta\sqrt{k}\sqrt{P}\cos(\Phi),$$

$$(4.10) \quad \frac{d\Phi}{dt} = \Omega - \alpha k(N - \beta) - \eta\sqrt{k}\frac{\sqrt{P}}{A_2}\sin(\Phi),$$

$$(4.11) \quad T\frac{dN}{dt} = P - N - (1 + 2N)A_2^2.$$

It describes how the variables A_2 , N , and Φ evolve during the time duration when $A_1 = 0$, $N(s - \theta) = 0$, $A_1(s - \theta) = \sqrt{P}$.

4.4.1 Steady states

The steady state solutions satisfy

$$(4.12) \quad 0 = k(N - \beta)A_2 + \eta\sqrt{k}\sqrt{P}\cos(\Phi),$$

$$(4.13) \quad 0 = \Omega - \alpha k(N - \beta) - \eta\sqrt{k}\frac{\sqrt{P}}{A_2}\sin(\Phi),$$

$$(4.14) \quad 0 = P - N - (1 + 2N)A_2^2.$$

We consider here the case where $\Omega = 0$. Equations (4.12)-(4.14) simplify as

$$(4.15) \quad \Phi_s = \arctan(\alpha),$$

$$(4.16) \quad A_{2s}^2 = \frac{P - N_s}{(1 + 2N_s)},$$

$$(4.17) \quad \eta = -\frac{\sqrt{1 + \alpha^2}}{\sqrt{P}}A_{2s}\sqrt{k}(N_s - \beta).$$

4.4.2 Hopf bifurcations

After linearization around the steady states obtained, we obtain the following characteristic determinant for the growth rate λ

$$\begin{vmatrix} k(N_s - \beta) - \lambda & -\eta\sqrt{k}\sqrt{P}\sin(\Phi_s) & kA_{2s} \\ \eta\sqrt{k}\frac{\sqrt{P}}{A_{2s}}\sin(\Phi_s) & -\eta\sqrt{k}\frac{\sqrt{P}}{A_{2s}}\cos(\Phi_s) - \lambda & -\alpha k \\ -\frac{2}{T}(1 + 2N_s)A_{2s} & 0 & -\frac{1}{T}(1 + 2A_{2s}^2) - \lambda \end{vmatrix} = 0.$$

Substituting the steady state solutions from previous section, we obtain the following equation

$$\begin{aligned} 0 = & -\lambda^3 + \lambda^2 \left[2k(N_s - \beta) - \frac{1}{T} \left(1 + 2\frac{P - N_s}{(1 + 2N_s)} \right) \right] \\ & + \left[\begin{array}{l} -k^2(N_s - \beta)^2 - \alpha^2 k^2(N_s - \beta)^2 - \frac{2}{T}(P - N_s)k \\ + \frac{1}{T} \left(1 + 2\frac{P - N_s}{(1 + 2N_s)} \right) 2k(N_s - \beta) \end{array} \right] \lambda \\ & - (1 + \alpha^2) \frac{1}{T} \left(1 + 2\frac{P - N_s}{(1 + 2N_s)} \right) k^2(N_s - \beta)^2 \\ & - \frac{2}{T}(P - N_s)(1 + \alpha^2)k^2(\beta - N_s). \end{aligned}$$

We introduce $\lambda = i\sigma$, σ corresponds to the Hopf bifurcation frequency, and decompose in real and imaginary parts. This allows us to find the following Hopf bifurcation conditions

$$\begin{aligned}
 (4.18) \quad & \sigma^2 = k^2 (N_s - \beta)^2 + \alpha^2 k^2 (N_s - \beta)^2 + \frac{2}{T} (P - N_s) k \\
 & - \frac{1}{T} \left(1 + 2 \frac{P - N_s}{(1 + 2N_s)} \right) 2k (N_s - \beta), \\
 (4.19) \quad & 0 = \sigma^2 \left[2k (N_s - \beta) - \frac{1}{T} \left(1 + 2 \frac{P - N_s}{(1 + 2N_s)} \right) \right] + \frac{2}{T} (P - N_s) (1 + \alpha^2) k^2 (\beta - N_s) \\
 & + (1 + \alpha^2) \frac{1}{T} \left(1 + 2 \frac{P - N_s}{(1 + 2N_s)} \right) k^2 (N_s - \beta)^2.
 \end{aligned}$$

These two equations corresponds to the Hopf bifurcation conditions.

4.4.3 Approximations

For simplification purpose, we consider $T \gg 1$ and the following scalings

$$N_s = O(T^{-1/2}); P = O(1); \beta = O(T^{-1}); k = O(1).$$

Those approximations are chosen from the usual values used in literature [60, 61, 79, 212].

We introduce (4.18) into Eq. (4.19). The leading order leads to

$$0 = 2k^3 N_s^3 (1 + \alpha^2) + \frac{4}{T} P k^2 N_s - \frac{2}{T} P (1 + \alpha^2) k^2 N_s,$$

and after simplifications

$$(4.20) \quad N_s = -\sqrt{\frac{P (\alpha^2 - 1)}{Tk (1 + \alpha^2)}}.$$

Hence, we obtain an explicit expression for N_s as a function of the parameters P , T , k , and α . We now introduce (4.20) into (4.18) to obtain an expression for the Hopf bifurcation frequency and keep the leading order. It leads to

$$(4.21) \quad \sigma^2 = \frac{P}{T} k (1 + \alpha^2).$$

and therefore to the expression of the frequency f_{H_2} observed at the H_2 bifurcation point :

$$(4.22) \quad f_{H_2} = \frac{1}{2\pi} \sigma = \frac{1}{2\pi} \sqrt{\frac{P}{T} k (1 + \alpha^2)} = f_{RO} \sqrt{\frac{k}{2} (1 + \alpha^2)}$$

This expression includes the relaxation oscillation frequency f_{RO} and also a dependency on the linewidth enhancement factor α and the gain ratio k . It explains the numerical observations of section 4.3.4 when varying the laser parameters *i.e.* an increase of the frequency of oscillations on plateau when increasing P , k , α or decreasing T . It also confirms that the delay has no influence of this frequency.

In Fig. 4.19, we represent in dashed line the Hopf bifurcation frequencies f_{H_2} obtained from Eq. (4.22) when varying the pumping current P . We observe a good agreement with the numerical observations of Eqs. (5.7)-(5.10) represented by crosses. Even if we considered that β is $O(1/T)$, we note that this assumption provides a good approximation of f_{H_2} . For comparison purpose, we also show the theoretical value of f_{RO} , the frequency at the Hopf bifurcation H_1 at low feedback rate [$\eta = 0.013$ of Fig. 4.8(a)]. When increasing P , the frequency at H_1 remains very close to the theoretical value of f_{RO} while the frequency observed at H_2 follows the trend of f_{RO} but remains at a higher value. This is again in agreement with the experimental observation of Fig. 4.6(b).

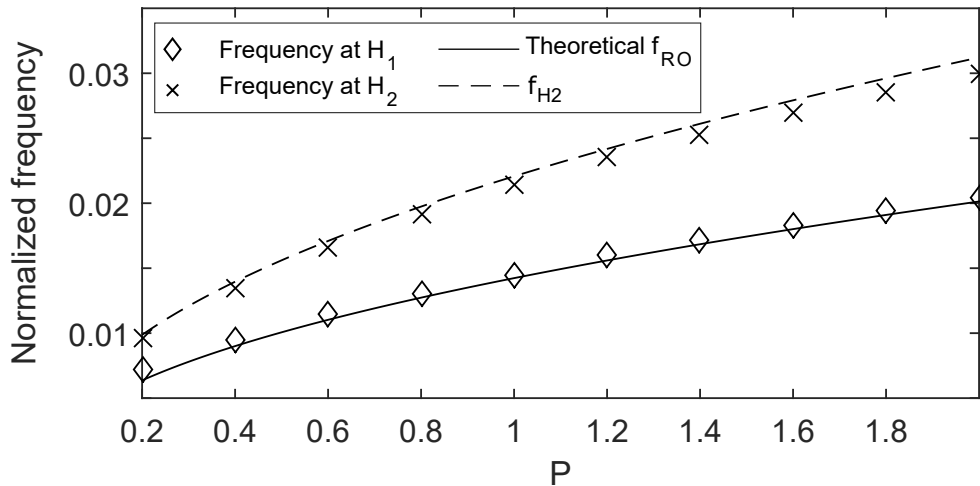


Figure 4.19: Numerical and analytical frequency observed at the bifurcation points H_1 and H_2 as function on P using the same parameters as in Fig. 4.8.

4.5 Conclusion and perspectives

In conclusion, we have demonstrated a bifurcation scenario that induces sustained oscillations over a slow polarization switching at a frequency different from the relaxation frequency and from the external-cavity frequency in a laser diode. A polarization-rotated optical feedback induces a slow SW modulation of the laser polarizations and fast oscillations with possibly high modulation amplitude are observed on the upper state of the SW. Interestingly, although the polarization switching dynamics is induced by delayed optical feedback, that self-pulsation frequency does not scale with the time-delay. One could consider long delay i.e. quasi-continuous linear polarization emission and still observe sustained oscillations in the output power. Equation (4.22) shows that the resulting high-frequency of the fast oscillations has an interesting dependency on both f_{RO} and the linewidth enhancement factor hence suggesting experimentation on different laser devices. A secondary bifurcation on the self-pulsing dynamics may even show frequency components much higher than that given by Eq.(4.22) : In Fig. 4.20(a), we show an additional bifurcation scenario for $\alpha = 5$, $\beta = 0.01$ and $k = 0.98$. In Fig. 4.20(b), the reported H_1 and H_2 bifurcations remain with respectively a frequency of $f_{H_1} = f_{RO} = 0.011$ and $f_{H_2} = f_{RO} \sqrt{\frac{k}{2}(1 + \alpha^2)} = 0.04$ (3.6 times f_{RO}). However, we observe also a secondary bifurcation at $\eta = 0.13$ arising from the fast oscillations on plateau branch. This bifurcation scenario leads to frequency components in the RF spectrum [Fig. 4.20(b)] that go well beyond the frequency signatures of f_{RO} , f_{EC} and even higher frequencies than those corresponding to f_{H_2} . For $\tau_p = 1.14$ ps, the situation of Fig. 4.20(a) leads to oscillations at frequencies above $f_{H_2} = 35$ GHz while $f_{RO} = 9.64$ GHz. This is a dramatic increase of the laser self-modulation frequency when compared to f_{RO} .

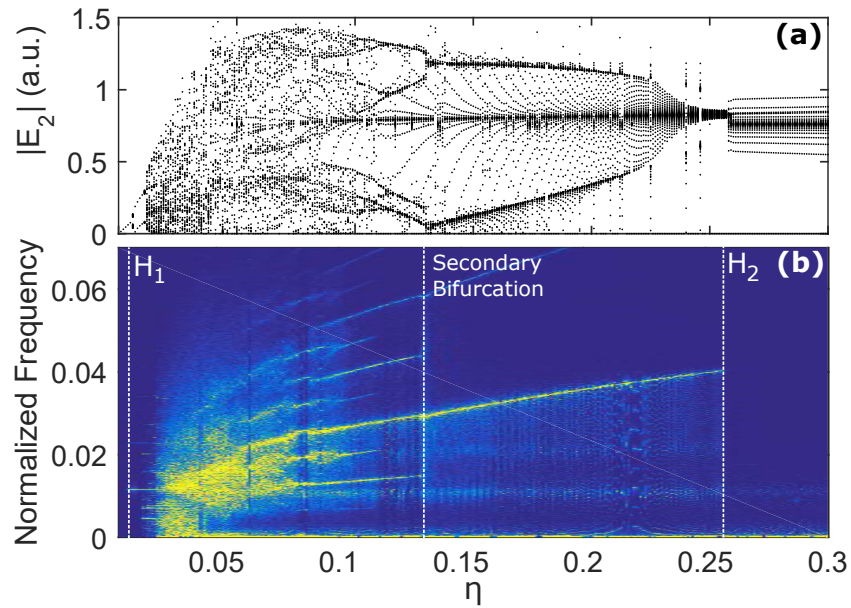


Figure 4.20: (a) Bifurcation diagram of $|E_2|$ versus η and (b) the corresponding spectrogram. $\beta = 0.01$, $k = 0.98$ and $\alpha = 5$. The other parameters are identical to those of Fig. 4.8.

Finally, first numerical simulations of a VCSEL subjected to a PROF configuration¹ shows that similar dynamics made of SW modulation with oscillation on plateaus can also be observed. However, experimentally, we expect modulation frequencies up to 20 – 25 GHz which are way beyond the detection bandwidth of our photodiodes. A confirmation would require a detection system in this range of bandwidth capable of measuring optical power variations of the order of 100 μ W.

¹based on the *San-Miguel Feng Moloney* model including PROF effect and noise

OPTICAL CHIMERA IN LIGHT POLARIZATION

In this chapter, we focus on the generation of optical chimera states. Chimera states refer to a self-organization pattern characterized by the coexistence of two opposite dynamical behaviors : coherence (synchronization) and incoherence (desynchronization) in a network of coupled identical non-linear oscillators. This state was named by Strogatz *et al.* after the Greek legendary creature "*chimera*" made of disparate animal parts : a lion, a goat and a snake.

We first introduce the state-of-the-art on chimera states going from its first prediction in 2002 to the latest experimental demonstrations. We also provide a discussion on the onset of optical chimera states from laser diodes and show that among the few existing experimental studies, none of them strictly address the question of whether chimera states can arise from the inherent non-linearity of laser diodes.

In a second part, we provide a versatile experiment allowing the observation of chimera states from the polarization dynamics of a laser diode. Our study answers the previous question by proving that chimera states can be obtained from the non-linear coupling between carrier and photon in the active medium of the device taking advantage of the close analogy between delayed systems and spatially extended systems recently used in the observation of chimera states [215, 216]. In addition, our experimental observations are qualitatively well reproduced by numerical simu-

lations. We also report on the observation of multi-headed chimera characterized by several islands of coherence and incoherence. This multi-headed solution also shows multi-stability meaning that driving laser diode from different initial states lead to chimera states with different number of heads. Furthermore, we provide a method to control chimera-state and multi-headed chimera by varying the delay of a second weak isotropic feedback arm or changing the feedback strength of a PROF feedback. Finally, we summarize the chapter in Sec. 5.3 and propose some perspectives.

This work is based on a submitted paper :

Uy, C. H., Rontani, D., Weicker, L., and Sciamanna, M. (2018). Optical chimera in light polarization.

5.1 Chimera state : a coexistence of coherence and incoherence

The spontaneous occurrence of a homogeneous behavior in an heterogeneous network of coupled systems remains a fascinating phenomenon. The most striking example is the synchronous collective dynamics within large populations of interacting oscillators [217], including the synchronous flash of fireflies [218] and the adjustment of rythms of coupled pulsating lasers [219]. Contrariwise, Kuramoto and Battaktogh proved in 2002 [80] that an homogeneous system can exhibit heterogeneous behavior, *i.e.* a group of identical oscillators that are non-locally coupled may experience the coexistence of coherent (synchronized) and incoherent (unsynchronized) dynamics. This new type of collective dynamics was named after the legendary Greek creature "*chimera*".

In their work, while investigating the dynamic of a ring of identical coupled phase oscillators¹, they observed that, for a certain set of initial conditions, the oscillators exhibit two dramatically different behaviors from one another. Indeed, they showed that part of them were synchronized while the other part shows desynchronized dynamics. Since then, chimera states have gathered a lot of attention [220] in many different systems. Similarly to Kuramoto and Battaktogh, several numerical studies have investigated ring of non-locally coupled oscillators [80, 221–223]. Chimera state have also been numerically observed in different configuration : several interacting

¹similar natural frequency and homogeneously coupled

clusters of coupled oscillators [224, 225], 2D array of coupled oscillators [226, 227], on torus [228], and sphere [220].

5.1.1 Demonstration of spatially extended chimera states

Although chimera states have inspired a lot of theoretical studies, only few experimental demonstrations have been proposed so far. Indeed, from the first prediction of Chimera state by Kuramoto in 2002, only few experimental demonstrations have been conducted which involve oscillators of various natures. We hereby briefly introduce the main experimental investigations on spatially extended chimera state. By *spatially extended*, we mean experiments where each elementary oscillators are distinctively placed over the space (either 1D or 2D). The following reports are not an exhaustive lists of experimental observations of chimera state but rather some milestones in the field.

5.1.1.1 Chemical oscillators

Historically, the first experimental observation was shown in 2012 by Tinsley *et al.* [229]. Their experiment was carried out with two matrices of discrete chemical oscillators based on the photosensitive Belousov-Zhabotinsky (BZ) reaction. We will not go in detail on the chemical mechanism as it is very complex and involves around 18 different steps [230] but the macroscopic phenomenon making it an oscillator is as follows : a first process generates molecular bromine from bromide ion and a second one consumes the bromine to give again bromide ion. The addition of a specific catalyst leads to the production of additional bromine when subjected to an increase of lightning thus affecting the phase of the reaction. During the process, each oscillator is driven by a modulation of the lightning that depends on the mean phase of each matrix. With this setup they observed the emergence of a chimera state where the oscillators of one matrix are synchronized while they are completely unsynchronized in the other matrix.

In 2018, they conducted a similar experiment with only one matrix of oscillators [231] as shown in Fig. 5.1 (a). Here, each oscillator is non-locally coupled² to their close neighbors with an exponential decay of the coupling strength with the distance.

²by the lightning

When initializing the matrix with a phase singularity in the center of it, they reported on the emergence of a spiral-like chimera state with a core of incoherence and rotating coherent arms. In addition, when varying the delay³, they observed a transition from chimera state to full asynchronous dynamics over the whole matrix.

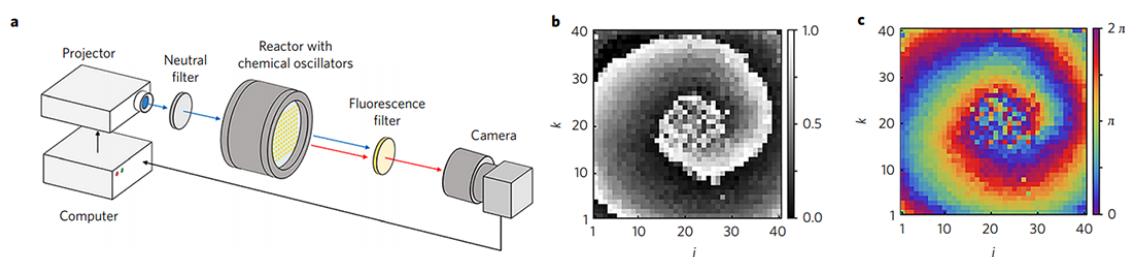


Figure 5.1: (a) Experimental setup. The BZ oscillators are organized in a 40x40 matrix. The camera records fluorescent light emitted by the catalyst. The image is sent to a computer which modulates an SLM inside the projector which shines the matrix. (b) Gray value recorded on the camera. (c) Oscillator phases interpreted from (b). The figure is taken from Ref. [231].

5.1.1.2 Optoelectronic oscillators

In 2012, Hagerstrom *et al.* [232] proposed a versatile experimental system allowing the investigation of various coupling configuration. To do so, their experiment relies on a Spatial-Light Modulator (SLM) as a stockpile of elementary oscillators, the liquid-crystal (LC) pixels. The coupling topology can be entirely decided by the user as it is fixed by an external computer. The experiment is shown in Fig. 5.2 (a). An SLM is shined by a linearly polarized light and each pixel locally modifies the polarization. A polarizing beam-splitter filters the light along one polarization direction and a camera records the transmitted beam. Doing so, the current state of the SLM is deducible. Depending on the topology, the coupling distribution and strength chosen by the user, a computer updates the SLM state.

³between the moment when the camera records the phases of the matrix and the moment when the projector shines the matrix with this information

5.1. CHIMERA STATE : A COEXISTENCE OF COHERENCE AND INCOHERENCE

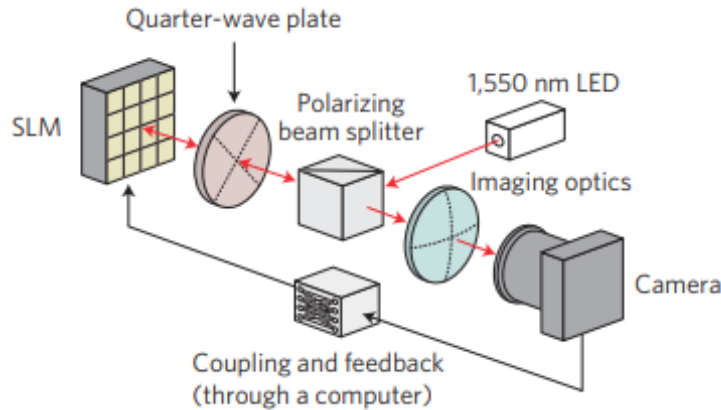


Figure 5.2: Optical configuration. Polarization optics create a nonlinear relationship between the spatially dependent phase shift applied by the SLM and the intensity of the light falling on the camera. Feedback and coupling are implemented using a computer. The figure and caption are taken from Ref. [232]

With this versatile experiment, he was able to induce a chimera state in 2 different configurations : a 1D ring and a 2D matrix where each oscillator is diffusively coupled to their neighbors. However, in 2012, the only two available experiments [229, 232] were criticized as the couplings were performed numerically [220]. It was in 2013 that a fully "analog" experiment was demonstrated with mechanical oscillators.

5.1.1.3 Mechanical oscillators

Inspired by Huygens' original synchronization experiment [233], Martens *et al.* carried out an experiment using two coupled clusters of metronomes [234] as shown in Fig. 5.3. In its simplest form, *i.e.* where only two metronomes are coupled as proposed by Huygens, they observed only two scenarios : either in-phase (IP) or anti-phase (AP) dynamics as shown in Fig. 5.3 (b). However, in Fig. 5.3 (c), when increasing the population of metronomes to 15 per clusters and for intermediate coupling strength between the clusters they reported on a chimera state that, similarly to the one of Tinsley *et al.* [229], was characterized by one cluster of coherence and another of incoherence. This state is shown to be at the boundary of IP and AP region.

Very recently, chimera state in a two-clusters configuration was explained by Abrams *et al.* [235] in the Kuramoto model framework. He demonstrated that

chimera state arises from a pitchfork bifurcation of a fully synchronized state (IP or AP) that breaks the symmetry and favors the synchronization of one cluster.

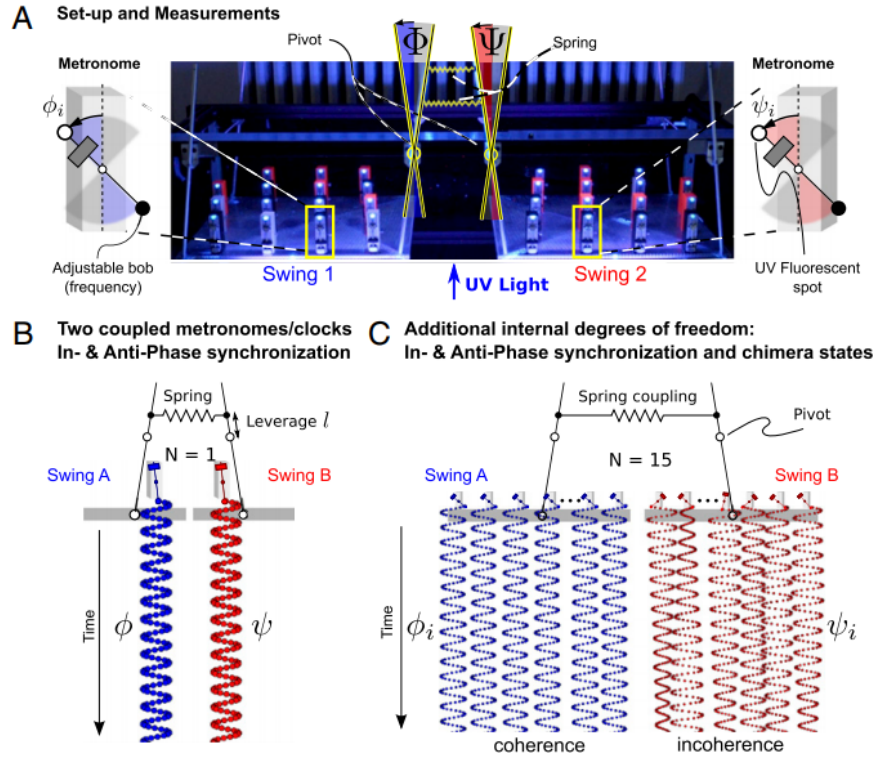


Figure 5.3: Experimental setup and measurements. Two swings are loaded with N metronomes each and coupled with adjustable springs. (a) Swing and metronome displacements are measured by digital tracking of UV fluorescent spots placed on the pendula and swings. (b) $N = 1$: Metronomes synchronize in anti-phase or in-phase motion. (c) $N = 15$: Symmetry-breaking chimera states with one metronome population synchronized and the other desynchronized, or vice versa. The figure and the caption are taken from [234]

5.1.2 Chimera states in optical spectrum and virtual-space

Historically, chimera states have been predicted on a spatially-extended system being a ring [80]. The first experimental demonstrations have also been conducted on matrices of oscillators [229, 232, 234]. However, there are also so far 3 examples of chimera states observed in systems where the oscillator-locations are not spatially defined [215, 216, 236]. We hereby introduce those experiments.

5.1.2.1 In the optical spectrum of a mode-locked laser

Mode-locked laser (MLL) is an extensively studied device for its capability to produce short optical pulses at high-frequency [237, 238]. It is known that the pulse train can be analyzed in the spectral domain as a comb of modes [239] that are individually described by its frequency, phase and amplitude. Therefore, each of them can be considered as a unique oscillator [236].

In 2014, Viktorov *et al.* [236] described in a MLL including a saturable absorber, the coexistence of mutually coherent modes and mutually incoherent modes, in other words a chimera state. When coherent (or locked), the optical linewidth of a mode doesn't vary much compared to its close neighbors. On the contrary, when incoherent (not broadens significantly. They showed that, when increasing the injection current of the laser, the system goes from fully coherent state (fully locked) to a mixed state where part of the modes are locked while the other part is not completely locked. With this demonstration, Viktorov *et al.* showed that chimera-state are not solely observable in a spatially-extended system.

Nonetheless, although subject to discussion, this system needs the addition of a nonlinear medium being the saturable absorber in addition to of the laser nonlinearity itself. This study has motivated our in order to investigate if a laser intrinsic non-linearity is sufficient or not for the observation of chimera-state.

5.1.2.2 In a virtual space from a time-delay system

Time-delay is known to enhance the dimension of a system by creating many co-existing attractors [240] leading to complex dynamics. In 1989, Ikeda *et al.* [241] proposed a method to observe hidden features of turbulent dynamics. They derived a delay-differential equation and show that it can be written as a discrete mapping of a spatial pattern; showing in the process the close analogy between high-dimensional temporal system and spatially extended system. Their idea is to divide the temporal data in periodical slices and create a 2D-representation by stacking them vertically. Doing so, features which have a periodicity close to the temporal length of the slices (usually the delay) can be visually investigated. The idea was generalized in 1991 by Arecchi *et al.* [242] and in 1996 by Giacomelli *et al.* [243]. This method has been used in many different systems such as : synchronization of chaotic systems [244], optoelectronic reservoir computing [245], temporal solitons in a feedback laser [246],

square-wave in Ikeda system [247] and in the study of chimera state [215, 216, 248].

For the latter case, in 2013, Larger *et al.* [215] reported on the observation of chimera states with only one physical oscillator using the above mentioned *space-time representation* that they named *Virtual chimera*. Their experiment consisted on an electronic circuit which can be modelled by a modified one-variable integro-differential Ikeda-like delayed equation [249] in which the feedback signal is bandpass-filtered. Both experiment and numerics showed that under a certain range of feedback strength⁴, the system exhibits periodic square-wave like oscillations with two distinct states : a lower quiescent state with no modulation and the upper state with irregular oscillations [see Fig. 5.4 (a)].

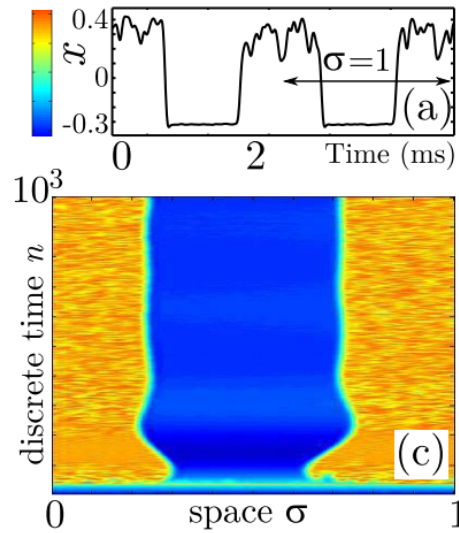


Figure 5.4: Virtual chimera in delay dynamics. (a) Asymptotic temporal waveform of a chimera (arb. units in amplitude are encoded in color for the space-time plots). (c) Virtual space-time representation of (a). The figure and the caption are taken from Ref. [215].

Following the space-time transformation procedure proposed by Arecchi *et al.* [242], the signal is sliced periodically with a time duration $\sigma = 1$ ⁵ indicated by an arrow in Fig. 5.4 (a) and stacked vertically in a space-time representation in Fig. 5.4

⁴i.e. amplitude of the feedback signal

⁵each slices of length σ is analogous to a temporal position in-between $[t, t + \tau]$ with t the time variable and τ the delay

5.1. CHIMERA STATE : A COEXISTENCE OF COHERENCE AND INCOHERENCE

(c) where the amplitude of the signal is now color-coded. With this analogy, each temporal slice becomes a spatially extended dimension in which a theoretically infinite number of oscillators is placed⁶. The vertical axis represents here the temporal evolution of those oscillators. As a result, they observed the formation of a chimera-like pattern with a region of coherence (in blue) where the oscillators behave similarly surrounded by a region of incoherence (in yellow) where the oscillators have erratic fluctuations. When initialized with proper conditions, this system is also able to exhibit *multi-headed chimera state* characterized by several clusters of coherence and incoherence within the same virtual space.

In 2015, Larger *et al.* [216] demonstrated a very similar behavior in the output wavelength of a DBR-laser⁷ diode subjected to an optoelectronic feedback as shown in Fig. 5.5. In this experiment, the active region of a CW laser is pumped by a constant current while its wavelength is tuned by the current i_{DBR} applied to the DBR grating. A fixed Fabry-Perot interferometer is placed at one output facet of the laser and depending on the emitted wavelength, modulates the overall output power which is converted the light into an electrical signal and then coupled back into the current i_{DBR} with a delay and a band-pass filtration. This system is mathematically equivalent to the one in Ref. [215].

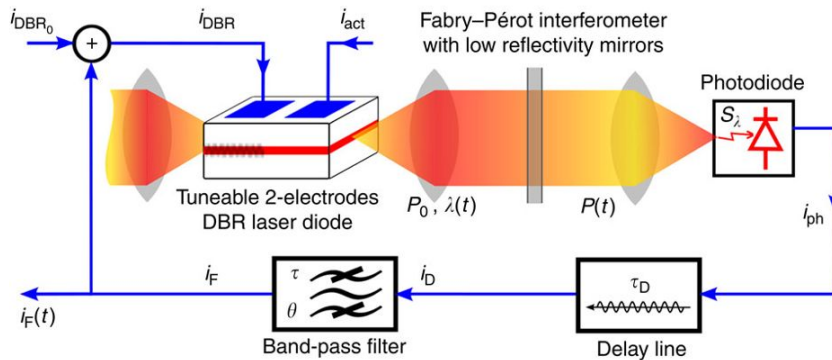


Figure 5.5: A tunable semiconductor laser setup is subjected to a non-linear delayed optoelectronic feedback allowing for highly controllable multiple head chimera states. The figure and the caption are taken from [216]

Larger *et al.* demonstrated that this system is able to exhibit virtual chimera and

⁶the elemental oscillators being located at each point of the slices of length σ

⁷DBR : Distributed Bragg reflector

multi-headed chimera but also that the corresponding model is very similar to the one used historically by Kuramoto and Battaktogh in 2002 [80].

5.1.3 Discussion on optical chimera state

As discussed in this thesis and demonstrated in hundred of articles in the literature [see Ref. [39] and references within], laser diodes are remarkable non-linear oscillators. Hence, a natural question is whether optical chimeras may be observed from the inherent properties of a laser diode *i.e.* the non-linear coupling that exists between its carrier population and its optical electrical field.

As described previously, in the vast majority of experiments on chimera states, light is either used as a coupling strength between the oscillators [229, 231], as a transduction that converts a polarization information into optical intensity [232] or as elemental oscillators [216, 236]. In the latter case, a laser diode produces the light.

In the study of Larger *et al.* [216], although the dynamics come from a laser diode, the opto-electronic feedback is not coupled to the active gain medium but rather to the DBR grating that controls the emission wavelength. As a result, the resulting chimera states does not arise from the intrinsic non-linearity of laser diode. On the other hand, in the study of Viktorov *et al.* [236], the non-linearity of a laser diode is needed to create the chimera state. However, a second source of non-linearity being the saturable absorber is also added externally to the laser itself. Hence one cannot directly conclude if chimera states can be observed solely from the non-linearity of a laser diode without another form of nonlinear transformation.

In the following, we will report on the observation of chimera states arising from the non-linearity of a laser diode based on the knowledge of our previously investigated polarization-rotated optical feedback (PROF) setup in Chapter 4. Indeed, as we have seen previously, laser diode subjected to a PROF can exhibit an asymmetric behavior with periodic switchings between quiescent state and oscillating dynamics in square-wave regime. Following the idea of Larger *et al.*, this regime can be seen as a chimera-state with the space-time analogy. However, one can still wonder if a PROF can be considered only as a linear transformation of the electrical field. To answer this question, the feedback configuration has to be mathematically described

5.1. CHIMERA STATE : A COEXISTENCE OF COHERENCE AND INCOHERENCE

in order to show the dependency of the output field⁸ \vec{E}_{out} as function of the input field \vec{E}_{in} . As a reminder, we show in Fig. 5.6 the configuration of a PROF arm consisting on a Faraday rotator which turns the polarization by 45° after each crossing of the light, a polarizer which filters the normally depressed polarization of the laser after being turned by 45° by the rotator, an attenuator and a mirror.

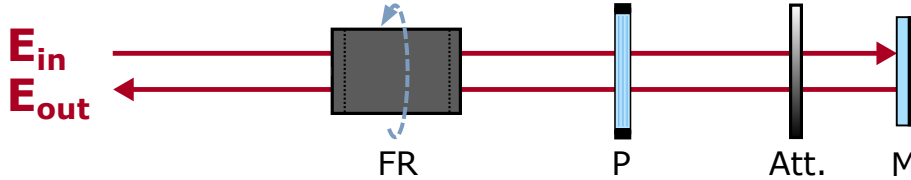


Figure 5.6: Polarization-rotated feedback arm. FR : Faraday rotator, P : Polarizer, Att. : Attenuator, M : mirror

As we are dealing with polarization modification of light, we propose to study this system in the *Jones formalism* framework. Let's also consider the general form of an arbitrary polarized electrical field \vec{E}_{in} :

$$(5.1) \quad \vec{E}_{in} = (E_1 \vec{x} + E_2 e^{j\phi} \vec{y}) e^{j\omega t - jkz} = \begin{pmatrix} E_1 \\ E_2 e^{j\phi} \end{pmatrix} e^{j\omega t - jkz}$$

where \vec{x} and \vec{y} are the unitary dimension vectors of the transverse plane. We arbitrary consider the TE field E_1 of an EEL in the direction \vec{x} and the TM field E_2 in \vec{y} . ϕ is the phase delay between the \vec{x} and \vec{y} component of \vec{E}_{in} . ω is the optical pulsation, t a time variable, k the wave-vector that has only one component in the direction of propagation \vec{z} .

The equivalent Jones matrices for the Faraday rotator (FR) which turns the polarization by an angle δ of 45° , the polarizer (P) turned at $\delta = 45^\circ$ and the attenuator (Att) with a transmission ratio α_{att} are :

$$(5.2) \quad \text{FR} \equiv \begin{pmatrix} \cos \delta & \cos \delta \\ \cos \delta & \cos \delta \end{pmatrix} = \frac{\sqrt{2}}{2} \cdot \begin{pmatrix} 1 & -1 \\ 1 & 1 \end{pmatrix}$$

$$(5.3) \quad \text{P} \equiv \begin{pmatrix} \cos \delta \cos \delta & \cos \delta \sin \delta \\ \sin \delta \cos \delta & \sin \delta \sin \delta \end{pmatrix} = \frac{1}{2} \cdot \begin{pmatrix} 1 & 1 \\ 1 & 1 \end{pmatrix}$$

⁸after crossing the feedback arm

$$(5.4) \quad \text{Att} \equiv \alpha_{att} \cdot \begin{pmatrix} 1 & 0 \\ 0 & 1 \end{pmatrix}$$

From Eqs. (5.2)-(5.4), we deduce the equivalent Jones matrix after one round-trip in the PROF arm :

$$(5.5) \quad \text{PROF} \equiv \frac{\alpha_{att}^2}{8} \begin{pmatrix} 1 & -1 \\ 1 & 1 \end{pmatrix} \cdot \begin{pmatrix} 1 & 1 \\ 1 & 1 \end{pmatrix} \cdot \begin{pmatrix} 1 & 0 \\ 0 & 1 \end{pmatrix} \cdot \begin{pmatrix} 1 & 0 \\ 0 & 1 \end{pmatrix} \cdot \begin{pmatrix} 1 & 1 \\ 1 & 1 \end{pmatrix} \cdot \begin{pmatrix} 1 & -1 \\ 1 & 1 \end{pmatrix} = \alpha_{att}^2 \begin{pmatrix} 0 & 0 \\ 0 & 1 \end{pmatrix}$$

As a result, the relation between \vec{E}_{in} and \vec{E}_{out} is given by :

$$(5.6) \quad \vec{E}_{out} = \alpha_{att}^2 \begin{pmatrix} 0 & 0 \\ 0 & 1 \end{pmatrix} \cdot \vec{E}_{in} = \alpha_{att}^2 \begin{pmatrix} 0 \\ E_1 \end{pmatrix} e^{j\omega t - jkz}$$

From Eq. 5.6, we can state that a polarization-rotated feedback is a linear transformation of the input field as it results from a linear mathematical operation.

5.2 Chimera state in laser polarization

As discussed previously, the motivation of this chapter is to show that chimera states can arise from the inherent non-linearity of a laser diode. We propose here a very simple setup based on the one investigated in Chapter 4. As previously reported, such a system can exhibit periodic polarization switching accompanied by oscillations on the upper state. We have described the case where the oscillations were almost sinusoidal but it is also possible to obtain chaotic oscillations. From this dynamic, we show that virtual chimera-states can be obtained with the space-time analogy of *Arecchi et al.* [178] and we propose a convenient way to control its spatial pattern through the use of an isotropic feedback.

5.2.1 Experimental setup

The experimental setup, sketched in Fig. 5.7, is similar to the one introduced in Chapter 4 with the exception of an additional isotropic feedback arm. It comprises

a commercial edge-emitting laser (EEL) JDS SDL-5400 at 852 nm. We operate at $J = 85$ mA (six times the threshold current) and at 25° C. The laser emits in its TE mode while the TM mode is suppressed by 44 dB. The beam is collimated and sent into three arms with two 30:70 beam-splitters. In the polarization rotated arm, a Faraday rotator is inserted in the external cavity and turns both TE and TM polarizations by 45° . The TM mode is then filtered with a polarizer while the mirror reflects the TE mode to the rotator, which turns again the polarization by 45° . As a result, the TE mode is injected in the laser with the same direction as the TM mode with a delay set to $\tau_1 = 8$ ns and a feedback ratio set to 28.5%. The feedback ratio is deduced from the calibration of the attenuation wheel and from the knowledge of the transmittance of the beam-splitter. In the detection arm, we measure the dynamics of the TM mode with a 12 GHz Newfocus 1554-B photodiode and a 36 GHz Lecroy oscilloscope. As is discussed below, a second isotropic feedback with delay τ_2 is later used to control the chimera states.

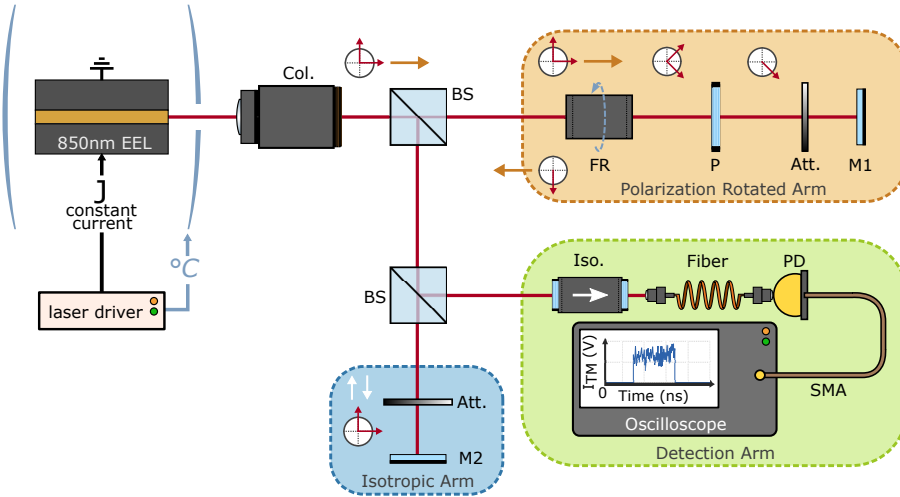


Figure 5.7: Setup of a laser diode subjected to both a polarization rotated optical feedback and an isotropic optical feedback. The polarization state is schematically represented along the light path. Col., collimator lens; BS, beam-splitter; FR, Faraday rotator; P, polarizer; Att., Attenuator; M1 and M2, mirrors; Iso., isolator; PD, photodiode.

5.2.2 Theoretical model

The numerical investigation is also based on a 2-modes in the Lang-Kobayashi framework as in Chapter 4 but we consider here the effect of an additional isotropic feedback arm. The model reads as follows

$$(5.7) \quad \dot{E}_1 = (1 + i\alpha)NE_1 + \eta_2 E_1(s - \theta_2)\exp(-i\phi) + n_1,$$

$$(5.8) \quad \dot{E}_2 = (1 + i\alpha)k(N - \beta)E_2 + \eta_1\sqrt{k}E_1(s - \theta_1)$$

$$(5.9) \quad + \eta_2 E_2(s - \theta_2)\exp(-i\phi) + n_2,$$

$$(5.10) \quad T\dot{N} = P - N - (1 + 2N)[|E_1|^2 + |E_2|^2],$$

where $E_{1,2}$ are the TE and TM fields, respectively. s is the time normalized by the photon lifetime τ_p . For simplicity, we consider $\tau_p = 1$ ps. N is the carrier density. $n_j\sqrt{R}\xi_j$ ($j = 1, 2$) are two white Gaussian noises with variance R and zero mean. $\theta_1 = \tau_1/\tau_p$ and $\theta_2 = \tau_2/\tau_p$ are respectively the normalized PROF and isotropic delay, α the linewidth enhancement factor, η_1 and η_2 are the PROF and isotropic feedback rates respectively, T the ratio of carrier to cavity lifetime, k the gain coefficient ratio between the TM and TE modes, β the TM mode additional losses, and P the pump parameter above threshold. In the following, the simulated field intensity $I_{TM} = |E_2|^2$ is filtered with a 12 GHz low-pass filter to match experimental bandwidth. The fixed parameters are $\theta_1 = 8000$, $\eta_1 = 0.12$, $\alpha = 5$, $T = 150$, $k = 0.95$, $\beta = (1 - k)/(2k)$, $P = 1$ and $R = 10^{-12}$.

5.2.3 Observation of virtual chimera states

Under the influence of the PROF with a 28.5% of feedback ratio⁹, the lasers shows periodical polarization switchings between both the transverse electric (TE) and transverse magnetic (TM) polarizations but with chaotic oscillations on the upper state of the plateaus as depicted in Fig. 5.8(a.1). The periodicity of the switchings is of $\Sigma = 2\tau_1 + \epsilon = 16.3$ ns with $\epsilon = o(\tau_1) = 0.3$ ns is a small time-lag induced by the internal time-scales of the EEL. In Fig. 5.8(a.2), we use a space-time representation proposed by Arecchi *et al.* [242] for the evolution of the TM field intensity I_{TM} . The time evolution of I_{TM} is divided in slices of duration Σ . Each slice stands for a

⁹the influence of the second isotropic feedback is not considered yet

virtual space S_v composed of an infinite number of virtual oscillators positioned in between $[0, \Sigma]$. The slices are incrementally stacked vertically and represent the time evolutions of the virtual oscillators.

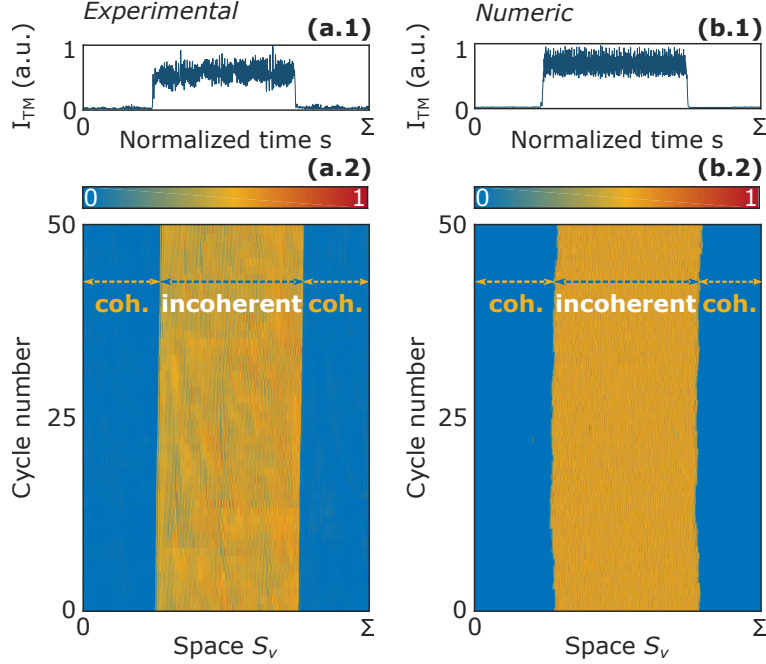


Figure 5.8: Stationary chimera in space-time representation. Time evolution of the field intensity I_{TM} in the time interval $[0, \Sigma]$ obtained (a.1) experimentally and (b.1) numerically. (a.2) and (b.2) are the corresponding space-time representation over 50 periods. I_{TM} intensity level is normalized and color-coded. Numerical simulations are initialized with a $2\theta_1$ -periodic sine function.

This representation shows a chimera-like time evolution of a spatially extended systems with two distinct regions : a homogeneous region, where all virtual oscillators behave coherently and a heterogeneous region, where the oscillators behave incoherently from each other. This chimerical behavior is stationary *i.e.* it lasts experimentally over at least tens of minutes with the same spatial partition between both regions.

In Fig. 5.8(b.1), we show the numerical time evolution of I_{TM} without isotropic feedback. The model is initialized with a $2\theta_1$ -periodic sin function. As in the experiment, we observe a quiescent state on the lowest plateau whereas the upper one has a chaotic dynamic. The space-time representation is also very similar to the one

obtained experimentally with a stationary chimera state divided into a coherent region and an incoherent region.

5.2.4 Stabilization of multi-headed chimeras with a 2^{nd} delay

So far, we have demonstrated that a laser diode subjected to a PROF is able to exhibit virtual chimera in the dynamic of the depressed polarization of the laser. In this experiment, we also show that chimera state can arise from solely the non-linear coupling of the electrical field with the carrier population. In addition, we will demonstrate in this section that this system can have more complex spatial pattern which can be stabilized and controlled by the use of the second isotropic feedback.

Indeed, analytically, it is possible to demonstrate that a simple PROF system allows polarization switching solutions at a periodicity of $(2\theta_1)/(2n + 1)$ with n a positive integer that arise from a cascade of Hopf bifurcations [79]. However, these harmonic solutions appear to be unstable in numerical simulations and have been recently stabilized in experiment by adding a second weak isotropic optical feedback [79]. As demonstrated in [250, 251], the addition of a time delay has a substantial impact on chimera states by creating and maintaining them. Phenomenologically, the addition of a second delay plays here two main roles : it is used (i) as a perturbation to pull the laser out from the strong attraction of the $2\theta_1$ -periodicity solution and (ii) as a buffer that memorizes the current solution and as a force that keeps the system on it. In the following, we have fixed the isotropic feedback ratio to only 0.9% which is 31 times weaker than the PROF feedback. The experimental coupling of the feedback light into the laser cavity being unknown, we chose numerically to set even weaker isotropic feedback strength $\eta_2 = 0.002$ in the model which is 60 times weaker than η_1 .

In Fig. 5.9(a.1), when setting the isotropic delay τ_2 to 9.4 ns, the TM intensity I_{TM} dynamics shows three groups of switchings in the time interval $\Sigma = 2\tau_1 + \epsilon = 16.5$ ns that is very close to the one of Fig. 5.8. Unlocking the third harmonic of the fundamental 2τ -periodicity leads to a change of the spatio-temporal pattern in Fig. 5.9(a.2). We observe experimentally a stationary chimera state split into three regions of incoherence. We later refer to this type of dynamics as a multi-headed chimera states as in Ref. [216]. Here, we have a 3-headed chimera state. Numerical simulation are consistent with the experiment when setting the isotropic delay θ_2 in

between [10000, 11800] (*i.e.* [10, 11.8] ns considering $\tau_p = 1$ ps). We show an example with $\theta_2 = 10000$ in Fig. 5.9(b.1). Here, the model is initialized with a $2\theta_1/3$ -periodic sin function.

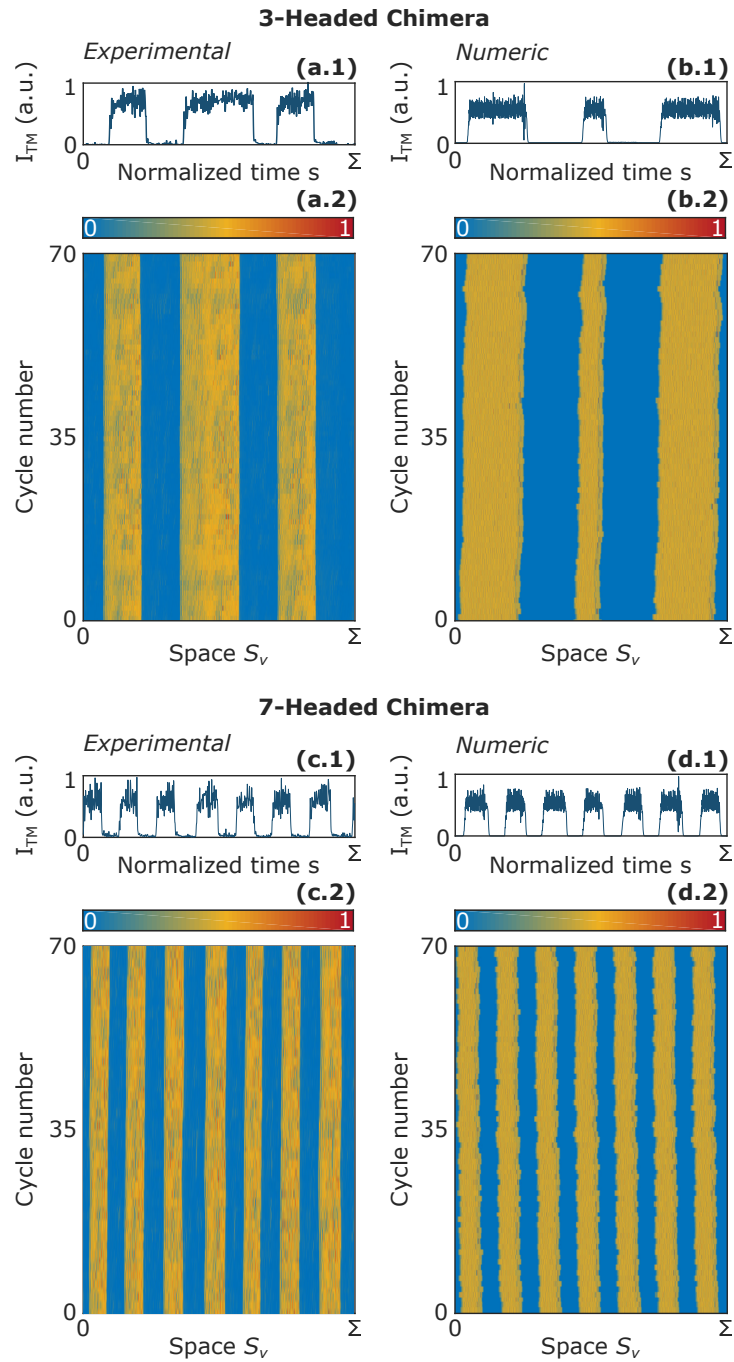


Figure 5.9: Experimental and Numerical multi-headed chimera. 3-headed chimera : (a.1) Temporal and (a.2) space-time representation of experimental data. (b.1) Temporal and (a.2) space-time representation of numerical data. 7-headed chimera : (c.1) Temporal and (c.2) space-time representation of experimental data. (d.1) Temporal and (d.2) space-time representation of numerical data.

In addition, it is also possible to control the number of incoherent cores in multi-headed chimera by carefully adjusting the delay of the second isotropic feedback. We show in Fig. 5.9 (c.1) and (c.2) the experimental temporal evolution of I_{TM} and its spatio-temporal representation when increasing τ_2 up to 9.8 ns. In Fig. 5.9(c.1), the system shows a polarization switching periodicity of 2.34 ns $\approx 2\tau_1/7$ that, therefore, gives rise to a 7-headed chimera in Fig. 5.9 (c.2). In order to obtain the same result numerically, the model has been initialized with a $2\theta_1/7$ -periodic sin function. We show in Fig. 5.9(d.1) and (d.2), the numerical temporal and spatio-temporal representation of I_{TM} showing a 7-headed-chimera for $\theta_2 = 11500$. Without this specific initialization, the laser polarization dynamic ends into a 1-head chimera only, hence, suggesting a "number of heads" multi-stability.

5.2.5 Multi-stability and chimera-heads mechanisms

To unveil this multi-stability property of the system, the number of chimera-heads is color-mapped in Fig. 5.10 (a-b) while scanning the delay parameters θ_1 and θ_2 and keeping other parameters fixed. Constant initialization leads to only one-head chimera solution (not shown here). In contrast, in Fig. 5.10 (a), the simulations are initialized with a $2\theta_1/3$ -periodic sin function. Although the one-head chimera is the predominant solution, regions of 3 and 5-headed chimera can be achieved. Even more complicated solution patterns emerge when initializing with a higher order sine function. In Fig. 5.10 (b), the simulations are initialized with a $2\theta_1/5$ -periodic sine function. New regions of different solutions arise over the previous reported solutions of Fig. 5.10 (a) with even more heads up to 11 hence demonstrating the multi-stability property of the system for fixed values of delay τ_1 and τ_2 .

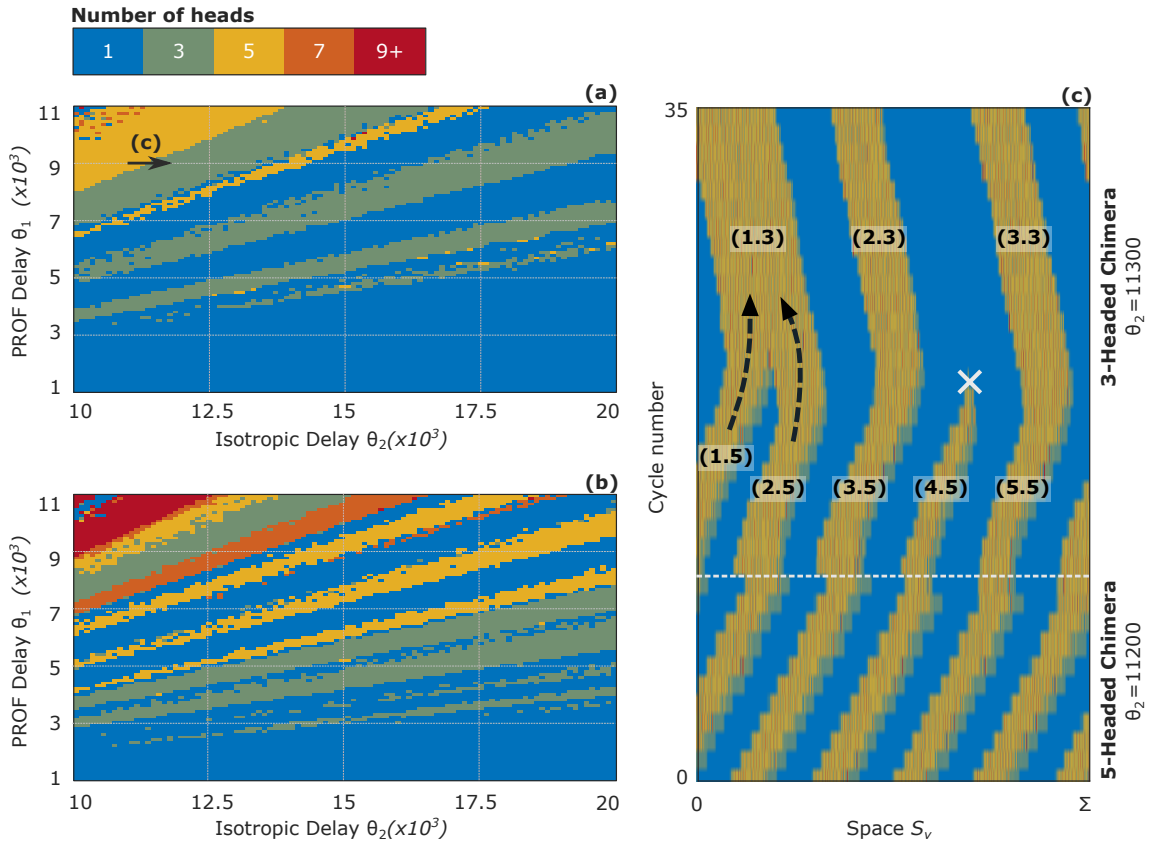


Figure 5.10: Mapping of the number of chimera-heads in (θ_1, θ_2) space for (a) $2\theta_1/3$ -periodic sin function initialization and (b) $2\theta_1/7$ -periodic sin function initialization. (c) Dynamic in spatio-temporal representation when crossing region of 5-Headed chimera to 3-Headed chimera (indicated by an arrow in Fig.5.10(a))

In Fig. 5.10(c), we show the spatio-temporal representation of I_{TM} when transitioning the system from a 5-headed chimera region to a 3-headed chimera region. The onset of the transition is marked by a white dashed line. While the system settles in a 5-headed chimera state, pulling it to a 3-heads chimera dynamics leads to a slow spatial drift of the chimera heads followed by a merging of the heads (1.5) and (2.5), the death of the (4.5) head and the survival of the (3.5) and (5.5) heads.

In the vast majority of experimental studies, a careful seeding is mandatory to observe the chimera states [229, 231, 232, 234] or to unlock high-order multi-headed chimera [215, 216]. In our experiment, although the first order chimera state (1-head chimera) is inherent to the PROF setup and therefore does not need any particular

initialization, we have demonstrated a simple method to control the order of the multi-headed chimera states without the use of seeding : varying the delay of the coherent isotropic feedback, we are able to drive the system into different orders of multi-headed chimeras.

5.2.6 Influence of the initialization and of the feedback strength

In the previous sections, we have shown that the addition of the second weak isotropic feedback to the PROF configuration can unlock several solution characterized by the number of chimera-heads. In addition, we demonstrated multi-stability between several solutions for a fixed set of parameters with the initialization as a critical aspect in the selection of the solution. However, contrary to the numerics, no particular initialization is performed in the experiment. In addition, we have shown that both the isotropic feedback delay and the PROF delay impacts on the observed solution.

In this section, we first discuss the effect of random initialization and then investigate the role of other parameters on the observed solution. It is also worth mentioning that without considering the spontaneous noise emission of the laser, we observed similar behavior as in Chapter 4 *i.e.* the square-wave (SW) slow modulation shows an additional intermediate plateau that lengthens the expected 2τ or $2\tau/(2n + 1)$ -periodicity of the SW.

5.2.6.1 Influence of the initialization

Previously, in order to unlock different solutions of chimera-head number, we initialized our simulations with a sine function of different periodicity. Without the isotropic feedback, only a 1-Headed chimera state is observed both experimentally and numerically. On the contrary, with the isotropic feedback, we are able to observe experimentally higher order chimera-head solutions. Numerically, if no initialization is used, only the 1-Headed chimera solution obtained. However, different solutions can still be obtained when initializing the system with random values as shown in Fig. 5.11. In this case, we recognize the same structure as in Fig. 5.10 but the high order solutions are less likely to be stabilized.

As a result, we show here that although we do not use any initialization in the experiment, high order chimera-head solution can be unlocked by the noise in the system. In addition, it also suggests the use of an external source of modulation to force the system into a specific solution such as an electrical modulator on the pumping current or an optical modulator on the isotropic feedback arm in order to apply a sinusoidal perturbation on the system.

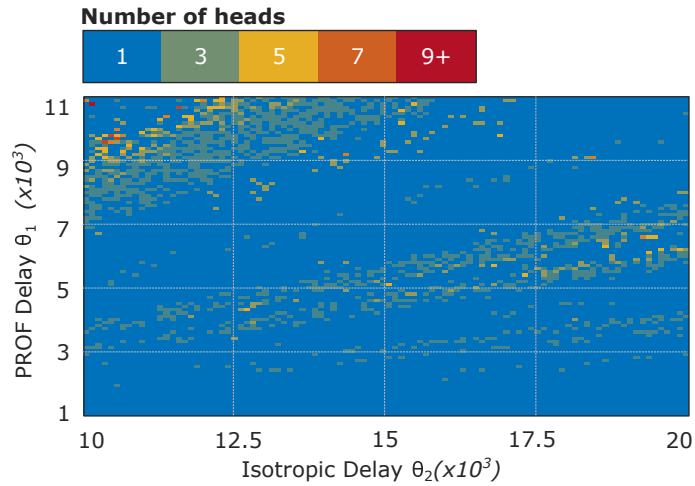


Figure 5.11: Mapping of the number of chimera-heads in (θ_1, θ_2) space for a random initialization of the simulations. Θ_2 is set to 12500 and the other parameters are identical to those used in Fig. 5.10 (a-b)

5.2.6.2 Influence of the PROF strength

So far, we have investigated the influence of both the PROF and isotropic feedback delays on the observed chimera state solution. We hereby discuss about the influence of the PROF and the isotropic feedback strength.

Influence of the PROF strength on the type of chimera-state

In 2016, Kemeth *et al.* [252] proposed a simple and convenient mathematical tools allowing the identification of chimera states and their classification in a different categories based on the g_0 -function as shown in Fig. 5.12 More detail on the procedure to obtain g_0 can be found in their work [252]. It measures the evolution of the spatial partition between coherent and incoherent regions over time.

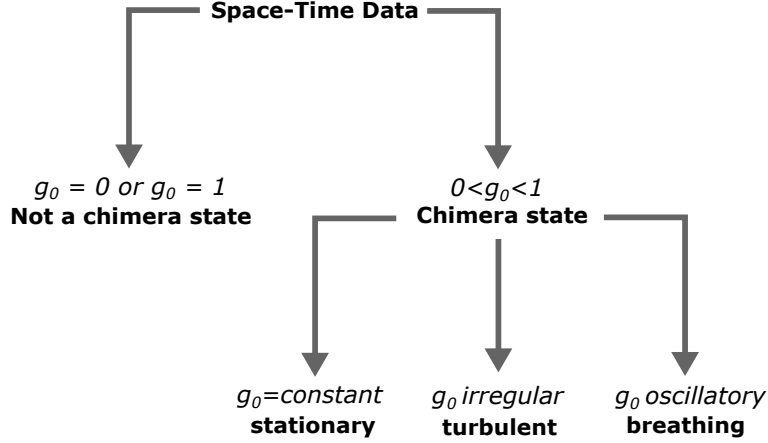


Figure 5.12: Classification of chimera states proposed by Kemeth *et al.* in Ref. [252] based on the g_0 -function.

When $g_0 = 0$ (*resp.* $g_0 = 1$), all oscillators are desynchronized (*resp.* fully synchronized) and hence, the spatio-temporal pattern is not a chimera-state. On the contrary when for a chimera-state, $0 < g_0 < 1$. In addition, among the chimera-state, different cases can be discriminated when considering the temporal evolution of the oscillators state: stationary chimera for g_0 constant, turbulent chimera for g_0 irregular and breathing for g_0 oscillating.

Here, we apply the same methodology on our system for different values of PROF strength η_1 . We show in Fig. 5.13 (a) the bifurcation diagram of the TE field intensity I_{TM} when varying the PROF strength η_1 with same parameters as in Fig.5.8. Here, we focus on the range of $\eta_1 \in [0.05, 0.5]$ where interesting behaviors are observed. However, one can find more detail on analogous scenario in Chapter 4.

We chose some representative cases along the bifurcation diagram (marked by the red arrow) and report in Fig. 5.13 (b-e) the temporal trace, the spatio-temporal representation and the corresponding g_0 -function.

- For $\eta_1 \in [0.08, 0.1]$: the g_0 -function is irregular meaning that we have here a turbulent chimera state where regions of coherence and incoherence evolve here randomly over time as illustrated in Fig. 5.13 (b).
- For $\eta_1 \in [0.1, 0.22]$: the g_0 -function is constant meaning that we have a stationary chimera-state where the spatial partition between coherent and incoherent

regions remains almost unchanged over time as illustrated in Fig. 5.13 (c). This case is identical to the one reported in Fig. 5.8.

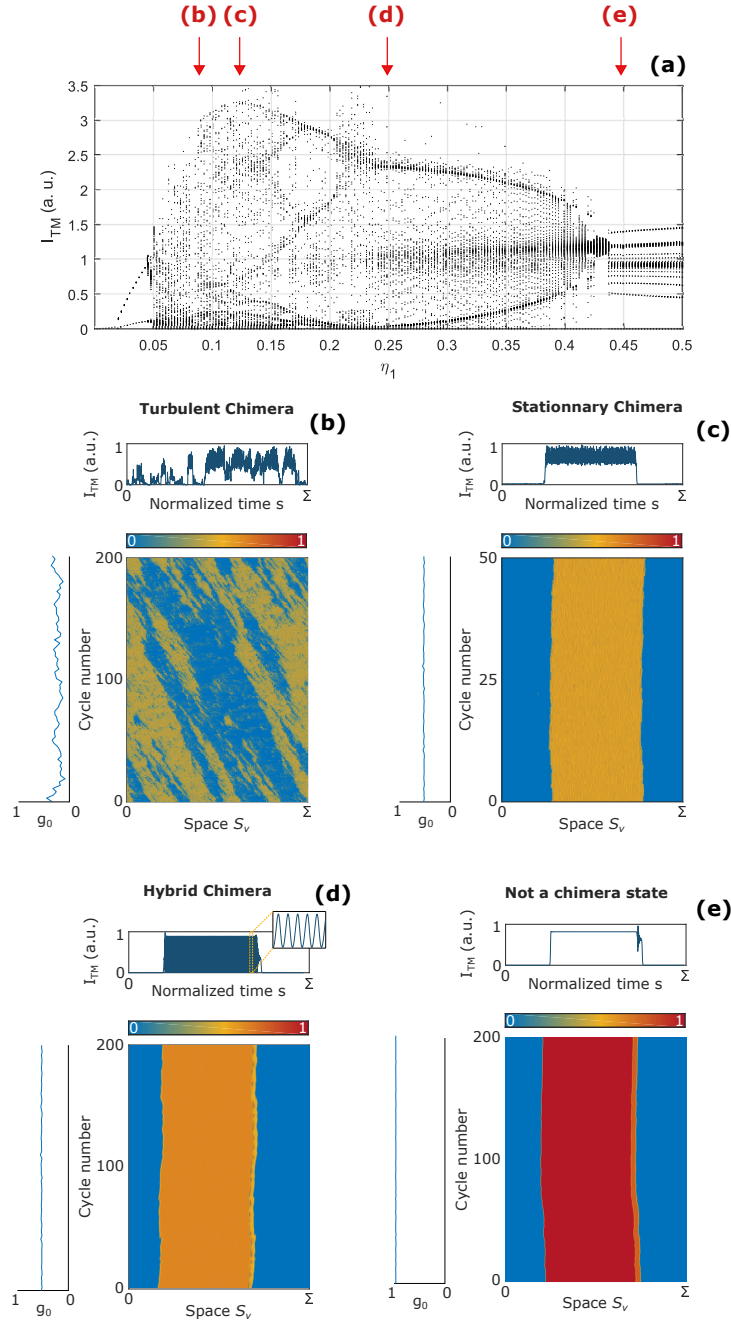


Figure 5.13: (a) Bifurcation diagram of I_{TM} as function of η_1 for identical parameters as in Fig. 5.8. (b-e) Time trace, spatio-temporal representation and g_0 -function taken along the bifurcation diagram (marked by a ref arrow in panel (a))

- For $\eta_1 \in [0.22, 0.43]$: the g_0 -function is also constant meaning that we have also a stationary chimera-state. However, when looking at the time trace in Fig. 5.13 (b), one can note that the "unsynchronized" region is oscillating. As far as we know, such type of chimera has not been reported yet and we label it as *Hybrid chimera state*.
- For $\eta_1 \in [0.43, 0.5]$: $g_0 = 1$ meaning that we do not have a chimera state anymore as illustrated in Fig. 5.13 (e). This transition matches the Hopf bifurcation previously studied in Chapter 4.

Influence of the PROF strength on the number of chimera heads

We here investigate the effect of the PROF strength on the observed number of heads in stationary chimera state regime. In Fig. 5.14 (a) (*resp.* (b)) we fix the isotropic feedback delay θ_2 to 12500 (*resp.* θ_2 to 9000) and vary η_1 while setting the other parameters and the initialization identical to the simulations of Fig. 5.10 (b). We map the number of heads observed when varying η_1 in-between $[0.85, 1.5]$ and θ_2 in-between $[10000, 20000]$ for Fig. 5.14 (a) and θ_1 in-between $[1000, 11000]$ for Fig. 5.14 (b). In both panels, the particular case where $\eta_1 = 0.12$ corresponds to an horizontal scan at $\theta_1 = 9000$ or a vertical scan at $\theta_2 = 10000$ in Fig. 5.10 (b).

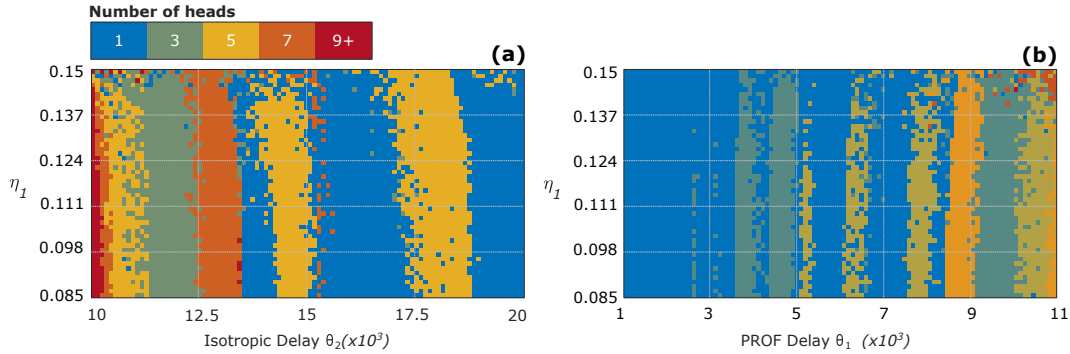


Figure 5.14: Mapping of the number of chimera-heads in (a) (θ_2, η_1) space and in (b) (θ_1, η_1) space. We initialize with a $2\theta_1/7$ -periodic as in Fig. 5.10 (b) with identical parameters.

The different solutions are organized in vertical stripes in Fig. 5.14 meaning that, when varying θ_1 or θ_2 , the value of η_1 does not influence the number of heads observed. Hence, experimentally, for a given laser (fixed parameters and injection

current/temperature), only the values of both delays play a role in the selection of the number of heads solution. It is also worth mentioning that, for $\eta_1 > 0.2$, the chimera states switch from stationary to hybrid as discussed previously.

5.3 Conclusion

To sum up, we have introduced the concept of chimera that refers to a self-organization pattern occurring in a network of identical oscillators. It is characterized by the coexistence of two dramatically different behaviors : coherence and incoherence. Since its theoretical prediction in 2002, there have been few experimental demonstrations of chimera states. However, the diversity of systems in which it has been observed suggests that chimera states might be more generic than expected. In addition, although first predicted in spatially-extended network, several studies have shown that chimera states can be observed within coupled oscillators that are not spatially defined such as the modes of mode-locked lasers or in a virtual space using the close analogy between space and temporal dynamic created by a delay.

In this chapter, we also demonstrate both numerically and experimentally the capability of a commercial laser diode to carry out chimera states through its inherent non-linear coupling between its carrier population and the light electrical field. Furthermore, this feature is brought by the laser polarization dynamics when driven by a coherent PROF configuration. The addition of a second feedback arm governs the obtained chimera pattern with different numbers of heads making this experiment very flexible to study physics of chimeras, their creations, evolutions and destructions. We also identify different type of chimera states such as turbulent, stationary and hybrid chimera state which are unlocked when varying the PROF strength.

Further study might be to reproduce such experiment with a VCSEL. Indeed, as also discussed in the conclusion of Chapter 4, such square-wave dynamic with oscillation on plateau is expected from simulation to be more robust when the net gains of the polarization modes are very close. Another perspective would be to study chimera states with two coupled-laser diodes. Indeed, it has been demonstrated that orthogonally coupled EEL might lead to square-wave oscillations [212, 253]. It would therefore be interesting to see if, first, virtual chimera states can be observed in the dynamic of both lasers and second, how those chimera states interact. Finally, a

challenging perspective would be to investigate if chimera states are achievable with even more coupled laser diodes through for example evanescent fields in VCSEL grown on the same wafer or through a global feedback. Theoretically, chimera states have been predicted in those systems [254, 255].

CONCLUSION

Throughout this thesis, we have unveiled new experimental, numerical and analytical results on different configurations of external-cavity laser diodes. We have chosen to focus on laser-polarization dynamics induced by a delay for its ability to enhance the complexity of the outcome dynamics. The aim of this final chapter is to summarize our main findings and to highlight the perspectives motivated by our work. Based on the main achievements detailed in this manuscript, we can envision some interesting perspective for future work. Each chapter being almost independent from each other, we can also split those perspectives chapter by chapter.

6.1 Summary, contributions and perspectives

This manuscript can be divided into two main parts : Chapter 2 and 3 dealing with VCSELs subjected to isotropic optical feedback and Chapter 4 and 5 focusing on EELs subjected to polarization-rotated optical feedback (PROF). The change of the laser has been imposed by technical limitations (weak output power of VCSELs and low sensitivity photodiodes). Nevertheless, we are convinced that our findings on EELs can be also obtained with VCSELs which is not always true the other way around.

In **Chapter 2**, we investigated the polarization dynamics and RF spectrum of a VCSEL subjected to an isotropic optical feedback in the framework of Low-Frequency Fluctuations (LFF) regime.

- First, we reminded the origin of polarization instabilities observed in free-running VCSELs. Indeed, VCSEL polarization behaviors greatly differ from those observed in EEL. This is mainly due to the difference in term of semiconductor structures. While the transverse profile of the active medium in EEL induces high losses for one linear polarization (LP) direction (favoring only one main LP mode), the circular profile of VCSEL cannot itself determine the lasing LP mode. A more in-depth study of the crystallographic structure of the active medium is therefore required to understand the polarization selection mechanism. It involves a meticulous analysis of the modal gain and losses inside the active medium that vary with the injection current and the device temperature. Nonetheless, the stability of the lasing LP mode remains weak in a large range of operating parameters and polarization switching is often observed when varying the current and/or temperature or by applying a weak external perturbation such as optical feedback.
- Second, we introduced the San Miguel-Feng-Moloney (SFM) model, a set of rate equations that models the VCSEL polarization behavior. This model differs from the more classic Lang-Kobayashi (LK) equations in the way that it considers a 4-level energy system with electronic recombination involving their spin mechanism. We also detailed the SFM model accounting for the delay induced by an isotropic optical feedback and provided mathematical approach of the so-called external-cavity modes (ECM) and antimodes. ECMs and antimodes are steady-state solutions of external-cavity laser characterized by their gain and optical frequency. In addition, while ECMs are stable solutions and act as attractors, their antimode counterparts are unstable and destabilize the system.
- Next, we focus on the so-called LFF regime in VCSEL under isotropic optical feedback. This regime is characterized by the different time-scale dynamics : a low-frequency modulation showing randomly distributed power drops and a high-frequency modulation at the external-cavity frequency and the relaxation

oscillation frequency of the laser. Due to the intrinsic polarization-instabilities in VCSEL, LFF modulation can also be observed in the VCSEL polarization dynamics and two types of LFF can be identified : Type-I LFF where both LP modes are correlated at the LFF frequency and Type-II where they are anti-correlated at the LFF frequency. Looking at the RF spectrum of both LP mode, we observed an unexpected double-peak structure arising at the external-cavity frequency region. Its location always follows the external cavity frequency and the splitting between the both peaks depends of the injection current. Our experimental and numerical investigations show that while the LP modes are anti-correlated at the low-frequency part of the structure, the correlation at the high-frequency component changes depending on the type of LFF.

- The origin of this double-peak structure can be explained when looking at the trajectory of the system in a projected phase-space. In the LFF regime, the trajectory is strongly attracted towards the ECM of highest gain. However, time to time, it may get in the immediate vicinity of the closest antimode which repels the system from the attraction of the ECM. When isolating the trajectory around the ECM, the corresponding RF spectrum only shows the highest-frequency peak of the double-peak structure. Considering then the trajectory around the antimode, the lowest-frequency peak appears. Hence, while the attraction of the ECM imposes a resonance at the high-frequency peak, the antimode lengthens the trajectory creating another resonance at the low-frequency peak. As a result, this push-pull effect between the ECM and antimode is at the origin of the double-peak structure.
- Finally, we checked that this double-peak structure does not only arise from the polarization interplay in VCSEL but is rather generic to external-cavity laser diode. To do so, we simulate a single-mode and single round-trip LK model and verified that the double-peak structure can also be retrieved. The genericity of this phenomenon is also confirmed by many reports from the literature as discussed in Section 2.2.4. We have brought here an explanation for their observations.
- **Perspectives** : In this chapter, we highlighted the role of the polarization inter-

play on the overall dynamic of VCSELs mainly in their correlation properties. As shown in Ref. [134], the gain anisotropy has a considerable impact on the type of LFF observed *i.e.* on the polarization correlation properties. In addition, Panajotov *et al.* [214] suggested an experiment where the use of a strain on a VCSEL may dramatically alter its polarization behavior. Hence, it would be interesting to study such system in the framework of this chapter *i.e.* by inducing a switch of LFF type when varying the strain strength. Furthermore, being able to drive the polarization interplay would be interesting in reservoir computing applications as shown in the work of *Ir. Jeremy Vatin et al.* (to be published) where an external-cavity VCSEL is used as the non-linear oscillator of the reservoir.

In **Chapter 3**, we investigated the ability of a VCSEL to generate Rogue Waves (RW) or Extreme Events (EE) from its polarization dynamics in LFF regime.

- First, we reminded the historical background of RW in oceanography. RWs are unusually huge waves that spontaneously arises from a relatively calm sea without obvious warning. Since the XXth century, records of RW have become more and more numerous and might sometimes be dangerous for ships and oil platforms. Since then, many studies attempted to explain the physical origin of such monstrous phenomenon. One promising way to understand RWs has been found to be with optical experiment from a practical point of view and from its close analogy with wave propagation in oceans [172]. In addition, although a good comprehension of the underlying physics of RW is of great interest for oceanography, its has also found some interest in modern telecommunication systems [182] which has also motivated our study.
- Among the studies of RW in optics, some groups have focused on RW generation in the output power of a laser diode under different configurations. However, none of them has ever looked at the multimode effects on the RW generation rate. In our study, we brought another viewpoint on the field by analyzing the RW generation rate in the total output power of a laser showing simultaneously dynamics in its two orthogonal polarizations and compared the multimode case to the monomode case.

- Our study relies on the same configuration as in Chapter 2 *i.e.* a VCSEL subjected to an isotropic optical feedback modeled by the SFM rate equations. First, we identified two types of RWs : scalar and vectorial EEs. Scalar EEs are EEs in the total output power provided by solely one of the two polarizations while vectorial EEs are provided simultaneously by the two polarizations. In the first case, the EEs is linearly polarized while in the second it is elliptically polarized.
- In order to confirm that our measurements of EEs are consistent with usual observations of RWs, we checked that their intensity and temporal distributions match those in oceanography. We first observed a deviation of the peak intensity (*i.e.* the wave elevation) from a purely Gaussian law. The deviation is mainly observed at high peak intensity as observed in several reports of oceanographic RWs. In addition, as the feedback strength increases, the number of intense events grows. Next, we analyzed the temporal partition of the EEs by looking at the waiting-times between successive events. The statistics reveal one peculiar feature induced by our delayed system. Indeed, it shows that part of the event occurrences are randomly distributed in time as expected from the oceanographic point of view but also that another part is correlated to each other. A closer look at the temporal signal shows trains of EEs separated by the delay of the external cavity.
- Next, we compared the generation rate of EEs between a two-polarization emission scenario (multimode) and a single polarization emission case (monomode). We observed that in the multimode case, when increasing the feedback strength, the ratio between the number of EEs and the number of peaks in the total intensity quickly saturated which differs from previous studies of laser diode dynamics. Indeed, in the monomode case, when increasing the feedback strength, we observed a constant increase of the EEs generation rate. In the multimode case, the saturation is explained from the polarization competition. Indeed, in that case, both polarization competes for the gain in the active medium inducing mainly an anti-correlated dynamic between them. This anti-correlation makes the total output power oscillate around its mean value hence compensating the increase of high intensity events when increasing the feedback strength. Therefore, a saturation is observed. On the contrary, in monomode

scenario, the total intensity only bursts from its quiescent state (from the noise floor) independently of the feedback strength inducing a constant growth of the EEs generation rate. As a result, the two-polarization emission scenario is an additional control parameter that can drive the generation rate of EEs.

- **Perspectives** : The most straightforward perspective of this chapter is to confirm experimentally our numerical results. However, the main challenge is to measure the polarization dynamics at high bandwidth and very low mean power. Indeed, each EEs turns out to last less than 100 ps (FWHM) and the LFF regime is mainly observed close to the threshold current of the laser. Using the VCSEL of Chapter 2, we typically have less than 10 μ W in each polarization which is too weak to be measured with our 12.5 GHz photodiode. As a result, a more sensitive detector is required such as a streak camera.

In **Chapter 4**, we investigated the generation of square-wave (SW) modulation accompanied by fast oscillations at frequency going beyond the relaxation oscillation frequency f_{RO} of a laser diode subjected to a polarization-rotated optical feedback (PROF).

- EELs are known to be very stable in term of light-polarization emission. Because of their geometrical configuration, EELs usually emit in a linear polarization parallel to the active-medium transverse profile. Contrary to VCSEL, isotropic optical feedback generally results in the destabilization of this polarization while the orthogonal linear polarization remains greatly depressed. First, we reminded in this chapter several techniques used to generate dynamics in the depressed mode often called *TM-mode* which consists on using polarization dependent components in the external cavity such as polarizers and polarization-rotating components.
- Next, we focused on the PROF configuration where the dominant mode (TE) is fed back inside the laser along the TM direction while the emitted TM mode is filtered by a polarizer. This setup is known to produce SW modulation in both modes at frequency close to half the external cavity frequency. We first reported the whole experimental bifurcations that lead to such SW regime going from oscillation at f_{RO} to more exotic waveforms when increasing the feedback

strength. Interestingly, we observed an intermediate regime where the TM mode exhibits SW modulation with high-speed oscillations of its plateaus at an unknown frequency.

- We experimentally analyzed the evolution of the oscillation of plateaus frequency when varying the experimental parameters and observed three main features : 1/ this frequency is always higher than f_{RO} , 2/ it increases with the feedback and the injection current, 3/ it doesn't scale with the delay.
- To understand the origin of such dynamic and its dependency of the system parameters, we numerically implemented a 2-polarization LK model that accounts for the PROF feedback. While the pure SW regime is obtained for mid to large value of TE/TM gain ratio, SW regime with oscillation can be unlocked at high value of gain ratio. Our simulations confirmed that the frequency of the oscillation on plateau is always higher than f_{RO} , increases with the current and does not vary with the delay. Further study on the dependency of this frequency to the system parameter shows that the higher the pumping current is, larger is the span of feedback strength where this regime is observed.
- Finally, we demonstrated analytically that these oscillations appear from a Hopf bifurcation on the initially steady-static upper plateau of the SW modulation. After few semi-empirical approximations, we showed that the frequency of plateau is proportional to f_{RO} but also grows with the TE/TM gain ratio and the linewidth enhancement factor.
- **Perspectives** : In this Chapter, we reported on a peculiar dynamics exhibited by an EEL under a PROF configuration. Experimentally, the observation of the fast oscillations on SW plateaus is confined in a very narrow span of feedback ratio. In order to lengthen this region, two parameters have to be changed : by increasing the injection current and/or the TE/TM gain ratio. For the first case, we drove our laser at almost the maximum injection current but still struggle to increase the region of feedback ratio where this dynamic is observed. For the second case, it would be interesting to try the same experiment with a VCSEL known for their high polarization-competition. First numerical investigations using SFM equations show that similar dynamics can be obtained. In addition, as the oscillation frequency on plateau increases with f_{RO} , we expect very

high-speed oscillations. However, the main drawback is to be able to detect the dynamic at very high-bandwidth (higher than 20 GHz) with a maximum output power of about 0.5 – 1 mW on average in each polarization.

In **Chapter 5**, we investigated the ability of a laser diode to generate virtual chimera states from its polarization dynamics.

- Chimera states are a new paradigm in the science of high-dimension network. It refers to the coexistence of synchronous (coherence) and asynchronous (incoherence) clusters in large network of identical oscillators. In the first part of the chapter, we introduced the historical background of chimera state in general physics from its prediction in 2002 to its first experimental observations in 2012. However, although it has been extensively studied, experimental observations of chimera states remain scarce.
- Reports of chimera states concern a large variety of scientific fields going from chemistry to mechanics showing the universality of chimerical behavior in Nature. Experimental observations of chimera states have also been conducted in optical systems in two different experiments. In the one hand, Viktorov *et al.* [236] study the emergence of chimera state in a mode-locked laser where the elemental oscillators are the emitted photons. In their experiment, chimera state arises from the phase-locking and phase-unlocking of groups of photons. In the other hand, Larger *et al.* [216] introduced the concept of virtual chimera in a delayed system. In their study, the network of oscillators is created from the space-time analogy of delayed systems [243] : a virtual space is built from periodic slices of the time signal. They showed that delayed systems are reproduce many chimera-state mechanisms.
- In a second part of the chapter, we showed that a laser diode subjected to a PROF is capable of producing chimera states. More interestingly, the chimera states are observed in the polarization dynamics. Indeed, our PROF system generates periodic SW modulation of the orthogonal polarization modes (TE and TM) and for intermediate value of feedback strength, chaotic oscillations appear on the upper state of the SWs. Building-up a virtual space from the space-time analogy, we both observed experimentally and numerically a virtual chimera-

state where regions of chaotic (*resp.* quiescent) oscillations are analogous to asynchronous (*resp.* synchronous) behavior of oscillators.

- Next, we add a weak isotropic feedback to our system. The effect of this second delay is twofold : 1/ it unlocks more regions of coherence/incoherence and 2/ it drives and stabilizes the number of those clusters. We experimentally and numerically demonstrated the existence of 3 and 7 regions of coherence/incoherence also called 3-(7-)headed chimera-state.
- We also unveiled multi-stability in term of multi-headed chimera states. Indeed, experimentally, different solutions can be stabilized for identical parameters. Numerically, this multi-stability is demonstrated by initializing the simulations with different initial conditions. We also investigated the mechanisms involved in the transition between different solutions such as the death, the merging and the survival of chimera-head.
- **Perspectives :** The perspectives of this work are multiple. Indeed, first, one natural extension is to reproduce such experiment with VCSELs taking advantage of their polarization instabilities. In addition, as suggested in Chapter 4, SW modulation with oscillations on plateaus are expected to be easier to obtain with VCSEL rather than EELs. Second, it would be very challenging to study spatially extended system in which several laser diodes are coupled to each other through for example a global feedback as suggested in Ref. [254]. Finally, the non-linear dynamic exposed in this Chapter is also of interest in chaotic LIDAR (CLIDAR) applications. Indeed, extensive efforts have been made to produce periodic time-windows of chaotic oscillations as in Ref. [256] where the laser is periodically switched on and off by modulating the pump or in Ref. [73] where an acousto-optics modulator is used to periodically block the chaotic output light. Here, we propose a simple feedback setup that inherently produces such waveform.

RÉSUMÉ DE LA THÈSE

Au cours de cette thèse, nous avons exploré de nouveaux résultats expérimentaux, numériques et analytiques sur différentes configurations de diodes laser à cavité externes. Nous nous sommes concentrés sur la dynamique de polarisation créée par un délai pour sa capacité à émuler la complexité des dynamiques induites. Le but de ce chapitre est de résumer les principales découvertes et d'y souligner les perspectives de recherche qui en découlent.

Résumé, contributions et perspectives

Ce manuscrit peut être divisé en deux macro parties : les chapitres 2 et 3 dans lesquels nous avons étudié principalement la dynamique de VCSEL sujet à une rétroaction optique isotropique et les chapitres 4 et 5 où nous nous sommes concentrés sur les diodes lasers émettant par la tranche (EEL) sujets à une rétroaction optique à rotation de polarisation (PROF). Le changement de structure laser a été motivé par des limitations techniques (faible puissance optique des VCSEL et faible sensibilité des photodiodes rapides). Néanmoins, nous sommes convaincus que nos résultats sur les EELs peuvent également être obtenus avec des VCSELs -ce qui n'est pas toujours vrai dans l'autre sens-.

Dans le **Chapitre 2**, nous avons étudié la dynamique de polarisation et le spectre

RF d'un VCSEL sujet à une rétroaction optique principalement en régime de Low-Frequency Fluctuations (LFF).

- Premièrement, nous avons rappelé les origines des instabilités de polarisation observées dans les VCSELs sans perturbation. En effet, le comportement en polarisation des VCSEL diffère grandement de celui observé sur les EEL. Ceci est principalement dû à la différence en terme de structure semiconducteur. Alors que le profil transverse de la zone active dans les EEL induit des grandes pertes pour une des polarisations linéaires (LP), la géométrie circulaire des VCSEL ne peut, seule, favoriser l'émission d'un mode polarisation en particulier. Une étude plus approfondie de la structure cristallographique de la zone active est alors nécessaire pour comprendre les mécanismes de sélection de la polarisation. Ces derniers prennent en compte une analyse méticuleuse des gains et pertes pour chaque mode de polarisation à l'intérieur de la zone active qui varient avec le courant et la température. Néanmoins, la stabilité du mode de polarisation dominant reste souvent faible sur de grande plage de paramètre et des switching de polarisation sont souvent observés lorsque ces paramètres sont modifiés où lorsqu'une perturbation externe est appliquée telle qu'une rétroaction optique.
- Dans un second temps, nous avons introduit le modèle de San Miguel-Feng-Moloney (SFM), un ensemble d'équations d'évolution utilisé pour modéliser le comportement en polarisation des VCSEL. Ce modèle diffère d'un modèle plus classique appelé Lang-Kobayashi (LK) dans le sens où SFM considère 4 niveaux d'énergie incorporant des recombinaisons de spin. Nous avons également détaillé le modèle SFM étendu aux effets d'une rétroaction optique et avons introduit la notion de modes de cavité externe (ECM) et la notion d'antimode. Les ECM et les antimodes sont des solutions quiescentes de laser à cavité externe. Ils sont caractérisés par leur gain et leur fréquence optique. De plus, alors que les ECM sont des solutions stables et agissent tels des attracteurs du système, leurs analogues antimodes sont eux instables et déstabilisent le système.
- Par la suite, nous avons abordé le régime LFF dans les VCSEL sujets à une rétroaction optique. Ce régime est caractérisé par des dynamiques à plusieurs échelles de temps : une modulation à basse fréquence montrant des chutes

brusques de puissance aléatoirement dans le temps et une dynamique à hautes fréquences mixant la fréquence de cavité externe et la fréquence de relaxation du laser. Du aux instabilités de polarisation intrasèques des VCSEL, le régime LFF peut également être observé dans la dynamiques des deux polarisations. Ainsi deux types de LFF peuvent être observés : le Type-I où les deux modes sont corrélés à la fréquence LFF et les Type-II où ils y sont anti-corrélés. En étudiant le spectre RF des deux modes, nous avons observé une structure en double-pic inattendue autour de la région de fréquence de cavité externe. La position de la structure suit continuellement la position de la fréquence de cavité externe lorsque le délai est varié et la séparation fréquentielle entre les pics dépend du courant d'injection. Nos études expérimentales et numériques montre qu'alors que les modes de polarisation sont toujours anti-corrélés à la fréquence basse du double-pic, leur corrélation change sur la composante haute fréquence en fonction du type de LFF observé.

- L'origine de ce double-pic peut être expliquée en étudiant la trajectoire du système dans l'espace des phases. En régime LFF, la trajectoire est fortement attirée vers l'ECM le plus stable. Cependant, de temps en temps, elle peut s'approcher d'un antimode (instable) qui la repoussent brusquement au-loin dans l'espace des phases. En isolant la trajectoire autour de l'ECM le plus stable, le spectre RF ne montre uniquement que le pic de haute fréquence de la structure. En considérant en plus la trajectoire autour de l'antimode, le pic de basse fréquence commence à émerger. Ainsi, alors que l'attraction par l'ECM impose une certaine fréquence de résonance au pic de haute fréquence, l'antimode allonge la trajectoire créant ainsi une nouvelle fréquence de résonance à la basse fréquence. En conséquence, cet effet "push-pull" entre les ECM et les antismodes est à l'origine du double-pic.
- **Perspectives :** Dans ce chapitre, nous avons souligné le rôle de l'interaction entre polarisation sur le dynamique globales du VCSEL. Comme démontré dans la Ref. [134], l'anisotropie du laser a un rôle considérable dans la sélection du type de LFF observée *i.e.* sur les propriétés de corrélation entre polarisation. De plus, Panajotov *et al.* [214] ont suggéré une expérience où l'utilisation d'une contrainte mécanique sur un VCSEL peut modifier le comportement en polarisation de ce dernier. Ainsi, il serait intéressant d'étudier un tel laser dans

le contexte de ce chapitre *i.e.* en sélectionnant expérimentalement le type de LFF recherché par une modification de la contrainte mécanique.

Dans le **Chapitre 3**, nous avons étudié la capacité d'un VCSEL à générer des ondes scélérates, ou Rogue Wave (RW) ou Extreme Events (EE), depuis la dynamique de polarisation en régime LFF.

- Dans un premier temps, nous avons rappelé la chronologie historique derrière le concept de RW en océanographie. Les RWs sont des vagues inhabituellement hautes qui émergent spontanément sur une mer relativement calme et sans signe précurseur. Depuis le XX^e siècle, des enregistrements de RW sont devenus de plus en plus nombreuses (grâce notamment à l'amélioration des technologies). Ces vagues peuvent, dans la plupart des cas être extrêmement dangereuses pour les navires et les plateformes pétrolières. Depuis, de nombreuses études ont tenté d'expliquer l'origine physique de ces phénomènes. Une manière prometteuse de comprendre les RWs est de passer par des expériences optiques de par l'aspect pratique et grâce à l'analogie très proche avec les physiques de propagations des vagues en océanographie [172]. De plus, bien que une compréhension de la physique sous-jacentes aux RW est d'un grand intérêt pour l'océanographie, elle est également très intéressante pour les systèmes de télécommunication modernes [182].
- Parmi les études de RW en optique, certains groupes se sont concentrés sur la génération de RW à partir de la puissance optique de diodes laser soumis à différentes configurations expérimentales. Néanmoins, aucune d'entre eux ne s'est penché sur l'aspect multimodes dans la génération de RW. Dans nos études, nous apportons un nouveau point de vue sur le sujet en analysant le taux de génération de RW dans la puissance totale du laser montrant simultanément des dynamiques dans les deux modes de polarisation. Nous comparons également nos résultats en multimode avec des observations usuelles faites en monomode.
- Notre étude s'appuie sur la même configuration expérimentale que le Chapitre 2, c'est-à-dire un VCSEL soumis à une rétroaction optique isotrope pouvant être modélisé par le même jeu d'équation SFM. Dans un premier temps, nous

avons identifié deux types de RWs : scalaire et vectoriel. Les RW scalaires sont des RW dans la puissance totale provenant uniquement d'un des deux modes de polarisation alors que les RW vectorielles proviennent eux simultanément des deux modes de polarisation. Dans le premier cas, ces RWs sont linéairement polarisées alors que dans le second, ils sont polarisés elliptiquement.

- Afin de confirmer que nos mesures de RWs sont consistantes avec les observations usuelles de RWs en océanographie, nous avons vérifié que les distributions d'intensités et d'occurrence temporelle correspondent à celles obtenues en océanographie. Nous avons observé une déviation de la distribution en intensité au niveau des hautes valeurs par rapport à une distribution purement Gaussienne, tendance usuellement observé dans l'étude de RW en océanographie. De plus, en augmentant de taux de rétroaction, le nombre d'évènement intensité augmente. Par la suite, nous avons analysé la séparation temporelle en RWs successives. La statistique révèle une tendance spécifique à notre système à retard. En effet, elle montre qu'une partie des évènements sont distribués de manière aléatoire dans le temps (ce qui est usuellement observé en océanographie) mais qu'il existe également des évènements qui sont corrélés entre eux dans le temps. Une observation fine des traces temporelles montre des trains de RWs séparés d'une valeur de délai.
- Enfin, nous avons comparé le taux de génération de RWs entre le scénario multimode (2 polarisations) et le scénario monomode (1 polarisation). Nous avons observé que dans le cas multimode, lorsque le taux de rétroaction augmente, le ratio entre le nombre de RWs et le nombre total de pics dans la puissance totale sature; ce qui diffère des études précédents sur la dynamique de laser "monomode". En effet, dans le cas monomode, lorsque le taux de rétroaction augmente, le taux de génération de RWs augmente constamment. Dans le cas multimode, la saturation est expliqués par la compétition modale. En effet, dans ce cas, les deux polarisations se partagent le gain dans la zone active entraînant surtout des dynamiques anti-corrélés entre elles. Cette anti-corrélations fait osciller la puissance totale autour de sa valeur moyenne, ce qui compense l'augmentation du nombre d'évènement intenses lorsque le taux de rétroaction augmente. Ainsi, une saturation est observée. Au contraire, dans le cas monomode, l'intensité totale fluctue à partir du niveau de bruit (quasiment

à partir d'une puissance nulle) indépendamment du taux de rétroaction. Ainsi, nous observons dans ces cas-là une augmentation constante de taux de génération de RWs. En conséquence, une émission multimode est un paramètre de contrôle supplémentaire sur le taux de génération de RWs.

- **Perspectives :** La perspective la plus évidente pour cette partie est de confirmer expérimentalement nos prédictions numériques. Cependant, le challenge est de mesurer des dynamiques de polarisation à très hautes fréquences et avec une puissance optique très faible. En effet, chaque RW dure moins de 100 ps (FWHM) et le régime LFF est observé très proche du seuil d'émission laser *i.e.* à très basse puissance. En utilisant le VCSEL du chapitre 2, nous avons environ 10 μ W dans chaque polarisation ce qui est extrêmement faible pour notre photodiode 12.5 GHz.

Dans le **Chapitre 4**, nous avons étudié la génération d'onde carrée (SW) accompagnée d'oscillations rapides et des fréquences dépassant la fréquence de relaxation f_{RO} d'une diode laser soumise à une rétroaction optique à rotation de polarisation (PROF)

- Les EELs sont connus pour être très stables en terme d'état de polarisation de la lumière. À cause de leur géométrie, les EELs émettent généralement une polarisation linéaire parallèle au profil transverse de la zone active. Contrairement aux VCSELs, un feedback isotropique résulte généralement sur une déstabilisation de cette polarisation alors que la polarisation orthogonale reste grandement dépréviée. Dans un premier temps, nous avons rappelé dans ce chapitre quelques techniques utilisées pour générer des dynamiques dans le mode déprécié aussi appelé *TM-mode* qui consistent en l'utilisation d'éléments sensibles à la polarisation dans la cavité externe tels que des polariseurs et des rotateurs de polarisations.
- Par la suite, nous nous concentrons sur la configuration PROF où le mode dominant (TE) est réinjecté dans le laser suivant la direction TM alors que le mode TM est filtré par un polariseur. Cette configuration est connue pour produire des modulations SW dans chaque mode à une fréquence proche de la moitié de la fréquence de cavité externe. Nous reportons d'abord les bifurcations

observées expérimentalement menant à de telles oscillations carrées allant d'oscillations à f_{RO} à des formes d'onde plus exotiques lorsque l'on augmente le taux de rétroaction. Nous observons également un régime intermédiaire où le mode TM exhibe des modulations SW accompagnées d'oscillations très hautes fréquences sur ces plateaux à une fréquence inconnue.

- Nous analysons expérimentalement l'évolution de la fréquence d'oscillation sur plateaus lorsque les paramètres expérimentaux sont variés. Nous avons observé trois résultats majeurs : 1/ cette fréquence est toujours supérieure à f_{RO} , 2/ elle augmente lorsque la rétroaction et le courant d'injection augmentent, 3/ elle ne varie pas avec la valeur du délai.
- Afin de comprendre l'origine d'une telle dynamique et sa dépendance avec les paramètres du système, nous avons implémenté numériquement un modèle LK comprenant les 2 polarisations ainsi que la rétroaction PROF. Alors que le régime SW s'obtient pour des valeurs de ratio de gain TE/TM moyenne et grande, le régime SW avec oscillations sur plateau s'observe pour de grande valeur de ratio de gain. Nos simulations confirment que la fréquence de ces oscillations sur plateau est toujours supérieure à f_{RO} , augmente avec le courant et ne varie pas avec le délai.
- Enfin, nous démontrons analytiquement que ces oscillations apparaissent à partir d'une bifurcation de Hopf sur le plateau haut initialement quiescent. Après quelques approximations semi-empiriques, nous avons montré que la fréquence sur plateau est proportionnelles à f_{RO} mais aussi à des paramètres intrinsèques du laser telles que la ratio de gain TE/TM et le facteur α .
- **Perspectives** : Dans ce chapitre, nous avons montré une dynamique particulière d'une EEL sujet à une rétroaction PROF. Expérimentalement, l'observation d'oscillations rapides sur les plateaux des SW est confinée dans une région très fine de taux de rétroaction. Afin d'agrandir cette région, deux paramètres doivent être variés : augmenter le courant d'injection et/ou augmenter le ratio de gain TE/TM. Pour le premier cas, nous avons injecté notre laser très proche du courant maximal; néanmoins la région de rétroaction où la dynamique est observée reste fine. Pour le second cas, il serait intéressant d'essayer la même expérience avec un VCSEL, connu pour avoir un gain très proche entre le mode

TE et TM. Nos premiers résultats numériques sur VCSEL utilisant le modèle SFM montre des dynamiques très similaires. De plus, puisque la fréquence sur plateau augmente avec f_{RO} , nous nous attendons à des fréquences extrêmement élevées avec un VCSEL. Néanmoins, le principal inconvénient est d'être capable de mesurer une telle dynamique avec une bande passante très élevée (supérieur à 20 GHz) et avec une puissance maximum comprise entre 0.5 – 1 mW en moyenne dans chaque polarisation.

Dans le **Chapitre 5**, nous avons étudié la capacité d'une diode laser à générer des états chimériques virtuels depuis ses dynamiques de polarisation.

- Les états chimériques sont un nouveau paradigme dans la science des réseaux de très hautes dimensions. Ils font référence à la coexistence entre groupes synchrones (cohérents) et asynchrones (incohérents) dans un réseau d'oscillateur identiques. Dans une première partie de ce chapitre, nous avons introduit l'état de l'art des états chimériques depuis leur prédiction en 2002 à leur première observation en 2012. Néanmoins, bien que les états chimériques ont été largement étudiés depuis, les observations expérimentales restent rares.
- Les observations d'états chimériques concernent une très grande variété de domaines scientifiques allant de la chimie à la mécanique démontrant l'universalité des comportements chimériques dans la Nature. Les observations expérimentales d'états chimériques ont également été conduites dans des systèmes optiques dans deux expériences différentes. Viktorov *et al.* [236] ont étudié l'émergence de ces états dans des lasers "mode-locked" où les oscillateurs élémentaires sont les photons eux-mêmes. Dans leur expérience, les états chimériques proviennent de groupes verrouillés et non-verrouillés en phase. Dans l'expérience de Larger *et al.* [216], ils introduisent le concept de chimères virtuelles dans un système à retard. Dans leur étude, le réseau d'oscillateurs est créé depuis une analogie spatio-temporelle entre systèmes à retard et systèmes spatialement étendus [243]. Un espace virtuel est construit à partir de coupes périodiques du signal temporel. Ils montrent qu'un système à retard peuvent reproduire plusieurs mécanismes liés aux états chimériques.
- Dans une seconde partie de ce chapitre, nous avons montré qu'une diode laser sujet à une rétroaction PROF est capable de produire des états chimériques. De

manière intéressantes, les états chimériques sont observés dans la dynamique de polarisation. En effet, notre système PROF génère des modulation SW périodique et pour des valeurs intermédiaires de rétroaction, des oscillations chaotiques apparaissent sur le plateau haut de la SW. En construisant l'espace virtuel sus-mentionné, nous observons expérimentalement et numériquement un état chimérique virtuel où les régions de chaos (*resp.* quiescence) sont analogues aux régions asynchrones (*resp.* synchrones) entre oscillateurs.

- Par la suite, nous ajoutons une rétroaction isotropique très faible au système. L'effet de ce deuxième retard est dual : 1/ il permet de débloquent plus de régions de cohérence/incohérence et 2/ il contrôle et stabilise le nombre de ces groupes. Nous avons démontré expérimentalement et numériquement l'existence de 3 et 7 régions de cohérence/incohérence aussi appelées états chimériques à 3 et 7 têtes.
- Nous avons également démontré une multi-stabilité en terme de nombre de têtes. En effet, expérimentalement, différentes solutions peuvent être stabilisées pour des paramètres identiques. Numériquement, cette multi-stabilité est démontré en initialisant les simulation avec différentes conditions initiales. Nous avons également analysé les mécanismes en jeu lors de transitions entre différentes solutions tels que la mort, la fusion et la survie de têtes chimériques.
- **Perspectives** : Les perspectives de ce travail sont multiples. En effet, dans un premier temps, une extension serait de reproduire cette expérience avec un VCSEL bénéficient ainsi de ses instabilités de polarisation. De plus, comme suggéré dans le Chapitre 4, les modulations SW avec oscillations sur plateaus sont plus facilement générées avec un VCSEL qu'avec un EEL. Deuxièmement, il serait extrêmement challenging d'étudier la génération d'états chimériques sur un système spatialement étendu fait de multiples lasers interconnectés avec par exemple une rétroaction globales comme suggéré dans la Ref. [254]. Enfin, la dynamique non-linéaire exposée dans ce chapitre peut également être utile pour les applications de LIDAR chaotiques. En effet, beaucoup d'efforts ont été porté vers la génération de fenêtres périodiques d'oscillations chaotiques et d'états éteints (puissance nulle) comme par exemple dans le Ref. [256] où le laser est périodiquement allumé puis éteint par une source de courant modulé

externe ou dans la Ref. [73] où un modulateur acousto-optique est utilisé pour bloquer périodiquement une lumière chaotique. Ici, nous proposons un système à rétroaction relativement simple capable de produire seul une telle forme d'onde

BIBLIOGRAPHY

- [1] Fabien Bretenaker and Nicolas Treps.
Laser: 50 years of discoveries.
World Scientific, 2014.
- [2] C.H. Twones.
How the Laser Happened.
Oxford University Press, 1999.
- [3] James P Gordon, Herbert J Zeiger, and Charles H Townes.
Molecular microwave oscillator and new hyperfine structure in the microwave spectrum of n h 3.
Physical Review, 95(1):282, 1954.
- [4] James P Gordon, Herbert J Zeiger, and Charles H Townes.
The maser—new type of microwave amplifier, frequency standard, and spectrometer.
Physical Review, 99(4):1264, 1955.
- [5] Arthur L Schawlow and Charles H Townes.
Infrared and optical masers.
Physical Review, 112(6):1940, 1958.
- [6] Theodore H Maiman et al.
Stimulated optical radiation in ruby.
Nature, 187:493–494, 1960.
- [7] Ali Javan, William R Bennett Jr, and Donald R Herriott.
Population inversion and continuous optical maser oscillation in a gas discharge containing a he-ne mixture.

BIBLIOGRAPHY

- Physical Review Letters*, 6(3):106, 1961.
- [8] Robert N Hall, Gunther E Fenner, JD Kingsley, TJ Soltys, and RO Carlson.
Coherent light emission from gaas junctions.
Physical Review Letters, 9(9):366, 1962.
- [9] Albert Einstein.
Strahlungs-emission und-absorption nach der quantentheorie.
Verh. Deutsch. Phys. Gesell., 18:318–323, 1916.
- [10] Albert Einstein.
Zur quantentheorie der strahlung.
Mittl. Phys. Gesell. Zurich, 18:47–62, 1916.
- [11] George Horace Brooke Thompson.
Physics of semiconductor laser devices.
Chichester, Sussex, England and New York, Wiley-Interscience, 1980. 572 p.,
1980.
- [12] Herbert Kroemer.
A proposed class of hetero-junction injection lasers.
Proceedings of the IEEE, 51(12):1782–1783, 1963.
- [13] Haruhisa Soda, Ken-ichi Iga, Chiyuki Kitahara, and Yasuharu Suematsu.
Gainasp/inp surface emitting injection lasers.
Japanese Journal of Applied Physics, 18(12):2329, 1979.
- [14] K Iga and HE Li.
Vertical-cavity surface-emitting laser devices.
Springer, 2003.
- [15] Mutsuo Ogura, Wei Hsin, Ming-Chiang Wu, Shyh Wang, John R Whinnery,
SC Wang, and Jane J Yang.
Surface-emitting laser diode with vertical gaas/gaalas quarter-wavelength
multilayers and lateral buried heterostructure.
Applied physics letters, 51(21):1655–1657, 1987.

-
- [16] JL Jewell, A Scherer, SL McCall, Yong-Hee Lee, S Walker, JP Harbison, and LT Florez.
Low-threshold electrically pumped vertical-cavity surface-emitting micro-lasers.
Electronics Letters, 25(17):1123–1124, 1989.
- [17] Krassimir Panajotov, Boris Ryvkin, Jan Danckaert, Michael Peeters, Hugo Thienpont, and Irina Veretennicoff.
Polarization switching in vcsel's due to thermal lensing.
IEEE Photonics Technology Letters, 10(1):6–8, 1998.
- [18] G Verschaffelt, K Panajotov, J Albert, B Nagler, M Peeters, J Danckaert, I Veretennicoff, and H Thienpont.
Polarisation switching in vertical-cavity surface-emitting lasers: from experimental observations to applications.
OPTOELECTRONICS REVIEW, (3):257–268, 2001.
- [19] MC Cox, NJ Copner, and B Williams.
High sensitivity precision relative intensity noise calibration standard using low noise reference laser source.
IEE Proceedings-Science, Measurement and Technology, 145(4):163–165, 1998.
- [20] Alexei Baranov and Eric Tournie.
Semiconductor Lasers: Fundamentals and Applications.
Elsevier, 2013.
- [21] Charles K Kao.
Optical fiber systems: technology, design, and applications.
McGraw-Hill New York, 1982.
- [22] Emmanuel Desurvire, Jay R Simpson, and PC Becker.
High-gain erbium-doped traveling-wave fiber amplifier.
Optics Letters, 12(11):888–890, 1987.
- [23] Guillaume Labroille, Bertrand Denolle, Pu Jian, Philippe Genevieux, Nicolas Treps, and Jean-François Morizur.

BIBLIOGRAPHY

- Efficient and mode selective spatial mode multiplexer based on multi-plane light conversion.
Optics express, 22(13):15599–15607, 2014.
- [24] 10 pb/s: Cailabs’ multiplexer helps achieve a new fiber-capacity world record over a multimode fiber.
http://www.cailabs.com/wp-content/uploads/2017/10/20170928_PR-CAILabs_World-Record-KDDI.pdf.
Accessed: 2018-07-13.
- [25] Genevieve Gariepy, Francesco Tonolini, Robert Henderson, Jonathan Leach, and Daniele Faccio.
Detection and tracking of moving objects hidden from view.
Nature Photonics, 10(1):23–26, 2016.
- [26] Steven H Strogatz and Donald E Herbert.
Nonlinear dynamics and chaos.
Medical Physics-New York-Institute of Physics, 23(6):993–995, 1996.
- [27] Edward N Lorenz.
Deterministic nonperiodic flow.
Journal of the atmospheric sciences, 20(2):130–141, 1963.
- [28] Tien-Yien Li and James A Yorke.
Period three implies chaos.
The American Mathematical Monthly, 82(10):985–992, 1975.
- [29] Hermann Haken.
Analogy between higher instabilities in fluids and lasers.
Physics Letters A, 53(1):77–78, 1975.
- [30] H Haken and H Sauermann.
Nonlinear interaction of laser modes.
Zeitschrift für Physik, 173(3):261–275, 1963.
- [31] H Haken.
Theory of intensity and phase fluctuations of a homogeneously broadened laser.

- Zeitschrift für Physik*, 190(3):327–356, 1966.
- [32] FT Arecchi, GL Lippi, GP Puccioni, and JR Tredicce.
Deterministic chaos in laser with injected signal.
Optics communications, 51(5):308–314, 1984.
- [33] Jorge R Tredicce, Fortunato Tito Arecchi, Gian Luca Lippi, and Gian Piero Puccioni.
Instabilities in lasers with an injected signal.
JOSA B, 2(1):173–183, 1985.
- [34] CO Weiss, W Klische, PS Ering, and M Cooper.
Instabilities and chaos of a single mode nh₃ ring laser.
Optics communications, 52(6):405–408, 1985.
- [35] EHM Hogenboom, W Klische, CO Weiss, and A Godone.
Instabilities of a homogeneously broadened laser.
Physical review letters, 55(23):2571, 1985.
- [36] L Casperson.
Spontaneous coherent pulsations in laser oscillators.
IEEE Journal of Quantum Electronics, 14(10):756–761, 1978.
- [37] CO Weiss and H King.
Oscillation period doubling chaos in a laser.
Optics Communications, 44(1):59–61, 1982.
- [38] CO Weiss, A Godone, and A Olafsson.
Routes to chaotic emission in a cw he-ne laser.
Physical Review A, 28(2):892, 1983.
- [39] Marc Sciamanna and K Alan Shore.
Physics and applications of laser diode chaos.
Nat. Photonics, 9(3):151–162, 2015.
- [40] Chang-Hee Lee, Tae-Hoon Yoon, and Sang-Yung Shin.
Period doubling and chaos in a directly modulated laser diode.
Applied Physics Letters, 46(1):95–97, 1985.

- [41] YC Chen, HG Winful, and JM Liu.
Subharmonic bifurcations and irregular pulsing behavior of modulated semiconductor lasers.
Applied Physics Letters, 47(3):208–210, 1985.
- [42] M Sciamanna, A Valle, P Megret, M Blondel, and K Panajotov.
Nonlinear polarization dynamics in directly modulated vertical-cavity surface-emitting lasers.
Physical Review E, 68(1):016207, 2003.
- [43] TB Simpson, JM Liu, A Gavrielides, V Kovanis, and PM Alsing.
Period-doubling route to chaos in a semiconductor laser subject to optical injection.
Applied Physics Letters, 64(26):3539–3541, 1994.
- [44] Sebastian Wieczorek, Bernd Krauskopf, Thomas Backer Simpson, and Daan Lenstra.
The dynamical complexity of optically injected semiconductor lasers.
Physics Reports, 416(1-2):1–128, 2005.
- [45] Ignace Gatara, Marc Sciamanna, Jordi Buesa, Hugo Thienpont, and Krassimir Panajotov.
Nonlinear dynamics accompanying polarization switching in vertical-cavity surface-emitting lasers with orthogonal optical injection.
Applied Physics Letters, 88(10):101106, 2006.
- [46] Florian Denis-le Coarer, Ana Quirce, Pablo Pérez, Angel Valle, Luis Pesquera, Marc Sciamanna, Hugo Thienpont, and Krassimir Panajotov.
Injection locking and polarization switching bistability in a 1550 nm vcsel subject to parallel optical injection.
IEEE Journal of Selected Topics in Quantum Electronics, 23(6):1–10, 2017.
- [47] Atsushi Uchida, Tilmann Heil, Yun Liu, Peter Davis, and Tahito Aida.
High-frequency broad-band signal generation using a semiconductor laser with a chaotic optical injection.
IEEE journal of quantum electronics, 39(11):1462–1467, 2003.

- [48] Chih-Hao Chang, Lukas Chrostowski, and Connie J Chang-Hasnain.
Injection locking of vcsels.
IEEE J. Sel. Top. Quant., 9(5):1386–1393, 2003.
- [49] Martin Virte, Krassimir Panajotov, Hugo Thienpont, and Marc Sciamanna.
Deterministic polarization chaos from a laser diode.
Nature Photonics, 7(1):60, 2013.
- [50] TR Raddo, K Panajotov, B-HV Borges, and M Virte.
Strain induced polarization chaos in a solitary vcsel.
Scientific Reports, 7(1):14032, 2017.
- [51] R Tkach and AR Chraplyvy.
Regimes of feedback effects in 1.5- μm distributed feedback lasers.
Journal of Lightwave technology, 4(11):1655–1661, 1986.
- [52] F De Tomasi, E Cerboneschi, and E Arimondo.
Asymmetric pulse shape in the lff instabilities of a semiconductor laser with optical feedback.
IEEE journal of quantum electronics, 30(10):2277–2280, 1994.
- [53] Takuya Sano.
Antimode dynamics and chaotic itinerancy in the coherence collapse of semiconductor lasers with optical feedback.
Physical Review A, 50(3):2719, 1994.
- [54] GHM Van Tartwijk, AM Levine, and D Lenstra.
Sisyphus effect in semiconductor lasers with optical feedback.
IEEE Journal of Selected Topics in Quantum Electronics, 1(2):466–472, 1995.
- [55] T Heil, I Fischer, W Elsässer, and A Gavrielides.
Dynamics of semiconductor lasers subject to delayed optical feedback: The short cavity regime.
Physical Review Letters, 87(24):243901, 2001.
- [56] Andrzej Tabaka, Krassimir Panajotov, Irina Veretennicoff, and Marc Sciamanna.

- Bifurcation study of regular pulse packages in laser diodes subject to optical feedback.
Physical Review E, 70(3):036211, 2004.
- [57] Andrzej Tabaka, Michael Peil, Marc Sciamanna, Ingo Fischer, Wolfgang Elsäßer, Hugo Thienpont, Irina Veretennicoff, and Krassimir Panajotov. Dynamics of vertical-cavity surface-emitting lasers in the short external cavity regime: Pulse packages and polarization mode competition.
Physical Review A, 73(1):013810, 2006.
- [58] Andreas Karsaklian Dal Bosco, Delphine Wolfersberger, and Marc Sciamanna. Super-harmonic self-pulsations from a time-delayed phase-conjugate optical system.
Applied Physics Letters, 105(8):081101, 2014.
- [59] Emeric Mercier, Armelle Even, Elodie Mirisola, Delphine Wolfersberger, and Marc Sciamanna. Numerical study of extreme events in a laser diode with phase-conjugate optical feedback.
Phys. Rev. E, 91(4):042914, 2015.
- [60] Athanasios Gavrielides, Thomas Erneux, David W Sukow, Guinevere Burner, Taylor McLachlan, John Miller, and Jake Amonette. Square-wave self-modulation in diode lasers with polarization-rotated optical feedback.
Optics letters, 31(13), 2006.
- [61] Gaetan Friart, Lionel Weicker, Jan Danckaert, and Thomas Erneux. Relaxation and square-wave oscillations in a semiconductor laser with polarization rotated optical feedback.
Optics express, 22(6):6905–6918, 2014.
- [62] Alexis PA Fischer, Ole K Andersen, Mirvais Yousefi, Steven Stolte, and Daan Lenstra. Experimental and theoretical study of filtered optical feedback in a semiconductor laser.
IEEE journal of quantum electronics, 36(3):375–384, 2000.

- [63] Mirvais Yousefi and Daan Lenstra.
Dynamical behavior of a semiconductor laser with filtered external optical feedback.
IEEE Journal of Quantum Electronics, 35(6):970–976, 1999.
- [64] Cisco visual networking index: Forecast and methodology, 2016–2021.
<https://www.cisco.com/c/en/us/solutions/collateral/service-provider/visual-networking-index-vni/complete-white-paper-c11-481360.html>.
Accessed: 2018-07-15.
- [65] Sheng-Kai Liao, Wen-Qi Cai, Wei-Yue Liu, Liang Zhang, Yang Li, Ji-Gang Ren, Juan Yin, Qi Shen, Yuan Cao, Zheng-Ping Li, et al.
Satellite-to-ground quantum key distribution.
Nature, 549(7670):43, 2017.
- [66] Apostolos Argyris, Dimitris Syvridis, Laurent Larger, Valerio Annovazzi-Lodi, Pere Colet, Ingo Fischer, Jordi Garcia-Ojalvo, Claudio R Mirasso, Luis Pesquera, and K Alan Shore.
Chaos-based communications at high bit rates using commercial fibre-optic links.
Nature, 438(7066):343, 2005.
- [67] Louis M Pecora, Thomas L Carroll, Gregg A Johnson, Douglas J Mar, and James F Heagy.
Fundamentals of synchronization in chaotic systems, concepts, and applications.
Chaos: An Interdisciplinary Journal of Nonlinear Science, 7(4):520–543, 1997.
- [68] Rajarshi Roy and K Scott Thornburg Jr.
Experimental synchronization of chaotic lasers.
Physical Review Letters, 72(13):2009, 1994.
- [69] Claudio R Mirasso, Pere Colet, and Priscila García-Fernández.
Synchronization of chaotic semiconductor lasers: Application to encoded communications.
IEEE Photonics Technology Letters, 8(2):299–301, 1996.

- [70] Xiao Ai, Richard Nock, John G Rarity, and Naim Dahnoun.
High-resolution random-modulation cw lidar.
Applied optics, 50(22):4478–4488, 2011.
- [71] Fan-Yi Lin and Jia-Ming Liu.
Chaotic lidar.
IEEE journal of selected topics in quantum electronics, 10(5):991–997, 2004.
- [72] Fan-Yi Lin, Shiou-Yuan Tu, Chien-Chih Huang, and Shu-Ming Chang.
Nonlinear dynamics of semiconductor lasers under repetitive optical pulse injection.
IEEE Journal of Selected Topics in Quantum Electronics, 15(3):604–611, 2009.
- [73] Chih-Hao Cheng, Chih-Ying Chen, Jun-Da Chen, Da-Kung Pan, Kai-Ting Ting, and Fan-Yi Lin.
3d pulsed chaos lidar system.
Optics express, 26(9):12230–12241, 2018.
- [74] C Masoller and NB Abraham.
Low-frequency fluctuations in vertical-cavity surface-emitting semiconductor lasers with optical feedback.
Physical Review A, 59(4):3021, 1999.
- [75] Marc Sciamanna, K Panajotov, H Thienpont, I Veretennicoff, P Mégret, and M Blondel.
Optical feedback induces polarization mode hopping in vertical-cavity surface-emitting lasers.
Optics letters, 28(17):1543–1545, 2003.
- [76] Yanhua Hong, Jon Paul, Paul S Spencer, and K Alan Shore.
Optical feedback dependence of anticorrelation polarization dynamics in vertical-cavity surface-emitting lasers.
JOSA B, 23(11):2285–2290, 2006.
- [77] Y Mitsuhashi.
Polarization control of an antireflection-coated gaalas laser diode by an external optical feedback.

- Journal of Applied Physics*, 53(12):9200–9201, 1982.
- [78] WH Loh, Y Ozeki, and Chung L Tang.
High-frequency polarization self-modulation and chaotic phenomena in external cavity semiconductor lasers.
Applied Physics Letters, 56(26):2613–2615, 1990.
- [79] Gaetan Friart, Guy Verschaffelt, Jan Danckaert, and Thomas Erneux.
All-optical controlled switching between time-periodic square waves in diode lasers with delayed feedback.
Optics letters, 39(21):6098–6101, 2014.
- [80] Yoshiki Kuramoto and Dorjsuren Battogtokh.
Coexistence of coherence and incoherence in nonlocally coupled phase oscillators.
Nonlinear Phenom. Complex Syst., 5(4):380–385, 2002.
- [81] SA Blokhin, JA Lott, A Mutig, G Fiol, NN Ledentsov, MV Maximov, AM Nadochiy, VA Shchukin, and D Bimberg.
Oxide-confined 850 nm vcsels operating at bit rates up to 40 gbit/s.
Electronics Letters, 45(10):501–503, 2009.
- [82] K Drogemuller, D Kuhl, J Blank, M Ehlert, T Kracker, J Hohn, D Klix, V Plickert, L Melchior, I Schmale, et al.
Current progress of advanced high speed parallel optical links for computer clusters and switching systems.
In *Electronic Components & Technology Conference, 2000. 2000 Proceedings. 50th*, pages 1227–1235. IEEE, 2000.
- [83] Mitsuaki Shimizu, Fumio Koyama, and Kenichi Iga.
Polarization characteristics of mocvd grown gaas/gaalas cbh surface emitting lasers.
Japanese journal of applied physics, 27(9R):1774, 1988.
- [84] J Martin-Regalado, JLA Chilla, JJ Rocca, and P Brusenbach.
Polarization switching in vertical-cavity surface emitting lasers observed at constant active region temperature.

- Applied physics letters*, 70(25):3350–3352, 1997.
- [85] T Mukaihara, N Ohnoki, Y Hayashi, N Hatori, F Koyama, and K Iga.
Excess intensity noise originated from polarization fluctuation in vertical-cavity surface-emitting lasers.
IEEE Photonics Technology Letters, 7(10):1113–1115, 1995.
- [86] YC Chen and JM Liu.
Direct polarization switching in semiconductor lasers.
Applied Physics Letters, 45(6):604–606, 1984.
- [87] Testsuhiko Ikegami.
Reflectivity of mode at facet and oscillation mode in double-heterostructure injection lasers.
IEEE Journal of quantum electronics, 8(6):470–476, 1972.
- [88] Jan Haes, Bart Demeulenaere, Roel Baets, D Lenstra, TD Visser, and H Blok.
Difference between te and tm modal gain in amplifying waveguides: analysis and assessment of two perturbation approaches.
Optical and Quantum Electronics, 29(2):263–273, 1997.
- [89] MP Van Exter, AK Jansen van Doorn, and JP Woerdman.
Electro-optic effect and birefringence in semiconductor vertical-cavity lasers.
Physical Review A, 56(1):845, 1997.
- [90] AK Jansen van Doorn, MP Van Exter, and JP Woerdman.
Elasto-optic anisotropy and polarization orientation of vertical-cavity surface-emitting semiconductor lasers.
Applied physics letters, 69(8):1041–1043, 1996.
- [91] Giovanni Giacomelli, Francesco Marin, and Ivan Rabbiosi.
Stochastic and bona fide resonance: An experimental investigation.
Physical Review Letters, 82(4):675, 1999.
- [92] Kent D Choquette, Richard P Schneider, Kevin L Lear, and Ronald E Leibenguth.
Gain-dependent polarization properties of vertical-cavity lasers.
IEEE Journal of Selected Topics in Quantum Electronics, 1(2):661–666, 1995.

- [93] Maria Susana Torre and Cristina Masoller.
Dynamical hysteresis and thermal effects in vertical-cavity surface-emitting lasers.
IEEE Journal of Quantum Electronics, 46(12):1788–1794, 2010.
- [94] G Giacomelli, F Marin, M Gabrysch, KH Gulden, and M Moser.
Polarization competition and noise properties of vcsels.
Optics communications, 146(1-6):136–140, 1998.
- [95] Kent D Choquette, DA Richie, and RE Leibenguth.
Temperature dependence of gain-guided vertical-cavity surface emitting laser polarization.
Applied physics letters, 64(16):2062–2064, 1994.
- [96] JW Scott, SW Corzine, DB Young, and LA Coldren.
Modeling the current to light characteristics of index-guided vertical-cavity surface-emitting lasers.
Applied physics letters, 62(10):1050–1052, 1993.
- [97] J Talghader and JS Smith.
Thermal dependence of the refractive index of gaas and alas measured using semiconductor multilayer optical cavities.
Applied Physics Letters, 66(3):335–337, 1995.
- [98] A Valle, J Sarma, and KA Shore.
Spatial holeburning effects on the dynamics of vertical cavity surface-emitting laser diodes.
IEEE Journal of Quantum Electronics, 31(8):1423–1431, 1995.
- [99] A Valle, L Pesquera, and KA Shore.
Polarization behavior of birefringent multitransverse mode vertical-cavity surface-emitting lasers.
IEEE Photonics Technology Letters, 9(5):557–559, 1997.
- [100] D Vakhshoori, JD Wynn, GJ Zydzik, RE Leibenguth, MT Asom, K Kojima, and RA Morgan.

- Top-surface emitting lasers with 1.9 v threshold voltage and the effect of spatial hole burning on their transverse mode operation and efficiencies. *Applied physics letters*, 62(13):1448–1450, 1993.
- [101] B Ryvkin, K Panajotov, A Georgievski, J Danckaert, M Peeters, G Verschaffelt, H Thienpont, and I Veretennicoff.
Effect of photon-energy-dependent loss and gain mechanisms on polarization switching in vertical-cavity surface-emitting lasers. *JOSA B*, 16(11):2106–2113, 1999.
- [102] BS Ryvkin and AM Georgievskii.
Polarization selection in vcsels due to current carrier heating. *Semiconductors*, 33(7):813–819, 1999.
- [103] M San Miguel, Q Feng, and Jerome V Moloney.
Light-polarization dynamics in surface-emitting semiconductor lasers. *Physical Review A*, 52(2):1728, 1995.
- [104] Krassimir Panajotov and Franco Prati.
Polarization dynamics of vcsels.
In *VCSELs*, pages 181–231. Springer, 2013.
- [105] Martin Virte, Krassimir Panajotov, and Marc Sciamanna.
Bifurcation to nonlinear polarization dynamics and chaos in vertical-cavity surface-emitting lasers. *Physical Review A*, 87(1):013834, 2013.
- [106] Rihab Al-Seyab, Kevin Schires, Nadir Ali Khan, Antonio Hurtado, Ian D Henning, and Michael J Adams.
Dynamics of polarized optical injection in 1550-nm vcsels: theory and experiments. *IEEE Journal of Selected Topics in Quantum Electronics*, 17(5):1242–1249, 2011.
- [107] Angel Valle, Ignace Gatere, Krassimir Panajotov, and Marc Sciamanna.
Transverse mode switching and locking in vertical-cavity surface-emitting lasers subject to orthogonal optical injection.

-
- IEEE Journal of Quantum Electronics*, 43(4):322–333, 2007.
- [108] Florian Denis-le Coarer, Ana Quirce, Ángel Valle, Luis Pesquera, Marc Sciamanna, Hugo Thienpont, and Krassimir Panajotov.
Polarization dynamics induced by parallel optical injection in a single-mode vcsel.
Optics letters, 42(11):2130–2133, 2017.
- [109] NC Gerhardt, MY Li, H Jähme, H Höpfner, T Ackemann, and MR Hofmann.
Ultrafast spin-induced polarization oscillations with tunable lifetime in vertical-cavity surface-emitting lasers.
Applied Physics Letters, 99(15):151107, 2011.
- [110] María Susana Torre, Cristina Masoller, and Paul Mandel.
Transverse and polarization effects in index-guided vertical-cavity surface-emitting lasers.
Physical Review A, 74(4):043808, 2006.
- [111] Rainer Michalzik.
VCSELs: fundamentals, technology and applications of vertical-cavity surface-emitting lasers, volume 166.
Springer, 2012.
- [112] Martin Virte, Emeric Mercier, Hugo Thienpont, Krassimir Panajotov, and Marc Sciamanna.
Physical random bit generation from chaotic solitary laser diode.
Optics express, 22(14):17271–17280, 2014.
- [113] Jai-Ming Liu and Ying-Chin Chen.
Digital optical signal processing with polarization-bistable semiconductor lasers.
IEEE journal of quantum electronics, 21(4):298–306, 1985.
- [114] Takashi Mori, Yasuhiro Yamayoshi, and Hitoshi Kawaguchi.
Low-switching-energy and high-repetition-frequency all-optical flip-flop operations of a polarization bistable vertical-cavity surface-emitting laser.
Applied Physics Letters, 88(10):101102, 2006.

- [115] Hitoshi Kawaguchi, Takashi Mori, Yuuki Sato, and Yasuhiro Yamayoshi.
Optical buffer memory using polarization-bistable vertical-cavity surface-emitting lasers.
Japanese journal of applied physics, 45(9L):L894, 2006.
- [116] Igor Žutić, Jaroslav Fabian, and S Das Sarma.
Spintronics: Fundamentals and applications.
Reviews of modern physics, 76(2):323, 2004.
- [117] S Hallstein, JD Berger, M Hilpert, HC Schneider, WW Rühle, F Jahnke, SW Koch, HM Gibbs, G Khitrova, and M Oestreich.
Manifestation of coherent spin precession in stimulated semiconductor emission dynamics.
Physical Review B, 56(12):R7076, 1997.
- [118] Markus Lindemann, Tobias Pusch, Rainer Michalzik, Nils C Gerhardt, and Martin R Hofmann.
Demonstrating ultrafast polarization dynamics in spin-vcsels.
In *Vertical-Cavity Surface-Emitting Lasers XXII*, volume 10552, page 1055209.
International Society for Optics and Photonics, 2018.
- [119] Mantas Lukoševičius and Herbert Jaeger.
Reservoir computing approaches to recurrent neural network training.
Computer Science Review, 3(3):127–149, 2009.
- [120] Daniel Brunner, Miguel C Soriano, Claudio R Mirasso, and Ingo Fischer.
Parallel photonic information processing at gigabyte per second data rates using transient states.
Nature communications, 4:1364, 2013.
- [121] Lennert Appeltant, Miguel Cornelles Soriano, Guy Van der Sande, Jan Danckaert, Serge Massar, Joni Dambre, Benjamin Schrauwen, Claudio R Mirasso, and Ingo Fischer.
Information processing using a single dynamical node as complex system.
Nature communications, 2:468, 2011.
- [122] J Vatin, D Rontani, and M Sciamanna.

- Enhanced performance of a reservoir computer using polarization dynamics in vcsels.
Optics Letters, 49:4497–4500, 2018.
- [123] Apostolos Argyris, Evangellos Grivas, Michael Hamacher, Adonis Bogris, and Dimitris Syvridis.
Chaos-on-a-chip secures data transmission in optical fiber links.
Optics express, 18(5):5188–5198, 2010.
- [124] Takahisa Harayama, Satoshi Sunada, Kazuyuki Yoshimura, Jun Muramatsu, Ken-ichi Arai, Atsushi Uchida, and Peter Davis.
Theory of fast nondeterministic physical random-bit generation with chaotic lasers.
Physical review E, 85(4):046215, 2012.
- [125] Satoshi Sunada, Takahisa Harayama, Peter Davis, Ken Tsuzuki, Ken-ichi Arai, Kazuyuki Yoshimura, and Atsushi Uchida.
Noise amplification by chaotic dynamics in a delayed feedback laser system and its application to nondeterministic random bit generation.
Chaos: An Interdisciplinary Journal of Nonlinear Science, 22(4):047513, 2012.
- [126] Andreas Karsaklian Dal Bosco, Naoki Sato, Yuta Terashima, Shoma Ohara, Atsushi Uchida, Takahisa Harayama, and Masanobu Inubushi.
Random number generation from intermittent optical chaos.
IEEE Journal of Selected Topics in Quantum Electronics, 23(6):1–8, 2017.
- [127] U Zabit, OD Bernal, and T Bosch.
A self-mixing displacement sensor compensating parasitic vibration with a mems accelerometer.
In *Sensors, 2011 IEEE*, pages 1386–1389. IEEE, 2011.
- [128] FFM De Mul, MH Koelink, AL Weijers, Jan Greve, JG Aarnoudse, R Graaff, and ACM Dassel.
A semiconductor laser used for direct measurement of the blood perfusion of tissue.
IEEE transactions on biomedical engineering, 40(2):208–210, 1993.

- [129] Yanhua Hong, Paul S Spencer, and K Alan Shore.
Suppression of polarization switching in vertical-cavity surface-emitting lasers by use of optical feedback.
Optics letters, 29(18):2151–2153, 2004.
- [130] Salam Nazhan, Zabih Ghassemlooy, Krishna Busawon, and Asghar Gholami.
Investigation of polarization switching of vcsel subject to intensity modulated and optical feedback.
Optics & Laser Technology, 75:240–245, 2015.
- [131] CHL Quay, IZ Maxwell, and JA Hudgings.
Coherence collapse and redshifting in vertical-cavity surface-emitting lasers exposed to strong optical feedback.
Journal of Applied Physics, 90(12):5856–5858, 2001.
- [132] L Chrostowski, P Bala Subrahmanyam, Y Zhou, and CJ Chang-Hasnain.
Vcsel tolerance to optical feedback for inter-chip optical interconnects.
In *Semiconductor Laser Conference, 2004. Conference Digest. 2004 IEEE 19th International*, pages 113–114. IEEE, 2004.
- [133] M Giudici, S Balle, T Ackemann, S Barland, and Jorge R Tredicce.
Polarization dynamics in vertical-cavity surface-emitting lasers with optical feedback: experiment and model.
JOSA B, 16(11):2114–2123, 1999.
- [134] Marc Sciamanna, Cristina Masoller, Neal B Abraham, Fabien Rogister, Patrice M egret, and Michel Blondel.
Different regimes of low-frequency fluctuations in vertical-cavity surface-emitting lasers.
JOSA B, 20(1):37–44, 2003.
- [135] M Sondermann, H Bohnet, and T Ackemann.
Low-frequency fluctuations and polarization dynamics in vertical-cavity surface-emitting lasers with isotropic feedback.
Physical Review A, 67(2):021802, 2003.
- [136] AV Naumenko, NA Loiko, M Sondermann, and T Ackemann.

- Description and analysis of low-frequency fluctuations in vertical-cavity surface-emitting lasers with isotropic optical feedback by a distant reflector.
Physical Review A, 68(3):033805, 2003.
- [137] Yanhua Hong and K Alan Shore.
Influence of optical feedback time-delay on power-drops in vertical-cavity surface-emitting lasers.
IEEE journal of quantum electronics, 41(8):1054–1057, 2005.
- [138] C Henry and R Kazarinov.
Instability of semiconductor lasers due to optical feedback from distant reflectors.
IEEE Journal of Quantum Electronics, 22(2):294–301, 1986.
- [139] Jesper Mork, Bjarne Tromborg, and Jannik Mark.
Chaos in semiconductor lasers with optical feedback: Theory and experiment.
IEEE Journal of Quantum Electronics, 28(1):93–108, 1992.
- [140] Junji Ohtsubo.
Semiconductor lasers: stability, instability and chaos, volume 111.
Springer, 2012.
- [141] Ch Risch and C Voumard.
Self-pulsation in the output intensity and spectrum of gas-algaas cw diode lasers coupled to a frequency-selective external optical cavity.
Journal of Applied Physics, 48(5):2083–2085, 1977.
- [142] I Fischer, GHM Van Tartwijk, AM Levine, W Elsässer, E Göbel, and D Lenstra.
Fast pulsing and chaotic itinerancy with a drift in the coherence collapse of semiconductor lasers.
Physical review letters, 76(2):220, 1996.
- [143] T Ackemann, M Sondermann, A Naumenko, and NA Loiko.
Polarization dynamics and low-frequency fluctuations in vertical-cavity surface-emitting lasers subjected to optical feedback.
Applied Physics B, 77(8):739–746, 2003.

- [144] Markus Sondermann and Thorsten Ackemann.
Correlation properties and drift phenomena in the dynamics of vertical-cavity surface-emitting lasers with optical feedback.
Optics express, 13(7):2707–2715, 2005.
- [145] Joachim Sacher, Wolfgang Elsässer, and Ernst O Göbel.
Intermittency in the coherence collapse of a semiconductor laser with external feedback.
Physical review letters, 63(20):2224, 1989.
- [146] LN Langley, KA Shore, and J Mørk.
Dynamical and noise properties of laser diodes subject to strong optical feedback.
Optics letters, 19(24):2137–2139, 1994.
- [147] Pascal Besnard, Belhacem Meziane, KAMEL Ait-Ameur, and S Stephan.
Microwave spectra in external-cavity semiconductor lasers: Theoretical modeling of multipass resonances.
IEEE Journal of Quantum electronics, 30(8):1713–1722, 1994.
- [148] M Giudici, C Green, G Giacomelli, U Nespolo, and JR Tredicce.
Andronov bifurcation and excitability in semiconductor lasers with optical feedback.
Physical Review E, 55(6):6414, 1997.
- [149] MP Van Exter, RFM Hendriks, JP Woerdman, and CJ Van der Poel.
Explanation of double-peaked intensity noise spectrum of an external-cavity semiconductor laser.
Optics communications, 110(1-2):137–140, 1994.
- [150] Roy Lang and Kohroh Kobayashi.
External optical feedback effects on semiconductor injection laser properties.
IEEE journal of Quantum Electronics, 16(3):347–355, 1980.
- [151] Damien Rontani, Alexandre Locquet, Marc Sciamanna, David S Citrin, and Silvia Ortin.

- Time-delay identification in a chaotic semiconductor laser with optical feedback: a dynamical point of view.
IEEE Journal of Quantum Electronics, 45(7):879–1891, 2009.
- [152] Theodore Y Wu.
Long waves in ocean and coastal waters.
Journal of Engineering Mechanics, 107(EM3):501–522, 1981.
- [153] John W Miles.
On the generation of surface waves by shear flows.
Journal of Fluid Mechanics, 3(2):185–204, 1957.
- [154] Hiroo Kanamori.
Mechanism of tsunami earthquakes.
Physics of the earth and planetary interiors, 6(5):346–359, 1972.
- [155] Hajime Mase, Tomohiro Yasuda, and Nobuhito Mori.
Real-time prediction of tsunami magnitudes in osaka bay, japan, using an artificial neural network.
Journal of Waterway, Port, Coastal, and Ocean Engineering, 137(5):263–268, 2011.
- [156] Paul C Liu.
A chronology of freauqe wave encounters.
Geofizika, 24(1):57–70, 2007.
- [157] Frank Graziano.
The Millennial New World.
Oxford University Press on Demand, 1999.
- [158] Dennis Jerry and Wolff Glenn.
The Bird in the Waterfall: Exploring the Wonders of Water.
HarperCollins Publishers, 1996.
- [159] L Draper.
'freak' ocean waves.
Weather, 21(1):2–4, 1966.

BIBLIOGRAPHY

- [160] Efim Pelinovsky, Christian Kharif, et al.
Extreme ocean waves.
Springer, 2008.
- [161] Alfred R Osborne, Miguel Onorato, and Marina Serio.
The nonlinear dynamics of rogue waves and holes in deep-water gravity wave trains.
Physics Letters A, 275(5-6):386–393, 2000.
- [162] Christian Kharif, Efim Pelinovsky, and Alexey Slunyaev.
Rogue Waves in the Ocean.
Springer, 2009.
- [163] George Z Forristall.
On the statistical distribution of wave heights in a storm.
Journal of Geophysical Research: Oceans, 83(C5):2353–2358, 1978.
- [164] Leo H Holthuijsen.
Waves in oceanic and coastal waters.
Cambridge university press, 2010.
- [165] TAA Adcock, PH Taylor, S Yan, QW Ma, and PAEM Janssen.
Did the draupner wave occur in a crossing sea?
In *Proceedings of the Royal Society of London A: Mathematical, Physical and Engineering Sciences*, volume 467, pages 3004–3021. The Royal Society, 2011.
- [166] M Onorato, T Waseda, A Toffoli, L Cavaleri, O Gramstad, PAEM Janssen, T Kinoshita, Jaak Monbaliu, N Mori, AR Osborne, et al.
Statistical properties of directional ocean waves: the role of the modulational instability in the formation of extreme events.
Physical Review Letters, 102(11):114502, 2009.
- [167] Miguel Onorato, S Residori, U Bortolozzo, A Montina, and FT Arecchi.
Rogue waves and their generating mechanisms in different physical contexts.
Physics Reports, 528(2):47–89, 2013.

- [168] AN Ganshin, VB Efimov, GV Kolmakov, LP Mezhov-Deglin, and Peter VE McClintock.
Observation of an inverse energy cascade in developed acoustic turbulence in superfluid helium.
Physical Review Letters, 101(6):065303, 2008.
- [169] R Höhmann, U Kuhl, H-J Stöckmann, L Kaplan, and EJ Heller.
Freak waves in the linear regime: A microwave study.
Physical review letters, 104(9):093901, 2010.
- [170] H Bailung, SK Sharma, and Y Nakamura.
Observation of peregrine solitons in a multicomponent plasma with negative ions.
Physical review letters, 107(25):255005, 2011.
- [171] Yu V Bludov, VV Konotop, and Nail Akhmediev.
Matter rogue waves.
Physical Review A, 80(3):033610, 2009.
- [172] DR Solli, C Ropers, P Koonath, and B Jalali.
Optical rogue waves.
Nature, 450(7172):1054–1057, 2007.
- [173] A Montina, U Bortolozzo, S Residori, and FT Arcelli.
Non-gaussian statistics and extreme waves in a nonlinear optical cavity.
Phys. Rev. Lett., 103(17):173901, 2009.
- [174] Andreas Karsaklian Dal Bosco, Delphine Wolfersberger, and Marc Sciamanna.
Extreme events in time-delayed nonlinear optics.
Opt. Lett., 38(5):703–705, 2013.
- [175] Susanne Lehner and H Gunther.
Extreme wave statistics from radar data sets.
In *Geoscience and Remote Sensing Symposium, 2004. IGARSS'04. Proceedings. 2004 IEEE International*, volume 3, pages 1880–1883. IEEE, 2004.
- [176] Yaron Bromberg and Hui Cao.
Generating non-rayleigh speckles with tailored intensity statistics.

- Physical Review Letters*, 112(21):213904, 2014.
- [177] Marco Leonetti and Claudio Conti.
Observation of three dimensional optical rogue waves through obstacles.
Applied Physics Letters, 106(25):254103, 2015.
- [178] FT Arecchi, U Bortolozzo, A Montina, and S Residori.
Granularity and inhomogeneity are the joint generators of optical rogue waves.
Phys. Rev. Lett., 106(15):153901, 2011.
- [179] Nicolas Marsal, Vianney Caulet, Delphine Wolfersberger, and Marc Sciamanna.
Spatial rogue waves in a photorefractive pattern-forming system.
Opt. Lett., 39(12):3690–3693, 2014.
- [180] D Pierangeli, F Di Mei, C Conti, AJ Agranat, and E DelRe.
Spatial rogue waves in photorefractive ferroelectrics.
Physical review letters, 115(9):093901, 2015.
- [181] Simon Birkholz, Erik TJ Nibbering, Carsten Brée, Stefan Skupin, Ayhan Demircan, Goëry Genty, and Günter Steinmeyer.
Spatiotemporal rogue events in optical multiple filamentation.
Physical review letters, 111(24):243903, 2013.
- [182] Sergey Vergeles and Sergei K Turitsyn.
Optical rogue waves in telecommunication data streams.
Physical Review A, 83(6):061801, 2011.
- [183] Cristian Bonatto, Michael Feyereisen, Stéphane Barland, Massimo Giudici, Cristina Masoller, José R Rios Leite, and Jorge R Tredicce.
Deterministic optical rogue waves.
Phys. Rev. Lett., 107(5):053901, 2011.
- [184] Jose A Reinoso, Jordi Zamora-Munt, and Cristina Masoller.
Extreme intensity pulses in a semiconductor laser with a short external cavity.
Phys. Rev. E, 87(6):062913, 2013.

- [185] Daeyoung Choi, Michael J Wishon, J Barnoud, CY Chang, Y Bouazizi, A Lockett, and DS Citrin.
Low-frequency fluctuations in an external-cavity laser leading to extreme events.
Phys. Rev. E, 93(4):042216, 2016.
- [186] AR Osborne, M Onorato, and M Serio.
Nonlinear fourier analysis of deep-water, random surface waves: theoretical formulation and experimental observations of rogue waves.
In *Proc 14th Aha Huliko a Winter Workshop, Honolulu, Hawaii*, 2005.
- [187] Dayou Qian, Neda Cvijetic, Junqiang Hu, and Ting Wang.
108 gb/s ofdma-pom with polarization multiplexing and direct detection.
Journal of Lightwave Technology, 28(4):484–493, 2010.
- [188] M Sciamanna, C Masoller, F Rogister, P Mégret, NB Abraham, and M Blondel.
Fast pulsing dynamics of a vertical-cavity surface-emitting laser operating in the low-frequency fluctuation regime.
Phys. Rev. A., 68(1):015805, 2003.
- [189] Fabio Baronio, Antonio Degasperis, Matteo Conforti, and Stefan Wabnitz.
Solutions of the vector nonlinear schrödinger equations: evidence for deterministic rogue waves.
Phys. Rev. Lett., 109(4):044102, 2012.
- [190] S Residori, U Bortolozzo, A Montina, F Lenzini, and FT Arcchi.
Rogue waves in spatially extended optical systems.
Fluctuation and Noise Letters, 11(01):1240014, 2012.
- [191] C Lecaplain, Ph Grellu, JM Soto-Crespo, and Nail Akhmediev.
Dissipative rogue waves generated by chaotic pulse bunching in a mode-locked laser.
Phys. Rev. Lett., 108(23):233901, 2012.
- [192] Marcelo G Kovalsky, Alejandro A Hnilo, and Jorge R Tredicce.
Extreme events in the ti: sapphire laser.
Opt. Lett., 36(22):4449–4451, 2011.

- [193] Peter H Westfall.
Kurtosis as peakedness, 1905–2014. rip.
The American Statistician, 68(3):191–195, 2014.
- [194] Peter AEM Janssen.
Nonlinear four-wave interactions and freak waves.
Journal of Physical Oceanography, 33(4):863–884, 2003.
- [195] Nobuhito Mori and Peter AEM Janssen.
On kurtosis and occurrence probability of freak waves.
Journal of Physical Oceanography, 36(7):1471–1483, 2006.
- [196] Paul E Anderson, Henrik Jeldtoft Jensen, LP Oliveira, and Paolo Sibani.
Evolution in complex systems.
Complexity, 10(1):49–56, 2004.
- [197] Thomas O Richardson, Elva JH Robinson, Kim Christensen, Henrik J Jensen,
Nigel R Franks, and Ana B Sendova-Franks.
Record dynamics in ants.
PLoS one, 5(3):e9621, 2010.
- [198] Peter Müller, Chris Garrett, and A Osborne.
Rogue waves.
Oceanography, 18(3):66, 2005.
- [199] T Heil, I Fischer, and W Elsässer.
Coexistence of low-frequency fluctuations and stable emission on a single
high-gain mode in semiconductor lasers with external optical feedback.
Phys. Rev. A, 58(4):R2672, 1998.
- [200] G Huyet, JK White, AJ Kent, SP Hegarty, JV Moloney, and JG McInerney.
Dynamics of a semiconductor laser with optical feedback.
Phys. Rev. A, 60(2):1534, 1999.
- [201] K Ikeda, H Daido, and O Akimoto.
Optical turbulence: chaotic behavior of transmitted light from a ring cavity.
Physical Review Letters, 45(9):709, 1980.

- [202] K Ikeda, K Kondo, and O Akimoto.
Successive higher-harmonic bifurcations in systems with delayed feedback.
Physical review letters, 49(20):1467, 1982.
- [203] Shijun Jiang, Zeqi Pan, M Dagenais, RA Morgan, and K Kojima.
High-frequency polarization self-modulation in vertical-cavity surface-emitting lasers.
Applied physics letters, 63(26):3545–3547, 1993.
- [204] Hua Li, Angela Hohl, Athanasios Gavrielides, Hong Hou, and Kent D Choquette.
Stable polarization self-modulation in vertical-cavity surface-emitting lasers.
Applied physics letters, 72(19):2355–2357, 1998.
- [205] Neus Oliver, Miguel C Soriano, David W Sukow, and Ingo Fischer.
Dynamics of a semiconductor laser with polarization-rotated feedback and its utilization for random bit generation.
Optics letters, 36(23):4632–4634, 2011.
- [206] Fabien Rogister, Alexandre Locquet, Didier Pieroux, Marc Sciamanna, Olivier Deparis, Patrice Mégret, and Michel Blondel.
Secure communication scheme using chaotic laser diodes subject to incoherent optical feedback and incoherent optical injection.
Optics Letters, 26(19):1486–1488, 2001.
- [207] T Heil, A Uchida, P Davis, and T Aida.
Te-tm dynamics in a semiconductor laser subject to polarization-rotated optical feedback.
Physical Review A, 68(3):033811, 2003.
- [208] Athanasios Gavrielides, David W Sukow, Guinevere Burner, Taylor McLachlan, John Miller, and Jake Amonette.
Simple and complex square waves in an edge-emitting diode laser with polarization-rotated optical feedback.
Physical Review E, 81(5):056209, 2010.
- [209] David W Sukow, Taylor Gilfillan, Brenton Pope, Maria S Torre, Athanasios Gavrielides, and Cristina Masoller.

- Square-wave switching in vertical-cavity surface-emitting lasers with polarization-rotated optical feedback: Experiments and simulations. *Physical Review A*, 86(3):033818, 2012.
- [210] J Mulet, Massimo Giudici, Julien Javaloyes, and Salvatore Balle. Square-wave switching by crossed-polarization gain modulation in vertical-cavity semiconductor lasers. *Physical Review A*, 76(4):043801, 2007.
- [211] M Marconi, J Javaloyes, S Barland, M Giudici, and S Balle. Robust square-wave polarization switching in vertical-cavity surface-emitting lasers. *Physical Review A*, 87(1):013827, 2013.
- [212] David W Sukow, Athanasios Gavrielides, Thomas Erneux, Benjamin Mooneyham, Karen Lee, Jake McKay, and Josiah Davis. Asymmetric square waves in mutually coupled semiconductor lasers with orthogonal optical injection. *Physical Review E*, 81(2):025206, 2010.
- [213] Govind P Agrawal. Intensity dependence of the linewidth enhancement factor and its implications for semiconductor lasers. *IEEE Photonics Technology Letters*, 1(8):212–214, 1989.
- [214] K Panajotov, B Nagler, G Verschaffelt, A Georgievski, H Thienpont, J Danckaert, and I Veretennicoff. Impact of in-plane anisotropic strain on the polarization behavior of vertical-cavity surface-emitting lasers. *Applied Physics Letters*, 77(11):1590–1592, 2000.
- [215] Laurent Larger, Bogdan Penkovsky, and Yuri Maistrenko. Virtual chimera states for delayed-feedback systems. *Physical review letters*, 111(5):054103, 2013.
- [216] Laurent Larger, Bogdan Penkovsky, and Yuri Maistrenko. Laser chimeras as a paradigm for multistable patterns in complex systems.

Nature communications, 6:7752, 2015.

- [217] Steven Strogatz.
Sync: The emerging science of spontaneous order.
Penguin UK, 2004.
- [218] Hugh M Smith.
Synchronous flashing of fireflies.
Science, 82(2120):151–152, 1935.
- [219] Gregory D Vanwiggeren and Rajarshi Roy.
Communication with chaotic lasers.
Science, 279(5354):1198–1200, 1998.
- [220] Mark J Panaggio and Daniel M Abrams.
Chimera states: coexistence of coherence and incoherence in networks of
coupled oscillators.
Nonlinearity, 28(3):R67, 2015.
- [221] Daniel M Abrams and Steven H Strogatz.
Chimera states for coupled oscillators.
Physical review letters, 93(17):174102, 2004.
- [222] Daniel M Abrams and Steven H Strogatz.
Chimera states in a ring of nonlocally coupled oscillators.
International Journal of Bifurcation and Chaos, 16(01):21–37, 2006.
- [223] Yuri L Maistrenko, Anna Vasylenko, Oleksandr Sudakov, Roman Levchenko,
and Volodymyr L Maistrenko.
Cascades of multiheaded chimera states for coupled phase oscillators.
International Journal of Bifurcation and Chaos, 24(08):1440014, 2014.
- [224] Daniel M Abrams, Rennie Mirollo, Steven H Strogatz, and Daniel A Wiley.
Solvable model for chimera states of coupled oscillators.
Physical review letters, 101(8):084103, 2008.
- [225] Erik A Martens.

- Chimeras in a network of three oscillator populations with varying network topology.
Chaos: An Interdisciplinary Journal of Nonlinear Science, 20(4):043122, 2010.
- [226] Yoshiki Kuramoto and Shin-ichiro Shima.
Rotating spirals without phase singularity in reaction-diffusion systems.
Progress of Theoretical Physics Supplement, 150:115–125, 2003.
- [227] Erik A Martens, Carlo R Laing, and Steven H Strogatz.
Solvable model of spiral wave chimeras.
Physical review letters, 104(4):044101, 2010.
- [228] Mark J Panaggio and Daniel M Abrams.
Chimera states on a flat torus.
Physical review letters, 110(9):094102, 2013.
- [229] Mark R Tinsley, Simbarashe Nkomo, and Kenneth Showalter.
Chimera and phase-cluster states in populations of coupled chemical oscillators.
Nature Physics, 8(9):662, 2012.
- [230] AN Zaikin and AM Zhabotinsky.
Concentration wave propagation in two-dimensional liquid-phase self-oscillating system.
Nature, 225(5232):535, 1970.
- [231] Jan Frederik Tetz, Julian Rode, Mark R Tinsley, Kenneth Showalter, and Harald Engel.
Spiral wave chimera states in large populations of coupled chemical oscillators.
Nature Physics, 14(3):282, 2018.
- [232] Aaron M Hagerstrom, Thomas E Murphy, Rajarshi Roy, Philipp Hövel, Iryna Omelchenko, and Eckehard Schöll.
Experimental observation of chimeras in coupled-map lattices.
Nature Physics, 8(9):658, 2012.
- [233] C Huygens.
Oeuvres complètes.

Swets and Zeitlinger Publishers, 1967.

- [234] Erik Andreas Martens, Shashi Thutupalli, Antoine Fourrière, and Oskar Hallatschek.

Chimera states in mechanical oscillator networks.

Proceedings of the National Academy of Sciences, 110(26):10563–10567, 2013.

- [235] Tejas Kotwal, Xin Jiang, and Daniel M Abrams.

Connecting the kuramoto model and the chimera state.

Physical review letters, 119(26):264101, 2017.

- [236] Evgeny A Viktorov, Tatiana Habruseva, Stephen P Hegarty, Guillaume Huyet, and Bryan Kelleher.

Coherence and incoherence in an optical comb.

Physical review letters, 112(22):224101, 2014.

- [237] J Reichert, M Niering, R Holzwarth, M Weitz, Th Udem, and TW Hänsch.

Phase coherent vacuum-ultraviolet to radio frequency comparison with a mode-locked laser.

Physical Review Letters, 84(15):3232, 2000.

- [238] Th Udem, J Reichert, R Holzwarth, and TW Hänsch.

Absolute optical frequency measurement of the cesium d 1 line with a mode-locked laser.

Physical review letters, 82(18):3568, 1999.

- [239] JN Eckstein, AI Ferguson, and TW Hänsch.

High-resolution two-photon spectroscopy with picosecond light pulses.

Physical Review Letters, 40(13):847, 1978.

- [240] Kensuke Ikeda and Kenji Matsumoto.

High-dimensional chaotic behavior in systems with time-delayed feedback.

Physica D: Nonlinear Phenomena, 29(1-2):223–235, 1987.

- [241] K Ikeda and K Matsumoto.

Information theoretical characterization of turbulence.

Physical review letters, 62(19):2265, 1989.

- [242] FT Arecchi, G Giacomelli, A Lapucci, and R Meucci.
Two-dimensional representation of a delayed dynamical system.
Physical Review A, 45(7):R4225, 1992.
- [243] Giovanni Giacomelli and Antonio Politi.
Relationship between delayed and spatially extended dynamical systems.
Physical review letters, 76(15):2686, 1996.
- [244] Stefano Boccaletti, Jürgen Kurths, Grigory Osipov, DL Valladares, and CS Zhou.
The synchronization of chaotic systems.
Physics reports, 366(1-2):1–101, 2002.
- [245] Laurent Larger, Miguel C Soriano, Daniel Brunner, Lennert Appeltant, Jose M Gutiérrez, Luis Pesquera, Claudio R Mirasso, and Ingo Fischer.
Photonic information processing beyond turing: an optoelectronic implementation of reservoir computing.
Optics express, 20(3):3241–3249, 2012.
- [246] Bruno Garbin, Julien Javaloyes, Giovanna Tissoni, and Stéphane Barland.
Topological solitons as addressable phase bits in a driven laser.
Nature communications, 6:5915, 2015.
- [247] Michel Nizette.
Stability of square oscillations in a delayed-feedback system.
Physical Review E, 70(5):056204, 2004.
- [248] Vladimir Semenov, Anna Zakharova, Yuri Maistrenko, and Eckehard Schöll.
Delayed-feedback chimera states: Forced multiclusters and stochastic resonance.
EPL (Europhysics Letters), 115(1):10005, 2016.
- [249] Kensuke Ikeda.
Multiple-valued stationary state and its instability of the transmitted light by a ring cavity system.
Optics communications, 30(2):257–261, 1979.

- [250] A Zakharova, I Schneider, YN Kyrychko, KB Blyuss, Aneta Koseska, B Fiedler, and E Schöll.
Time delay control of symmetry-breaking primary and secondary oscillation death.
EPL (Europhysics Letters), 104(5):50004, 2013.
- [251] Eckehard Schöll, Sabine HL Klapp, and Philipp Hövel.
Control of self-organizing nonlinear systems.
Springer, 2016.
- [252] Felix P Kemeth, Sindre W Haugland, Lennart Schmidt, Ioannis G Kevrekidis, and Katharina Krischer.
A classification scheme for chimera states.
Chaos: An Interdisciplinary Journal of Nonlinear Science, 26(9):094815, 2016.
- [253] Cristina Masoller, David Sukow, Athanasios Gavrielides, and Marc Sciamanna.
Bifurcation to square-wave switching in orthogonally delay-coupled semiconductor lasers: Theory and experiment.
Physical Review A, 84(2):023838, 2011.
- [254] Fabian Böhm, Anna Zakharova, Eckehard Schöll, and Kathy Lüdge.
Amplitude-phase coupling drives chimera states in globally coupled laser networks.
Physical Review E, 91(4):040901, 2015.
- [255] Joniald Shena, Johanne Hizanidis, Vassilios Kovanis, and George P Tsironis.
Turbulent chimeras in large semiconductor laser arrays.
Scientific reports, 7:42116, 2017.
- [256] Chih-Ying Chen, Chih-Hao Cheng, Da-Kung Pan, and Fan-Yi Lin.
Experimental generation and analysis of chaos-modulated pulses for pulsed chaos lidar applications based on gain-switched semiconductor lasers subject to optical feedback.
Optics express, 26(16):20851–20860, 2018.

